Technische Universität München
Fakultät für Physik

Max-Planck-Institut für extraterrestrische Physik
European Southern Observatory

Gamma-ray bursts and their host galaxies

Cold gas and dust in the high-redshift interstellar medium

Jan Hendrik Bolmer

Vollständiger Abdruck der von der Fakultät für Physik der Technischen Universität München zur Erlangung des akademischen Grades eines

Doktor der Naturwissenschaften (Dr. rer. nat.)

genehmigten Dissertation.

Vorsitzender:		Prof. Dr. Alejandro Ibarra
Prüfer der Dissertation:	1.	Priv.-Doz. Dr. Jochen Greiner
	2.	Prof. Dr. Elisa Resconi

Die Dissertation wurde am 08.04.2019 bei der Technischen Universität München eingereicht und durch die Fakultät für Physik am 03.05.2019 angenommen.

Summary

One of the main research areas in astronomy deals with the cosmic evolution of galaxies and the interstellar medium (ISM). A specific subject aims at understanding the mass assembly of galaxies and their chemical enrichment from high to low redshift. The problem is that especially at very high redshifts it is impossible to resolve galaxies at the scales where the complicated processes of stellar nucleosynthesis, dust production, star formation, or feedback, are taking place. An alternative approach to emission based studies is thus to use bright quasars (QSOs) or gamma-ray bursts (GRBs) as background sources to study the illuminated regions in their line-of-sight in absorption.

The so-called damped Lyman-α systems (DLAs), apparent through their strong absorption features, are regularly detected in NIR/optical GRB afterglow spectra. These systems are associated with the early stages of galaxy evolution because they contain most of the neutral hydrogen in the universe and thus represent large reservoirs of gas available for star formation. Since GRBs are detected out to very high redshifts, the DLAs that are associated with their host galaxies, offer an ideal probe of the cold gas in star-forming regions in the early universe. By analyzing the amount and relative abundances of metals, molecules, and dust, based on the plethora of absorption features they imprint onto the simple, smooth and featureless, intrinsic power-law spectra of these sources, it is possible to study dust production mechanisms and the physical conditions of the diffuse ISM through cosmic time.

To measure the column densities of metals, molecules, and dust in GRB-DLAs, most of the previous studies relied on relatively old software, often based on least squares regression analysis techniques and χ^2 statistics. The issue is that these approaches can be very time consuming and naturally break down for a large number of free parameters or in case of strong degeneracies. Therefore, in order to effectively and consistently analyze the growing number of high-quality GRB spectra, an absorption line fitting library was developed for the purposes of this thesis. This library is entirely written in Python and is based on state-of-the-art Bayesian inference methods. It is easy to use, fast, and also easily extendable to, for example, emission line studies. The main ideas and features of the developed code are thus presented in Chapter 2 of this thesis.

In Chapter 3, GROND afterglow observations of GRBs at redshifts larger than $z > 4$ are presented, that are used to derive host galaxy dust column densities along their line-of-sight and to test if a supernovae-synthesized dust extinction curve is required for some of the bursts. Dust is known to be produced in the envelopes of asymptotic giant branch (AGB) stars, the expanded shells of supernovae (SN) remnants, as well as in situ grain growth within the ISM. However, the corresponding efficiency of each of these dust formation mechanisms at different redshifts remains a topic of debate. At redshifts $z \gtrsim 4$, it is widely believed that there was not enough time to form AGB stars in high numbers, hence the dust at this epoch is expected to be purely from SNe or subsequent grain growth in the ISM. The presented analysis shows that, in contrast to samples at mostly lower redshift, all of the GRB afterglows at $z > 4$ have a visual extinction of $A_V < 0.5$ mag

and that there is no evidence that the SN-like dust extinction curve provides a better fit to the data. Although the statistics are relatively low and the sample is likely biased, the fact that GRB host galaxies at $z > 4$ seem to contain less dust than at $z \sim 2$, could indicate a transition from SN-only dust to a mixture of both formation channels as is generally recognized in local galaxies.

In Chapter 4, a large sample of X-shooter GRB afterglow spectra for bursts at $z > 2$ is presented. This sample is used to study the metallicity and dust depletion effects in the neutral interstellar medium at high redshift and to answer the question of whether (and why) there might be a lack of molecular hydrogen in GRB-DLAs. It is found that absorption from H_2 is in fact detected in 6 out of the 22 GRB afterglow spectra with molecular fractions ranging between $f \simeq 5 \cdot 10^{-5}$ and $f \simeq 0.04$. These H_2-bearing GRB-DLAs are found to be associated with significant dust extinction, $A_V > 0.1$ mag, and dust-to-metals ratios $\mathcal{DTM} > 0.4$, confirming the importance of dust grains for the production of molecules. The overall fraction of H_2 detections in GRB-DLAs is $\geq 27\%$ (41% including three additional tentative detections), which is three to four times larger than in the general QSO-DLA population. For redshifts $2 < z < 4$, and considering column densities $\log N(\mathrm{H\,I}) > 21.7$, the H_2 detection fraction is 60–80% in GRB-DLAs and in extremely-strong QSO-DLAs. This can be explained by the fact that both GRB- and QSO-DLAs with high neutral hydrogen column densities are probed by sight-lines with small impact parameters, indicating that the absorbing gas is associated with the inner regions of the absorbing galaxy, where the gas pressure is higher, and the conversion of H I to H_2 takes place. In the case of GRB hosts, this diffuse molecular gas is located at distances $\gtrsim 500$ pc from the GRB and hence is unrelated to the star-forming region where the event occurred.

These results strengthen the importance of GRBs as probes of the diffuse molecular gas in the ISM of galaxies in the early universe. Therefore, in Chapter 5, the prospects for future research of the physical conditions in the identified H_2-bearing GRB-DLAs are outlined. Also, possible studies on the influence of the GRB on its surroundings are discussed.

Zusammenfassung

Eines der Hauptforschungsgebiete der Astronomie befasst sich mit der Evolution von Galaxien und dem Interstellaren Medium (ISM). Hierbei zielt ein spezifischer Themenbereich auf das Verständnis der Massenanreicherung von Galaxien und ihrer chemischen Entwicklung vom frühen Universum bis zum heutigen Zeitpunkt ab. Das Problem ist, dass es vor allem bei sehr hohen Rotverschiebungen unmöglich ist, Galaxien auf den Skalen aufzulösen, auf denen stellare Nukleosynthese, Staubproduktion, Sternentstehung oder *Feeback* Prozesse stattfinden. Ein alternativer Ansatz zu emissionsbasierten Studien ist es deshalb, helle Quasare (QSOs) oder *Gamma-Ray-Bursts* (GRBs) als Hintergrundquellen zu verwenden, um die von ihnen "durchleuchteten" Galaxien zu untersuchen. Die sogenannten *Damped Lyman-α-Systeme* (DLAs), die sich durch ihre starken Absorptionsmerkmale zeigen, werden regelmäßig in GRB Spektren nachgewiesen. Diese Systeme stehen im Zusammenhang mit frühen Stadien der Galaxienentwicklung, da sie den größten Teil des neutralen Wasserstoffs im Universum enthalten und somit große Gasreservoirs für die Entstehung von Sternen bereitstellen. Da GRBs bis zu sehr hohen Rotverschiebungen beobachtet werden können, bieten die mit ihren Muttergalaxien assoziierten DLAs eine ideale Möglichkeit, das kalte Gas in Sternentstehungsregionen des frühen Universums zu untersuchen. Durch Bestimmung der gesamten und relativen Menge an Metallen, Molekülen und Staub, lassen sich, basierend auf der Fülle an Absorptionslinien, die diese auf den relativ einfachen und strukturlosen intrinsischen Spektren dieser Quellen hinterlassen, Rückschlüsse auf Staubentstehung und die physikalischen Bedingungen in diffusem und molekularem Gas im ISM gewinnen.

Zur Messung der Säulendichte von Metallen, Molekülen und Staub in GRB-DLAs stützen sich die meisten Studien auf relativ alte Software, die häufig auf der Regressionsanalyse mit Methode der kleinsten Quadrate und χ^2-Statistiken beruht. Das Problem ist, dass diese Ansätze sehr zeitintensiv sein können und bei einer großen Anzahl freier Parameter oder bei starken Entartungen zwischen diesen unbrauchbar werden. Deshalb, und um die wachsende Anzahl hochwertiger GRB Spektren effektiv und konsistent zu analysieren, wurde für diese Dissertation eine Bibliothek zur Analyse von Absorptionslinien entwickelt. Diese Bibliothek ist vollständig in Python geschrieben und basiert auf dem neuesten Stand Bayesianischer "Fitting Methoden". Sie ist einfach zu bedienen, schnell und auch leicht erweiterbar, z. B. auf Emissionslinienstudien. Die wichtigsten Ideen und Attribute des entwickelten Codes werden daher in Kapitel 2 dieser Arbeit skizziert.

In Kapitel 3 werden GROND Beobachtungen von GRBs bei Rotverschiebungen von mehr als $z > 4$ vorgestellt. Diese werden dazu verwendet, den Staubgehalt entlang der Sichtlinie in der Muttergalaxie zu bestimmen und um zu testen, ob eine durch Supernovae synthetisierten Staub erklärbare Extinktionskurve erforderlich ist, um die Form der gemessenen Spektren zu erklären. Es ist bekannt, dass Staub in den Hüllen von asymptotischen Riesenzweigsternen (AGB), in den Überresten von Supernovae sowie durch in situ Wachstum innerhalb dem ISM erzeugt wird. Die entsprechende Effizienz jedes

dieser Staubbildungsmechanismen bei verschiedenen Rotverschiebungen ist jedoch ein umstrittenes Thema. Es wird allgemein angenommen, dass bei Rotverschiebungen $z \gtrsim 4$ nicht genügend Zeit zur Verfügung stand, um AGB-Sterne in hoher Anzahl zu bilden. Daher wird erwartet, dass der Staub in dieser Epoche allein vom SNe oder dem nachfolgenden Wachstum im ISM stammt. Die vorgelegte Analyse zeigt, dass im Gegensatz zu GRBs mit meist niedrigerer Rotverschiebung, alle GRBs bei $z > 4$ eine visuelles Extinktion von nur $A_V < 0.5$ mag aufweisen und dass es keinen Hinweis darauf gibt, dass die SN-artige Staub-Extinktionskurve einen besseren Fit an die Daten liefert. Obwohl das Sample relativ klein und wahrscheinlich unausgewogen ist, könnte die Tatsache, dass GRB-Muttergalaxien bei $z > 4$ weniger Staub enthalten als bei $z \sim 2$, auf einen Übergang von nur-SN-Staub zu einer Mischung beider Formationskanäle hinweisen. Sowie er von Galaxien im nahen Universum bekannt ist.

In Kapitel 4 wird ein Sample von X-Shooter Spektren für GRBs bei Rotverschiebung $z > 2$ vorgestellt. Dieses Sample wird dazu verwendet, die Metallizität und den Staubgehalt im neutralen ISM bei hoher Rotverschiebung zu untersuchen und um die Frage zu beantworten, ob (und warum) molekularer Wasserstoff nur selten in GRB-DLAs detektiert wird. Tatsächlich finden sich Absorptionslinien von H_2 in sechs der 22 GRB Spektren mit einem molekularen Anteil von $f \simeq 5 \cdot 10^{-5}$ bis $f \simeq 0.04$. Diese H_2-beinhaltenden GRB-DLAs zeigen außerdem einen signifikanten Staubgehalt, $A_V > 0,1$ mag, und Staub-zu-Metall-Verhältnisse von $\mathcal{DTM} > 0,4$, was die Bedeutung von Staub für die Produktion von Molekülen bestätigt. Der Gesamtanteil der H_2-Detektionen bei GRB-DLAs beträgt circa $\gtrsim 27\%$ (oder 41% einschließlich drei eventueller Detektionen) und ist damit drei- bis viermal so hoch wie der in der allgemeinen QSO-DLA-Population. Für Roteverschiebungen von $2 < z < 4$ und für Säulendichten größer als $\log N(\mathrm{H\,I}) > 21,7$ beträgt der Anteil H_2-beinhaltender GRB- und QSO-DLAs jeweils 60–80%, was durch die Tatsache erklärt werden kann, dass GRB- und QSO-DLAs mit hohen Säulendichten von neutralen Wasserstoff, Sichtlinien mit kleinen *impact*-Parametern entsprechen. Dies weist darauf hin, dass das absorbierende Gas in den inneren Bereichen der absorbierenden Galaxie zu finden ist, dort wo der Gasdruck höher ist und die Umwandlung von H I zu H_2 stattfindet. Im Fall von GRB-Muttergalaxien befindet sich dieses diffuse molekulare Gas vermutlich in einem Abstand von mehr als ~ 500 pc und steht daher in keinem Zusammenhang mit der sternbildenden Region, in der der GRB stattgefunden hat.

Diese Ergebnisse bekräftigen die Bedeutung von GRBs als Proben des diffusen, molekularen Gases im ISM von Galaxien des frühen Universums. Daher werden in Kapitel 5 die Aussichten für zukünftige Erforschung der physikalischen Bedingungen in den gefundenen, H_2-beinhaltenden GRB-DLAs skizziert. Des Weiteren werden mögliche Untersuchungen des Einflusses von GRBs auf ihre Umgebung diskutiert.

Contents

in memory of Harry Seeger

Chapter 1

Introduction

The purpose of this introduction is to outline the major concepts of the relevant astrophysical aspects of this work. As the goal of this thesis is to study the cold gas and dust in the interstellar medium of high-redshift galaxies, the topic is first embedded in the bigger picture of the evolution of galaxies and the chemical enrichment of the ISM, which is described in Sect. 1.1. Sect. 1.2 then provides an overview of the field of gamma-ray burst (GRB) science in general, because, in this thesis, GRBs are used as background sources to study the neutral gas and dust within their host galaxies line-of-sight. As shown in Sect. 1.3, metals, molecules, and dust usually imprint a plethora of absorption features onto the spectra of these sources, making it possible to study the physical conditions of diffuse molecular gas and star-forming regions in the early universe. Finally, in the last section of this Chapter (Sect. 1.4), some essential aspects of the used instrumentation are briefly described.

1.1 The interstellar medium and star formation

The interstellar medium (ISM) is broadly defined as the gas and dust between the stars, and it arguably represents one of the most crucial components of galaxies (e.g., Draine, 2011). The evolution of the content of heavy elements, that is elements heavier than hydrogen and helium, in the ISM, and especially their relative chemical abundances and spatial distribution, hold valuable information that is relevant to our understanding of the formation of stars and thus the cosmic evolution of galaxies (see Maiolino & Mannucci, 2019, for a recent review). The chemical enrichment of galaxies, from the first population of stars formed from pristine primordial gas to the stellar population and the ISM observed in local galaxies today, is understood as the result of a cosmic *baryon cycle*.

Besides hydrogen, deuterium, the majority of helium and a small fraction of lithium, which are created from primordial nucleosynthesis, almost all of the other known elements are produced by nuclear fusion reactions in stars or the explosive burning and photodisintegration associated with the end stages of stellar evolution. While, for example, oxygen is produced on relatively short timescales by the core-collapse of short-lived, massive stars, iron production is dominated by type Ia supernovae (SNe) and thus delayed relative oxygen. Other elements have contributions from both kinds of SNe and are also produced in the envelopes of asymptotic giant branch (AGB) stars, e.g., carbon. The

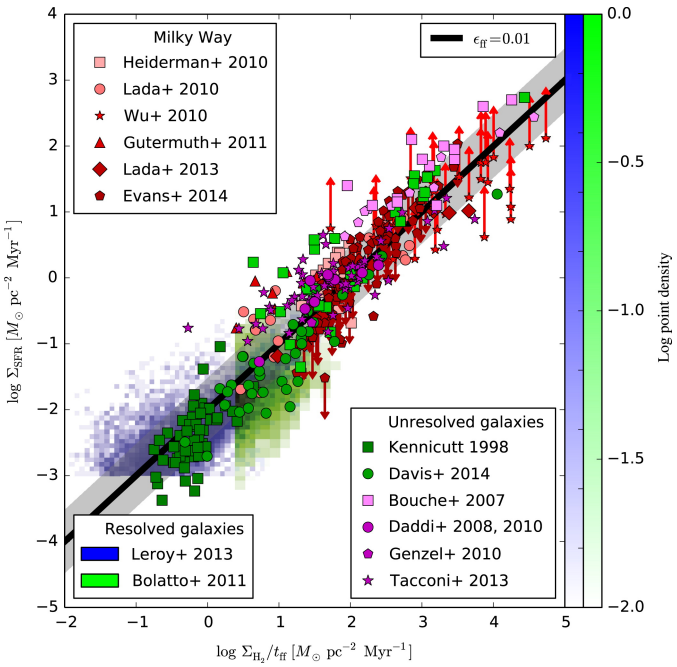

Figure 1.1: Surface density of star formation versus surface density of molecular gas normalized by estimating the free-fall time. The strong correlation found for galactic clouds, nearby galaxies, high-z disks, and starbursts is consistent with a simple, local, volumetric law of star formation, in which the star formation rate is simply about 1% of the molecular gas mass per local free-fall time (Krumholz et al., 2012). The figure is adapted from Krumholz (2014).

amount of metals injected into the ISM by each of these processes, the so-called *stellar yield*, thus highly depends on the progenitors mass, metallicity, and other properties.[1]

In the baryon cycle, the different stellar generations are thought to be connected through the ISM, where high mass stars lose many baryons out into the ISM which cool, form molecular clouds and collapse to form the next generation of stars. This cycle, however, is nowhere near a closed system. Cosmic inflows, galactic outflows, gas recycling, feedback from SNe and active galactic nuclei (AGN), as well as merger histories play a crucial role as well. Also, in contrast to dark matter, baryons are subject to complex processes like radiative transfer, dissipation, or dust depletion, which makes it very challenging to model the baryon cycle with computer simulations or to study these processes in distant, high-redshift galaxies.

Nevertheless, especially studies of star-forming regions within the Milky Way and other local galaxies, undoubtedly show that there is a strong correlation between the presence of molecular gas and star formation (Bigiel et al., 2008; Kennicutt & Evans, 2012; Leroy et al., 2013). For example, Krumholz et al. (2012) find a strong correlation between the surface density of star formation and the surface density of molecular gas normalized by

[1] In astronomy, the metallicity, that is the content of metals relative to the total mass of baryons, which is dominated by hydrogen and helium, is defined as $Z \equiv M_{\rm metals}/M_{\rm baryons}$.

estimated free-fall time (see Fig. 1.1). This correlation holds for different environments from galactic clouds, nearby galaxies, high-z disks, and starbursts, and is consistent with a simple, local, volumetric law of star formation, in which the star formation rate is simply about 1% of the molecular gas mass per local free-fall time. The efficiency of star formation is thus surprisingly low on galactic size and timescales, much lower than what would be expected if cold gas collapsed directly into stars (McKee & Ostriker, 2007; Utomo et al., 2018), indicating that galactic dynamics, magnetic fields, turbulence, and destructive feedback play important roles (e.g., Padoan et al., 2012; Meidt et al., 2018, and references therein). For molecular clouds with active star formation, or in the densest parts of star-forming clouds, higher values of $\epsilon_{\rm ff} = 10\%$ to 50% are observed (Murray, 2011; Evans et al., 2014; Lee et al., 2016; Raskutti et al., 2016).

Interstellar clouds are usually classified based on their temperature, density, dust, as well as molecular content (e.g., Draine, 2011). *Diffuse atomic clouds* are under the full influence of the interstellar radiation field so that most of the molecules and dust particles get destroyed by photo-dissociation. While hydrogen is mostly in its neutral form, atoms with lower ionization potentials are almost fully ionized. *Diffuse molecular clouds* contain more hydrogen and also some dust, creating an outer photo-dissociation region (PDR), which can provide shielding for the molecular hydrogen H_2 within the cloud. If even more protection from the interstellar radiation field is offered by large amounts of dust ($1 < A_V < 5$ mag) and high column densities of neutral and molecular hydrogen, i.e., in *translucent clouds*, also carbon starts to transition from its ionized atomic into the neutral atomic (C I) or molecular (CO) form. Finally, dense or *giant molecular clouds* (GMCs), which have a substantial dust content ($A_V > 5$ mag) and reach very low temperatures of 10 to 50 K, provide so much shielding that cosmic rays become the dominant source of ionization, such that carbon becomes almost entirely molecular and the electron abundance becomes increasingly low. As a consequence, the gas in these clouds becomes strongly self-gravitating, enabling the formation of stars.

An example of a dark molecular cloud is shown in Fig. 1.2. The upper right inset of this figure shows a typical illustration of the "onion" like structure. The outer blue ring is the PDR composed of mainly hydrogen and dust. The PDR shields the inner regions (red and black) of the GMC from the interstellar radiation field, enabling the formation of H_2. The formation process of H_2 is exothermic so that it is primarily formed on dust grain surfaces where the dust can act as a catalyst to take away some of the formation energy (Hollenbach et al., 1971; Cazaux & Spaans, 2004). This ring-like structure is seen in the observations from Zuo et al. (2018), showing that the CO emission comes only from an embedded region of the cloud (see the left and lower right panel in Fig. 1.2).

The problem with molecular clouds is that they can only be resolved within the Milky Way or other relatively nearby galaxies. In more distant galaxies, and especially at very high redshifts, during the early stages of chemical enrichment, it is only possible to measure galaxy integrated properties, and it is thus not possible to study the local scales that dominate the process of star formation.

However, another approach to study the physical conditions of the cold gas and dust in star formation regions in galaxies of the early universe is through the use of background

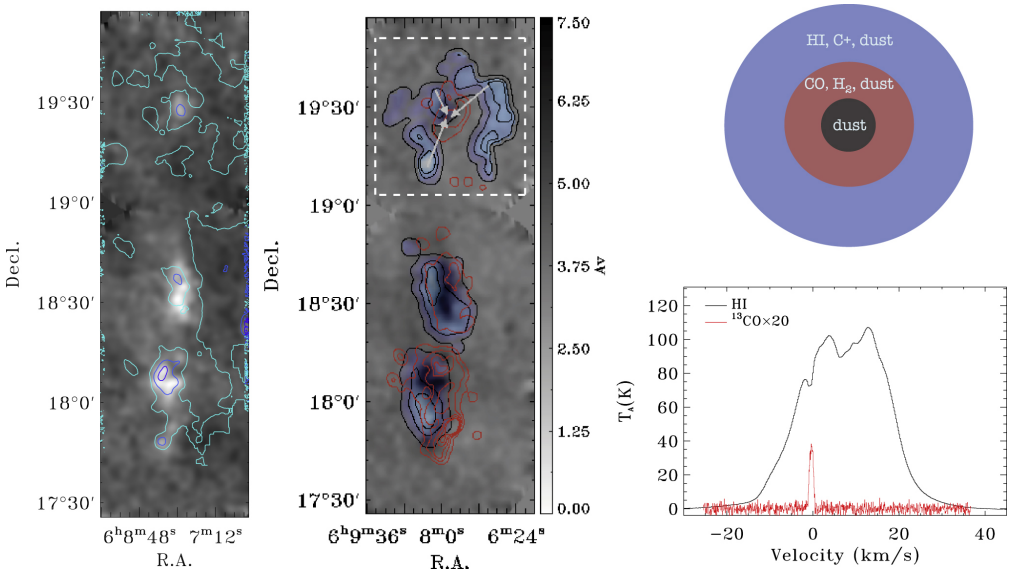

Figure 1.2: Example of a dark molecular cloud in the Milky Way. The left and middle insets show the 2MASS extinction overlaid with the dust temperature (light blue to dark blue are 12K, 13K, and 14K) and with the ratio of [H I]/[H_2] column densities (black contour and blue shadow) as well as [13CO]/[H2] column density (red), respectively. The upper right inset is an "onion" like model of the molecular cloud and the lower right inset shows the H I and ^{13}CO emission spectra of the source at Decl. 19°30′. The figure is adapted from Zuo et al. (2018).

sources like quasars or gamma-ray bursts. These luminous sources probe individual sight-lines through a galaxy and make it possible to measure the chemical abundances, trace dust production, or infer properties like density and temperature of individual star-forming regions. The analysis of absorption lines systems in the spectra of these sources are thus complementary to galaxy integrated emission measurements. As presented in this thesis, GRBs can, for example, be used to study dust production mechanism in the early universe (Sect. 3). Also, as shown in Sect. 4, H_2 is now commonly detected in GRB-DLAs, demonstrating that GRBs are ideal probes of the diffuse and possibly also translucent ISM in galaxies at redshift $z > 2$.

1.2 Gamma-ray bursts

Gamma-ray bursts (or γ-ray bursts, GRBs) are short, intense flashes of γ-rays that for a short moment in time outshine the entire galaxy in these wavelengths. Although the first GRBs were already detected in the late 1960s by US military satellites (Klebesadel et al., 1973), it took dedicated missions like BATSE on board of the Compton Gamma Ray Observatory and until 1997 to confirm the expected extra-galactic nature of these events (e.g., Metzger et al., 1997). Detections of a multi-wavelength, *afterglow* emission (Costa et al., 1997; van Paradijs et al., 1997; Frail et al., 1997) and accompanying supernovae (SNe) (Galama et al., 1998) pointed to a scenario, where GRBs are the result of the

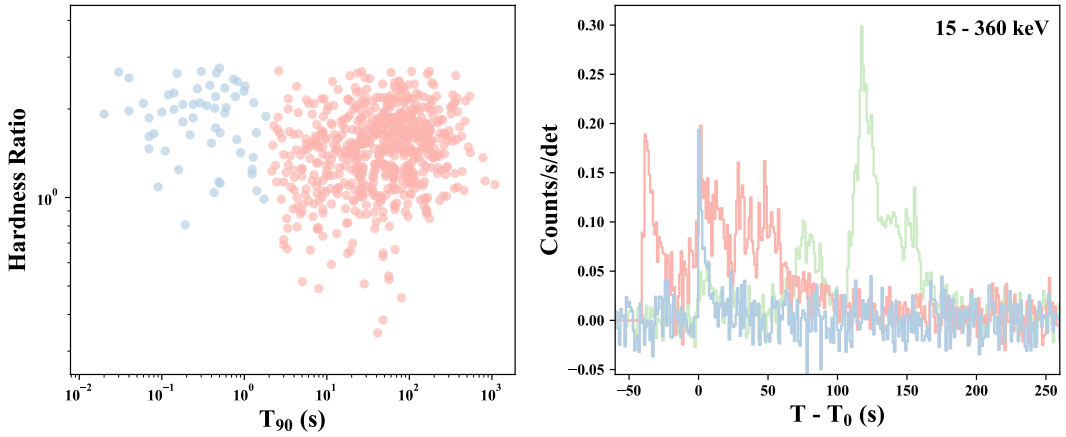

Figure 1.3: Hardness ratio versus duration of the prompt emission, T_{90}, for all GRBs observed with *Swift*/BAT until the end of 2012 (left, data taken from Baumgartner et al., 2013). A K-Means clustering algorithm (SKLEARN.CLUSTER.KMEANS) clearly identifies two groups of objects, short GRBs with a duration of $T_{90} < 2$ s (blue), and long GRBs with $T_{90} > 2$ s (red). The plot to the right shows three example GRB BAT light-curves, demonstrating the variability between different events and the existences of multiple peaks.

violent death of stars, now often referred to as the most extreme explosion in the Universe (energy release of about $\gtrsim 10^{51}$ ergs).

Now, more than 20 years later, and especially after the launch of the hugely successful Neil Gehrels *Swift* observatory (Gehrels et al., 2004), the field of GRB astronomy has undergone a revolution (e.g., Schady, 2017, for a recent review). Not only did the increasing number of follow-up observations, enabled by the arcsecond localization and rapid follow up with *Swift*, lead to rapid progress in understanding the physical processes governing these events (although many challenges remain), GRBs were also recognized to be ideal probes of the early Universe.

The following two sections thus provide an overview of the current understanding of the GRB phenomenon (Sect. 1.2.1), and how especially the long-duration variety of GRBs can be used as tools with which to study the cosmic history of star-formation and the ISM of high-redshift galaxies (Sect. 1.2.2). Hereby the focus lies on the most significant recent developments rather than the long-established results.

1.2.1 Observations and theory

The GRB prompt emission in γ-rays, which spans at least six orders of magnitude from 10^{-3} to 10^3 s, can be highly variable showing multiple peaks and substructures on a millisecond timescale (see Fig. 1.3). A measurement of the duration was thus defined as the time interval that contains 90% of the counts made by the detector, T_{90}. When looking at the hardness ratio, that is the fluence in, e.g., the $\sim 100 - 300$ keV divided by that in the $\sim 50 - 100$ keV energy band, and T_{90}, a bimodal distribution is seen. This bimodality led to the classifications of *"short-hard"* and *"long-soft"* bursts, and thus to

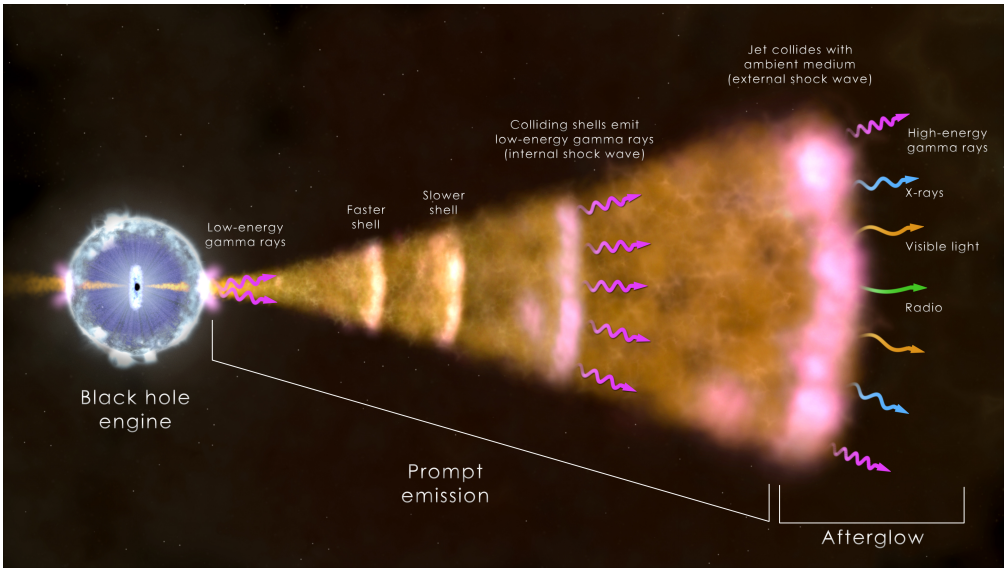

Figure 1.4: Illustration of the GRB fireball model. The core collapse of a massive star forms a black hole or magnetar with an accretion disk around it, which drives a relativistic jet into space. The observed prompt γ-ray and afterglow X-ray to radio lightcurves and spectra arise from the hot gas near the black hole, shell collisions within the jet, and from the jet's interaction with the ambient medium, that is the host ISM or progenitor wind (image obtained from NASA).

the idea that (at least) two different progenitor channels must exist; one for long GRBs (LGRBs) and one for short GRBs (SGRBs) (Melia, 2009, see also Fig. 1.3). Shortly after the prompt γ-ray detection and in the case that the GRB is well localized, emission in longer wavelengths, the so-called *afterglow*, can be observed from X-ray to radio frequencies (see Fig. 1.5).[2] The spectrum of the afterglow shows characteristic power-law segments that are connected by break frequencies, which was interpreted early on as evidence for a synchrotron origin of the emission (Sari et al., 1998; Granot & Sari, 2002).

Based on various theoretical arguments made from the detected prompt and afterglow emission as well as other direct evidence, it is now well established that LGRBs are caused by collapsing massive stars, whereas SGRBs are the result of merging compact binaries like two neutron stars or a neutron star with a black hole (more on the progenitors below).

First direct evidence, for the so-called *collapsar model* of LGRBs (Woosley, 1993), came from the detection of a broad-lined Type Ic SN associated with GRB 980425 (Galama et al., 1998, see also below). In this scenario, which is schematically illustrated in Fig. 1.4, the explosion mechanism is driven by the compact object that forms at the time of the collapse of the iron core of a massive star, leading to the formation of either a stellar-mass black hole (MacFadyen & Woosley, 1999) or a rapidly rotating neutron-star (a *magnetar*, Bucciantini et al., 2007, and references therein). After the collapse,

[2] For about $\sim 30\%$ of LGRBs no afterglow is detected at NIR/optical wavelength. Different studies (e.g., Greiner et al., 2011; Covino et al., 2013) showed that these *dark* bursts are obscured by substantial amounts of dust in their host galaxies line-of-sight.

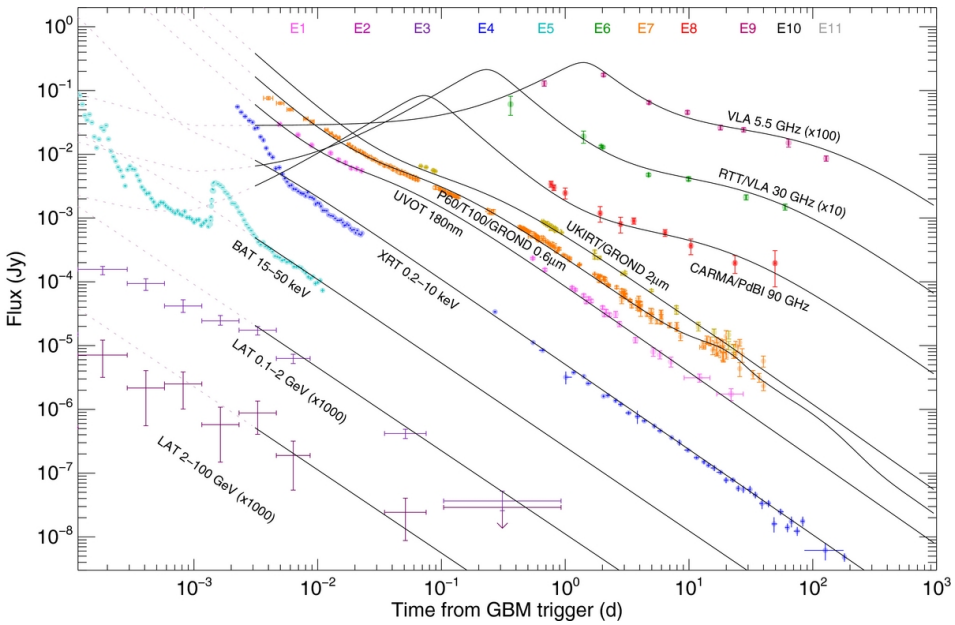

Figure 1.5: Multi-wavelength afterglow of GRB 130427A from 1 to 10^{16} GHz. The figure is taken from Perley et al. (2014).

an accretion disk develops around the compact object, ejecting relativistic shocks that are interacting with the circumburst environment. Since these relativistically expanding *fireballs* would convert most of their internal energy into kinetic energy of the entrained baryons, the outflow must interact with an ambient medium like the host ISM or the progenitor wind, that causes it to shock, in order to produce the observed afterglow radiation (e.g., Melia, 2009). While these *external shocks* can explain at least in part the observed synchrotron radiation at lower energies (see Fig. 1.4)[3], this relatively simple model fails to explain the large flares, unexpected plateau phases and chromatic breaks that are now commonly observed in X-ray, NIR/optical and radio afterglow light-curves (e.g., Schady, 2017; Ruffini et al., 2018).

Nevertheless, the most important aspect of the GRB afterglow for this thesis is that the spectral shape in the NIR/optical wavelength is generally best described by a simple power-law with index β, which is certainly the case in the standard forward-shock afterglow model. In this model, the decay and energy spectral indices α and β are defined by $F \propto (t)^{-\alpha}\nu^{-\beta}$. A simple power-law means that it is relatively easy to differentiate the afterglow radiation from the absorption features that are imprinted onto the spectra by intervening material like dust or gas.

[3]The prompt, i.e. very early γ- and X-ray, emission require a different explanation like multiple *internal shocks* or mini-jets (Burgess et al., 2018)

LGRB progenitors and their host galaxies [4]

Much research currently focuses on the progenitors of LGRBs. As mentioned before, the association of LGRBs with the death of massive stars is now proven beyond any reasonable doubt (Woosley & Bloom, 2006). Since the first groundbreaking detections of accompanying SNe to GRB 980425 (Galama et al., 1998, Fig. 1.6) and 030329 (Hjorth et al., 2003), there are now more than 40 known events that are spatially and temporally connected to broad-lined Ic SNe (SNe Ic-BL), although only a dozen of them are confirmed spectroscopically (Modjaz et al., 2016). SNe Ic-BL are known to be the result of the core-collapse of massive ($M \gtrsim 10 M_{\odot}$), Wolfe-Rayet (WR) type stars, that lost their hydrogen and helium envelopes previous to the explosion (see, e.g., Cano et al., 2017, for a recent review on the *GRB-SN connection*).[5] Spectroscopic observations of the accompanying SN are only possible for GRBs at $z \lesssim 1$ (e.g., Xu, de Ugarte Postigo et al., 2013; D'Elia et al., 2015), where it is possible to detect the photometric SN signature as a contribution to the late time luminosity of the afterglow. While for almost all such GRBs *SN bumps* are observed after a couple of days, there are three exceptional cases for which, despite deep follow-up observations, no accompanying SN could be identified (Fynbo, Watson et al., 2006; Tanga et al., 2018; MichałowskI et al., 2018). Although these authors have good arguments that these SN-less GRBs might require a different type of progenitor, it is worth noticing that none of these GRBs has a redshift directly measured from afterglow spectroscopy. Also, miss-identifications of the low-redshift hosts are unlikely but still possible, and the non-identification of an accompanying SN could also be explained by large amounts of absorbing dust in a scenario where these GRBs exploded in a dwarf companion located behind the potential host galaxies.

On the other hand, the fact that not all SNe Ic-BL produce a GRB suggests that GRB progenitors require unique properties, such as a high angular momentum, possibly near the critical rotation rate (e.g., Burrows et al. (2007); see also Dessart et al. (2017); Barnes et al. (2018) for more recent considerations based on GRB and Ic-BL SNe progenitors). Such a GRB progenitor candidate was recently found by Callingham et al. (2019): a massive WR star in a binary system, that lost its hydrogen envelope due to extremely anisotropic winds. The launch of such winds should usually decrease the angular momentum required to power a GRB, which could in this case, however, be contained from the interaction with the stellar companion. These results thus suggest that at least some LGRB progenitors are formed in binary systems.

Besides the knowledge gained from multi-wavelength light-curve and spectral modeling of afterglow and accompanying supernovae light, other clues about the properties and

[4] In the case of SGRBs, it was long speculated that they were formed from the binary NS-NS or NS-BH merger (see, e.g., Berger, 2014, for a review on SGRBs). For example, their host galaxies are often ellipticals and no accompanying SNe are found, indicating that SGRBs cannot be related to massive stars (Gehrels et al., 2005; Barthelmy et al., 2005; D. B. Fox et al., 2005). In 2017, the detection of gravitational waves from the merger of two neutron stars and the simultaneous detection of an SGRB, set an end to these speculations (LIGO Scientific Collaboration & Virgo Collaboration, 2017, unless there are more than one type of sGRB.).

[5] None of the observed GRB-SN spectra shows evidence for hydrogen or helium (see, e.g., Modjaz et al., 2016).

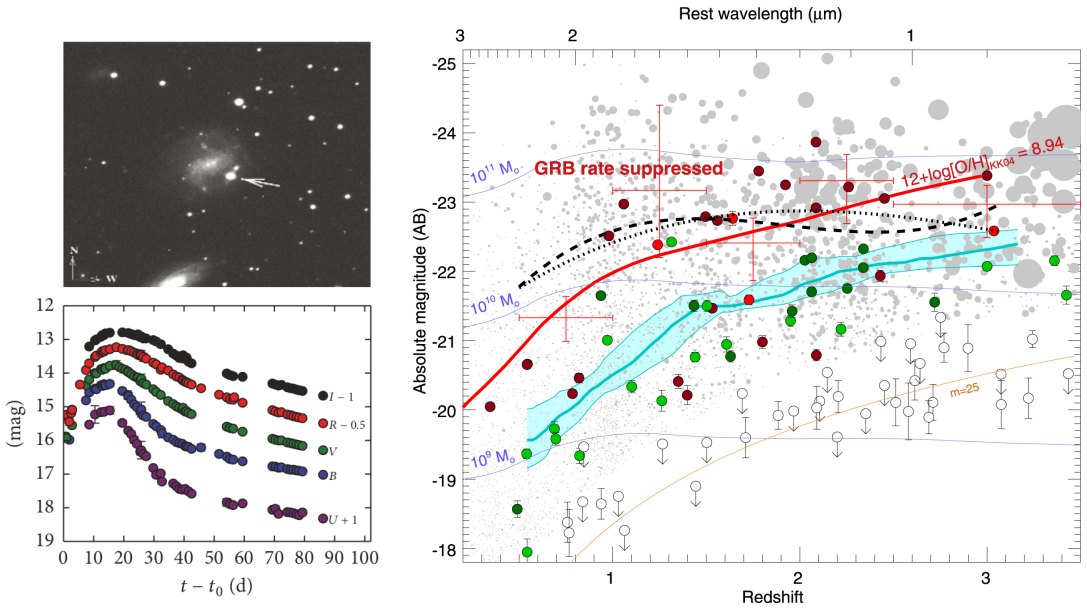

(a) SN 1998bw Type Ic associated with GRB 980425. Figure taken from Cano et al. (2017).

(b) Absolute magnitude versus redshift of GRB host galaxies (colored) in comparison to field galaxies (gray). Figure taken from Perley, Tanvir et al. (2016).

Figure 1.6: Knowledge about GRB progenitors comes from (a) observations of the accompanying SN, or (b) from host galaxy properties. The solid red curve in the right figure shows the apparent threshold of GRB production for a metallicity of $\log[\mathrm{O/H}] = 8.94$ (converted to luminosity).

formation of GRB progenitors can come from observations of their host galaxies and birthplaces.

Unlike for nearby core-collapse supernovae, for which high-resolution pre-explosion images of the host galaxies are available in some cases, such that the progenitors can be studied directly (Smartt, 2015), GRBs are at cosmological distances and also much rarer. There are currently only about a few known events at $0.01 < z < 0.3$, where at least the progenitor star-forming region can be resolved with IFU data (e.g., Krühler et al., 2017; Izzo et al., 2017, for hosts at $z < 0.1$), but otherwise we are restricted to measurements of host integrated properties (e.g., Perley, Krühler et al., 2016). Since the metal content of the progenitor star, which was suggested to be relatively low ($Z \lesssim 0.2\,Z_\odot$, Hirschi et al., 2005; Yoon & Langer, 2005; Woosley & Bloom, 2006, to maintain high angular momentum), might play a significant role in the formation of an LGRB, a lot of research was focused on measuring the metallicities of GRB host galaxies. And indeed, except for a handful of cases (see Sect. 1.2.2), the metallicities of the host galaxies are found to be sub-solar, suggesting a mild threshold at about $Z \sim 0.3$ to $0.6\,Z_\odot$ for LGRB production (e.g., Krühler et al., 2015; Perley, Tanvir et al., 2016; Bignone et al., 2017, see Fig. 1.6

and also Sect. 1.2.2).[6] This metallicity threshold, however, is still higher than what is expected from the standard collapsar model. Possible explanations are a significant differential rotation of the progenitor star (Georgy et al., 2012), or, as suggested earlier, that LGRBs are produced from stars in binary systems: for example, critically rotating single helium stars, that are the result of a post-main-sequence merger of cluster binaries with almost equal-mass components (van den Heuvel & Portegies Zwart (2013); see also Petrovic et al. (2005) or Izzard et al. (2004) for other binary system models).[7]

In the future, more spatially resolved spectroscopic observations of GRB host galaxies are required to learn more about the environmental conditions, that is the physical properties of the stellar populations, that enable the formation of the LGRB progenitors.

Finally, there is now also increasing evidence for a newly identified class of so-called ultra-long GRBs (ULGRBs, Levan et al., 2014; Evans et al., 2014), for which the prompt γ-ray emission lasts for more than one and up to $\sim$ 20 ks (e.g. GRB 091024A (Virgili et al., 2013), 101225A (Thöne et al., 2011), 111209A (Greiner, Mazzali et al., 2015), 121027A Hou et al. (2014), and 130925A (Greiner et al., 2014; Schady et al., 2015)). It is not yet clear whether different channels of LGRB formation exist, or if we see the tail of the duration distribution (as suggested by, e.g., Virgili et al., 2013), which is hard to detect due to the Earth-limb constraint of the γ-ray satellites such as *Swift*. Different progenitors for ULGRBs have been suggested, ranging from tidal disruption events (TDEs), magnetars, and low-metallicity blue supergiants. While TDEs are basically ruled out from the fact that GRB 130925A was observed with an explicit offset to the galactic center (Schady et al., 2015), GRB 111209A and its associated SN 2011kl are in favor of another explanation (Greiner, Mazzali et al., 2015). The spectral shape of SN 2011kl resembled that of superluminous supernovae (SLSNe, e.g, Quimby et al., 2011; Gal-Yam, 2018), suggesting that a link between these two phenomena exists, such as the scenario where extra energy is injected from a common magnetar central engine (the light-curves of SN 2011kl are not consistent with those observed for SN associated with the death of blue supergiants).

The field of GRB research has recently also entered the now so often called *era of multi-messenger astronomy*, meaning that, in addition to the already broad γ-ray to radio wavelength coverage, these events have now also been observed with gravitational wave detectors (LIGO/Virgo, LIGO Scientific Collaboration & Virgo Collaboration, 2017) and also at sub-TeV energies with the MAGIC Cherenkov Telescopes (Mirzoyan, 2019). Especially the detection of gravitational waves from the merger of two neutron stars provided the first direct evidence for the progenitors of short GRBs, which result in a kilonova that leads to the production of r-process elements (Smartt et al., 2017; Pian et al., 2017).

[6] Similar evidence comes from the studies of Japelj et al. (2016); Arabsalmani, Møller et al. (2018), who find that GRB hosts appear to track the mass-metallicity relation of the general population of star-forming galaxies at $z = 2.6$, but only with a small offset towards lower metallicities.

[7] Alternatively, it is possible that the oxygen abundances often used to determine the host metallicity, are overestimated by $\sim$ 0.2 to 0.5 dex.

1.2.2 GRBs as probes of the early Universe

While GRBs are interesting physical phenomena themselves, their cosmic distances also make them powerful probes of the early Universe.

For example, as a result of their extremely high luminosities, GRBs can be detected at very high redshift ($z > 6$), where they point to a region of star-formation, irrespective of their host galaxies magnitude, mass, and size, and therefore act as direct, dust-independent messengers of early stars and galaxies during the era of reionization or even before (Lamb & Reichart, 2000). So, although the number of GRBs identified at $z > 6$ remains small, they can offer an independent measure of the contribution to cosmic star-formation from the first galaxies and an understanding of the population of high-redshift galaxies in general, complementary to, for example, deep field observations (e.g. Bouwens et al., 2012). Additionally, GRBs are the only signals of individual stars currently available from these redshifts.

To date, the four most distant GRBs known are GRB 090423 at $z = 8.26$ (Tanvir et al., 2009), 090429 at $z \sim 9.4$ (Cucchiara et al., 2011), 100905A at $z \sim 7.9$ (Bolmer et al., 2018), and 120923A at $z \sim 7.8$ (Tanvir et al., 2018). The host galaxies of none of these GRBs could be detected (e.g., Tanvir et al., 2012). McGuire et al. (2016), however, observed three GRB host galaxies at redshifts $z = 5.913$ (GRB 130606A), $z = 6.295$ (GRB 050904), and $z = 6.327$ (GRB 140515A) with the HST, finding that their half-light radii and luminosities are consistent with those of Lyman-break galaxies at $z \sim 6$. These results support the proposition that the bulk of star formation, and hence integrated UV luminosity at $z > 6$, arises in galaxies below the detection limits of deep-field observations (see also Tanvir et al., 2012).

There are a couple of reasons why only a handful of very high-redshift GRBs have been observed to date. On the one hand, only the brightest bursts at $z > 6$, with $\log L_{\gamma,\mathrm{iso}}/\mathrm{ergs}^{-1} > 52$, can be detected by *Swift*/BAT (see Fig. 7 in Tanvir et al., 2018). On the other hand, the redshift of these bursts can then only be determined if they are rapidly observed and detected in the NIR bands.[8] An additional hindrance to detect GRBs at high redshift is the dust in their host galaxies line-of-sight. Although recent studies find evidence that GRBs at $z > 4$ show less dust extinction than at lower redshift (Bolmer et al., 2018; Zafar, Møller et al., 2018), only small amounts of dust are sufficient to make a detection impossible at NIR/optical wavelength, even with 8-m telescopes.

Another question is, whether GRB host galaxies indeed sample the general population of star-forming galaxies, as was, for example, suggested by Savaglio et al. (2009), or if a metallicity threshold for the formation of LGRB progenitors exists. For example, recent studies show that, although a handful of GRBs are associated with near-solar or super-solar metallicity environments (e.g., Krühler et al., 2012; Savaglio et al., 2012; Elliott et al., 2013; Schady et al., 2015)[9], GRBs in general seem to favour low metallicities

[8] It is likely that other GRBs at $z > 6$ are already contained in, for example, the *Swift* sample. However, they were not luminous enough in the NIR/optical wavelength, such that their redshift could not be determined from absorption lines or a photometric drop-out due to the Lyman-α forest.

[9] The previous claim of a high-metallicity host environment for the GRB 020819, turned out to be the result of a misidentification of the host galaxy (Perley et al., 2017).

(Graham & Fruchter, 2013; Vergani et al., 2015) and thus follow star formation only below a threshold of about 1/2 to 1/3 solar metallicity (Krühler et al., 2015; Schady et al., 2015; Perley, Tanvir et al., 2016; Vergani et al., 2017; Graham & Fruchter, 2017). At high redshifts ($3 < z < 5$), however, where galaxies had less time for the built up of metals, GRB host galaxies were shown to indeed trace UV metrics of Lyman Break Galaxies, (Greiner, Fox et al., 2015), strengthening their use as independent probes of star formation in the early Universe.

Similar to QSOs (e.g., Fan et al., 2006), high-redshift GRBs can also be used to directly study the epoch of reionization (EoR), corresponding to $6 < z < 10$ (McGreer et al., 2015; Planck Collaboration, 2016). The EoR is the period over which the ionizing radiation from the first stars and galaxies led to the second major phase change of hydrogen in the Universe, that consequently became transparent again. The last neutral patches of the IGM absorb photons and cause long stretches of negligible flux, the so-called *Gunn-Peterson troughs*, in the spectra of very distant QSOs and GRBs ($z > 6$), which can be used to map the ionization fraction of the IGM and thus the time and duration of the, likely complex, process of reionization (e.g., Greiner, Krühler, Fynbo et al., 2009). GRBs have some advantages, but also some disadvantages compared to QSOs. GRBs have a very simple intrinsic spectrum, that is easier to model than the emission of a QSO (e.g., Greig et al., 2017), and during the first couple of hours, they are much brighter than any known QSO at $z > 6$. However, as mentioned before, only a handful of very high-redshift GRBs have been observed to date, and for only a fraction of them an analysis of the absorption imprinted by the IGM was possible (Chornock et al., 2013, 2014; Totani et al., 2006; Totani et al., 2014). Additionally, the majority of GRB afterglow spectra show very high hydrogen column densities that are associated with the host galaxy, which makes it harder to measure the opacity of the IGM. Nevertheless, the obtained results are comparable to those found from quasar spectra, that is that the process of re-ionization must have ended between $5.5 < z < 6$.

While being a hindrance when trying to measure the opacity of the high redshift IGM, the neutral hydrogen column densities associated with GRB host galaxies can alternatively be used to determine the average escape fraction, $f_{\rm esc}$, of Lyman limit photons produced by stars (Chen et al., 2007; Fynbo et al., 2009). Only if enough photons, i.e., $f_{\rm esc} > 0.1 - 0.2$, at this limit can leave the virial radius of the galaxy, the UV light of the first galaxies alone is sufficient to be responsible for the reionization of the IGM (Robertson et al., 2015; Tanvir et al., 2019). The problem is that the high-redshift galaxies found in the Hubble Ultra Deep Field or those magnified by the Hubble Frontier Fields clusters are not numerous enough to to explain the process of reionization. The rest of the required ionizing radiation is thus normally attributed to the faint end of the luminosity function, i.e., faint galaxies that are below the detection thresholds of the current instrumentation (e.g., Bouwens et al., 2015; Livermore et al., 2017; Hansen & Haiman, 2004). Recently, Tanvir et al. (2019) determined an average escape fraction of $f_{\rm esc} = 0.005$, based on observations of a sample of 140 GRBs at $1.7 < z < 6.7$, suggesting that stars provide only a small contribution to the ionization budget at $z < 5$, which is particularly a problem for the above mentioned hypothesis that low-metallicity dwarf

galaxies with high specific star formation rates dominate the process. Other sources that could potentially contribute to the process of reionization are faint QSOs, X-ray binaries, or even decaying/annihilating particles (e.g., Khaire et al., 2016; Madau & Fragos, 2017; Hansen & Haiman, 2004).

GRBs and their host galaxies can also be used to shed light on galaxy formation and the cosmic evolution of the ISM, by making use of the possibility to combine absorption line and emission line studies, made possible though the fading nature these events. For example, Arabsalmani, Møller et al. (2018) studied the relations between metallicity, stellar mass, and gas kinematics of GRB host galaxies at $0.3 < z < 3.4$ and find, that the correlation between velocity and metallicity has a much smaller scatter for emission than for absorption lines, indicating that individual sight-lines are not representative of the overall properties of the host galaxy, like stellar mass or metallicity. In theory, as previously suggested by other authors, the metallicities inferred from the absorption lines imprinted by the ISM in the line-of-sight of the host, could be used to calibrate the commonly used emission line diagnostics (Castro-Tirado et al., 2010). These emission line diagnostics use ratios of strong emission lines (like [OII] or [OIII] to Hα or Hβ) to derive an oxygen abundance $12 + \log \mathrm{O/H}$ as a measure of the metal content. The problem is that these diagnostics depend on a proper calibration and can differ by 0.7 dex for the same galaxies (Kewley & Ellison, 2008). The idea to use GRBs to calibrate these emission line diagnostics is the following: at redshift $z > 1.7$, the Lyman-α line is shifted into the UV and the neutral hydrogen column density in the host galaxies line-of-sight can be measured in order to directly determine the metallicity [X/H], with X usually being Zn or S. For redshifts $z < 3$, where most emission lines are not yet shifted into the NIR, this absorption based metallicity can be compared to the one inferred from strong-line diagnostics, typically based on physical conditions present in low-redshift galaxies (e.g. Maiolino et al., 2008; Steidel et al., 2014). One issue is, that both methods trace the metal enrichment of the gas in different regions of galaxy. While the absorption method probes the metal enrichment of gas extended to the outer regions of the GRB host galaxy, the metallicity measured from emission lines is integrated over all star-forming H II regions of the host. So far, for only one burst, GRB 121024A at $z = 2.30$ (Friis et al., 2015), it was possible to simultaneously determine the metallicity of the host galaxy from both, afterglow absorption lines as well as strong emission-line diagnostics. For this fairly massive host, with $\log(M_\star/M_\odot) \sim 10$, these measured metallicities are indeed consistent.[10] From the samples of Selsing et al. (2018) (absorption) and Krühler et al. (2015) (emission) one can estimate that the comparison of emission and absorption line metallicities should be possible for another ~ 20 objects, which would be an interesting future project.

The absorption features imprinted on the afterglow spectrum by the ISM of the host galaxies, that is from gas, dust, and molecules, are the main subject of this thesis and their

[10] MUSE observations of the host of GRB 980425 associated with SN 1998bw also suggest that the typical offsets (several kpc) between GRBs and their host galaxies center should have a relatively small impact on the abundance determination for higher redshift GRB sites (Krühler et al., 2017).

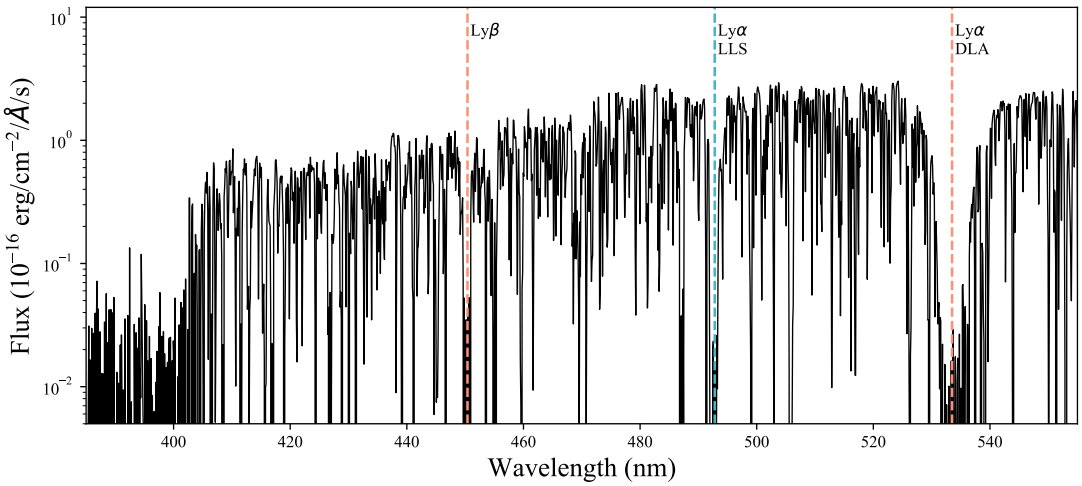

Figure 1.7: X-shooter spectrum of QSO [HB89] 0000-263 (Sánchez-Ramírez et al., 2016). A strong absorber at $z = 3.390$ with $\log N(\mathrm{H\,I}) > 20.3$, classified as a DLA, and a Lyman Limit system at $z = 3.055$ with $\log N(\mathrm{H\,I}) \sim 19$, are indicated by the dashed lines.

relevance for a variety of astrophysical research fields are thus outlined in the following section.

1.3 Damped Lyman-α systems and GRB host galaxies in absorption

Neutral hydrogen gas can be detected in the line-of-sight toward QSOs and GRBs, based on the relatively strong Lyman-α absorption feature that it imprints onto the spectra of these sources (see Fig. 1.7). These absorption systems that contain most of the neutral hydrogen in the universe are associated with the early stages of galaxy and star formation (McKee & Ostriker, 2007). Fig. 1.8 shows the neutral hydrogen column density distribution function, $f(N(\mathrm{H\,I}), z)$, at redshift $z \sim 3$, which is defined as the number of Lyman-α lines per unit column density $dN(\mathrm{H\,I})$, per unit absorption distance dX (e.g., Altay et al., 2011; Sánchez-Ramírez et al., 2016). This function, $f(N_{\mathrm{H\,I}}, z)$, displays two characteristic features: a flattening above $\log N(\mathrm{H\,I}) \gtrsim 17.2$ and a subsequent steepening around $\log N(\mathrm{H\,I}) \gtrsim 20.3$.

The more hydrogen a system contains the more shielding is provided against ionizing radiation, explaining the flattening of the curve at $\log N(\mathrm{H\,I}) \gtrsim 17.2$. Once a specific column density is reached, i.e., $\log N(\mathrm{H\,I}) \gtrsim 20.3$, the gas becomes almost entirely neutral, enabling the production of dust and molecules. This transition from H I to H_2 effectively steepens the H I column density distribution function and determines the high-end cutoff at $\log N(\mathrm{H\,I}) \sim 22.5$. As shown in Fig. 1.8, the three different categories of absorption systems, as defined by these characteristic features, are referred to as the *Lyman-α forest*, *Lyman Limit*, and *Damped Lyman-α systems*.

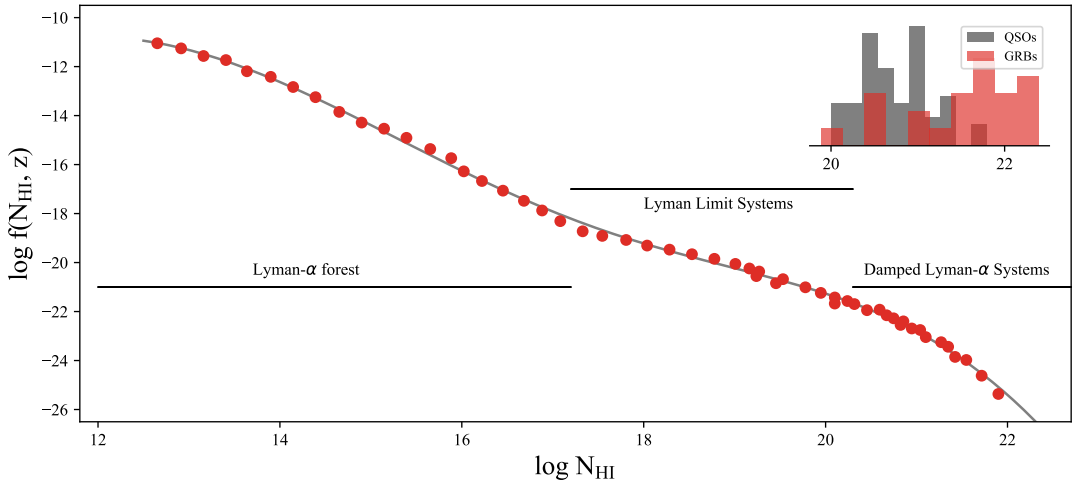

Figure 1.8: H I column density distribution function, $f(N(\mathrm{H\,I}), z)$, at $z \sim 3$ (based on the data from Altay et al. (2011) and references therein). The function show a characteristic flattening above $\log N(\mathrm{H\,I}) > 17.2$ and a steepening around $\log N(\mathrm{H\,I}) > 20.3$, caused by increased self-shielding and the transformation of H I to H_2, respectively. The inset shows two histograms over $\log N(\mathrm{H\,I})$ for the QSO-DLAs sample from Noterdaeme et al. (2008) and the GRB-DLAs from (Bolmer, J. et al., 2019, Sect. 4), as labeled.

Lyman limit systems (LLSs) with column densities $17.2 \lesssim \log N(\mathrm{H\,I}) \lesssim 20.3$, are likely associated with cold gas streams accreting toward galaxies, galactic winds, pristine gas in the IGM, or the remnants of low-energy SNe from (likely low-mass) Population III stars (e.g., Wiseman, Perley et al., 2017; Rahmani et al., 2018; Robert et al., 2019). Systems with $\log N(\mathrm{H\,I}) < 17.2$ are referred to as the Lyman-α forest (e.g., Kim et al., 2002), because they imprint a plethora of lines onto the spectra of QSOs and GRBs. This Lyman-α forest is a natural consequence of the web-like distribution of matter from ΛCDM cosmological models, and its evolution is governed by the Hubble expansion and the ionizing UV background flux (Bolton et al., 2017).

The subject of this thesis are Damped Lyman-α systems (DLAs, see Wolfe et al., 2005, for a standard review). From the ground, they can only be detected at redshift $z \gtrsim 1.7$, where the Lyman-α line is shifted into the ultraviolet band of, e.g., X-shooter (Vernet et al., 2011, see also Sect. 1.4.3). DLAs are usually associated with galaxies, where they probe the neutral ISM, i.e., the gas that is dominated by H I and singly ionized metals, having relatively small velocities (few hundred km/s), and also a negligible ionization fraction ($< 2\%$; De Cia, 2018, and referenced therein). While QSOs sample random galaxies in their line-of-sight, GRB-DLAs are usually associated with the host galaxy. This difference becomes apparent when looking at the distribution of $\log N(\mathrm{H\,I})$ for samples of QSO and GRB DLAs (see Fig. 1.8). On average, GRBs probe higher column densities (Fynbo et al., 2009; Tanvir et al., 2019), because they tend to originate from the inner regions of their host galaxy (Fruchter et al., 2006; Lyman et al., 2017) where the gas pressure is higher, and star-formation takes place. QSOs on the other hand,

as random background sources, are more likely to probe the outer regions of foreground galaxies (quantified with the *impact parameter*, e.g., Arabsalmani et al., 2015).

Besides Lyman-α, one usually detects a wealth of other rest-frame ultra-violet absorption lines imprinted onto the QSO and GRB spectra (Christensen et al., 2011), predominantly from singly-ionized metal species, residing in the cold, neutral gas associated with the DLA (S II, Fe II, Mg II, Si II, Zn II, Cr II etc.).[11] For each of these species, it is possible to measure the column density $N(\mathrm{X})$, which is defined as the integral over the number density $n(\mathrm{X})$ along the whole line-of-sight through the DLA. Column densities can be measured by fitting the absorption lines with Voigt profiles, a method which will be extensively discussed in Sect. 2.1 and Sect. 4.2. Based on the column density of non-refractory elements, which are elements only slightly depleted onto dust grains and thus representative of the total gas phase abundance (see below), like Zinc and Sulfur, one can directly measure the metallicity [X/H] of the DLA by using Eq. 1.1. The relative abundance of two elements X and Y is defined as the ratio of their column densities relative to the Solar value.[12]

$$[\mathrm{X/Y}] = \log\left(N(\mathrm{X})/N(\mathrm{Y})\right) - \log\left(N(\mathrm{X})/N(\mathrm{Y})\right)_{\odot} \tag{1.1}$$

QSO- and GRB-DLAs are found to probe a large range of metallicities spanning three orders of magnitude from $-3 \lesssim [\mathrm{X/H}] \lesssim 0$ (or $10^{-3} \lesssim Z_{\odot} \lesssim 1$). (Noterdaeme et al., 2008; Rafelski et al., 2012; Bolmer, J. et al., 2019). On average, the metallicities decrease by a factor of 50-100 from today to $z = 5$, however, with a relatively large scatter, reflecting the fact that, especially QSO-DLAs, select galaxies with a range of different masses and metallicities at any given cosmic time (Rafelski et al., 2014; De Cia et al., 2018, see Fig. 1.9). In general, the metallicities of DLAs are higher than those of LLS. Lehner et al. (2016), for example, find that the metallicity distribution of partial and full LLS at $2.3 < z < 3.3$ toward QSOs is centred at $[\mathrm{X/H}] \sim -2$, which is much lower than the metallicity of the majority of GRB- and QSO-DLAs at these redshifts, which is centred between $[\mathrm{X/H}] \sim -1.5$ and -1 (Cen, 2012; Bolmer, J. et al., 2019). This is indicating, as mentioned before, that LLS are more likely associated with reservoirs of metal-poor, cool gas in the IGM, able to feed galaxies to prevent the end of star formation, as commonly seen in cosmological simulations. Chemical abundances of DLAs, on the other hand, are usually similar to those observed for (dwarf) galaxies, with some interesting exceptions. In a series of papers Cooke et al. (2016, 2017) identified the most metal poor DLAs known

[11] Also, high-ionization absorption lines, like O VI, C IV, N V, S IV, or Si IV, are commonly detected in GRB afterglow spectra. These could be related to the H II region hosting the GRB, but are unlikely to a DLA, because the measured N V column densities were found to be uncorrelated with any of the DLA properties such as metallicity, $\log N(\mathrm{H\,I})$, or dust depletion, consistent with an observed blue-shift of the high-ionization lines (Heintz et al., 2018, see also A. J. Fox et al., 2008). High ionization lines were also proposed to explain the discrepancy between the X-ray absorption seen in afterglow spectra and the one inferred from optical (rest frame UV) spectroscopy, where the latter typically an order of magnitude lower (the so-called *missing gas problem*; Schady et al., 2011, and references therein).

[12] Solar abundances are commonly adopted from Asplund et al. (2009), following the recommendations of Lodders et al. (2009).

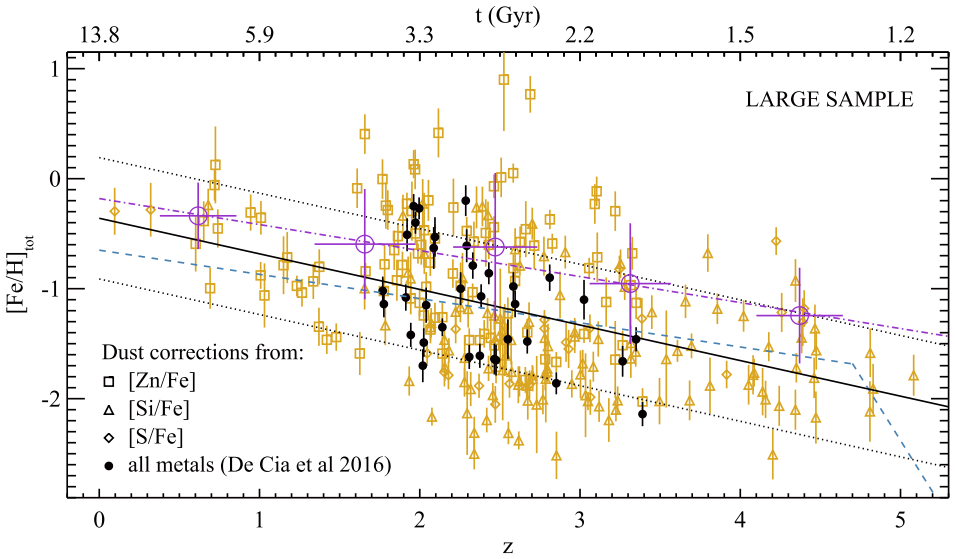

Figure 1.9: Dust corrected metallicity versus redshift for a large sample of QSO DLAs. The metallicities decrease by a factor of 50-100 from today to $z = 5$. The figure is taken from De Cia et al., 2018.

to date with metallicities of only about [X/H] ~ -3.4 to -2.8. These metallicities are inconsistent with the yields of pair-instability SNe, but could be the result of pristine gas that was enriched exclusively by the first generation of stars.

Since its first discovery in the mid 80s (Levshakov & Varshalovich, 1985), molecular hydrogen is occasionally detected in about $\sim$ 10% of QSO DLAs(Ledoux et al., 2003; Noterdaeme et al., 2008). As expected from the observed strong steepening of $f(N_{\rm H\,I}, z)$ at $\log N({\rm H\,I}) \gtrsim 21.5$, the fraction of H_2 bearing QSO-DLAs increases to 60-80% at these H I column densities (Noterdaeme, Srianand et al., 2015; Noterdaeme, Petitjean & Srianand, 2015). It was thus very surprising that, despite dedicated searches, H_2 was only detected in very few cases of GRB-DLAs (Prochaska et al., 2009; Friis et al., 2015; D'Elia et al., 2014; Krühler et al., 2013), because GRBs generally display very high H I column densities (see Fig. 1.8) and trace star formation. It was thus suggested that the radiation from the GRB destroyed most of the H_2, or that the UV radiation field in GRB host galaxies is exceptionally strong (Tumlinson et al., 2007). This question will further be addressed in Sect. 4 (see also Bolmer, J. et al., 2019), based on a systematic search for absorption from H_2 in the X-shooter GRB afterglow legacy sample (Selsing et al., 2018).

The presence of cold and molecular gas is regulated by the amount of dust in the ISM. On the one hand, dust grains provide the seeds that enable the formation of H_2, on the other hand, dust lowers the photo-dissociation from the interstellar radiation field by shielding the inner regions of the cloud. The amount of dust in the GRB host galaxies line-of-sight can be measured in two independent ways. One approach is to fit the observed afterglow spectrum (or photometric SED) with theoretical extinction curve models (Fitzpatrick & Massa, 1986) or with templates for typical sight-lines in

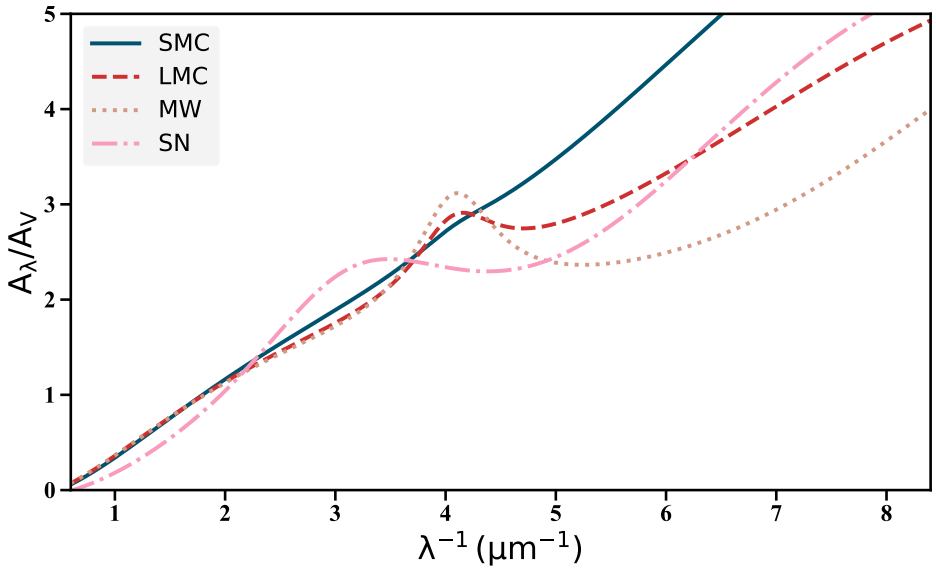

Figure 1.10: Extinction curves observed towards sight-lines in the Milky Way (MW), and the Small and Large Magellanic Clouds (SMC, LMC) (Pei, 1992). Additionally, an extinction curve expected for supernova-synthesized dust, and as found toward a high-redshift quasar (Maiolino et al., 2004), is plotted (SN).

the Milky Way or the Large and Small Magellanic Clouds (Pei, 1992). As an example, four extinction curves are shown in Fig. 1.10. One can see that the extinction typically increases from red to blue wavelength, reflecting the composition and size distribution of the dust particles (Draine, 2011). The extinction curves observed for typical sight-lines in the MW and LMC show another characteristic strong feature at 2175 Å, which is believed to be associated with carbonaceous dust grains (Mishra & Li, 2017), like nano-sized graphitic grains (e.g., Mathis, 1994) or polycyclic aromatic hydrocarbon (PAH) molecules (e.g., Steglich et al., 2010). The majority of GRB afterglow SEDs is best fit with the SMC extinction curve (e.g., Greiner et al., 2011; Zafar, Watson, Tanvir et al., 2011), but in a few cases a clear 2175 Å bump is identified (Krühler et al., 2008; Prochaska et al., 2009; Perley et al., 2011; Zafar et al., 2012; Zafar, Watson et al., 2018)[13]. Recently, Heintz et al. (2019) analyzed a sample of GRB-DLAs with evidence for cold gas, finding that the 2175 Å dust extinction feature is exclusively detected in GRBs with significant visual extinction ($A_V > 0.5$ mag) and strong carbon C I absorption with an equivalent with of $W_r(\lambda 1560) > 0.6$ Å, strengthening the case that carbonaceous dust is responsible for the feature.

A few years ago Fynbo et al. (2014) found very peculiar absorption properties in the afterglow spectrum of GRB 140506A at $z = 0.889$. The very strong feature could either be modelled with a giant 2175 Å extinction bump or, more likely, as an effect of multiple scattering on dust grains in a dense environment, similar to what is seen in some cases of

[13]The 2175 Å feature is also very rare in case of QSO absorbers (e.g., Ma et al., 2018).

reddened supernovae and active galactic nuclei (e.g., Goobar, 2008; Leighly et al., 2014; Amanullah et al., 2014).

Another unusual extinction curve was found toward a high-redshift QSO, which Maiolino et al. (2004) interpreted as the result of absorption from supernova-synthesized dust. The idea is that at redshift $z > 6$ (only one Gyr after the Big Bang) there was not enough time to form AGB stars in high numbers, such that the dust at this epoch must be purely from SNe or subsequent grain growth in the ISM. The model from Todini & Ferrara (2001) predicts a characteristic flattening between 3000 Å and 1700 Å followed by a steep decline for SN-type extinction (see Fig. 1.10), which was also observed for two GRBs at $z > 6$ (Perley et al., 2010; Jang et al., 2011; Stratta et al., 2007, 2011, but see Zafar et al., 2010). As presented in Sect. 3, Bolmer et al. (2018) tested if the SN-type extinction curve provides a better model for GRBs at $z > 4$ than the extinction curves observed in the local universe. They do not find any evidence for the need of a different, SN-type extinction curve for GRBs at very high-redshift, partly because almost none of the afterglow SEDs is significantly reddened by dust. The fact that these GRB afterglows at $z > 4$ generally show only little extinction by dust (< 0.5 mag), could either point to a transition in dust production mechanism in the early universe, or that we suffer from an observational bias. This is because GRBs with $A_V > 0.5$ mag at $z > 4$ are almost impossible to detect in optical wavelength with current instrumentation (Bolmer et al., 2018; Zafar, Møller et al., 2018, and the discussion in Sect. 3).

Another way to estimate the amount of dust in DLAs is by measuring the strength of *dust depletion*, which is defined as the amount of metals removed from the gas phase due to their condensation onto dust grains (e.g., Spitzer & Jenkins, 1975). Refractory elements with higher condensation temperatures, like Silicon and Iron, can be highly depleted from the gas phase in the diffuse ISM (e.g., 90-99% of iron is missing from the gas phase in the ISM of the Milky way; Jenkins, 1987, 2009; De Cia et al., 2016), whereas volatile elements like Zinc and Sulfur are only marginally depleted (only up to about 10%; De Cia et al., 2018; Bolmer, J. et al., 2019).

The strength of dust depletion can thus be either measured by comparing the abundances of refractory with volatile elements, that is with the dust depletion factor [Zn/Fe] (see Sect. 4); or by comparing the elemental abundances observed in the gas phase with a reference of the total (gas plus dust) abundance, like measured in the Milky Way (Savage & Sembach, 1996; Jenkins, 2009; De Cia et al., 2013).[14] The problem is that solar abundances cannot be generalized and used for other galaxies or high-redshift DLAs with different nucleosynthesis and lower metallicities. De Cia et al. (2016) therefore studied the relative abundances of a large sample of QSO-DLAs and Galactic absorbers, finding homogeneous properties of dust depletion in the ISM. They found that the depletion δ of various elements like Zn, O, P, S, Si, Mg, Mn, Cr, and Fe strongly correlates with [Zn/Fe] (see Fig. 1.11, **a**). This allowed them to derive canonical depletion patterns, which can be used to measure dust-corrected metallicities, the dust-to-metal ratio, $\mathcal{DTM}$, or the dust extinction A_V in DLA absorbers (De Cia et al., 2016; Wiseman, Schady et al., 2017;

[14] Reference values are now also available for the LMC and SMC (Tchernyshyov et al., 2015; Jenkins & Wallerstein, 2017).

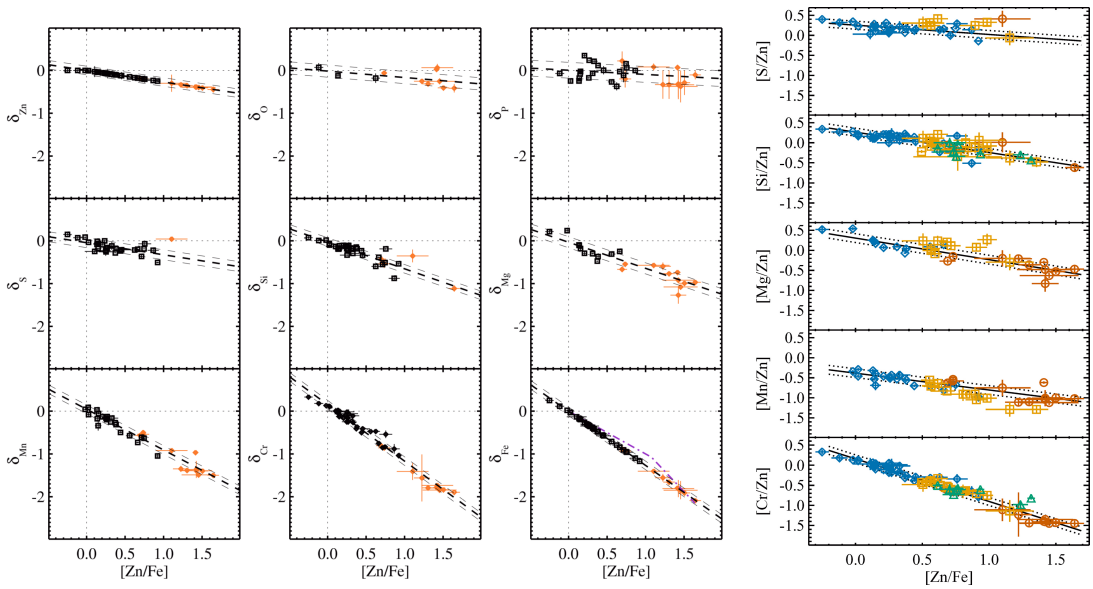

(a) Dust Depletion Sequences for different elements measured in QSO-DLAs.

(b) Relative abundances versus depletion factor.

Figure 1.11: (a) The depletion δ of an element is defined as the fraction of that element still remaining in the gas phase and the dust fraction is thus $1 - 10^{\delta}$ (De Cia et al., 2016).**(b)** Metal and dust properties in the cold ISM follow a similar behaviour in indifferent environments (De Cia, 2018), that is in the Galaxy (orange), for SMC and LMC (green and blue), and for DLAs (blue).

Bolmer, J. et al., 2019, see also Sect. 4). In a follow-up paper, (De Cia, 2018) found that the same sequences of relative abundances are valid for the Galaxy, the Magellanic Clouds, as well as high redshift DLAs. Dust and metal properties thus seem to follow a similar behavior in different environments, depending on the local physical conditions in the ISM but regardless of the star formation history, indicating that the dominant fraction of dust is mainly built up by grain-growth (see Fig. 1.11, **b**).

By comparing the measured gas-phase abundances with those predicted by chemical evolution models, Vladilo et al. (2018) find that the dust abundance ratios of $(\mathrm{Si/Fe})_d$ and $(\mathrm{Mg/Fe})_d$ decrease by almost two orders of magnitude in the metallicity range between 0.01 and $\sim 1\ Z_{\odot}$. These results suggest that mechanisms of dust production in DLAs are metallicity-dependent. For example, type II SNe appear to be more important contributors to the dust composition at low metallicity (i.e. $[\mathrm{Fe/H}] < -0.6$), whereas at higher metallicities grain growth in the ISM (dust accretion) seems to be the most important process.

The dust content derived from the depletion analysis does not seem to follow the trends observed for SED-inferred A_V values, and in some cases, the values are not consistent (Wiseman, Schady et al., 2017; Bolmer, J. et al., 2019). From a sample of GRBs behind C I absorbers, Heintz et al. (in prep.) found evidence that the dust extinction measured

from SED fitting, and therefore, in particular, the 2175 Å bump, is a result of the dust located in the same molecular cloud that is responsible for the C I absorption. The dust measured from the depletion analysis, on the other hand, is based on the integrated column density of metals along the whole line-of-sight.

Finally, its worth noting, that DLAs can also be used to measure the evolution of the cosmic microwave background temperature from carbon monoxide excitation (e.g., Noterdaeme et al., 2011), or to analyze the limits of the cosmological variation in the proton-to-electron mass (e.g., Malec et al., 2010).

These results underline the remarkable capability of using QSO- and GRB-DLAs to probe the evolutionary properties of star forming regions in high-redshift galaxies, especially concerning cold gas, molecules and dust in the diffuse ISM.

1.4 Instrumentation

This section provides a short overview over the instrumentation used to collect the data for this thesis. The analysis in Bolmer et al. (2018) is mostly based on NIR/optical photometric data taken with GROND (2.2m in La Silla, Chile) as well as X-ray data gathered by the XRT instrument on board of the the Neil Gehrels *Swift* Observatory (see Chapter 3). The results of Bolmer, J. et al. (2019) are based a on a sample of GRB afterglow spectra taken with the X-shooter spectrograph mounted on UT2 at the VLT in Paranal, Chile (see Chapter 4). As an example, in Fig. 1.12, the full GROND, XRT and X-shooter data of the afterglow of GRB 130606A are presented.

1.4.1 The 7-channel imager GROND

The 7-channel *Gamma-Ray Optical and Near-infrared Detector* (GROND), is an imaging instrument that can observe in four optical ($g'r'i'z'$) and three near-infrared (JHK_s) channels simultaneously. It was primarily designed for the rapid follow-up and classification of gamma-ray burst afterglows and other transients like variable stars, supernovae or microlensing events (Greiner et al., 2008). However, to observe in seven channels simultaneously has been proven to be a real benefit for other astronomical research areas as well. Since its commissioning at the MPG 2.2m telescope at La Silla (ESO, Chile) in April/May 2007, GROND observations over the last 10 years have also played a role in a large variety of other astrophysical areas ranging from distant quasars to exoplanets (see Greiner, 2019, for a summary of the first 10 years of GROND observations).

The GROND field of view is large enough to locate the NIR/optical GRB afterglows in the typical error circles distributed by *Swift*/XRT and also large enough to cover enough stars for a proper calibration ($10' \times 10'$ in the NIR and $5.4' \times 5.4'$ in the optical). At the same time, the CCDs have a pixel scale that is less than the mean seeing in order to allow accurate photometry. After entering the instrument, the light is split using dichroics (short wavelength part is reflected, the long passes through). The GROND $g'r'i'z'$ bands are identical to the Sloan system, except for the i' band, and the NIR infrared bands JHK_s are similar to those of the 2MASS survey.

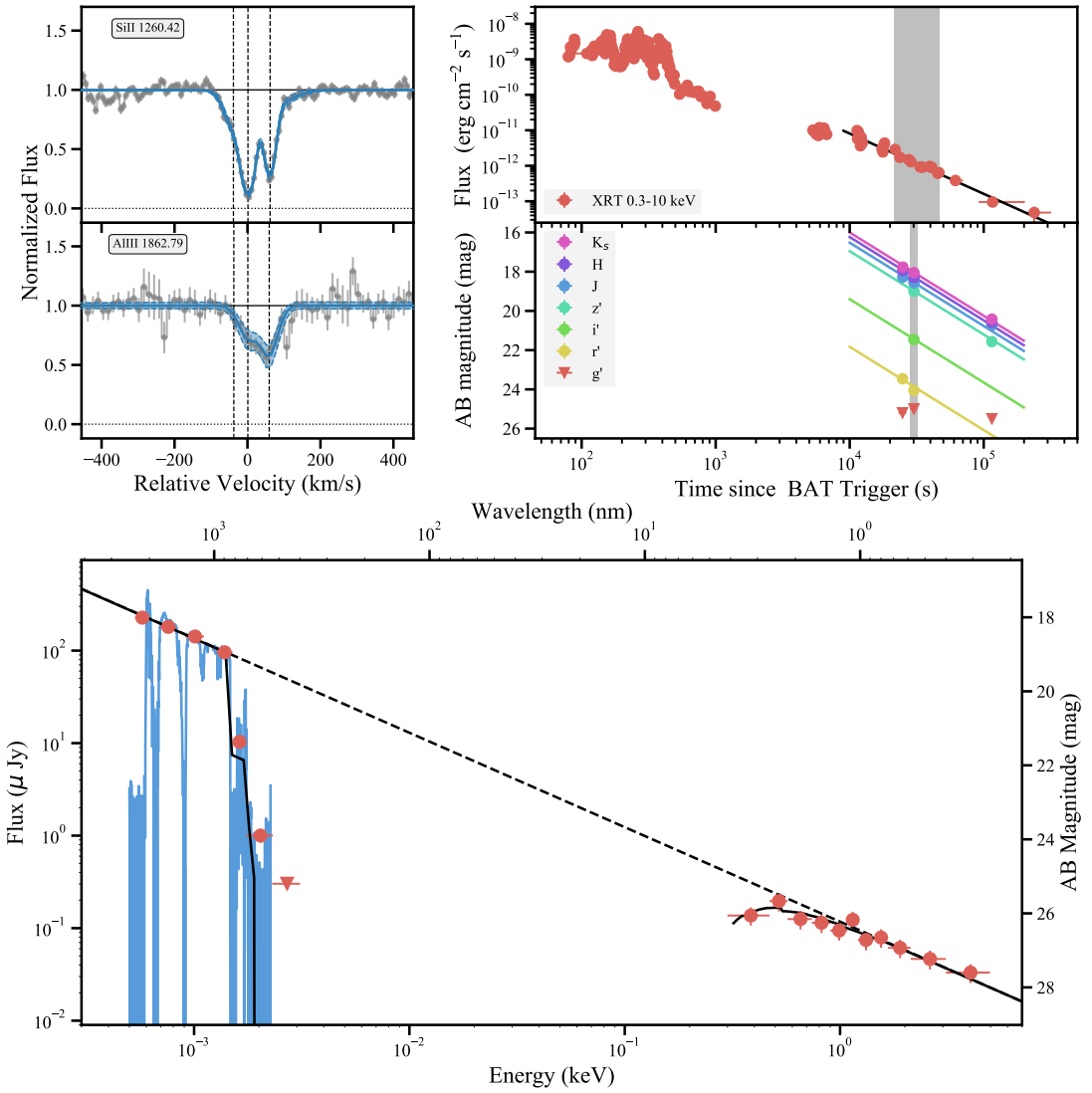

Figure 1.12: GROND, XRT and X-shooter data for GRB130606A. The upper right inset displays the XRT X-ray and GROND NIR/optical afterglow light-curves. The grey shaded areas mark the time intervals that were chosen to create the spectral energy distribution that is plotted in the lower inset. The full X-shooter spectrum is plotted on top of the GROND data points, and as an example, two absorption lines are shown in the inset on the upper left.

GROND can operate in a Rapid Response Mode (RRM), automatically ending any ongoing observations once an observable GRB is detected by, e.g. *Swift*/BAT, such that GRB afterglows can be observed as early as $\gtrsim 2$ minutes after the trigger (see for example the GRB140614A GROND light curve in Fig. 3.22). Otherwise, depending on the brightness of the afterglow, predefined OBs of, e.g. 4, 8, 20 or 30 minutes integration time, or sequences of these can be chosen manually.

With an exposure of only about 60 minutes, the instrument reaches limiting AB magnitudes of ~ 24 to 25 mag in the optical and ~ 21.5 to 22.5 mag in the NIR bands, which is remarkable for a 2.2m telescope.

Analysis of GROND data is usually done with a data reduction pipeline written in Python that was first presented in Krühler et al. (2008) and makes use of the standard *Image Reduction and Analysis Facility tasks* (IRAF; Tody, 1993) and other software like `SExtractor` or `SCAMP` for source extraction, astrometry and photometry. For more details see Section 3.2.4 in Chapter 3.

One of the most critical aspects of observing in seven NIR/optical channels simultaneously, is that a photometric redshift for objects at $z \gtrsim 3$ can be determined based on the Lyα break (e.g., Krühler, Schady et al., 2011; Rau et al., 2012; Bolmer et al., 2018). Additionally, dust properties of the intervening, absorbing material can be inferred by fitting extinction curves to the broadband spectral energy distribution (e.g., Bolmer et al., 2018; Krühler et al., 2008; Greiner et al., 2011).

1.4.2 XRT on board of the *Swift* satellite

The *Swift* Gamma-Ray Burst Mission (Gehrels et al., 2004), launched in 2004, is a powerful multi-wavelength observatory primarily designed for GRB astronomy. Besides the Burst Alert Telescope (BAT), which detects and locates GRBs with an accuracy of $1'$ to $4'$, the satellite is also equipped with the X-ray telescope (XRT) (Burrows et al., 2005) and the Ultraviolet/Optical Telescope (UVOT) (Roming et al., 2005). The former provides the position of the X-ray afterglow with typical errors of approximately 1-6$''$ and within only a couple of minutes of the burst onset, which consequently led to a revolution of the field of GRB astronomy by allowing rapid, ground-based follow-up at NIR/optical wavelengths (see Schady, 2017, for a recent review of GRB science in the Swift era). The XRT observes in the energy range 0.2-10 keV down to a sensitivity of about $\sim 10^{-14}\,\mathrm{erg\,cm^{-2}s^{-1}}$ for a 10^4 s exposure with its CCD-22 detector (effective area of $> 120\,\mathrm{cm}^2$ at 1.6 keV and an angular resolution of about 18-22$''$; the field of view is $23.6 \times 23.6'$). The XRT starts to obtain GRB afterglow spectra and lightcurves from about one minute after the BAT detection (slewing time of about 20-75 s depending on the GRB position on the sky) and continues the follow-up for a couple of days or even weeks, depending on the brightness of the afterglow. To do so, the XRT automatically switches between different readout modes to avoid saturation of the CCD within the first minutes or hours while at the same time preserving as much information as possible (see Burrows et al., 2005, for more details).

For this work (see Sect. 3), archival X-ray afterglow data of GRBs at $z > 4$ were retrieved from the public *Swift*/XRT repository (Evans et al., 2009) and the spectra

were re-binned and analyzed using the NASA HEAsoft Swift package distribute by HEASARC (for more details see Sect. 3.2.1 in Chapter 3).

In contrast to expectations, no Fe emission lines or other features are detected in typical XRT GRB afterglow spectra, and ground-based multi-channel imagers like GROND or spectrographs like VLT/X-shooter are required to determine the redshift of the GRB.

1.4.3 The VLT/X-shooter spectrograph

The X-shooter cross-dispersed échelle spectrograph was installed at the Cassegrain focus of UT2 (Kueyen) as the first 2nd generation instrument in 2009 (Vernet et al., 2011).[15] With a single exposure, the instrument can cover the whole spectral range from 300 to 2500 nm with intermediate resolution ($R \sim 4000 - 17\,000$). Through the use of two dichroics, the light is split into three separate spectroscopic arms: the ultraviolet-blue (UVB), the visual (VIS), and the near-infrared (NIR) arm, which cover the wavelength range 300 - 550 nm, 550 - 1020 nm, and 1020 - 2480 nm, respectively. For each arm, all science observation slits are $11''$ wide, but different slit widths are available, e.g., $0.4''$, $0.7''$, $0.9''$, $1.2''$, $1.5''$and $5''$ in case of the VIS arm. Usually, the slit width is chosen based on the seeing in Paranal in order to optimize spectral resolution and signal-to-noise. Besides GRB afterglows, the X-shooter sciences cases range from brown dwarfs, young stellar objects and T Tauri stars in the Milky Way to distant quasars and lensed galaxies. A great advantage of X-shooter is, that due to the broad wavelength coverage, the redshift of the given target does not need to be known in advance, but can be determined based on Lyα or other absorption lines, like for the majority of GRBs studied in this thesis (see especially Chapter 4).

The GRBs that entered the sample of (Bolmer, J. et al., 2019, see Setc. 4) were usually observed in Target-of-Opportunity mode and with slit widths of $1.0''$, $0.9''$, and $0.9''$ for the UVB, VIS, and NIR-arm, respectively. A comprehensive description of the X-shooter data reduction is presented in Selsing et al. (2018). Since for some of the GRBs, the observatory seeing full width at half maximum (FWHM) was considerably smaller than the slit width, Selsing et al. (2018) used observations of telluric standard stars that were taken shortly before or after the afterglow observations with identical instrument settings in order to determine the instrumental resolution. This was done by fitting a selection of telluric lines with Voigt profiles and calculating the corresponding FWHM, which we can then be converted to a delivered resolution. Results from a linear model fitted to the resolution values in the NIR and VIS arm can be used to determine the resolution in the UVB arm, where no telluric lines are present. Also, the resolution for medium to low signal-to-noise afterglow spectra can be estimated this way. The spectral resolution is used to convolve the Voigt profiles that are fitted to the absorption lines detected in the GRB afterglow spectra.

[15] For some time X-shooter was also mounted at UT3 (Melipal)

Chapter 2

Absorption line analysis via Bayesian inference

2.1 The Voigt profile

Absorption lines that are imprinted onto the spectra of QSOs and GRBs by any foreground material are usually best described by the so-called *Voigt* line profile. The Voigt profile is defined as the convolution of a Gaussian and a Lorentzian, where the Gaussian accounts for the thermal and turbulent motion of the atoms and ions, i.e., Doppler broadening, and the Lorentzian for the uncertainty of the transition frequencies (e.g., Draine, 2011, see also Fig. 2.1).

Usually a number of n Voigt line profiles – according to the number of required absorption components – are fitted to the observed spectra simultaneously with the continuum flux, F_c, of the GRB. The model for such an absorption profile in velocity space is described as follows.

$$F_\mathrm{model} = F_\mathrm{c} \cdot \prod_{j=1}^{n} e^{-\tau_j}; \quad F_\mathrm{c} = A + Bv + Cv^2 \tag{2.1}$$

Here, the optical depth τ is given by

$$\tau = \frac{\pi e^2}{m_\mathrm{e} c} f_{ik} \lambda_{ik} N \cdot \phi_V \left(v - v_0, \frac{b}{\sqrt{2}}, \Gamma \right) \tag{2.2}$$

where ϕ_V is the Voigt profile in velocity space, and with f_{ik}, λ_{ik} and Γ, being the oscillator strength, wavelength and damping constant for transition $i \rightarrow k$. The latter three are known to relatively high precision from laboratory experiments (e.g., H. L. Morgan & Edmunds, 2003), such that v_0, N and b are the only free parameters.

The Voigt profile is related to the real part of the Faddeeva function $w(z)$[1] and given by

$$\phi_V = \frac{\mathrm{Re}\left(w(z)\right)}{b\sqrt{\pi}} \tag{2.3}$$

[1]The Faddeeva function is defined as $w(z) = e^{-z^2}\mathrm{erfc}(-iz)$; https://docs.scipy.org/doc/scipy-0.19.1/reference/generated/scipy.special.wofz.html

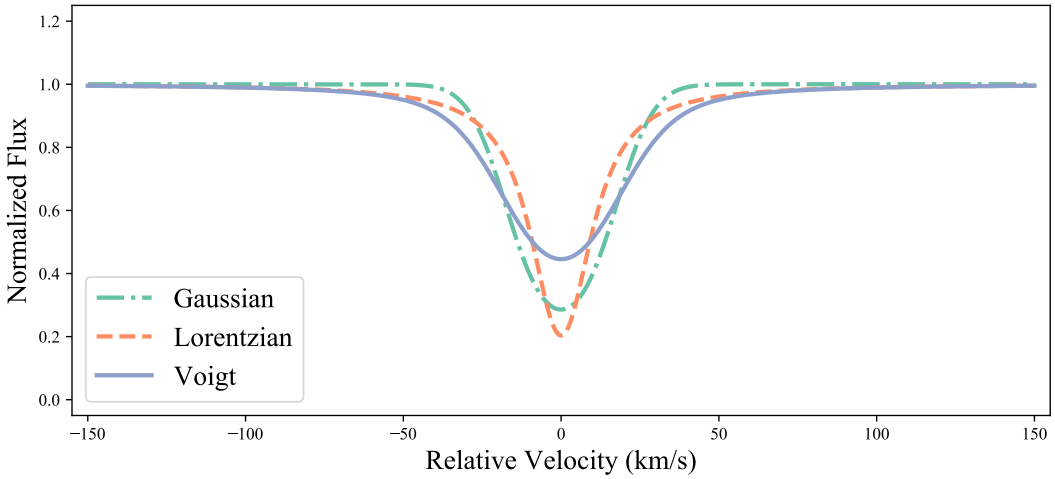

Figure 2.1: The Voigt absorption profile in comparison to a Gaussian and a Lorentzian.

where z is defined as

$$z = \frac{v - v_0 + i\Gamma}{b} \tag{2.4}$$

In case of a GRB afterglow spectrum, which is usually best described by a simple power law, a second order polynomial is sufficient to model the background flux, which adds another three free parameters A, B, and C:

$$F_c = A + Bv + Cv^2 \tag{2.5}$$

The parameters of interest when studying the physical properties of the ISM or star-forming regions in high-redshift galaxies are the relative velocities of the individual absorption components (v_0), the broadening parameter (b) of each line as well as the column density of the atoms, ions or molecules ($\log N$). Typical software tools used to fit absorption lines, like VPFIT[2] or FITLYMAN (Fontana & Ballester, 1995), rely on least squares regression analysis techniques and χ^2 statistics. The issue is that these approaches can be very time consuming and naturally break down for a large number of free parameters or in case of strong degeneracies. In case a spectrum shows evidence for, e.g., three or more absorption components, which is common for GRB afterglows, the number of free parameters quickly grows to more than $n_\theta > 10$. Therefore, state-of-the-art Bayesian Inferences methods, which make use of Monte Carlo Markov Chains to sample the posterior distributions of these parameters, are the method of choice.

[2] https://www.ast.cam.ac.uk/~rfc/vpfit.html

2.2 Monte Carlo Markov Chains and Bayesian inference

Fitting Bayesian statistical models by using Markov chain Monte Carlo (MCMC) methods has become a standard tool for parameter estimation in astronomy during the past decade (Sharma, 2017).

When using Bayesian inferences, one is interested in the probability distribution of a specific set of model parameters. For example, given an observed GRB spectrum (data D) and the Voigt profile model (M, as defined in the previous Sect. 2.1), it is desirable to know the probability distribution P over the column density and the broadening parameter (the set of model parameters θ) of a specific absorption line. Based on Bayes' Theorem, this so-called *Posterior* distribution, $P(\theta|D, M)$, is equal to

$$P(\theta|D, M) = \frac{P(D|\theta, M)\, P(\theta)}{P(D)} \tag{2.6}$$

The first term on the right, $P(D|\theta, M)$, known as the *Likelihood*, expresses the probability to observe (or generate) the data D, given a set of parameters θ and a model M. $P(\theta)$ is the so-called *Prior*, specifying our prior knowledge (or lack of knowledge) of the set of parameters. $P(D)$, the often called *Evidence*, is a constant with the purpose of normalizing $\int P(\theta|D, M)\, d\theta$ to 1.

The predictions made from a Bayesian analysis are thus probability distributions instead of point estimates, which additionally allows for the quantification of uncertainty in the inferences. The problem is that the posterior is generally impossible to compute because in most cases a high-dimensional integration is required. Therefore stochastic sampling methods such as *Markov chain Monte Carlo* (MCMC) are used instead, which are a combination of Markov chains and Monte Carlo sampling (Betancourt, 2017).

For example, a new set of parameters θ_{t+1} can be generated by randomly drawing from a multivariate normal distribution with covariance matrix Σ that is centered around the previous set of parameters θ_t.

$$\theta_{t+1} = \text{Normal}(\theta_t, \Sigma) \tag{2.7}$$

Eventually, a Markov chain created this way should sample the whole parameter space of interest given a very large (infinite) number of iterations. The challenge, however, is to design an algorithm that is efficient and samples from the target distribution with finite computing time typically available for practical analysis. The classic example is the *Metropolis-Hastings* (MH) algorithm which is comprised of a proposal and a correction step. First, a new proposal set of parameters θ_{t+1} is created by using Eq. 2.7. Then, the posteriors of the new set and the previous set are compared by calculating the quotient, which conveniently cancels out the hard to compute denominator of Bayes' Theorem. If the new set of parameters has a higher probability, that is

$$\frac{P(D|\theta_{t+1}, M)\, P(\theta_{t+1})}{P(D|\theta_t, M)\, P(\theta_t)} > 1, \tag{2.8}$$

the proposal is accepted, otherwise it is rejected and another set of new parameter values is drawn. In other words, if the jump is closer to the mode, it is accepted, if not it is rejected, such that the Markov Chain finds the typical set and samples from it. The first steps for finding the typical set are usually referred to as the *warm-up* or *burn-in* phase and have to be discarded.

To calculate Eq. 2.7, a likelihood and priors have to be defined. For example, under the assumption of Gaussian errors of the data points $(x_i \pm \sigma_i)$, the likelihood function is best described by a normal distribution:

$$P\left(D|\theta, M\right) = \prod_i l_i = \prod_i \frac{1}{\sqrt{2\pi\sigma_i^2}} e^{-\frac{\left(x_i - \mu(\theta)\right)^2}{2\sigma_i^2}} \tag{2.9}$$

Alternatively, it can be useful to use a standard Cauchy (or Student-t) distribution instead, because it has higher weights on the tails and can thus account for outliers.

$$P\left(D|\theta, M\right) = \prod_i l_i = \prod_i \frac{1}{\pi\beta_i \left(1 + \frac{x_i - \mu(\theta)}{\beta_i}^2\right)} \tag{2.10}$$

In the case of absorption lines, $\mu(\theta)$ is calculated using the model given in Sect. 2.1 and the current values of the parameters θ_t. The priors are chosen subjectively, based on previous knowledge about the parameters. The column density of metals in GRB DLAs, for example, is usually in the range of $12 < \log N < 18$, such that a weakly informative, normal prior should be sufficient to steer the chain in the right direction.

$$P(\log N) \sim \text{Normal}(15, \sigma = 2.5) \tag{2.11}$$

A general problem of MH is that with an increasing number of dimensions of the parameter space, the chance to jump in the "right" direction decreases, such that smarter sampling algorithms are required (e.g., Adaptive MH, Gibbs, Hamiltonian Monte Carlo (HMC), Betancourt, 2017; Sharma, 2017, and references therein).

There is now a variety of libraries available for Bayesian analysis, such as EMCEE[3], PyMC, or Stan[4]. While EMCEE and PyMC are relatively easy to use, because they only require knowledge of Python, STAN is probably the most sophisticated and complex package that, however, requires writing C++ code.

To fit absorption lines in the spectra of GRB afterglows observed with X-shooter, I decided to use PyMC version 2.7.3 (Bolmer, J. et al., 2019, see also Sect. 4).[5] The developed code will be presented in more detail in the following section.

[3] http://dfm.io/emcee/current/
[4] https://mc-stan.org
[5] https://pymc-devs.github.io/pymc/

2.3 Absorption line fitting in PyMC

In Python, the Voigt profile function (Eq. 2.3 and 2.4) can be easly defined as

```
def voigt(x, sigma, gamma):

  z = (x + 1j*gamma) / (sigma * np.sqrt(2.0))
  V = wofz(z).real / (sigma * np.sqrt(2.0*np.pi))

  return V
```

where `wofz(z).real` is the real part of the Faddeeva function as imported from the Python package Scipy.[6] Here, `gamma` and `sigma` are the half-width at half-maximum (HWHM) of the Lorentzian profile and the standard deviation of the Gaussian profile, respectively.

The optical depth τ (Eq. 2.1 and 2.2) is then given by

```
def exp_tau(v, N, b, gamma, f, l0):

    A = (((np.pi*e**2) / (m_e*c))*f*l0*1E-13)*(10**N)

    tau = A * voigt(v, b / np.sqrt(2.0), gamma)

    return np.exp(-tau)
```

where v is the input velocity range, N the logarithm of the column density, b the broadening parameter and Γ, f, and l_0 the damping constant, the oscillator strength and rest frame wavelength for a given line, respectively.

For the continuum flux, F_c, a `Numpy` array of ones with the length of the input velocity array is created and multiplied by the background model (Eq. 2.5) and the given number of absorption lines (see Eq. 2.1). Finally the resulting model is convolved with the instrumental resolution using a Gaussian Kernel with the standard deviation $\sigma = \mathrm{FWHM}_{\mathrm{km/s}}/2\sqrt{2\ln 2}$ (`tf` is a factor used to transform the instrumental resolution from km/s to pixels).

```
sd = RES/(2*np.sqrt(2*np.log(2) * tf)
gk = Gaussian1DKernel(stddev=sd, mode='oversample')

conv_flux = np.convolve(flux, gk, mode='same')
```

For the Likelihood we assume a Cauchy distribution, ensuring that outliers are accounted for.[7] In PyMC a likelihood is defined by setting `observed=True`.

```
y = pymc.Cauchy('y', alpha=voigt_model, value=flux,
        beta=np.array(fluxerr)*2, observed=True)
```

[6] https://scipython.com/book/chapter-8-scipy/examples/the-voigt-profile/

[7] In Bolmer, J. et al. (2019) we used a Gaussian likelihood and ignored outliers by hand.

Here, `flux` and `fluxerr` are `Numpy` arrays containing the flux and its error in the given velocity range.

For the individual velocity components we initially always chose a flat prior for the whole input velocity range. Once the relative velocity of an absorption component is identified to be around $\sim v_0$ it is possible to choose a flat prior for $v_0 \pm \delta_v$, where δ_v is a small offset that can be defined in a parameter file (`paradic`) that is passed to the script. A typical offset would be ~ 5 km/s. Alternatively, v_0 can also be fixed to a certain value or a normal distribution around v_0 with a given σ_v.

```
1 if not 'v0' in paradic:
2   v0 = pymc.Uniform('v0', lower=-velo_range,
3                 upper=velo_range, doc='v0')
4
5 else:
6   v0 = pymc.Uniform('v0',
7                 lower=paradic['v0'][2],
8                 upper=paradic['v0'][3],
9                 doc='v0')
```

Very similar, for the broadening parameter a flat prior between the smallest resolvable value depending on the instrumental resolution (`lowb`) and 80 km/s is assumed. Otherwise, if specified in the parameter file, a flat prior around $b \pm \delta_b$, or a normal prior around b_0 with a given σ_b can be chosen.

```
1 if not 'b' in paradic:
2   b = pymc.Uniform('b', lower=lowb,
3                 upper=80, value=lowb+20, doc='b')
4
5 else:
6   if paradic['b'][0] == 'norm':
7         b = pymc.Normal('b', mu=paradic['b'][1],
8           tau=1.0 / (paradic['b'][3] -
9           para_dic['b'][1])**2, doc='b')
10
11  if paradic['b'][0] == 'flat':
12        b = pymc.Uniform('b', lower=paradic['b'][2],
13          upper=paradic['b'][3], doc='b')
```

For the column density N of every compinent i we chose an exponential prior, ensuring that lower values are preferred when there is no information about absorption in the data, that is the flux is consistent with the continuum emission within the noise. Theoretically it is also possible to choose different priors in case previous knowledge is available, like the normal prior suggested in the previous section.

```
1 N = pymc.Exponential('N' + str(i), beta=0.1,
2             value=15.0, doc='N' + str(i))
```

To sample from the posterior distribution, we use the PyMC `MCMC` class (the entire model is called `voigts()` in this case). Since the broadening parameter b and the column density N are highly correlated, it is better to use the Adaptive Metropolis step method for these two parameters. The Adaptive Metropolis step method works like a regular Metropolis step method, with the exception that the covariance matrix of the multivariate Gaussian proposal distribution (see Eq. 2.7) is updated based on previous iterations (Haario et al., 2001). This means that the algorithm "learns" how to better sample these parameters by adjusting the average step size.

The chains, or so-called *traces*, of each parameter, are then created with a number of n iterations and a burn-in phase of length m. Usually, it is good to use $n = 20\,000$ iterations and a warm-up phase of 10 000 steps, but these numbers highly depend on the number of lines and absorption components that are included in the fit. As a convergence diagnostic PyMC built-in Geweke z-scores can be used and it is always useful to additionally inspect the traces and posterior distributions visually. A fit takes typically only a couple of seconds or minutes so that it is always possible to increase the number of iterations. Additionally, as described above, it is easy to iteratively narrow or change priors in case some parameters are already constrained.

```
MDL = pymc.MCMC(voigts(velocity, flux, flux_err,
                f, gamma, l0, nvoigts, RES, paradic),
                db='pickle', 'result.pickle')
MDL.db
MDL.use_step_method(pymc.AdaptiveMetropolis,
                [MDL.N, MDL.b],
                scales={MDL.N: 3.0, MDL.b: 3.0})
MDL.sample(n, m)
scores = pymc.geweke(MDL)

MDL.db.close()
```

In `PyMC` the results can be stored in many different formats. Here, a `.pickle` file is chosen which can easily be handled with the standard Python library Pandas. Finally, the best fit values as well as different error estimates like quantiles can be immediately accessed through PyMC (here 'VPmodel' is the `pymc.deterministic` defined in the model function, i.e. the entire model and not just a single parameter).

```
N = MDL.stats()['N']['mean']
b = MDL.stats()['b']['mean']
yqmin = MDL.stats()['VPmodel']['quantiles'][2.5]
yqmax = MDL.stats()['VPmodel']['quantiles'][97.5]
yfit = MDL.stats()['VPmodel']['mean']
```

The above descriptions only highlight the basic ideas of the developed code as well as some general aspects of PyMC. The complete fitting library, that will potentially be published in a forthcoming paper, is far more sophisticated and contains a lot of additional features.

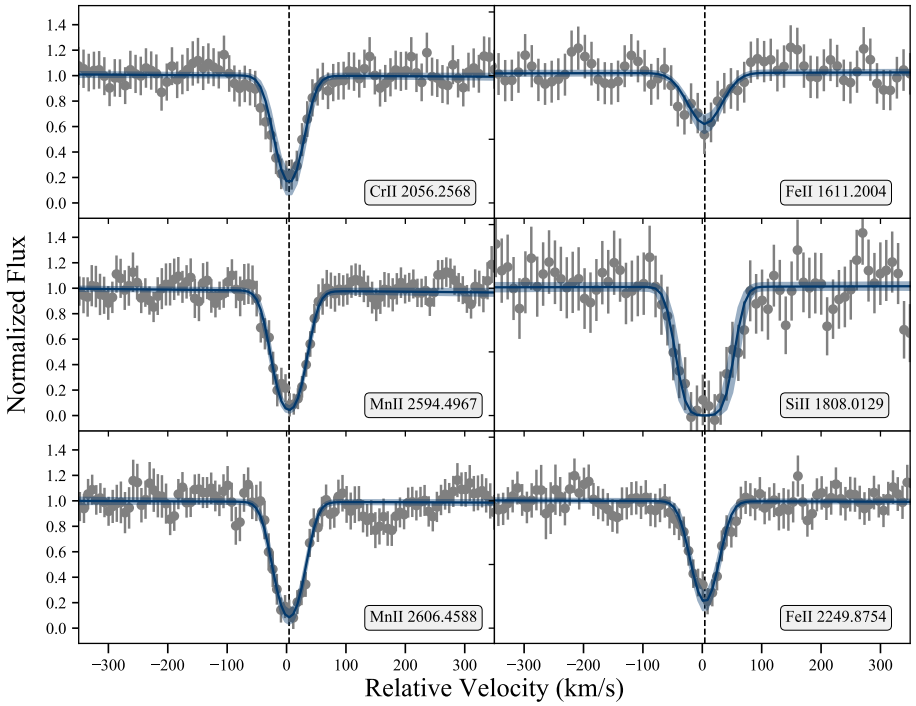

Figure 2.2: Results of a simultaneous fit of 6 different metal lines in the spectrum of GRB 151021A. All lines share the same v_0 and broadening parameter and the two iron lines as well as the two manganese share each the same column density parameter as well.

The main script, `vpfit.py`, can easily be executed from the command line, by specifying the following arguments: the path to the data files, which have to be in the standard ESO format[8], the rest-frame wavelength of the lines that should be considered for the fit (as in the second column of the provided `atom.dat` data file[9]), the reference redshift, the velocity range extracted from the spectrum around each line, the total number of iterations and the length of the burn-in phase, the name of the GRB (optional), the number of expected absorption components, and finally an initial guess for the relative velocity of each component (optional, for negative values an `m` for "minus" must be added in front of the number, e.g. `-v0 m30 m5 25`).

```
python vpfit.py --files spectra/GRB151021A_OB1_1.fits
  --lines 1611.2004 1808.0129 2056.2568 2249.8754
  2594.4967 2606.4588 --redshift 2.3297 --velocity_range 140
  --iterations 5000 --burn_in 4500 --grb_name GRB151021A
  --components 1 --v0 5.0
```

[8] see https://archive.eso.org/cms/eso-data/help/1dspectra.html

[9] This dat file was taken from the *Voigt profile fitting program* (https://www.ast.cam.ac.uk/~rfc/vpfit.html), but some values were updated (see Sect. 4).

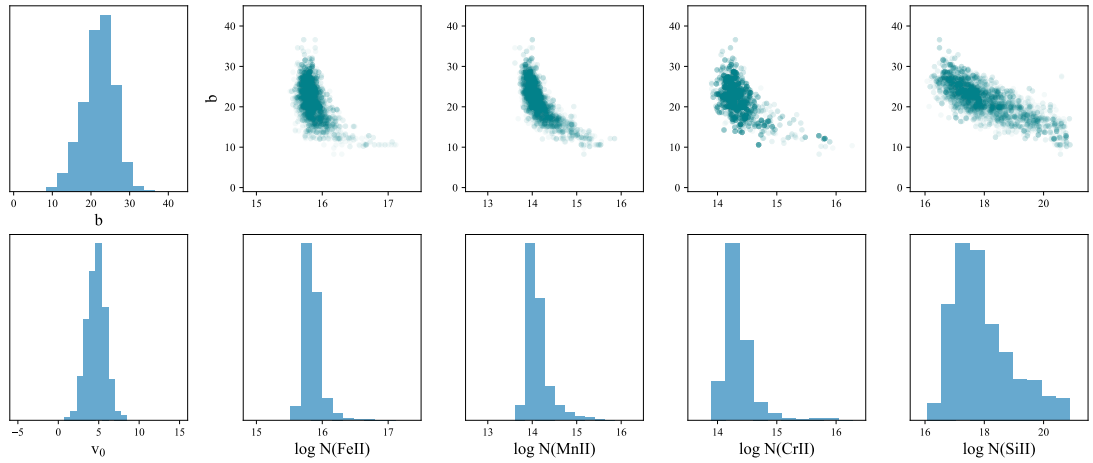

Figure 2.3: Histograms and pairwise scatter plots of the posterior distributions for the simultaneous fit of 6 absorption lines in the spectrum of GRB 151021A as shown in 2.2.

As an example, in Fig. 2.2 we show the result from fitting six different lines in the spectrum of GRB151021A simultaneously. These lines share the same broadening parameter and velocity components v_0 (see the example above). The corresponding histograms and pairwise scatter plots of the posterior distributions are shown in Fig. 2.3. One can see that the broadening parameter and column density can be highly degenerate, especially in the case of Si II (top right). Theoretically, due to the different masses of the atoms, each line should have a different broadening parameter, given a fixed temperature of the gas. However, differences are typically lower than what can be resolved with instruments like X-shooter, and it is thus recommended to fit multiple lines at the same time with a common broadening parameter. For Fe II, Mn II, and Cr II one can see clear peaks in the column density posterior distributions such that accurate values for the column density can be derived. In case of the saturated Si II line it is only possible to derive a lower limit, e.g., $\log N(\mathrm{Si\,II}) > 16.2$.

In the case of GRB151021A, the Si II line at 1808.0129 Å is clearly saturated. In other cases, however, a theoretically saturated line can appear unsaturated in the observed spectrum, because it is broadened by the instrumental resolution. This effect is called *hidden saturation* (e.g., Prochaska, 2006; Wiseman, Schady et al., 2017). Hidden saturation can have severe implications for the determination of the column density, and it is thus necessary to carefully investigate the posterior distributions after each fit. In case the column density and broadening parameter are highly degenerate, as a result of this effect, it is advisable to report lower limits, or not to use this line in the fit at all.

Another problem that occurs when dealing with spectra that have a relatively low resolution, like those from X-shooter ($R < 15\,000$), is, that it might not be possible to decompose all individual absorption components unambiguously. In this case the resultant b values might not be physical. This is demonstrated in Fig. 2.4, which shows the absorption profile of six different lines in the GRB 120327A afterglow spectrum. This

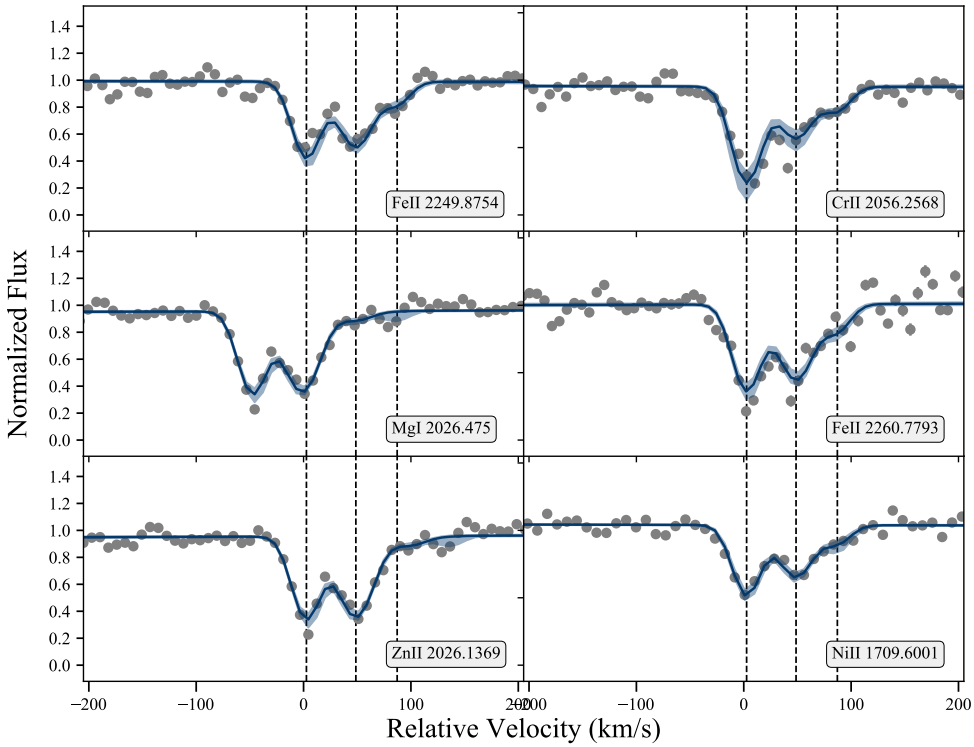

Figure 2.4: Results of a simultaneous fit of 6 different metal lines, with each three components in the spectrum of GRB 120327A. All lines share the same v_0 and broadening parameters and the two iron lines share the same three column density parameters as well.

spectrum has a resolution of $R = 10\,300$ or 29 km/s, and the absorption profile consists of at least three overlapping absorption components that are within only $\sim$ 80 km/s. Although it is possible to constrain the individual b values and column densities when fitting multiple lines together and to assume that the number of three absorption components is correct (see Fig. 2.5), one cannot exclude the possibility that more components with smaller b values are present.

As can be seen in Fig. 2.4, it can also happen that the absorption profiles of two different lines are blended. In the case of GRB 120327A, these lines are Zn II 2062.6603 and Cr II 2062.2359, as well as Mg I2026.4750 and Zn II 2026.1369 (these are the most common examples, but there are other cases as well). The program automatically checks if two or more lines overlap within the input velocity range and fits these lines simultaneously in the same frame.

Finally, when fitting two or more absorption components at the same time, it is also possible to constrain the instrumental resolution by leaving it as a free parameter. This can be done by including a resolution argument when executing the script from the command line, e.g., `--resolution 25 2`. In this case a normal prior with $\mu = 25$ km/s and $\sigma = 2$ km/s is put on the instrumental resolution. The instrumental resolution

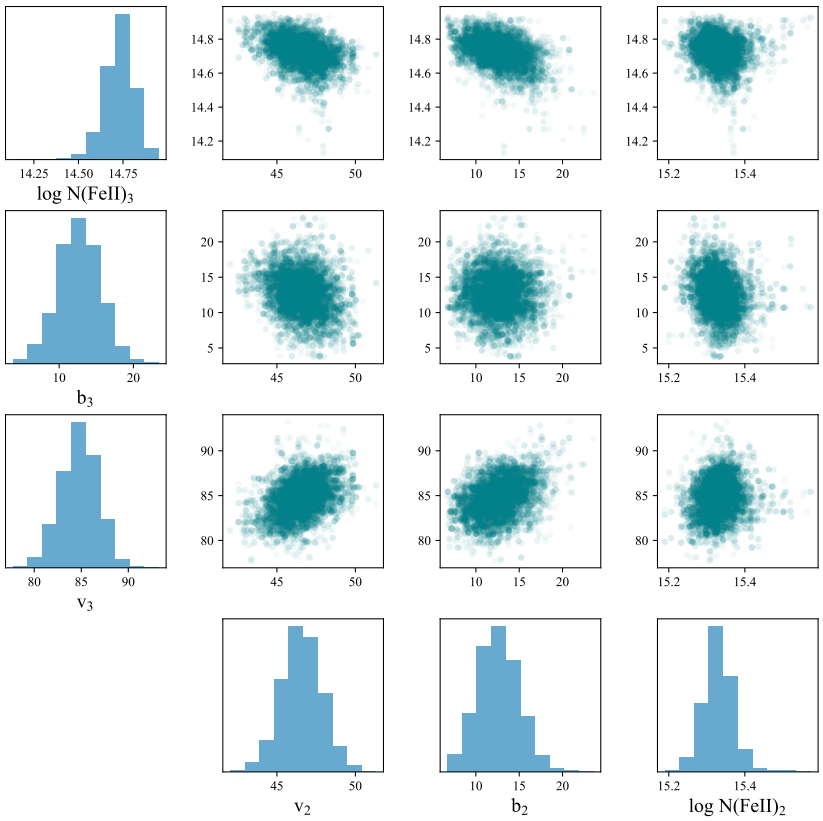

Figure 2.5: Histograms and pairwise scatter plots of the posterior distributions for the two iron lines at $v_0 \sim 47$ and $v_0 \sim 85$ km/s from the simultaneous fit of 4 metal lines in the spectrum of GRB 120327A (as shown in Fig. 2.4).

is highly degenerate with the column density and the broadening parameter, and this method should therefore only be used if it is not possible to determine the value by other means.

Chapter 3

Dust reddening and extinction curves toward gamma-ray bursts at $z > 4$

As published in Astronomy & Astrophysics, Volume 609, A62, January 2018
DOI: 10.1051/0004-6361/201731255
Dust reddening and extinction curves toward gamma-ray bursts at $z > 4$

Broadband photometric and spectroscopic observations of GRB afterglows are now routinely used to measure metal, molecule, and dust column densities along with depletion patterns or dust-to-metal ratios to high accuracy (e.g., Ledoux et al., 2009; Krühler et al., 2013; De Cia et al., 2013; Sparre et al., 2014; Wiseman, Schady et al., 2017; Bolmer, J. et al., 2019). Likewise, interstellar extinction curves have been tested out to very high redshifts (Zafar, Watson, Fynbo et al., 2011; Greiner et al., 2011; Perley et al., 2011; Schady et al., 2012), including detections of the characteristic 2175 Å bump (Krühler et al., 2008; Zafar et al., 2012) as known from the Milky Way (MW) and the Large Magellanic Cloud (LMC) or more unusual features (Savaglio & Fall, 2004; Perley et al., 2008; Fynbo et al., 2014), which might give new clues about dust production and properties throughout the Universe.

Measuring dust at high redshift, however, comes with substantial observational biases. Firstly, while $\gtrsim$ 90% of all *Swift*-detected GRBs ($>$ 1000) are detected and localized in X-rays with the *Swift*/XRT, only about 30% have a redshift estimate. Secondly, at redshifts $z > 2$ dust reddening forms an increasing hindrance in detecting the optical and near-infrared (NIR) afterglow. For instance, for a GRB at a redshift of $z = 4$, depending on the extinction law, a rest-frame $A_V = 1$ mag corresponds to an observer frame $A_V \sim 4$ to 5 mag, just due to redshifting the bandpass because the attenuation by dust usually increases from red to blue wavelengths. Heavily obscured afterglows, the so-called *dark* GRBs, are generally found to occur in more massive and redder galaxies (Krühler, Greiner et al., 2011; Rossi et al., 2012; Perley et al., 2013; Hunt et al., 2014), and it was argued that these bursts were more likely to be missed in follow-up campaigns.

Various approaches were therefore made to create optically unbiased samples of GRBs that are representative of the whole population. Cenko et al. (2009) and Greiner et al. (2011) for example chose only those GRBs that were observed within a few hours after the *Swift*/BAT trigger by instruments dedicated to observe every GRB. These and similar approaches, such as the BAT6 sample (Salvaterra et al., 2012; Covino et al., 2013) or the TOUGH (Hjorth et al., 2012) and SHOALS (Perley, Krühler et al., 2016;

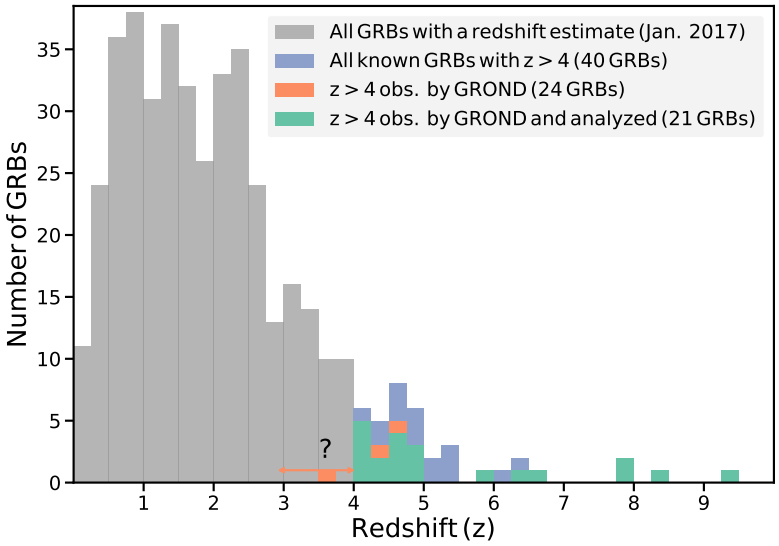

Figure 3.1: Distribution of GRBs per redshift bin ($\Delta z = 0.25$) for the events discussed in this paper compared to all LGRBs with a reported redshift estimate (indicated in gray; including all events before January 2017). A total of 40 bursts (blue) have a well-derived redshift estimate of $z > 4$; 24 (orange) of these have been observed with GROND, from which 21 (green) are analyzed in this paper.

Perley, Tanvir et al., 2016) surveys, find the percentage of *dark* GRBs to be around $\sim 20-40\%$ without necessarily considering a potential evolution with redshift. Although much smaller (< 100), these samples then reach a completeness in redshift of $> 90\%$. Furthermore, especially at even higher redshifts ($z > 3.5$), when optical and NIR SEDs and spectra are increasingly absorbed by the Lyman-α forest, additional absorption by dust can theoretically make a detection of the afterglow nearly impossible, even for 8-m class telescopes.

At redshifts ($z > 4-6$), when the Universe is thought to have been still too young to have formed AGB stars in high numbers, SNe are expected to be the main source of dust. However, it is still under debate how effectively dust is produced in the expanded shells of SNe and how high the contribution from AGB stars might be (Valiante et al., 2009; Hirashita et al., 2014). This is mainly because a high percentage of the SN produced dust might be destroyed by the reverse shock of the SN itself (Nozawa et al., 2007; Schneider, Omukai, Bianchi & Valiante, 2012). It is therefore likely that a significant initial production of dust in SN ejecta is required to explain the increasing evidence of large dust masses and high star formation rates found in high-redshift galaxies (e.g., through ALMA; Mancini et al., 2015; D. Watson et al., 2015; Laporte et al., 2017). Dust production in SN ejecta is observed in some local SNe remnants (Gomez et al., 2012; Indebetouw et al., 2014; Matsuura et al., 2015; De Looze et al., 2017) and predicted by some analytical models (Schneider, Omukai, Limongi et al., 2012; Silvia et al., 2012), which cover a broad range of possible dust survival rates or a significant contribution

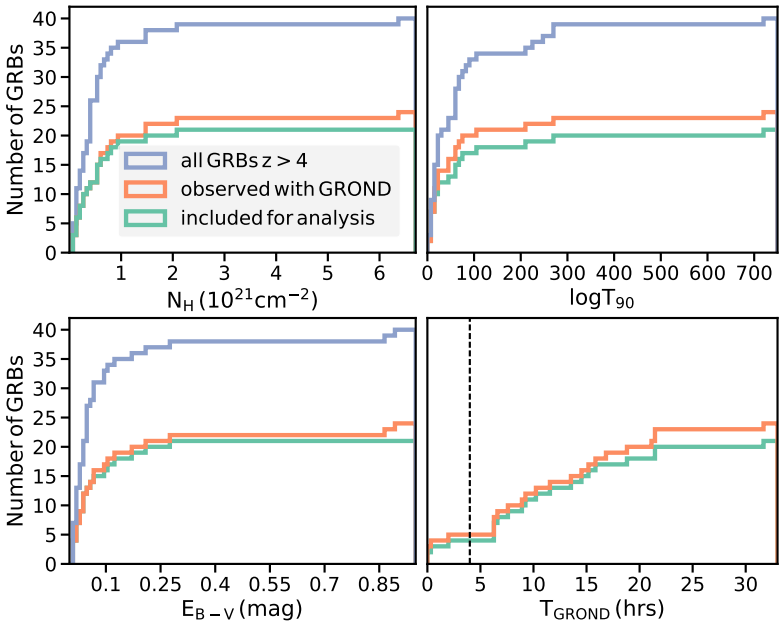

Figure 3.2: Cumulative distribution of the basic properties of the GRBs at $z > 4$. Shown are the galactic foreground reddening E_{B-V} and hydrogen column density $N_{\rm H}$, as well as the duration of the prompt emission T_{90} and the time of the first GROND observation $T_{\rm GROND}$. With two exceptions, all GRBs are behind modest galactic dust and hydrogen column densities (left panels). The value T_{90} is between 2 and 300 s for all of the GRBs with the only outlier being GRB 140614A with 720 s (top right panel). The majority of the GRBs were observed by GROND between 4 to 18 hrs after the trigger; only 6 are part of the unbiased GROND 4h sample (Greiner et al., 2011) (bottom right panel).

from subsequent grain growth in the ISM (Nozawa et al., 2012; Sarangi & Cherchneff, 2013; Nozawa et al., 2015; Michałowski, 2015).

The theoretical model from Todini & Ferrara (2001) shows, that SN-origin dust would produce a characteristic extinction curve, which could be measured in absorption systems toward background sources such as quasars and GRBs. Indeed, Maiolino et al. (2004) reported evidence for the SN origin of dust in a quasar at redshift $z = 6.2$ [1]. Similar evidence for extinction caused by SN synthesized dust was found in two GRB afterglows at a redshift of $z > 4.8$. While two different authors reached the same conclusion for GRB 071025 (Perley et al., 2010; Jang et al., 2011), the claim for SN-type dust in GRB 050904 is more controversial (Stratta et al., 2007; Zafar et al., 2010; Stratta et al., 2011).

The aim of this Chapter is to provide a detailed and consistent study of the dust extinction properties in the afterglows of the most distant GRBs, to find out about a potential evolution with redshift and whether a SN-like dust extinction curve is required for some of the bursts. The Chapter is arranged as follows: In Section 3.1 we describe the current sample of GRBs at $z > 4$. Section 3.2 presents our data analysis and reduction

[1] Hjorth et al. (2013) come to a different conclusion.

Table 3.1: All GRBs with a spectroscopic or photometric redshift estimate of $z \geq 4$ (until the 1. of January 2017).

GRB (yymmdd#)	Right Ascension (J2000)	Declination (J2000)	Error	Redshift (z)	Ref.	T_{90} (s)	E_{B-V} (mag)	$N_{\rm H}$ ($10^{21}\,{\rm cm}^{-2}$)	$T_{\rm GROND}$ (hrs)
GRBs with $z > 4$ observed with GROND									
071025	+23:40:17.11	+31:46:42.74	0″.20	$4.88^{+0.35}_{-0.35}$	(1)	109 ± 2	0.06	0.55	21.69
080825B	+13:56:48.29	−68:57:18.57	0″.25	$4.31^{+0.14}_{-0.15}$	(2)	50	0.21	2.09	6.64
080913	+04:22:54.73	−25:07:45.98	0″.31	6.733	(3)	8 ± 1	0.04	0.33	0.10
080916C	+07:59:23.32	−56:38:17.92	0″.37	$4.28^{+0.6}_{-0.10}$	(1)	~ 60	0.28	1.50	31.74
090205	+14:43:38.68	−27:51:10.10	0″.30	4.650	(4)	8.8 ± 1.8	0.10	0.80	6.39
090423	+09:55:33.27	+18:08:58.06	0″.29	8.26	(5)	10.3 ± 1.1	0.03	0.29	15.29
090429B	+14:02:40.10	+32:10:14.20	0″.30	$9.38^{+0.14}_{-0.32}$	(6)	5.5 ± 1.0	0.01	0.12	21.72
090516	+09:13:02.60	−11:51:14.90	0″.30	4.109	(7)	210 ± 65	0.04	0.45	14.60
100219A	+10:16:48.51	−12:34:00.50	0″.29	4.667	(8)	18.8 ± 5.0	0.07	0.65	9.20
100905A	+02:06:12.04	+14:55:45.80	0″.31	$7.88^{+0.75}_{-0.94}$	(1)	3.4 ± 0.5	0.05	0.54	16.02
111008A	+04:01:48.24	−32:42:32.87	0″.29	4.990	(9)	63.46 ± 2.19	0.01	0.10	6.43
120712A	+11:18:21.24	−20:02:01.41	0″.30	4.175	(10)	14.7 ± 3.3	0.04	0.36	9.25
120923A	+20:15:10.78	+06:13:16.30	0″.30	7.84	(11)	27.2 ± 3.0	0.13	0.98	18.95
130606A	+16:37:35.13	+29:47:46.61	0″.20	5.913	(12)	276.58 ± 19.31	0.02	0.20	6.43
131117A	+22:09:19.37	−31:45:44.22	0″.40	4.042	(13)	11.00 ± 3.16	0.02	0.15	0.05
140311A	+13:57:13.27	+00:38:32.11	0″.14	4.954	(14)	71.4 ± 9.5	0.03	0.25	11.72
140428A	+12:57:28.38	+28:23:06.88	0″.18	$4.68^{+0.52}_{-0.18}$	(1)	17.42 ± 5.90	0.01	0.09	2.05
140515A	+12:24:15.52	+15:06:16.62	0″.24	6.327	(15)	23.4 ± 2.1	0.02	0.23	13.76
140614A	+15:24:40.66	−79:07:43.20	0″.30	4.233	(16)	720 ± 120	0.11	0.82	0.54
151027B	+05:04:52.69	−06:27:01.07	0″.25	4.062	(17)	80.00 ± 35.78	0.18	0.58	7.76
151112A	+00:08:12.75	−61:39:48.47	0″.36	$4.27^{+0.24}_{-0.38}$	(1)	19.32 ± 31.24	0.01	0.18	10.43
GRBs with $z > 4$ observed with GROND that have been excluded from the sample									
080129	+07:01:08.20	−07:50:46.51	0″.28	4.349	(18)	48 ± 10	0.87	6.42	0.10
100518A	+20:19:09.33	−24:33:16.57	0″.28	$3.50^{+0.50}_{-0.62}$	(1)	25	0.07	0.63	17.13
131227A	+04:29:30.84	+28:52:58.92	0″.30	5.3	(19)	18.0 ± 1.6	0.90	1.51	21.39
All other GRBs with a redshift estimate of $z > 4$:									
000131	+06:13:31.1	−51:56:41.7	1″.1	4.500	(20)	96.3	0.05	0.41	-
050502B	+09:30:10.1	+16:59:47.9	1″.4	$5.2^{+0.3}_{-0.3}$	(21)	17.5 ± 0.2	0.03	0.36	-
050505	+09:27:03.3	+30:16:24.2	1″.4	4.275	(22)	60 ± 2	0.02	0.17	-
050814	+17:36:45.4	+46:20:21.8	1″.4	$5.77^{+0.12}_{-0.12}$	(23)	65^{+40}_{-20}	0.02	0.23	-
050904	+00:54:50.9	+14:05:09.3	3″.5	6.295	(24)	225 ± 10	0.05	0.45	-
050922B	+00:23:13.4	−05:36:17.3	1″.7	4.5 ± 0.5	(25)	250 ± 20	0.03	0.31	-
060206	+13:31:43.4	+35:03:02.8	1″.5	4.048	(26)	7 ± 2	0.01	0.09	-
060223A	+03:40:49.6	−17:07:49.8	1″.5	4.406	(27)	11 ± 2	0.10	0.69	-
060510B	+15:56:29.2	+78:34:11.8	1″.5	4.941	(28)	276 ± 10	0.04	0.41	-
060522	+21:31:44.9	+02:53:09.9	1″.4	5.11	(29)	69 ± 5	0.05	0.42	-
060927	+21:58:12.0	+05:21:49.0	1″.6	5.467	(30)	22.6 ± 0.3	0.05	0.46	-
100302A	+13:02:03.8	+74:35:23.7	1″.5	4.813	(31)	17.9 ± 1.7	0.02	0.19	-
100513A	+11:18:26.8	+03:37:40.8	1″.4	4.772	(32)	84 ± 21	0.05	0.42	-
120521C	+14:17:08.8	+42:08:41.5	1″.6	6.0	(33)	26.7 ± 4.4	0.01	0.11	-
140304A	+02:02:34.3	+33:28:25.7	1″.5	5.283	(34)	15.6 ± 1.9	0.07	0.60	-
140518A	+15:09:00.6	+42:25:05.7	2″.7	4.707	(35)	60.5 ± 2.4	0.01	0.15	-

Notes. Columns 5–10 are the redshift (photometric when given with errors, spectroscopic otherwise), corresponding reference, time interval T_{90} over which 90% of the total background-subtracted counts are observed (GRBs with $T_{90} > 2$ s are classified as long gamma-ray bursts (LGRBs)), galactic foreground reddening from Schlafly & Finkbeiner (2011), as retrieved from the NASA Extragalactic database (NED, `http://irsa.ipac.caltech.edu/applications/DUST/`), total galactic neutral hydrogen column density provided by Kalberla et al. (2005), and start of the GROND observations in hours after the GRB Trigger (rounded to two decimal places).

References. (1) this work; (2) Krühler, Schady et al. (2011); (3) Patel et al. (2010); (4) Fugazza et al. (2009); (5) Tanvir et al. (2009); (6) Cucchiara et al. (2011); (7) de Ugarte Postigo et al. (2009); (8) Mao et al. (2012); (9) Wiersema et al. (2011); (10) Xu et al. (2012); (11) Tanvir et al. (2018); (12) Xu, Malesani et al. (2013); (13) Hartoog et al. (2013); (14) Tanvir et al. (2014); (15) Chornock et al. (2014); (16) Krühler et al. (2014); (17) Xu et al. (2015); (18) Greiner, Krühler, McBreen et al. (2009); (19) Cucchiara & Cenko (2013); (20) Andersen et al. (2000); (21) Afonso et al. (2011); (22) Berger et al. (2006); (23) Curran et al. (2008); (24) Kawai et al. (2006); (25) Schulze et al. (2015); (26) Fynbo, Starling et al. (2006); (27) Chary et al. (2007); (28) Price et al. (2007); (29) Cenko et al. (2006); (30) Ruiz-Velasco et al. (2007); (31) Chornock et al. (2010); (32) Cenko, Perley et al. (2010); (33) Laskar et al. (2014); (34) Jeong et al. (2014); (35) Chornock et al. (2014).

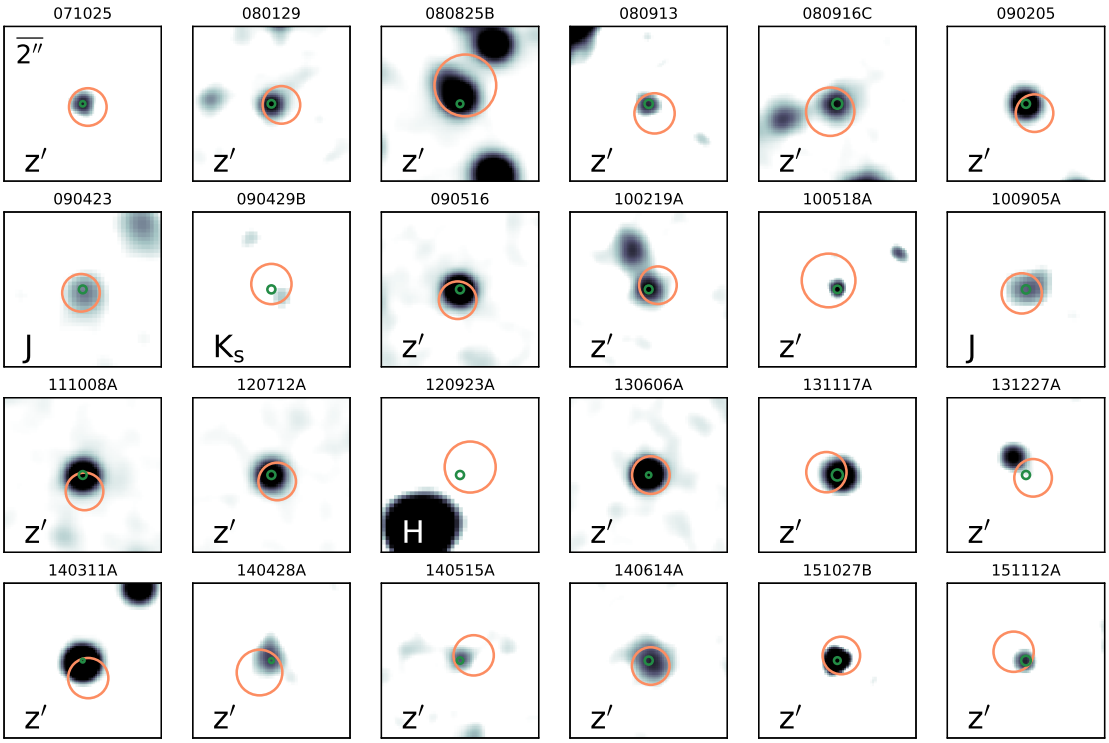

Figure 3.3: Thumbnails for the 24 GRBs observed with GROND. The orange circles represent the *Swift*/XRT 90% error circles as taken from www.swift.ac.uk/xrt_positions/, and the green circles show the position of the NIR/optical afterglow as given in Tab. 3.1. A 2″ scale bar is shown in the top left plot for GRB 071025 and the particular GROND filter is denoted in the bottom left corner of each finding chart. With the exception of GRBs 090429B, 120923A, and 131227A, we were able to detect the NIR/optical counterpart with GROND.

technique, and the main results are summarized in Section 3.3. Finally, we discuss the results and conclude in Section 3.4. Throughout the Chapter all magnitudes are given in the AB system and we adopt the convention that the GRB flux density is described by $F_\nu(t) \propto t^{-\alpha}\nu^{-\beta}$. Unless indicated otherwise, all errors are given at 1σ confidence.

3.1 The sample

The GRB afterglow sample presented here is based on selecting all 40 observed events with a previously reported spectroscopic or photometric redshift of $z > 4$ (complete up until 1 January 2017; see Fig. 3.1)[2]. This sample is presented in Tab. 3.1, which is divided into three parts. Of these 40 GRBs, we were able to observe 24 with GROND, and of these, 21 GRBs (top part) were selected for our analysis and 3 GRBs (middle part) were

[2]This was performed on the basis of the public GRB table maintained by one of the co-authors: http://www.mpe.mpg.de/~jcg/grbgen.html; bursts classified as short and redshift values reported with a question mark were ignored.

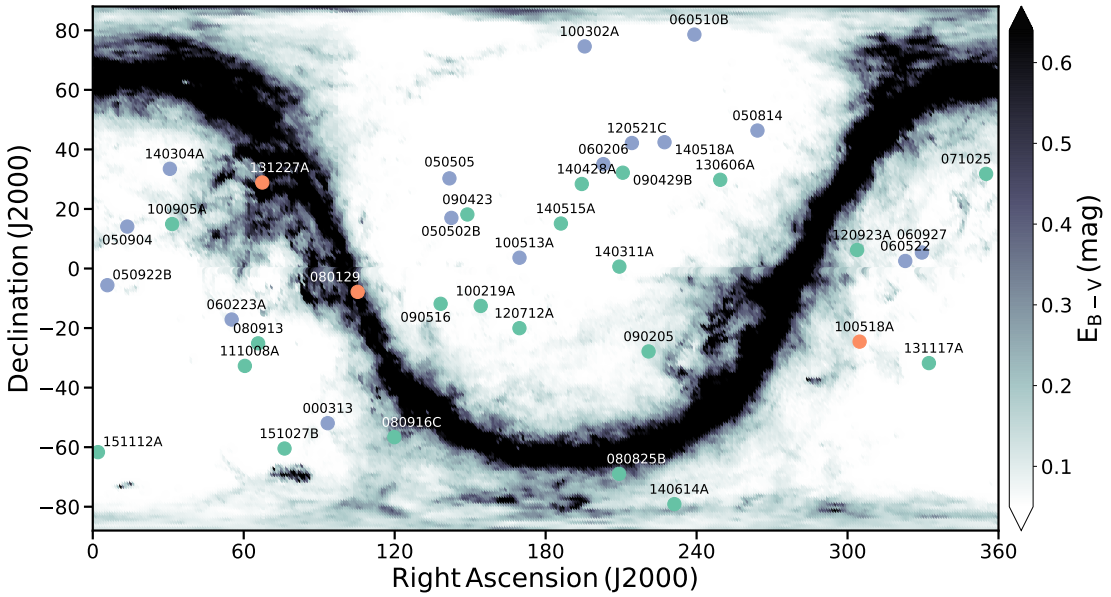

Figure 3.4: All-sky map of the galactic dust reddening E_{B-V} as given by Schlafly & Finkbeiner (2011). The GRBs analyzed here are indicated in green. Those indicated in orange were excluded from the sample and those colored in blue are all other known GRBs with a redshift of $z > 4$. The sky above Dec $> 44°$ cannot be observed from La Silla (Chile), where GROND is mounted at the 2.2m MPI telescope.

excluded for reasons given below. The remaining 16 GRBs at $z > 4$ are listed in the bottom portion of the table. These either occurred before the GROND commissioning in 2007, were too far north to be observable from Chile (see Fig. 3.4), or were not observable with GROND because of bad weather (GRB 100513A). For each GRB, we give the coordinates of the NIR/optical afterglow, redshift, duration of the prompt emission (T_{90}), galactic foreground reddening E_{B-V} and hydrogen column density ($N_{\rm H}$), as well as the time after which we started observing the afterglow with GROND ($T_{\rm GROND}$). These properties of the sample are also visualized in Fig. 3.2.

Two of the GRBs observed by GROND lie close to the galactic plane and are behind high galactic dust and hydrogen column densities, namely GRB 080129 and GRB 131227A, and were thus excluded from the sample (see Fig. 3.4). Additionally, we excluded GRB 100518A, because our analysis results in a photometric redshift of only $z_{\rm phot} = 3.50^{+0.50}_{-0.62}$ (see Sect. 3.2.4). Also only 4 out of the 21 analyzed GRBs are part of the unbiased GROND 4h-sample, which contains all GRBs that have been observed within at least 4 hrs post trigger (Greiner et al., 2011). However, a large percentage of the bursts could be observed between 4 and 18 hrs after their detection, during the first night in La Silla (Chile) usually providing a high chance of reliable detections in most of the seven GROND filter bands. Only three bursts (GRB 071025, 080916C, and 090429B) could not be observed with GROND during the first night of their trigger, mainly due bad weather in La Silla. Finally, although all 24 GRB afterglows observed with GROND

were also observed and detected with *Swift*/XRT, the prompt emission of three of these was initially detected by instruments on other satellites (GRB 080825B: *Agile*/GRID, GRB 080916C: *Fermi*/GBM+LAT, and GRB 100518A: *Integral*/IBIS).

3.2 Data reduction and analysis

For the aim of this project of the thesis all GRBs with a redshift of $z > 4$ and observed by GROND and *Swift*/XRT, were analyzed to create broadband SEDs to measure dust column densities and test extinction curves along their line-of-sight.

3.2.1 X-ray data analysis

The XRT X-ray light curves and spectra of the afterglow were taken from the automated data products provided by the public *Swift*/XRT repository (Evans et al., 2009). To ensure that there were at least 20 counts per bin, we further regrouped the spectral data from 0.3-10 keV in the chosen time interval from the photon counting mode (PC) alone with the *grappha* task from the HEAsoft package and the response matrices from CALDB (Version `v20120209`); this also ensured that bad columns could be ignored. In cases where no X-ray data were available simultaneously to the GROND observations, the XRT spectra were additionally flux normalized to the mid-time of the chosen GROND exposure using the temporal decay model, which best fit the XRT light curve. The common reference time was generally chosen to be after any optical rise/late-time re-brightening, steep decay, or plateau phase, at least in those cases where such a distinction was possible. We also avoided selecting time intervals from periods of X-ray flares or spectral evolution, i.e., time intervals of changing temporal decay.

3.2.2 Near-infrared and optical data analysis

We carried out GROND image reduction and photometry with the standard *Image Reduction and Analysis Facility* tasks (IRAF; Tody, 1993), as described in Krühler et al. (2008). The absolute calibration of the GROND observations in $g'r'i'z'$ was carried out with stars observed in the Sloan Digital Sky Survey (SDSS). In cases where the GRB was not in a field covered by the SDSS, an SDSS field and the GRB field were observed consecutively during photometric conditions to cross-calibrate the zero points. The absolute NIR calibration in JHK_s was performed using the Two Micron Sky Survey (2MASS; Skrutskie et al., 2006) stars within the field of the GRB. This method results in typical systematic errors of 0.03 mag for the $g'r'i'z'$ bands, 0.05 mag for the JH bands and 0.07 mag for the K_s band. Finally, before the fitting process, all magnitudes were corrected for the galactic foreground reddening according to the values given by Schlafly & Finkbeiner (2011) and listed in Tab. 3.1. The complete set of GROND photometry for the GRBs at $z > 4$ is given in Tab. 3.4.

As an example, the NIR/optical and XRT X-ray light curves of GRB 100905 are shown in Fig. 3.5. The light curves of all other GRBs are moved to the end of this Chapter

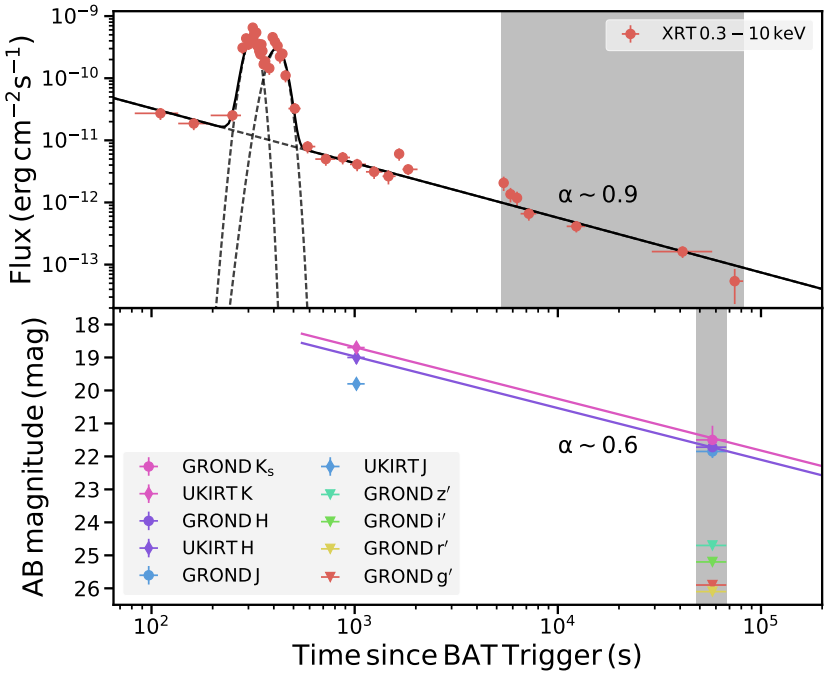

Figure 3.5: Near-infrared and optical and XRT X-ray light curves of GRB 100905A. In addition to the GROND detections and upper limits we also plot UKIRT J-, H- and K-band magnitudes as reported by Im et al. (2010). The XRT light curve shows some flaring activity between T_0+300 and T_0 + 600 s and is otherwise best fit with a single power law and a temporal decay slope of $\alpha_X \sim 0.9$. The GROND and UKIRT K- and H-band light curves indicate a temporal decay slope of $\alpha_o \sim 0.6$. The time intervals used to created the quasi-simultaneous broadband SED are indicated in gray.

(Fig. 3.13 to Fig. 3.23), where we also describe the light-curve analysis in more detail and list the best-fit models in Tab. 3.5.

3.2.3 Position of the near-infrared and optical afterglow

The position of the NIR/optical afterglow was determined by using the USNO or SDSS field stars as astrometric reference. For the majority of the GRBs we used the GROND z' band observations and averaged over all detections. For GRB 090423 and 100905A, which were not detected in z', we used the 2MASS field stars in the GROND J band. This method results in a typical absolute error of 0.″3 in each coordinate. For the bursts that were observed but not detected by GROND, namely GRB 090429, 120923A and 131227A, we collected coordinates from the literature (Cucchiara et al., 2011; Cucchiara & Cenko, 2013; Tanvir et al., 2018). For the rest of the bursts, in Tab. 3.1 we simply list the XRT positions taken from `http://www.swift.ac.uk/xrt_positions/`, which are typically good to $\sim 2''$; we only use the position given by Andersen et al. (2000) for GRB 000131.

3.2.4 Photometric redshifts

From the 24 GRBs observed with GROND, 15 have a spectroscopically measured redshift. All the other GRBs have photometric redshift measurements from the afterglow, of which some are studied in detail in refereed publications and others are only rough estimates that were published in GCNs. For the latter we here provide new and more precise constraints based on carefully analyzed and calibrated GROND data.

The photometric redshift for GRB 080825B of $z_{\rm phot} \sim 4.3$ was determined by Krühler, Schady et al. (2011) based on the Lyman-break technique, using multi-band photometry from GROND and UVOT. We used that same, robust and reliable method to determine and confirm photometric redshifts of $z_{\rm phot} > 4$ for GRB 071025, 080916C, 100905A, 140428A, and 151112A. For GRB 100518A, we cannot confirm the previously determined redshift of $z_{\rm phot} > 4$. As already noted by Kann et al. (2013), for GRB 131227A a detection with GROND is ambiguous, and finally, for GRB 090429B we used the photometric redshift determined by Cucchiara et al. (2011). All spectroscopic and photometric redshifts and the corresponding references are listed in Tab. 3.1.

Since this is the first time we publish the GROND data and a photometric redshift for GRB 100905A, we briefly describe the burst in the first of the following paragraphs. For the other five burst we summarize the main results and the corresponding figures are shown in Sect. 3.5.

GRB 100905A *Swift*/BAT triggered on GRB 100905A on September 6, 2010 at $T_0 =$ 15:08:14 UT (MJD = 55444.63072) with a duration of $\rm T_{90} = 3.4 \pm 0.5$ s (Barthelmy et al., 2010; Marshall et al., 2010). The XRT started observing the field around 100 s after the trigger. The UVOT observations only lead to upper limits (Siegel & Marshall, 2010). We started observing the field with GROND at around 13 hrs after the BAT trigger and detected the afterglow in J, H and $K_{\rm s}$ at a common position of RA, Dec = +02:06:12.04, +14:55:45.80 with an absolute accuracy of $0\farcs31$ in each coordinate (as for all of the other GRBs, the magnitudes and upper limits are given in Tab. 3.4). The afterglow was also detected in J, H, and K by Im et al. (2010) using the United Kingdom Infra-Red Telescope (UKIRT). The XRT X-ray, NIR, and optical light curves are shown in Fig. 3.5. Besides some flaring activity between $\rm T_0 + 300$ and $\rm T_0 + 600$ s, the XRT light curve is best fit with a single power law and a temporal decay index of $\alpha_{\rm X} = 0.88 \pm 0.03$. When compared to the UKIRT observations, our GROND magnitudes indicate a somewhat weaker fading of the NIR/optical afterglow ($\alpha_{\rm o} = 0.60 \pm 0.06$), when assuming a single power law decay.

Using the method presented in Krühler, Schady et al. (2011), we determine a photometric redshift of $z_{\rm phot} = 7.88^{+0.75}_{-0.94}$, when fitting the GROND magnitudes with a single power law, which is reddened by dust following the Small Magellanic Cloud (SMC) extinction law. The big errors are the result of the missing wavelength coverage between the z' and J band. The corresponding $\Delta\chi^2$ contours, given the best-fit spectral slope of $\beta = 0.45$, as well as the GROND SED and the redshift probability density function are shown in Fig. 3.6. Using only the GROND magnitudes we find no evidence for absorption by dust ($A_V = 0.00^{+0.27}_{-0.00}$ mag).

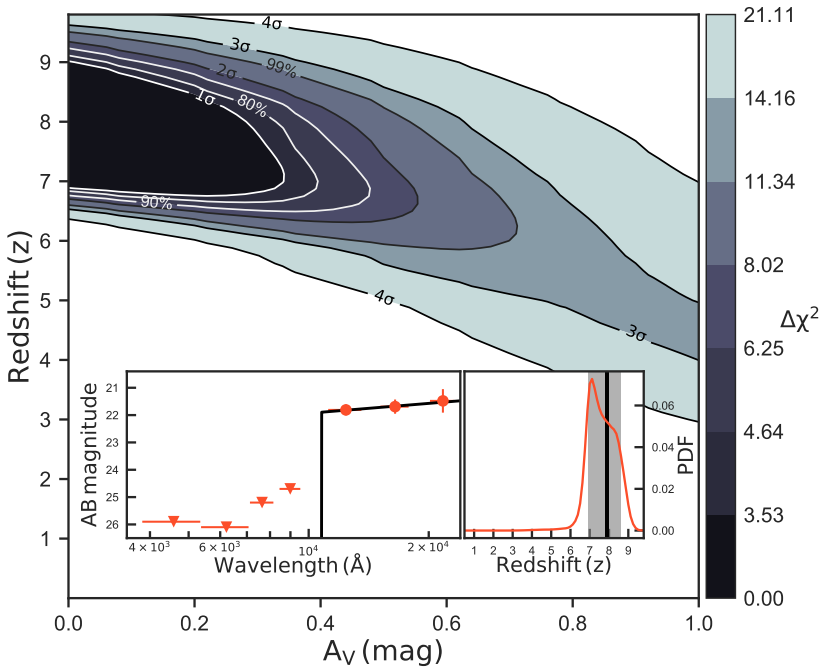

Figure 3.6: Contour plot of the $\Delta\chi^2$ values for each of fitted host-intrinsic visual extinction A_V and redshift (z) parameters for the best-fit power-law index of $\beta = 0.45$. For three degrees of freedom, the significance levels of 1σ (68.27%), 2σ (95.45%), 3σ (99.73%), and 4σ (99.99%) correspond to $\Delta\chi^2 = 3.53$, 8.02, 11.35 and 21.11, respectively. As shown in the left inset, the GROND SED is best fit with the SMC extinction curve, a power-law slope of $\beta = 0.45$, no dust extinction ($A_V = 0.00$ mag), and a photometric redshift of $z_{\rm phot} = 7.88^{+0.75}_{-0.94}$. In the inset on the right we also show the corresponding redshift probability density function. The gray shaded area indicates the 1σ confidence interval.

So far, no robust redshift measurement for this event is reported in the literature, but, if correct, it would make GRB 100905A one of the most distant GRBs known to date.[3]

The very high redshift interpretation is consistent with the non-detection of a host galaxy in deep NIR imaging from the Hubble Space Telescope. In a total of 10423 s of exposure in the WFC3/F140W filter, no host is detected down to a 3σ limiting magnitude of F140W > 28.5 mag$_{\rm AB}$. These faint magnitudes are characteristic for high-z GRB hosts in general (Tanvir et al., 2012; McGuire et al., 2016) and would be somewhat unexpected for a lower redshift ($z \sim 2$) galaxy hosting a dust-extinguished GRB (Krühler, Greiner et al., 2011).

GRB 071025 is best-fit with the SN-like dust extinction law, $A_V = 0.39^{+0.20}_{-0.14}$ mag and a photometric redshift of $z_{\rm phot} = 4.88 \pm 0.35$, which is consistent with the photometric redshifts of $4.4 < z_{\rm phot} < 5.2$ and $4.6 < z_{\rm phot} < 4.85^{+0.05}_{-0.10}$ reported by Perley et al.

[3] Starling et al. (2013) assumed a photometric redshift of $z = 7$, based on private communication with Im et al. and Littlejohns et al. (2013) list $z \sim 7.25$ without giving a reference.

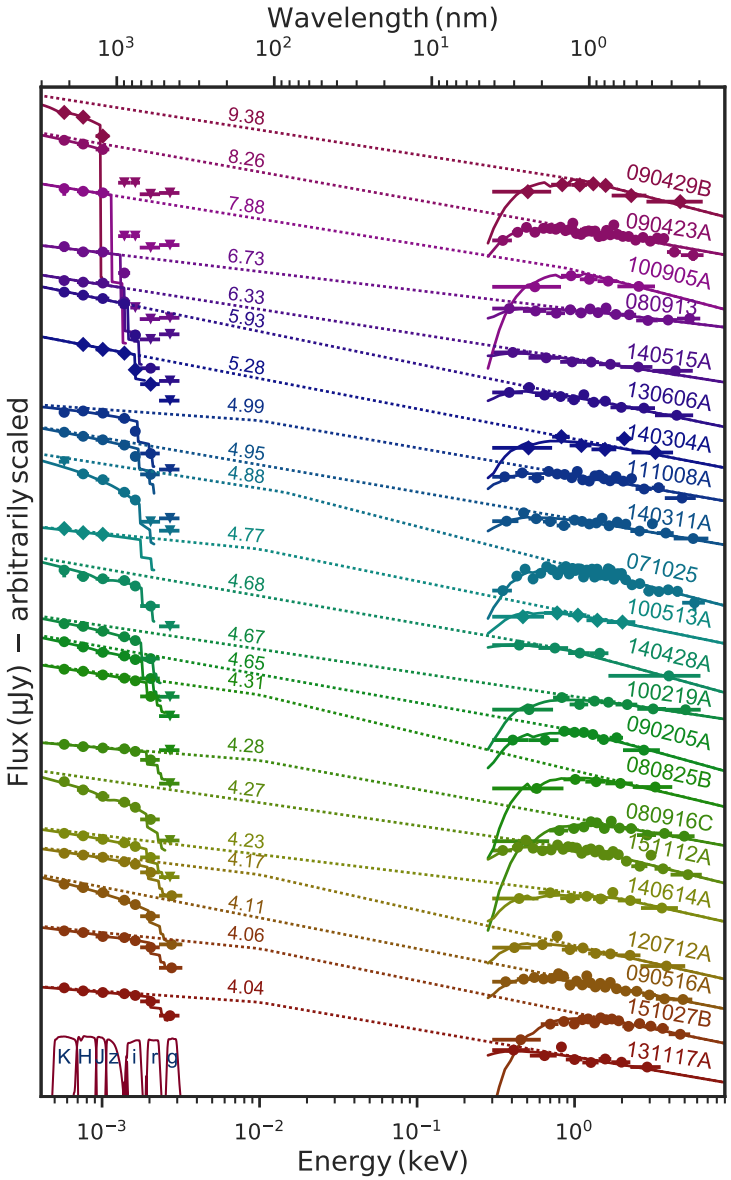

Figure 3.7: Spectral energy distribution for the 22 GRBs analyzed in this paper with increasing redshift from the bottom to top (as labeled). Data for GRBs detected with GROND are plotted with circles, data from other instruments with diamonds. The X-ray spectrum, if not available simultaneously to the NIR/optical data, was flux normalized to the mid-time of the chosen GROND exposure. Dashed lines indicate the unabsorbed best-fit models. Solid lines indicate the best-fit model including absorption: in the X-rays due to galactic plus host intrinsic absorption by medium weight metals; in the NIR/optical range due to host intrinsic absorption by dust (the data were corrected for galactic foreground reddening beforehand). The flux on the y-axis is completely arbitrary to get a better visualization. In the left corner at the bottom of the plot we also show the GROND filter curves.

(2010) and Jang et al. (2011), who also find evidence for extinction caused by supernova-synthesized dust. We limited the redshift parameter space to $z > 2$, to prevent a low-redshift solution that would be in strong disagreement with the results from the above-mentioned authors.

GRB 080916C is best fit with $z_{\rm phot} = 4.28^{+0.06}_{-0.10}$, $A_V = 0.11^{+0.08}_{-0.09}$ mag and the SMC extinction curve, which is consistent with the results from Greiner, Clemens et al. (2009).

GRB 100518A For GRB 100518A we cannot confirm the previously reported redshift of $z_{\rm phot} = 4.0^{+0.3}_{-0.5}$ (Greiner, Fox et al., 2015). Our GROND magnitudes, as listed in Tab. 3.4, are best fit with a $z_{\rm phot} = 3.50^{+0.50}_{-0.62}$ and a host intrinsic extinction of $A_V = 0.19^{+1.48}_{-0.19}$ mag, indicating that is is difficult to distinguish between a high redshift and low visual extinction or vice versa. The high redshift ($z \gtrsim 3$) nature of the GRB is further supported from late-time observations in the *VLT*/FORS2 R-band, not revealing a host galaxy down to a limit of > 28.7 mag (Greiner, Fox et al., 2015).

GRB 140428A is best fit with a photometric redshift of $z_{\rm phot} = 4.68^{+0.52}_{-0.18}$, which is in accordance with the estimate of $z \sim 4.7$ from the LRIS spectrum (Perley, 2014b), and the SN extinction law ($A_V = 0.36^{+0.06}_{-0.32}$ mag).

GRB 151112A is best fit with a photometric redshift of $z_{\rm phot} = 4.27^{+0.24}_{-0.38}$ and the SMC extinction law ($A_V = 0.08^{+0.34}_{-0.02}$ mag). This is consistent with the initial estimate from Bolmer et al. (2015).

3.2.5 The XRT X-ray, NIR, and optical GRB afterglow light curves

The GROND and XRT observations of the afterglow were supplemented – if available – by additional observations reported in the literature, to create and fit as well covered light curves as possible. To fit the afterglow light curves we used phenomenological models such as a single or smoothly broken power-law or a combination of both (similar to, e.g., Zaninoni et al., 2013). Flares and re-brightenings were modeled by adding a Gaussian component, and a possible contribution from the host galaxy was modeled by adding a constant term.

$$F_\nu(t) \propto t^{-\alpha_1} \left(+ \left(\left(\frac{t}{t_b} \right)^{-s\cdot\alpha_2} + \left(\frac{t}{t_b} \right)^{-s\cdot\alpha_3} \right)^{-1/s} \right) \left(+ e^{-\frac{1}{2}\cdot\left(\frac{t-t_{\rm mid}}{\sigma_t}\right)^2} \right) (+h) \qquad (3.1)$$

This method is sufficient to identify regions of temporal (and possibly spectral) evolution and to rescale XRT and/or GROND data to a common reference time. In most cases we kept the GROND data fixed and used the usually better covered XRT light curve to rescale the X-ray spectrum. We only used the model best fit to the GROND

light-curves for GRB 080825B, for which the XRT light curve consists of only four data points.

All the light curves and best-fit models are shown in Fig. 3.13 to Fig. 3.23. In each case, the gray shaded areas indicate the time intervals, which were chosen to create the quasi-simultaneous X-ray to NIR/optical broadband SEDs. Additionally, the best-fit models and parameters as well as the references for the data collected from the literature are given in Tab. 3.5.

Finally, for some of the GRBs, the GROND data are already published in various papers (GRB 080913 in Greiner, Krühler, Fynbo et al. (2009), GRB 080916C in Greiner, Clemens et al. (2009), 090423 in Tanvir et al. (2009), GRB 090429B in Cucchiara et al. (2011), and GRB 100219A in Thöne et al. 2013). However, due to improvements of the GROND data reduction pipeline and for reasons of consistency, we decided to re-analyze the data. The complete set of GROND magnitudes is given in Tab. 3.4.

3.2.6 Spectral energy distribution fitting

In theory, GRB afterglow spectra are featureless and non-thermal, synchrotron spectra made up of a number of connected power laws. Observations in the X-ray and optical/NIR regime, typically sample the same portion of the synchrotron spectrum, i.e. a single power law describes the X-ray to NIR SED; in some case however, synchrotron cooling frequency lies between the X-ray and optical/NIR spectral range, producing a change in spectral slope at higher energies. Hence, after rescaling XRT and GROND data to a common reference time and correcting the GROND magnitudes for the foreground reddening given in Tab. 3.1, the NIR/optical to X-ray broadband SEDs were fitted in XSPEC with the combined model of `PHABS·ZPHABS·ZDUST·POW` and `PHABS·ZPHABS·ZDUST·BKNPOW`. The redshift was fixed to that obtained from spectroscopic measurements of the afterglow, host, or photometric dropout, in this order of priority, either from literature or determined in this work. The galactic foreground hydrogen column densities were fixed to the values listed in Tab. 3.1 and in the case of a broken power law, the difference in slope between X-ray and NIR/optical wavelengths was fixed to 0.5, according to the standard fireball model for the slope difference around the cooling frequency and in line with the majority of GROND-measured SEDs (Greiner et al., 2011). Filters blueward of Lyman-α at the GRB redshift were ignored owing to additional absorption from the Lyman-α forest. All other parameters were left free and χ^2 was minimized when fitting each of the three extinction curves featured in the `ZDUST` model, namely those for the SMC and LMC as well as the Milky Way (MW), with a single or a broken power law. Additionally, for the burst showing evidence for dust extinction (i.e. $A_V > 0.1$ mag) we also fitted the model from Todini & Ferrara (2001) & Maiolino et al. (2004) for an extinction curve caused by supernova synthesized dust. Its most characteristic feature is the flattening between 3000 Å and 1700 Å followed by a steep decline (see Fig. 2 in Maiolino et al. 2004). The reason we explored only one out of various extinction curves proposed for SN-type dust is discussed in Sect. 3.4.

Especially for GRBs at high redshift, when more and more of the GROND bands are affected by absorption caused by the Lyman-α forest, it is not feasible to fit more

Table 3.2: Summary of the best-fit models and parameters of the 22 GRBs analyzed in this paper.

GRB	Redshift	Model	Ext. Curve	β_o [a]	A_V	E_{break}	Norm.	χ^2	χ^2_{red}	T_{SED} [b]
(yymmdd#)	fixed to				(mag)	(keV)	(keV/cm^2/s/keV)	(d.o.f.)		(hrs)
071025	4.900	bknpow	smc	$0.77^{+0.17}_{-0.08}$	$0.45^{+0.13}_{-0.14}$	$1.45 \cdot 10^{-2}$	$2.78 \cdot 10^{-4}$	40.1 (36)	1.11	22.4
080825B	4.310	bknpow	smc	$0.67^{+0.19}_{-0.03}$	$0.05^{+0.02}_{-0.02}$	$9.93 \cdot 10^{-3}$	$1.82 \cdot 10^{-3}$	2.9 (5)	0.58	12.4
080913	6.733	pow	smc[d]	$0.59^{+0.02}_{-0.02}$	$0.00^{+0.00}_{-0.00}$	.....	$1.02 \cdot 10^{-3}$	9.9 (12)	0.83	0.2
080916C	4.280	bknpow	smc[d]	$0.40^{+0.18}_{-0.02}$	$0.01^{+0.03}_{-0.01}$	$9.99 \cdot 10^{-3}$	$1.15 \cdot 10^{-3}$	12.3 (13)	0.95	32.6
090205A	4.650	bknpow	lmc	$0.88^{+0.04}_{-0.24}$	$0.14^{+0.04}_{-0.05}$	$1.24 \cdot 10^{+0}$	$1.61 \cdot 10^{-4}$	9.2 (9)	1.02	7.1
090423A	8.260	pow	smc	$0.88^{+0.04}_{-0.04}$	$0.08^{+0.09}_{-0.09}$	.....	$4.37 \cdot 10^{-5}$	28.0 (31)	0.90	17.3
090429B[c]	9.380	bknpow	lmc	$0.77^{+0.07}_{-0.29}$	$0.36^{+0.22}_{-0.21}$	$1.21 \cdot 10^{+0}$	$1.81 \cdot 10^{-4}$	2.2 (4)	0.55	2.9
090516A	4.109	pow	smc	$0.97^{+0.02}_{-0.02}$	$0.19^{+0.03}_{-0.03}$	.....	$1.62 \cdot 10^{-4}$	17.1 (23)	0.74	15.3
100219A	4.667	pow	smc	$0.74^{+0.03}_{-0.03}$	$0.15^{+0.04}_{-0.05}$	.....	$2.22 \cdot 10^{-4}$	4.2 (9)	0.47	11.4
100513A[c]	4.772	bknpow	smc	$0.50^{+0.09}_{-0.35}$	$0.04^{+0.24}_{-0.04}$	$9.94 \cdot 10^{-3}$	$6.30 \cdot 10^{-3}$	0.8 (3)	0.27	1.0
100905A	7.880	bknpow	mw[d]	$0.79^{+0.35}_{-0.33}$	$0.00^{+1.49}_{-0.00}$	$9.30 \cdot 10^{-1}$	$4.10 \cdot 10^{-5}$	0.9 (3)	0.30	16.0
111008A	4.990	bknpow	smc	$0.35^{+0.20}_{-0.01}$	$0.13^{+0.03}_{-0.07}$	$9.98 \cdot 10^{-3}$	$9.28 \cdot 10^{-3}$	27.0 (19)	1.42	6.8
120712A	4.175	bknpow	smc	$0.61^{+0.24}_{-0.02}$	$0.08^{+0.03}_{-0.08}$	$9.99 \cdot 10^{-3}$	$9.49 \cdot 10^{-4}$	9.5 (9)	1.06	10.6
130606A	5.931	pow	smc[d]	$1.01^{+0.02}_{-0.02}$	$0.00^{+0.02}_{-0.00}$	.....	$1.83 \cdot 10^{-4}$	7.1 (11)	0.65	8.4
131117A	4.042	bknpow	smc	$0.35^{+0.14}_{-0.02}$	$0.03^{+0.03}_{-0.03}$	$1.00 \cdot 10^{-2}$	$2.51 \cdot 10^{-2}$	10.4 (8)	1.30	0.1
140304A[c]	5.283	pow	smc[d]	$0.95^{+0.04}_{-0.03}$	$0.01^{+0.05}_{-0.01}$	.....	$2.04 \cdot 10^{-4}$	10.4 (6)	1.33	14.4
140311A	4.954	pow	smc	$0.85^{+0.02}_{-0.02}$	$0.07^{+0.03}_{-0.03}$	.....	$2.08 \cdot 10^{-4}$	20.6 (17)	1.21	9.8
140428A	4.680	bknpow	mw	$0.86^{+0.09}_{-0.30}$	$0.30^{+0.32}_{-0.23}$	$9.33 \cdot 10^{-1}$	$1.25 \cdot 10^{-4}$	7.2 (5)	1.44	2.6
140515A	6.327	pow	smc[d]	$0.77^{+0.04}_{-0.03}$	$0.00^{+0.10}_{-0.00}$	.....	$1.36 \cdot 10^{-4}$	3.7 (6)	0.62	14.6
140614A	4.233	bknpow	smc	$0.60^{+0.05}_{-0.05}$	$0.11^{+0.17}_{-0.05}$	$1.89 \cdot 10^{+0}$	$2.83 \cdot 10^{-4}$	5.2 (8)	0.65	4.1
151027B	4.062	bknpow	lmc	$0.50^{+0.08}_{-0.02}$	$0.10^{+0.05}_{-0.06}$	$1.00 \cdot 10^{-2}$	$4.21 \cdot 10^{-3}$	18.7 (16)	1.17	8.8
151112A	4.270	bknpow	lmc	$0.71^{+0.05}_{-0.06}$	$0.50^{+0.21}_{-0.11}$	$1.36 \cdot 10^{+0}$	$2.59 \cdot 10^{-4}$	21.4 (25)	0.86	11.4
071025	4.900	bknpow	sn	$0.80^{+0.16}_{-0.07}$	$0.57^{+0.18}_{-0.21}$	$9.99 \cdot 10^{-3}$	$3.40 \cdot 10^{-4}$	41.9 (36)	1.16	22.4
090205	4.900	pow	sn	$0.90^{+0.03}_{-0.03}$	$0.10^{+0.03}_{-0.03}$	...	$1.31 \cdot 10^{-4}$	13.7 (10)	1.37	7.1
090429B[c]	9.380	bknpow	sn	$0.72^{+0.06}_{-0.27}$	$0.19^{+0.22}_{-0.14}$	$1.19 \cdot 10^{+0}$	$1.75 \cdot 10^{-4}$	2.2 (4)	0.55	2.9
090516A	4.109	pow	sn	$0.98^{+0.02}_{-0.02}$	$0.24^{+0.04}_{-0.05}$	.....	$1.63 \cdot 10^{-4}$	26.4 (23)	1.15	15.3
100219A	4.667	pow	sn	$0.75^{+0.04}_{-0.04}$	$0.16^{+0.05}_{-0.05}$	.....	$2.21 \cdot 10^{-4}$	5.9 (9)	0.66	11.4
111008A	4.990	bknpow	sn	$0.38^{+0.21}_{-0.02}$	$0.18^{+0.05}_{-0.15}$	$9.96 \cdot 10^{-3}$	$9.47 \cdot 10^{-3}$	28.1 (19)	1.48	6.8
140428A	4.680	bknpow	sn	$0.74^{+0.15}_{-0.24}$	$0.15^{+0.13}_{-0.11}$	$2.36 \cdot 10^{-1}$	$2.36 \cdot 10^{-3}$	5.8 (5)	1.16	2.6
140614A	4.233	bknpow	sn	$0.32^{+0.31}_{-0.32}$	$0.27^{+0.09}_{-0.19}$	$9.94 \cdot 10^{-3}$	$2.89 \cdot 10^{-3}$	5.6 (8)	0.70	4.1
151027B	4.062	bknpow	sn	$0.51^{+0.07}_{-0.02}$	$0.09^{+0.03}_{-0.05}$	$9.93 \cdot 10^{-3}$	$3.31 \cdot 10^{-3}$	16.8 (16)	1.05	8.8
151112A	4.270	bknpow	sn	$0.71^{+0.06}_{-0.07}$	$0.41^{+0.11}_{-0.12}$	$1.35 \cdot 10^{+0}$	$2.59 \cdot 10^{-4}$	23.0 (25)	0.92	11.4

Notes. In the top section of the table we list the best-fit parameters from fitting the local extinction curves. In case we found evidence for a medium amount of dust ($A_V > 0.1$ mag), we also fitted the SN extinction curve, for which the corresponding best-fit parameters are listed at the bottom part of the table. [(a)] Spectral slope in the NIR/optical wavelength regime. In case the SED is best-fit with a broken power law (bknpow) the slope in the X-ray is fixed to $\beta_x = \beta_o + 0.5$, otherwise (pow) $\beta_x = \beta_o$ (see Section 3.2.6) [(b)] The common reference time where the broadband SED was created – in hrs after the prompt trigger. [(c)] Fit not performed with GROND data (see Section 3.2.7). [(d)] The extinction curve can basically not be identified since there is no evidence for extinction or the A_V is consistent with zero. However, we list the model resulting in the lowest χ^2_{red}.

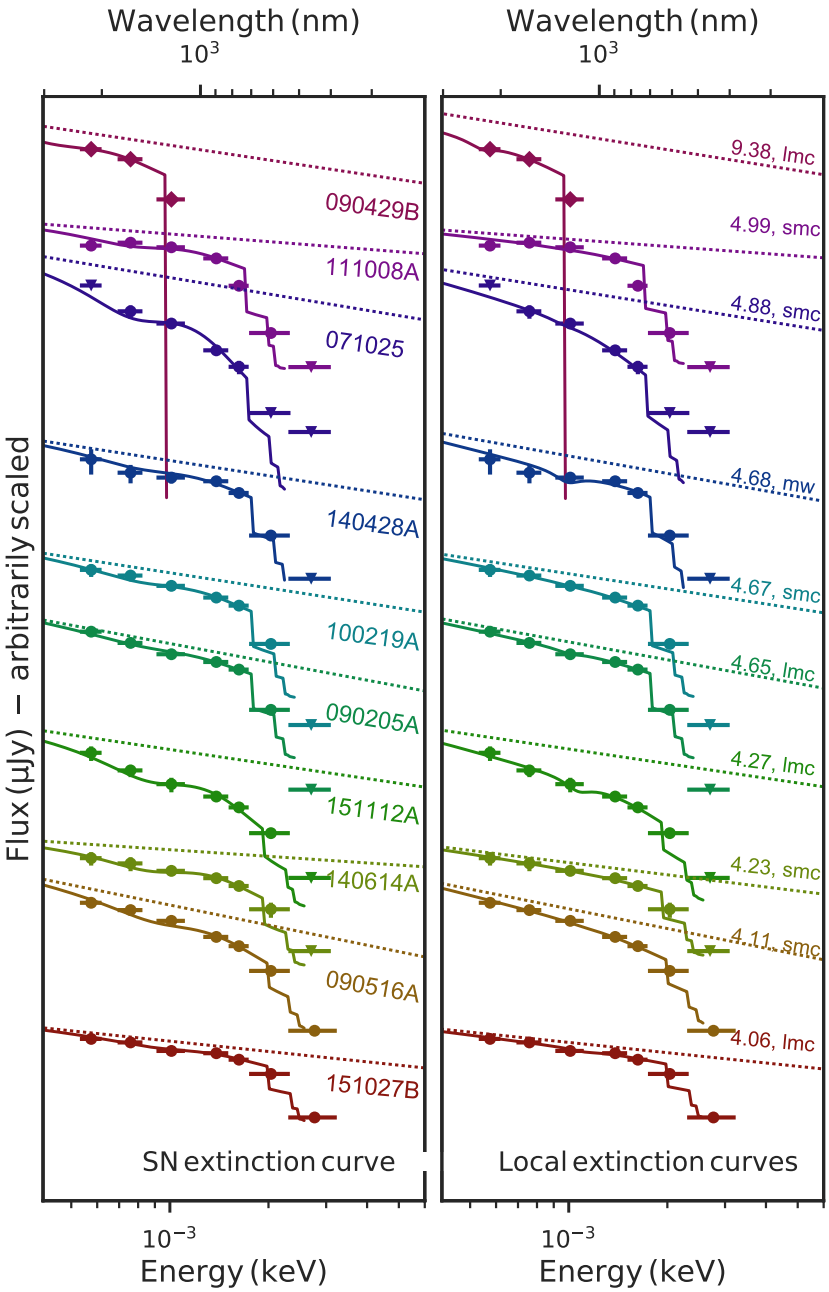

Figure 3.8: Similar to Fig. 3.7, but zoomed into the NIR/optical regime (the full plot is moved to the of the Chapter: Fig. 3.24). In the left inset we show the SEDs for the 10 GRBs that showed evidence for a medium amount of dust ($A_V > 0.1$ mag) fitted with the SN extinction curve. For comparison, in the right inset we show again the best result when performing the fit with local extinction curves. The goodness of fit is comparable in both scenarios (see Tab. 3.2 and Sect. 3.3).

general extinction curves that have more free parameters, such as R_V and the prominence of the 2175 Å feature; for example the extinction curves proposed by Cardelli et al. (1989) or Fitzpatrick & Massa (1986) (FM)[4]. This is also the reason for including quasi-simultaneous XRT data to fit the SED, so that the mostly unabsorbed and well-covered X-ray spectrum for energies $E > 0.8$ keV allows us to constrain better the spectral index; this means that we reduce the uncertainty for the NIR/optical spectral slope to the question of whether a spectral break of 0.5 is required or not.

The absorption of the X-ray spectrum by medium weight metals at energies below E < 0.8 keV is modeled with the XSPEC models `PHABS` & `ZPHABS`. However, the resulting host intrinsic hydrogen column densities $N_{\mathrm{H},X}$ will not discussed further here because we refer to the recent findings by Buchner et al. (2017), who have used a more more sophisticated model to fit XRT spectra. These authors find the distribution of $N_{\mathrm{H},X}$ to be consistent with sources being randomly distributed in an ellipsoidal gas cloud. This is in contrast to previous studies by, for example, Starling et al. (2013) or Campana et al. (2015), who find a positive dependence with redshift (as we do here), which could be interpreted as increasing absorption from the IGM with distance.

3.2.7 Additional data for GRBs at $z > 4$ not observed or detected with GROND

Our GROND observations for GRB 090429B only led to upper limits in all seven bands, and we therefore carried out the analysis on *Gemini*/NIRI JH- and K-band data published in Cucchiara et al. (2011). We did not carry out the fit for GRB 120923A ourselves, but used the visual extinction of $A_V = 0.06$ mag determined by Tanvir et al. (2018), who have used a very similar method for fitting simultaneous XRT and *Gemini-N*/NIRI data. Additionally, for two of the bursts that were not observed by GROND, namely GRB 100513A and 140304A, we used PAIRITEL JHK and RATIR $grizJH$ data for the analysis, respectively. So in total we analyzed and fitted 22 GRB broadband SEDs, 19 with GROND and 3 with NIR/optical data from different instruments. For the rest of the GRBs at $z > 4$, we collected A_V measurements from the literature, if available; these measurements are listed in Tab. 3.3.

3.3 Results

The results, i.e. the best-fit models and parameters, from fitting the combined NIR, optical, and X-ray SEDs with the local extinction curves are summarized in the top portion of Tab. 3.2 and a plot containing all the SEDs is shown in Fig. 3.7. As mentioned above, the SEDs of the 10 GRBs that show evidence for a small to medium amount of dust ($A_V > 0.1$ mag) were also fitted with the SN extinction curve. These SEDs are additionally plotted in Fig. 3.8, in comparison to the best results from the local extinction curves (zoomed into the NIR/optical regime; the full plot is moved to the end of the

[4] Also note that Zafar, Watson, Fynbo et al. (2011) find only four out of 42 GRBs to be better fit with the FM extinction law.

Table 3.3: Host intrinsic visual extinction for the GRBs at $z > 4$ that were not observed by GROND. All values are collected from the literature.

GRB yymmdd#	Redshift[a] (z)	A_V (mag)	Reference
000131	4.500	$0.29^{+0.18}_{-0.18}$	(1)
050502B	$5.2^{+0.3}_{-0.3}$	< 0.5	(2)
050505	4.275	$0.29^{+0.06}_{-0.06}$	(3)
050814	$5.77^{+0.12}_{-0.12}$	$0.23^{+0.15}_{-0.15}$	(1)
050904	6.295	< 0.32	(4)(5)
050922B	4.5 ± 0.5	...	...
060206	4.048	< 0.17	(6)
060223A	4.406	...	...
060510B	4.941	...	...
060522	5.11	...	...
060927	5.467	< 0.12	(7)
100302A	4.813	...	...
120521C	6.0	< 0.05	(8)
120923A[b]	7.84	0.06	(9)
140518A	4.707	$0.03^{+0.02}_{-0.02}$	(9)

Notes. [(a)] Photometric if given with errors, spectroscopic otherwise. [(b)] Observed by GROND but not detected.

References. (1) Curran et al. (2008); (2) Afonso et al. (2011); (3) Hurkett et al. (2006); (4) Zafar et al. (2010); (5) Stratta et al. (2011); (6) Covino et al. (2013); (7) Zafar, Watson, Tanvir et al. (2011); (8) Laskar et al. (2014); (9) Tanvir et al. (2018); (10) Littlejohns et al. (2015).

Chapter: Fig. 3.24). The corresponding parameters are given in the bottom portion of Tab. 3.2.

With these measurements we increase the number of determined A_V values for GRBs at $z > 4$ by a factor of ∼2 to 3. As previously observed for GRBs at lower redshift, the local extinction curves provide a good fit to the data, with the featureless SMC extinction curve usually best describing the observed magnitudes (Greiner et al., 2011; Zafar, Watson, Fynbo et al., 2011). We find that from the 22 modeled GRBs at $z > 4$, 16 are best fit with the SMC, and only 6 with the LMC or MW extinction curve. In contrast to other samples with GRBs at mostly $z < 4$, however, we find that all of the GRBs are only behind small to medium dust column densities ($A_V < 0.5$ mag) within their host galaxies line-of-sight, which is also true for the values collected from the literature (see Tab. 3.3). The distribution of our best-fit A_V values compared to those from the unbiased samples from Greiner et al. (2011) and Covino et al. (2013) and the data from Zafar, Watson, Fynbo et al. (2011), based on the GRB sample from Fynbo et al. (2009), is shown in Fig. 3.9. While all of these samples include a $\sim 20\%$ fraction of GRBs with $A_V > 0.5$ mag (and ∼3 to 5% with $A_V > 1.5$ mag), only $\sim 20\%$ of our GRBs at redshift

$z > 4$ have a visual extinction of $0.2 < A_V < 0.5$ mag, and the remaining $\sim 80\%$ have $A_V < 0.2$ mag. A two-sample Kolmogorov-Smirnov test returns a rejection probability of $p \sim 68\%$ for the null hypothesis that the A_V values from our GRBs at $z > 4$ and those from Greiner et al. (2011) are drawn from the same sample.

Considering the 10 SEDs that were also fitted with the SN extinction curve, we find that, besides GRB 090205 and 090516, the goodness of fit is comparable to the result from the local extinction curves, while for two of the bursts, GRB 140428A and 151027B, the SN extinction curve provides a better fit to the data. In case of GRB 140428A, the somewhat flat SED between the H- and z'-band can be identified with the flattening between (rest-frame) 3,000 Å and 1,700 Å of the SN extinction curve ($\chi^2_{\rm red} = 1.16$) or as a small (rest-frame) 2175 Å feature when fitting the MW extinction curve ($\chi^2_{\rm red} = 1.44$). This result is consistent with that from fitting the GROND SED to determine a photometric redshift, where we also find that the SN extinction curve is in better agreement with the data. For GRB 151027B we find $\chi^2_{\rm red} = 1.05$ for the SN extinction curve, compared to $\chi^2_{\rm red} = 1.17$ for the LMC extinction curve. However, because of the small amount of dust ($A_V \sim 0.10$ mag), it is hard to distinguish between the specific features of those extinction curves (see Fig. 3.8). Also, although the SMC extinction curve provides the best fit ($\chi^2_{\rm red} = 1.11$), GRB 071025 can also be well modelled with the SN extinction curve ($\chi^2_{\rm red} = 1.16$), which is in accordance with the results from Perley et al. (2010) and Jang et al. (2011) and with our result from fitting the GROND SED to determine a photometric redshift. GRB 071025 is, aside from GRB 151112A ($A_V \sim 0.5$ mag), also the burst for which we find the highest visual extinction (SMC: $A_V \sim 0.45$ mag, SN: $A_V \sim 0.57$ mag).

3.4 Discussion and conclusion

We have analyzed a sample of 40 GRBs at $z > 4$, of which 22 were used to measure the host intrinsic visual extinction A_V and study the shape of the dust extinction curves toward the GRB lines of sight. Since all of the bursts, including the above-mentioned cases of GRB 071025A and 140428A, can be modeled with locally measured extinction curves we cannot draw any firm conclusion about whether an SN-type dust extinction curve is truly required for some of the GRBs. Other SN-dominated extinction curves have been proposed by, for example, Bianchi & Schneider (2007); Hirashita et al. (2008, 2010), and Nozawa et al. (2015). But, since only the extinction curve from Todini & Ferrara (2001) and Maiolino et al. (2004) was available for us in an analytical form, we restricted our analysis to their results. A common feature, however, that these extinction curves share, is a strong steepening in the UV. This steepening is hard to measure at $z > 4$ anyway because of to the dominant absorption from the Lyman-α forest. Also, the low A_V values combined with a limited wavelength coverage limit the distinction of the various characteristic features. So from here, we focus the discussion to the somewhat unexpected lack of highly dust-extinguished GRBs, which can only be explained as a result of one or both of the following suppositions:

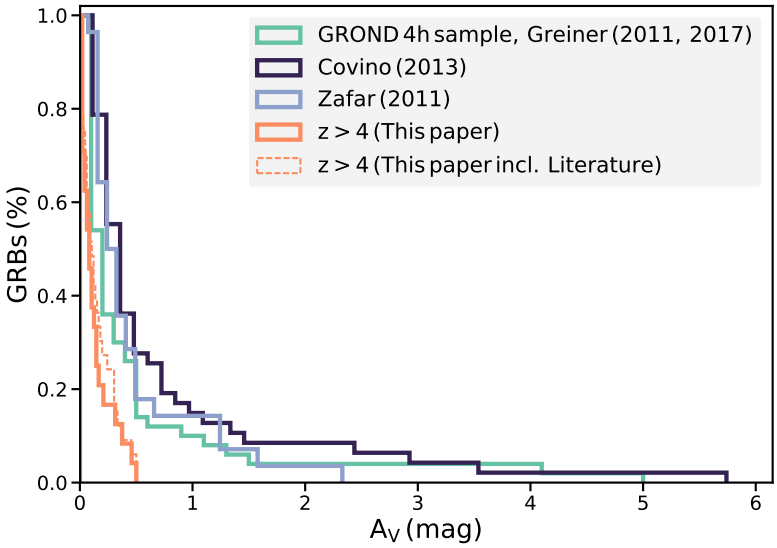

Figure 3.9: Normalized and reversed cumulative distribution of the host intrinsic dust extinction derived for the GRBs with redshift $z > 4$ from this work, compared to the BAT6 sample (Covino et al., 2013) and GROND 4h sample (Greiner et al., 2011), which are both unbiased samples. We also plot the data from Zafar, Watson, Fynbo et al. (2011), which is based on the GRB sample from Fynbo et al. (2009) and likely biased toward low extinction sight-lines.

1. At a redshift of $z > 4$, when the Universe was less than $\sim$ 1.6 Gyr old, not enough dust was present in young GRB host galaxies to cause visual extinctions of $A_V > 0.5$ mag.

2. High dust-extinguished GRBs at $z > 4$ are absent in our sample and other samples because their NIR/optical afterglow was too faint to be detected.

In order to check if the lack of higher extinguished afterglows can be explained with an observational bias, we calculated theoretical GROND detection thresholds for three of the afterglow SEDs from Tab. 3.2, by artificially placing them at redshifts between $0 < z < 10$. The SED for GRB 131117A corresponds to an epoch observed at just ~ 0.1 hrs after the trigger and is additionally very flat ($\beta_o \sim 0.25$). The SED of GRB 140311A is more representative of the GRBs studied here; this SED is much steeper ($\beta_o \sim 0.85$) and was created from the afterglow emission at $T_0 + 9.8$ hrs. For both of these bursts we assume a typical limiting magnitude in the GROND z' band of $z'_{\rm lim} = 24.2$ mag. As a more extreme example, we also calculate the detection threshold for the SED of the very high redshift GRB 090423, which corresponds to an observation taken at $T_0 + 17.3$ hrs ($\beta_o \sim 0.88$). Here we assume a typical GROND H-band limiting magnitude of $H_{\rm lim} = 22$ mag. Our results are represented by the dashed lines in Fig. 3.10, where we plot our A_V values against redshift in comparison to different GRB samples at mostly lower redshift. Above these lines, the dust extinction would be so high, that these GRBs would not have been detected by GROND (at the given time the SED was created, and if the GRB

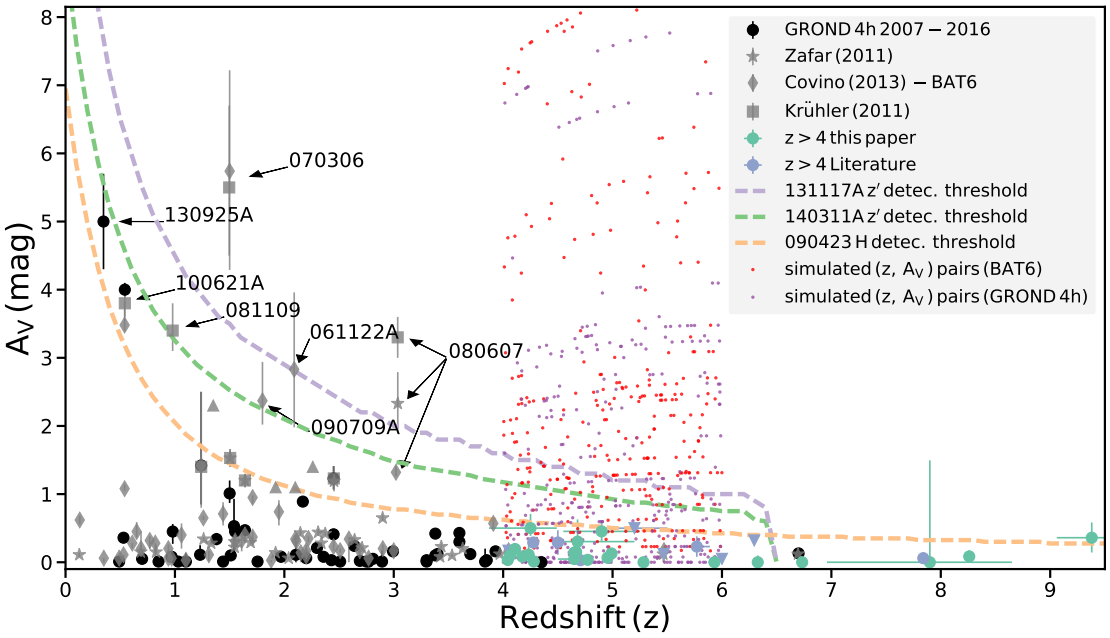

Figure 3.10: Host intrinsic visual dust extinction A_V toward the line-of-sight of the GRB plotted against redshift for the GRBs analyzed in this paper and in comparison to different samples at mostly lower redshift (Covino et al., 2013; Greiner et al., 2011; Krühler, Greiner et al., 2011; Zafar, Watson, Fynbo et al., 2011). The dashed lines represent the GROND detection thresholds for GRB 131117, 140311A and 090423 in the given band (see Sect. 3.4). Highly extinguished GRBs are labeled. The red and purple dots represent 500 from the 10^6 simulated (z, A_V(obs.)) pairs.

would have been detected from the redshift it was artificially placed at). One can see that a few exceptions fall above these lines. For example, GRB 070306 was observed with a larger telescope, and GRB 080607, 061222A, and 090709A were observed within a very short time after the *Swift*/BAT trigger (Cenko & Fox, 2006; Jaunsen et al., 2008; Cenko, Butler et al., 2010; Perley et al., 2011).

Although the detection thresholds for these burst clearly show that it is much harder to detect highly extinguished afterglows at $z > 4$, the absence of burst with $0.5 < A_V < 1.5$ mag, i.e., the lack of data points between these lines, given the size of our sample, seems somewhat unexpected. Therefore, to further test to what extent we suffer from an observational bias, we made the following Monte Carlo simulation. We derived the intrinsic brightness in the GROND z' band for the 17 GRBs at redshift $4.0 < z < 6.0$ and distributed random values out of the A_V distribution from the GROND 4h sample (Greiner et al., 2011) or the BAT 6 sample (Covino et al., 2013), by also putting each GRB at a random redshift between $4.0 < z < 6.0$.[5] We thus assume that the intrinsic brightness of the GRB is unrelated to the absorption by dust within the host galaxy.

[5]Since the extinction from dust increases from the red to blue wavelengths, this of course increases the extinction in the given (observer frame) band.

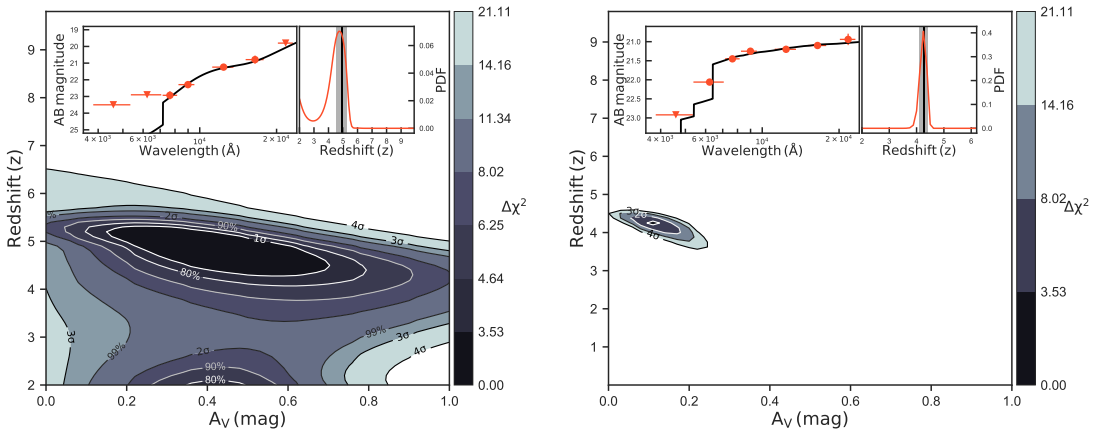

Figure 3.11: (a) GRB 071025 and (b) GRB 080916C

In Fig. 3.10 we plot 500 from 10^6 simulated (z, A_V(obs.)) pairs for both samples. In case of the A_V distribution from (Greiner et al., 2011), on average we would expect to find $n = 0.8 \pm 0.9$ bursts with $A_V > 0.5$ mag that are brighter than 24.2 mag in the z' band and $n = 2.0 \pm 1.3$ in case of the A_V distribution from the BAT 6 sample. The probabilities of detecting zero GRBs with $A_V > 0.5$ mag are $p = 43.6\%$ and $p = 11.4\%$, respectively. To detect at least one burst with $A_V > 0.5$ mag at a confidence of 1σ, it would require a sample size of $n = 21$ (GROND 4h sample) or $n = 10$ (BAT 6) GRBs. The different outcomes of the two samples can be explained by the higher fraction of bursts with $0.5 < A_V \lesssim 2.0$ mag in the sample from Covino et al. (2013), which are the only bursts we are theoretically able to detect at $z > 4$, given our brightness distribution. Although it is less clear regarding the A_V distribution from the GROND 4h sample, our sample size should be big enough to contain at least one GRB with $A_V > 0.5$ mag at least after also including the GRBs that were not observed with GROND.

Hence, these considerations suggest that we partly suffer from an observational bias toward highly extinguished GRBs, meaning that we cannot expect to easily detect bursts with $A_V > 0.5$ mag at $z > 4$ with a sensitivity of about ~ 24 mag (reachable with a 2m telescope). Nevertheless, our results can be interpreted as evidence, that GRB host galaxies at high redshift are on average less dusty than at $z \sim 2$.

To further test the occurrence of $A_V > 0.5$ mag at $z > 4$, very rapid observations at NIR wavelengths are required, which are difficult to achieve in large numbers from Chile since the South Atlantic Anomaly suppresses the number of night-time GRBs by more than a factor of two.

3.5 Additional tables and figures

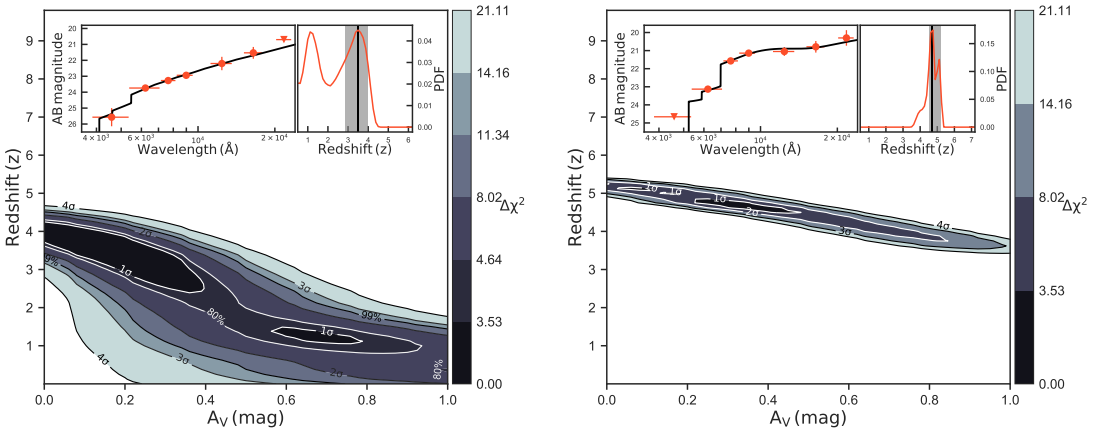

Figure 3.12: (a) GRB 100518A and (b) GRB 140428A

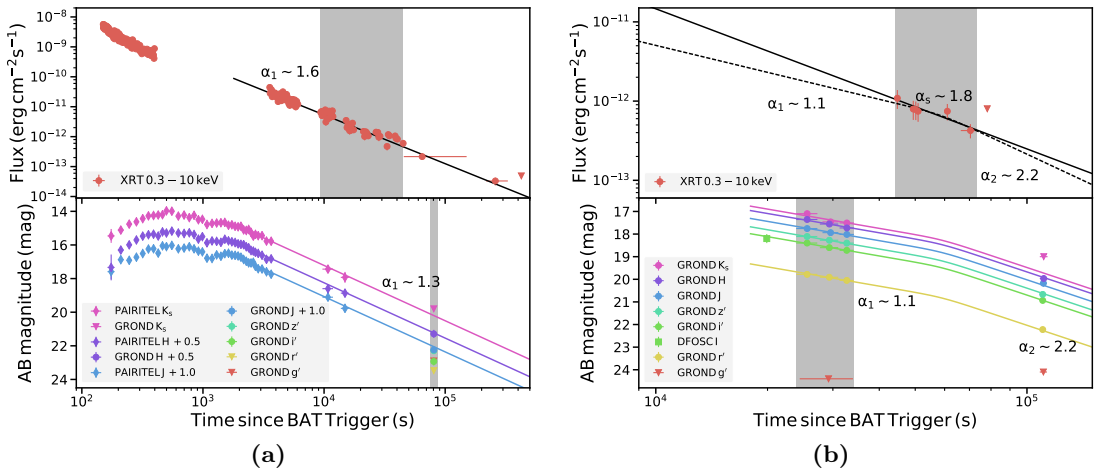

Figure 3.13: (a) GRB 071025 and (b) GRB 080825B

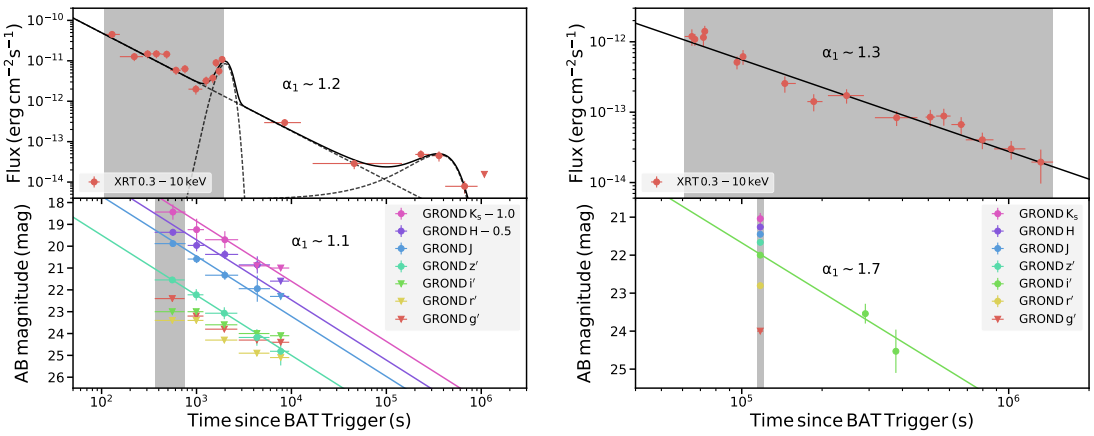

Figure 3.14: (a) GRB 080913 and (b) GRB GRB 080916C

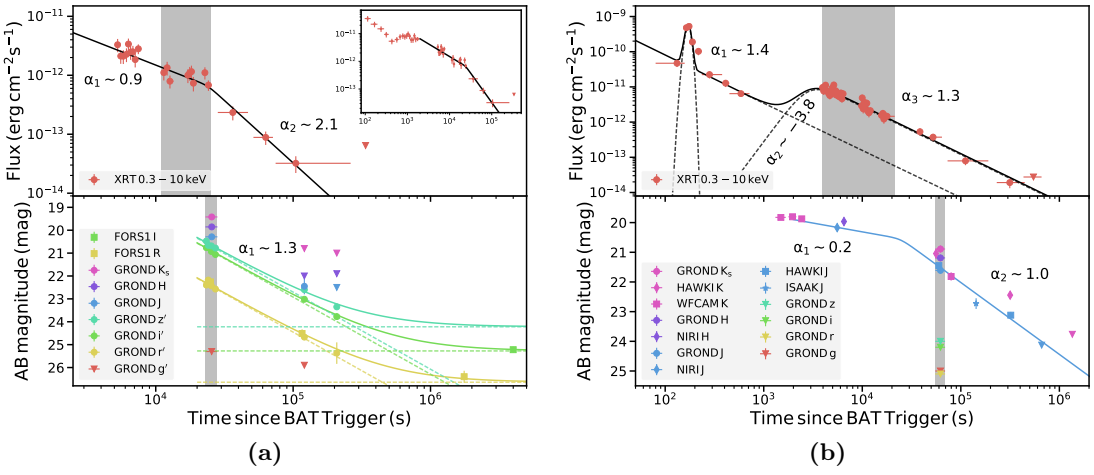

Figure 3.15: (a) GRB 090205 and (b) GRB GRB 090423

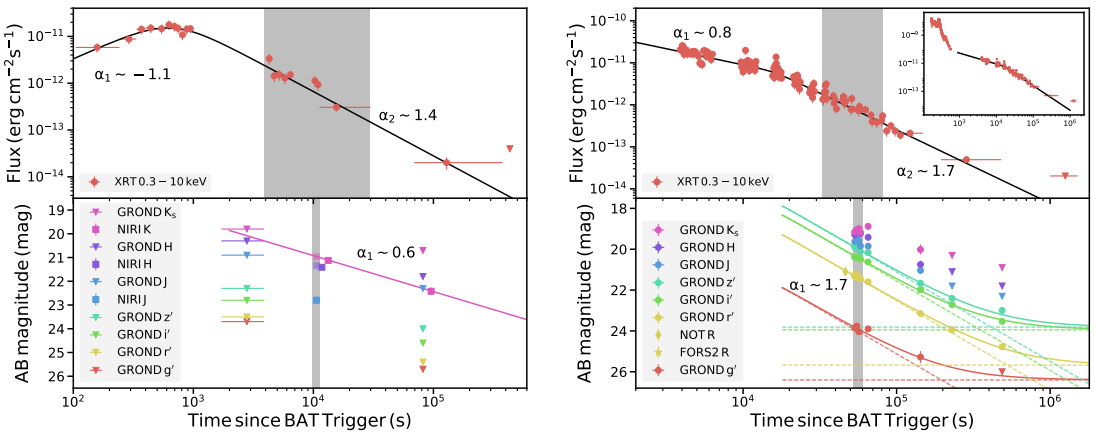

Figure 3.16: (a) GRB 090429B and (b) GRB 090516A

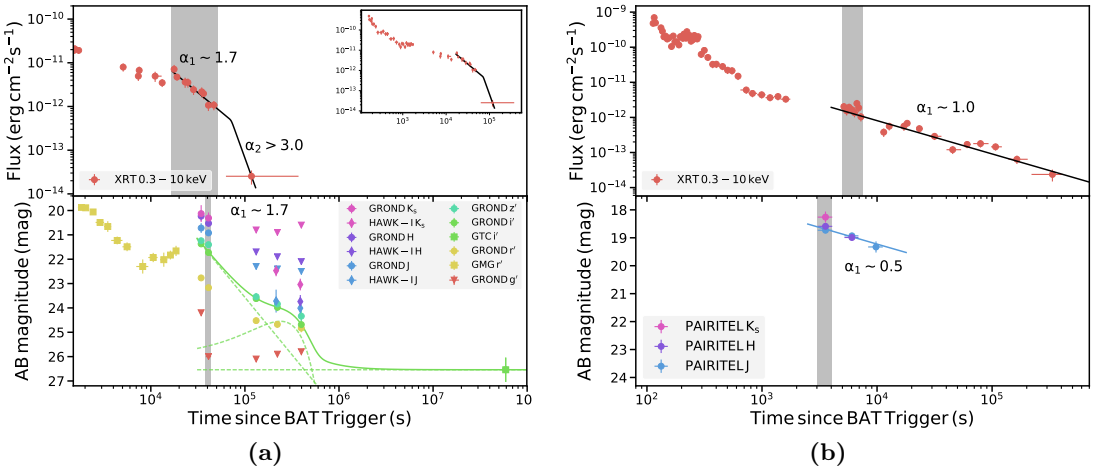

Figure 3.17: (a) GRB 100219A and (b) GRB 100513A

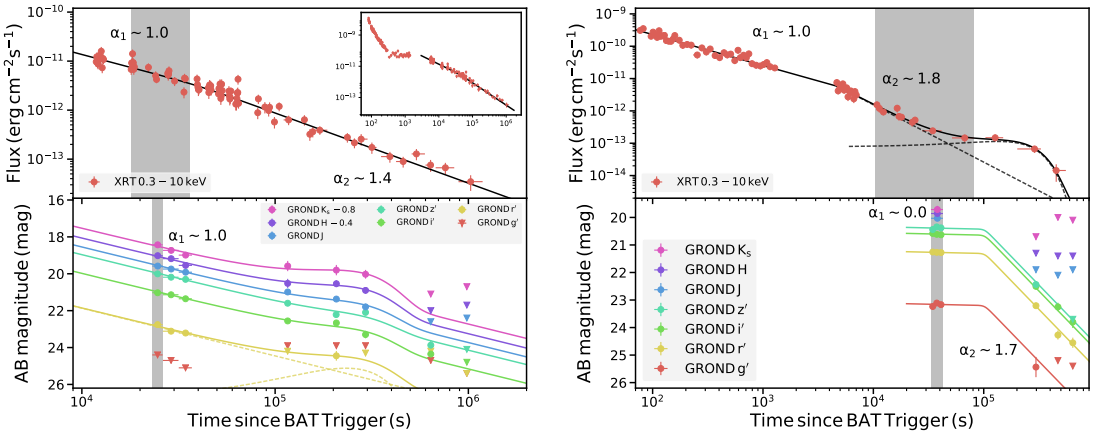

Figure 3.18: (a) GRB 111008A and (b) GRB 120712A

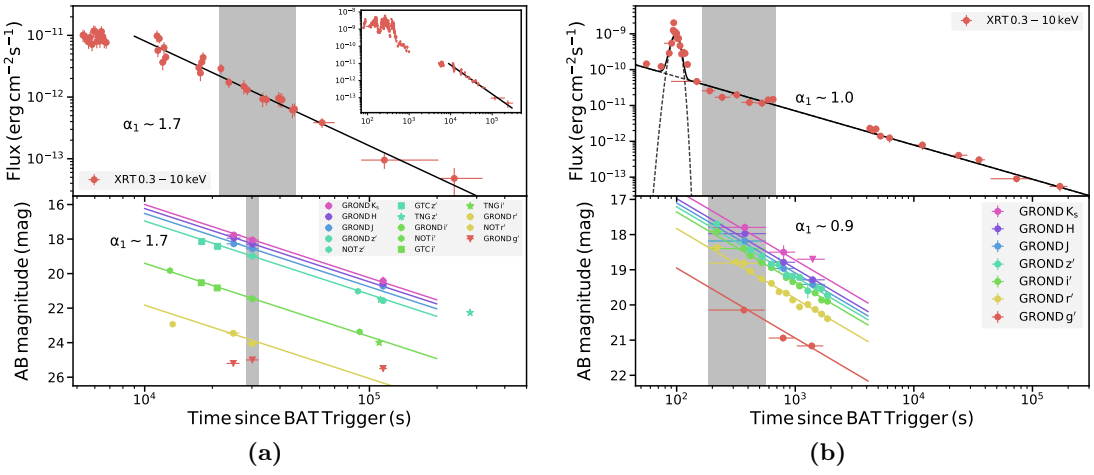

Figure 3.19: (a) GRB 130606A and (b) GRB 131117A

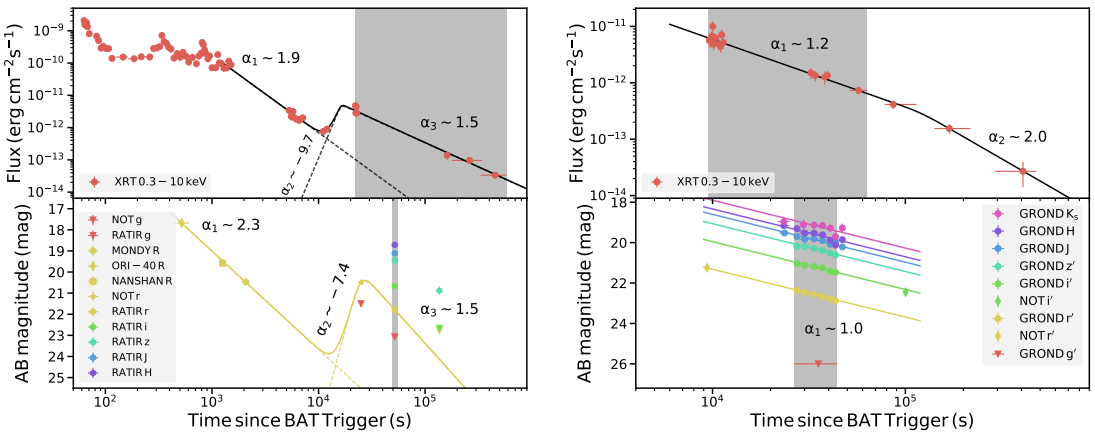

Figure 3.20: (a) GRB 140304A and (b) GRB 140311A

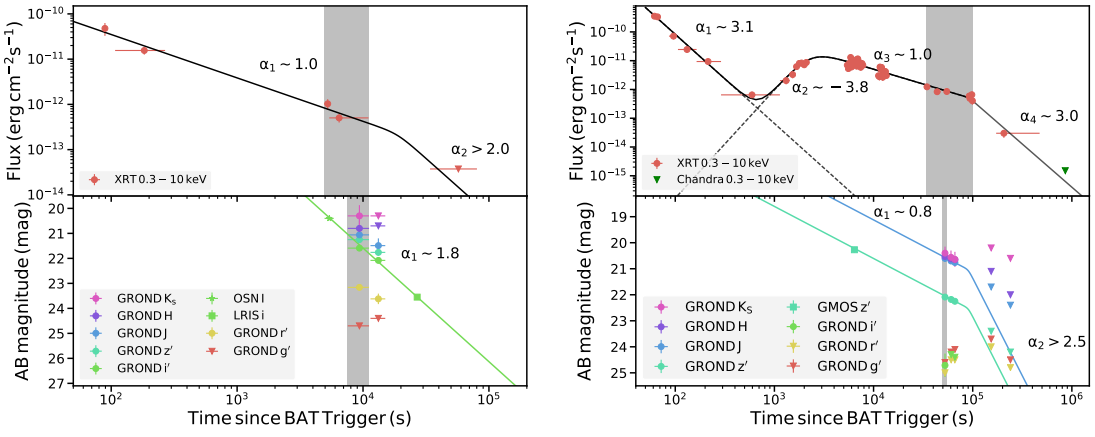

Figure 3.21: (a) GRB 140428A and (b) GRB 140515A

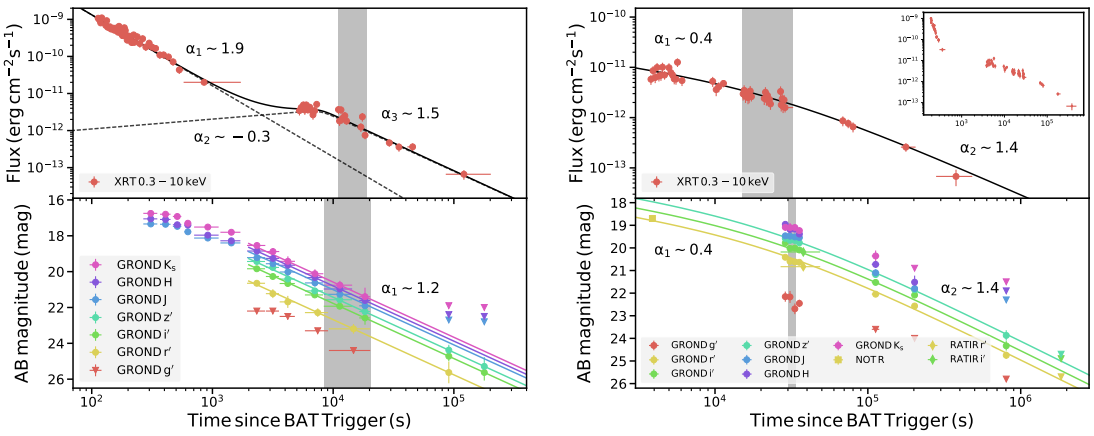

(a) (b)

Figure 3.22: (a) GRB 140614A and (b) GRB 151027B

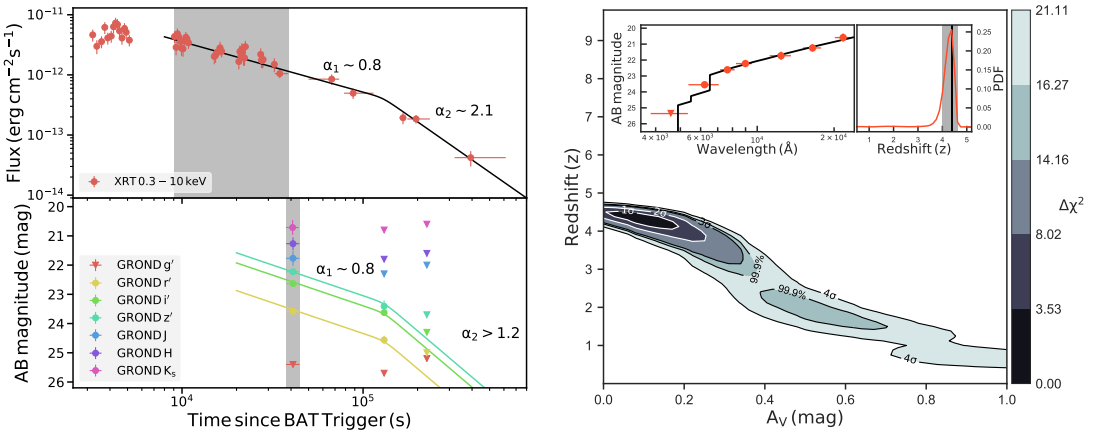

(a) Light-curve **(b)** Photometric redshift

Figure 3.23: GRB 151112A

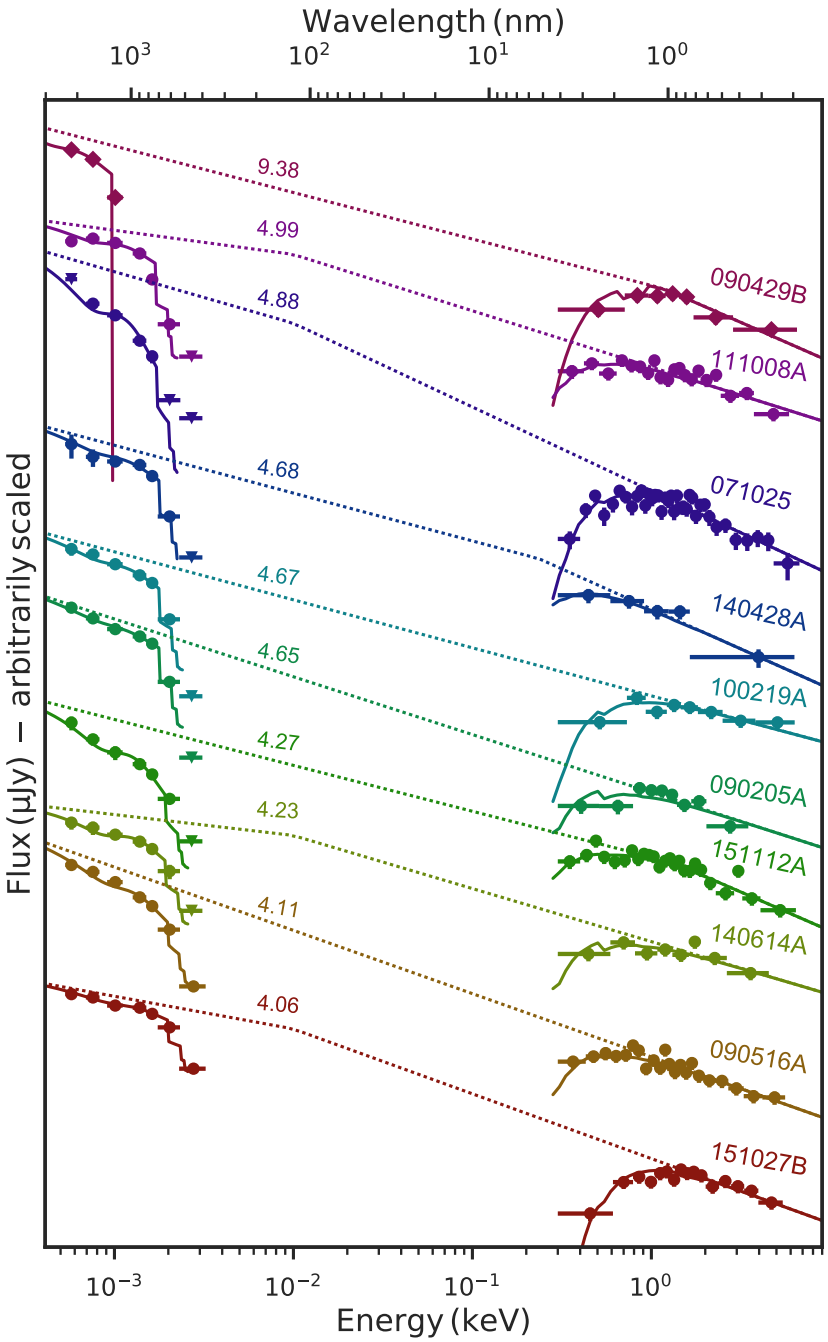

Figure 3.24: Same as Fig. 3.7, but for the 10 GRBs we additionally fitted with the SN-like dust extinction curve. These GRBs showed evidence for a medium amount of dust ($A_V > 0.1$ mag), when fitted with the local dust extinction curves.

Table 3.4: GROND photometry of the GRB afterglows.

$T_{\mathrm{GROND}}{}^{a}$ (s)	AB magnitude[b] g'	r'	i'	z'	J	H	K_s
GRB 071025B / T_0 = 04:08:54 UT (MJD = 54398.17285) (1)							
80533 ± 2452	> 25.2	> 24.5	22.93 ± 0.24	22.29 ± 0.13	21.24 ± 0.18	20.79 ± 0.24	> 19.8
GRB 080825B / T_0 = 17:46:40 UT (MJD = 54703.74074) (2)							
25566 ± 1670	> 24.6	19.78 ± 0.03	18.40 ± 0.03	18.11 ± 0.03	17.76 ± 0.06	17.36 ± 0.05	17.10 ± 0.08
29344 ± 1670	> 24.0	19.91 ± 0.03	18.60 ± 0.03	18.27 ± 0.03	17.94 ± 0.06	17.56 ± 0.06	17.46 ± 0.08
32695 ± 1431	> 24.3	20.05 ± 0.03	18.72 ± 0.03	18.40 ± 0.03	18.02 ± 0.06	17.73 ± 0.06	17.51 ± 0.08
110261 ± 1981	> 24.1	22.22 ± 0.04	20.93 ± 0.04	20.67 ± 0.05	20.17 ± 0.15	19.97 ± 0.14	> 18.8
29201 ± 4779	> 24.4	19.94 ± 0.03	18.62 ± 0.03	18.30 ± 0.03	17.92 ± 0.06	17.57 ± 0.05	17.41 ± 0.08
GRB 080913 / T_0 = 06:46:54 UT (MJD = 54722.28257) (3)							
556 ± 193	> 22.4	> 23.4	> 23.0	21.55 ± 0.14	19.88 ± 0.10	19.86 ± 0.16	19.44 ± 0.35
994 ± 189	> 23.2	> 23.4	> 23.0	22.23 ± 0.26	20.59 ± 0.18	20.46 ± 0.27	20.24 ± 0.50
1962 ± 730	> 23.8	> 24.3	> 23.6	23.07 ± 0.27	21.33 ± 0.21	20.88 ± 0.21	20.70 ± 0.39
4326 ± 1542	> 24.3	> 24.9	> 24.0	24.18 ± 0.38	21.95 ± 0.60	21.36 ± 0.39	> 20.9
7715 ± 1769	> 24.4	> 25.1	> 24.1	24.81 ± 0.65	> 22.3	> 21.6	> 21.0
GRB 080916C / T_0 = 00:12:45 UT (MJD = 54725.00885) (4)							
117308 ± 3045	> 24.0	22.80 ± 0.07	22.00 ± 0.05	21.66 ± 0.05	21.45 ± 0.06	21.26 ± 0.08	21.04 ± 0.15
GRB 090205 / T_0 = 23:03:14 UT (MJD = 54867.96058) (5)							
23348 ± 340	> 22.9	22.39 ± 0.14	20.76 ± 0.06	20.48 ± 0.05	20.16 ± 0.13	19.84 ± 0.15	19.25 ± 0.26
24111 ± 342	> 23.1	22.18 ± 0.10	20.75 ± 0.05	20.66 ± 0.05	20.17 ± 0.12	19.66 ± 0.12	19.60 ± 0.29
25396 ± 860	> 24.2	22.43 ± 0.06	20.93 ± 0.04	20.69 ± 0.04	20.49 ± 0.10	19.89 ± 0.09	19.87 ± 0.28
27201 ± 858	> 25.1	22.57 ± 0.05	21.06 ± 0.03	20.78 ± 0.03	20.34 ± 0.09	20.05 ± 0.13	19.70 ± 0.21
120692 ± 2656	> 25.9	24.67 ± 0.13	23.02 ± 0.07	22.60 ± 0.08	> 22.6	> 22.0	> 20.8
207844 ± 2677	> 25.2	25.37 ± 0.47	23.78 ± 0.15	23.35 ± 0.13	> 22.5	> 21.9	> 21.0
25534 ± 2525	> 25.3	22.50 ± 0.04	20.97 ± 0.03	20.64 ± 0.03	20.29 ± 0.07	19.85 ± 0.08	19.42 ± 0.12
GRB 090423 / T_0 = 07:55:19 UT (MJD= 54944.33008) (6)							
62136 ± 7076	> 25.0	> 25.1	> 24.2	> 24.0	21.61 ± 0.11	21.19 ± 0.11	20.89 ± 0.12
150527 ± 3557	> 24.6	> 24.8	> 24.7	> 23.2	> 22.5	> 21.9	> 21.1
GRB 090429B / T_0 = 05:30:03 UT (MJD= 54950.22920) (7)							
1902 ± 1081	> 23.7	> 23.5	> 22.8	> 22.3	> 20.9	> 20.3	> 19.8
81805 ± 3629	> 25.7	> 25.4	> 24.6	> 24.0	> 22.3	> 21.8	> 20.7
GRB 090516 / T_0 = 08:27:50 UT (MJD= 54967.35266) (8)							
53290 ± 724	23.86 ± 0.14	21.34 ± 0.03	20.39 ± 0.04	19.89 ± 0.04	19.63 ± 0.10	19.29 ± 0.10	19.16 ± 0.16
54959 ± 859	23.76 ± 0.10	21.40 ± 0.03	20.41 ± 0.03	19.96 ± 0.03	19.54 ± 0.08	19.17 ± 0.09	19.04 ± 0.13
56764 ± 861	24.04 ± 0.13	21.43 ± 0.03	20.43 ± 0.03	20.01 ± 0.03	19.57 ± 0.08	19.20 ± 0.10	18.99 ± 0.14
58112 ± 175	> 23.6	21.43 ± 0.06	20.47 ± 0.05	20.11 ± 0.05	19.84 ± 0.14	19.23 ± 0.16	19.18 ± 0.23
65203 ± 862	23.90 ± 0.29	21.60 ± 0.04	20.62 ± 0.03	20.17 ± 0.04	19.85 ± 0.09	19.42 ± 0.10	18.88 ± 0.14
143076 ± 859	25.28 ± 0.29	23.15 ± 0.06	21.99 ± 0.05	21.67 ± 0.06	21.00 ± 0.15	20.75 ± 0.20	20.01 ± 0.25
229907 ± 859	> 25.3	23.94 ± 0.15	22.72 ± 0.09	22.41 ± 0.13	> 21.8	> 21.1	> 20.3
487152 ± 3319	> 26.0	24.78 ± 0.15	23.53 ± 0.13	23.00 ± 0.15	> 22.3	> 21.8	> 20.9
55095 ± 2530	23.87 ± 0.07	21.40 ± 0.03	20.41 ± 0.03	19.92 ± 0.03	19.61 ± 0.07	19.18 ± 0.07	19.00 ± 0.10
GRB 100219A / T_0 = 15:15:46 (MJD = 55246.63606) (9)							
34248 ± 1130	> 24.2	22.77 ± 0.09	21.37 ± 0.06	21.24 ± 0.08	20.72 ± 0.20	20.23 ± 0.19	20.12 ± 0.34
41043 ± 2656	> 26.0	23.17 ± 0.05	21.73 ± 0.04	21.40 ± 0.04	20.92 ± 0.12	20.53 ± 0.13	20.31 ± 0.23
131666 ± 2672	> 26.1	24.52 ± 0.12	23.62 ± 0.10	23.54 ± 0.15	> 22.3	> 21.7	> 20.8
221279 ± 2528	> 25.9	24.68 ± 0.14	23.98 ± 0.15	22.84 ± 0.20	> 22.4	> 21.9	> 20.9
397579 ± 3575	> 25.8	24.83 ± 0.17	24.69 ± 0.27	24.34 ± 0.32	> 22.5	> 22.1	> 20.6
GRB 100518A / T_0 = 11:33:35 UT (MJD = 55334.48166) (10)							
71558 ± 9906	25.57 ± 0.57	23.74 ± 0.13	23.27 ± 0.18	22.94 ± 0.17	22.20 ± 0.42	21.53 ± 0.37	> 20.3
GRB 100905A / T_0 = 15:08:14 UT (MJD = 55444.63072) (11)							
57687 ± 9809	> 25.9	> 26.1	> 25.2	> 24.7	21.85 ± 0.20	21.72 ± 0.26	21.50 ± 0.43
GRB 111008A / T_0 = 22:12:58 UT (MJD = 55842.92567) (12)							
24653 ± 1512	> 24.4	22.76 ± 0.09	21.03 ± 0.04	20.00 ± 0.03	19.58 ± 0.06	19.42 ± 0.07	19.23 ± 0.10
28944 ± 2675	> 24.7	23.11 ± 0.09	21.14 ± 0.04	20.18 ± 0.03	19.74 ± 0.06	19.58 ± 0.08	19.53 ± 0.14
34402 ± 2682	> 25.1	23.21 ± 0.09	21.36 ± 0.04	20.30 ± 0.03	19.92 ± 0.06	19.95 ± 0.10	19.79 ± 0.15
116116 ± 1762	> 23.9	> 24.2	22.56 ± 0.11	21.60 ± 0.06	20.99 ± 0.15	20.92 ± 0.25	20.38 ± 0.28
207405 ± 3588	> 23.9	24.45 ± 0.26	22.67 ± 0.16	22.21 ± 0.11	21.37 ± 0.16	20.94 ± 0.18	20.60 ± 0.28
293685 ± 3582	> 23.9	> 24.3	23.30 ± 0.20	22.09 ± 0.11	21.80 ± 0.17	21.30 ± 0.18	20.83 ± 0.24
639133 ± 3576	> 24.7	> 24.2	24.35 ± 0.34	23.87 ± 0.27	> 22.6	> 22.0	> 21.1
982066 ± 1771	> 25.4	> 25.4	> 24.8	> 24.1	> 22.4	> 21.7	> 20.7
GRB 120712A / T_0 = 13:42:27 UT (MJD = 56120.57115) (13)							
34495 ± 1191	23.24 ± 0.09	21.26 ± 0.03	20.58 ± 0.04	20.44 ± 0.04	20.02 ± 0.09	19.90 ± 0.11	19.67 ± 0.18
37541 ± 1771	23.11 ± 0.06	21.27 ± 0.03	20.61 ± 0.03	20.34 ± 0.03	20.12 ± 0.08	19.78 ± 0.10	19.89 ± 0.22
41032 ± 1633	23.17 ± 0.07	21.28 ± 0.03	20.63 ± 0.03	20.38 ± 0.04	19.97 ± 0.08	19.95 ± 0.11	19.34 ± 0.17
297391 ± 2680	25.44 ± 0.37	23.21 ± 0.07	22.50 ± 0.08	22.44 ± 0.14	> 21.9	> 21.3	> 20.7
470194 ± 2447	> 25.2	24.27 ± 0.16	23.25 ± 0.15	...	> 22.1	> 21.4	> 20.0

Table 3.4: continued.

T_{GROND} [a] (s)	AB magnitude [b] g'	r'	i'	z'	J	H	K_s
641263 ± 1767	> 25.4	24.55 ± 0.19	23.80 ± 0.22	> 23.7	> 21.9	> 21.4	> 20.1
37984 ± 4681	23.17 ± 0.05	21.28 ± 0.03	20.62 ± 0.03	20.42 ± 0.03	20.03 ± 0.07	19.86 ± 0.08	19.71 ± 0.14
GRB 120923A / T_0 = 05:16:06 UT (MJD = 56193.21951) (14)							
72311 ± 4059	> 23.8	> 24.3	> 23.7	> 23.7	> 22.1	> 21.7	> 20.7
GRB 130606A / T_0 = 21:04:39 UT (MJD = 56449.87823) (15)							
24785 ± 1650	> 25.2	23.46 ± 0.09	...	...	18.28 ± 0.05	17.95 ± 0.05	17.77 ± 0.13
30132 ± 1937	> 25.0	24.05 ± 0.17	21.46 ± 0.05	18.99 ± 0.03	18.56 ± 0.05	18.30 ± 0.06	18.05 ± 0.08
114988 ± 4498	> 25.5	> 25.0	...	21.56 ± 0.06	20.73 ± 0.13	20.58 ± 0.26	20.42 ± 0.25
GRB 131117A / T_0 = 00:34:04 UT (MJD = 56613.02366) (16)							
218 ± 33	...	18.37 ± 0.03	17.91 ± 0.03	17.70 ± 0.04	...	...	...
418 ± 33	...	19.04 ± 0.04	18.60 ± 0.04	18.43 ± 0.04	...	...	...
520 ± 33	...	19.26 ± 0.04	18.80 ± 0.04	18.62 ± 0.05	...	...	...
629 ± 33	...	19.39 ± 0.04	18.94 ± 0.04	18.84 ± 0.04	...	...	...
730 ± 33	...	19.63 ± 0.04	...	18.85 ± 0.21	...	...	...
840 ± 33	...	19.67 ± 0.05	19.22 ± 0.04	19.16 ± 0.04	...	...	...
951 ± 33	...	19.86 ± 0.05	19.34 ± 0.04	19.19 ± 0.04	...	...	...
1087 ± 57	...	20.06 ± 0.04	19.46 ± 0.04	19.21 ± 0.04	...	...	...
1276 ± 57	...	19.99 ± 0.04	...	19.60 ± 0.22	...	...	...
1472 ± 57	...	20.13 ± 0.04	19.66 ± 0.05	19.47 ± 0.05	...	...	...
1668 ± 57	...	20.26 ± 0.05	19.86 ± 0.05	19.53 ± 0.05	...	...	...
1871 ± 57	...	20.39 ± 0.05	19.90 ± 0.05	19.73 ± 0.04	...	...	...
369 ± 184	20.15 ± 0.05	18.82 ± 0.03	18.40 ± 0.03	18.19 ± 0.04	18.18 ± 0.06	17.97 ± 0.06	17.80 ± 0.11
790 ± 194	20.94 ± 0.09	...	...	...	18.96 ± 0.08	18.79 ± 0.08	18.50 ± 0.20
1378 ± 348	21.17 ± 0.08	...	...	...	19.42 ± 0.08	19.29 ± 0.10	> 18.7
GRB 140311A / T_0 = 21:05:16 UT (MJD = 56727.87866) (17)							
27387 ± 865	> 23.9	22.36 ± 0.07	21.04 ± 0.04	20.18 ± 0.03	19.70 ± 0.07	19.31 ± 0.09	18.96 ± 0.21
30065 ± 1727	> 23.9	22.47 ± 0.05	21.11 ± 0.03	20.19 ± 0.03	19.83 ± 0.06	19.53 ± 0.09	...
33620 ± 1733	> 24.2	22.55 ± 0.05	21.19 ± 0.03	20.29 ± 0.03	19.81 ± 0.06	19.53 ± 0.08	19.13 ± 0.18
37169 ± 1734	> 25.7	22.68 ± 0.04	21.25 ± 0.03	20.38 ± 0.03	19.90 ± 0.06	19.62 ± 0.08	19.16 ± 0.16
40733 ± 1739	> 25.5	22.78 ± 0.04	21.42 ± 0.03	20.52 ± 0.03	20.08 ± 0.07	19.88 ± 0.09	19.28 ± 0.18
43437 ± 881	> 25.0	22.88 ± 0.07	21.47 ± 0.04	20.61 ± 0.04	20.02 ± 0.09	20.12 ± 0.15	19.70 ± 0.32
47144 ± 1219		NIR only			20.22 ± 0.11	19.85 ± 0.14	19.28 ± 0.22
35420 ± 8898	> 26.0	22.64 ± 0.03	21.24 ± 0.03	20.32 ± 0.03	19.87 ± 0.05	19.60 ± 0.06	19.27 ± 0.11
GRB 140428A / T_0 = 22:40:50 UT (MJD = 56775.94502) (18)							
9363 ± 1800	> 24.7	23.16 ± 0.12	21.59 ± 0.07	21.15 ± 0.08	21.06 ± 0.24	20.80 ± 0.32	20.30 ± 0.43
13242 ± 1782	> 24.4	23.62 ± 0.21	22.08 ± 0.11	21.76 ± 0.13	21.49 ± 0.29	> 20.7	> 20.4
618771 ± 1907	> 23.9	> 23.7	> 23.2	> 23.2	> 21.6	> 21.1	> 20.1
GRB 140515A / T_0 = 09:12:36 UT (MJD = 56792.38375) (19)							
52538 ± 3000	> 24.6	> 25.0	24.71 ± 0.45	22.09 ± 0.06	20.60 ± 0.14	20.53 ± 0.18	20.40 ± 0.25
60572 ± 2435	> 24.2	> 24.5	> 24.3	22.18 ± 0.06	20.70 ± 0.11	20.62 ± 0.15	20.56 ± 0.26
66119 ± 2693	> 24.1	> 24.5	> 24.4	22.25 ± 0.07	20.76 ± 0.11	20.65 ± 0.14	20.64 ± 0.29
153522 ± 1787	> 23.7	> 24.0	> 23.5	> 23.4	> 21.7	> 21.1	> 20.2
240133 ± 3814	> 24.5	> 24.8	> 24.5	> 24.2	> 22.4	> 22.0	> 20.6
GRB 140614A / T_0 = 01:04:59 UT (MJD = 56822.04513) (20)							
2331 ± 396	> 22.2	20.65 ± 0.13	19.84 ± 0.06	19.43 ± 0.06	19.22 ± 0.14	18.85 ± 0.14	18.54 ± 0.15
3165 ± 394	> 22.2	21.23 ± 0.25	20.27 ± 0.10	19.77 ± 0.07	19.56 ± 0.23	19.26 ± 0.20	18.88 ± 0.19
4209 ± 605	> 22.5	21.69 ± 0.33	20.66 ± 0.11	20.42 ± 0.11	20.02 ± 0.25	19.64 ± 0.23	19.43 ± 0.28
7038 ± 1203	...	...	21.30 ± 0.10	21.08 ± 0.11	20.63 ± 0.20	20.33 ± 0.20	20.12 ± 0.25
11337 ± 2973	...	...	21.93 ± 0.10	21.57 ± 0.12	21.27 ± 0.18	20.97 ± 0.25	20.76 ± 0.24
18358 ± 1916	...	...	22.58 ± 0.38	22.23 ± 0.33	21.90 ± 0.35	21.61 ± 0.39	21.40 ± 0.50
90787 ± 3616	> 25.1	25.63 ± 0.60	24.72 ± 0.28	24.38 ± 0.29	> 22.7	> 22.4	> 21.9
178637 ± 4062	> 25.3	> 25.6	25.63 ± 0.45	25.29 ± 0.52	> 22.8	> 22.5	> 20.0
7453 ± 1617	> 23.3	22.29 ± 0.24	...	...	...	...	...
14747 ± 5527	> 24.4	23.19 ± 0.27	...	...	...	...	...
GRB 151027B / T_0 = 22:40:40 UT (MJD = 57322.94491) (21)							
28839 ± 903	22.16 ± 0.23	20.41 ± 0.05	19.78 ± 0.04	19.58 ± 0.04	19.47 ± 0.09	18.96 ± 0.08	19.09 ± 0.16
30948 ± 1125	22.17 ± 0.26	20.59 ± 0.07	20.02 ± 0.06	19.66 ± 0.05	19.48 ± 0.10	19.19 ± 0.10	19.10 ± 0.20
33291 ± 1129	22.69 ± 0.24	20.62 ± 0.04	20.00 ± 0.04	19.67 ± 0.04	19.52 ± 0.07	19.17 ± 0.08	19.10 ± 0.14
35634 ± 1130	22.45 ± 0.16	20.64 ± 0.04	20.09 ± 0.04	19.77 ± 0.04	19.54 ± 0.07	19.39 ± 0.08	19.24 ± 0.14
112431 ± 6317	> 23.6	22.05 ± 0.07	21.53 ± 0.07	21.18 ± 0.06	21.10 ± 0.15	20.73 ± 0.16	20.36 ± 0.24
202273 ± 1606	> 24.0	22.57 ± 0.09	22.09 ± 0.09	21.85 ± 0.08	21.80 ± 0.25	21.53 ± 0.29	> 20.9
804300 ± 6436	> 25.8	24.75 ± 0.16	24.33 ± 0.21	23.87 ± 0.23	> 22.3	> 21.9	> 21.5
31733 ± 2686	22.46 ± 0.16	20.60 ± 0.04	19.98 ± 0.04	19.66 ± 0.04	19.47 ± 0.07	19.11 ± 0.07	18.95 ± 0.11
GRB 151112A / T_0 = 13:44:48 UT (MJD = 57338.57278) (22)							
41030 ± 3474	> 25.4	23.58 ± 0.09	22.63 ± 0.08	22.23 ± 0.09	21.74 ± 0.26	21.25 ± 0.22	20.59 ± 0.26

Table 3.4: continued.

T_{GROND} [a] (s)	AB magnitude [b] g'	r'	i'	z'	J	H	K_s
130717 ± 2389	> 25.7	24.56 ± 0.14	23.63 ± 0.12	23.50 ± 0.20	> 22.3	> 21.8	> 20.8
225119 ± 2393	> 25.2	> 25.0	> 24.3	> 23.7	> 22.0	> 21.6	> 20.6

Notes. [(a)] Mid-time of the GROND exposure in seconds after the detection of the prompt emission (T_0). [(b)] Magnitudes are not corrected for the Galactic foreground extinction given in Tab. 4.1. Upper limits are 3σ. Below the dashed lines we give the magnitudes of stacked observations. Empty entries (...) indicate technical problems, reflections rings at the position of the source, or when we used the magnitudes of stacked/single observations instead.

References. (1) Pagani et al. (2007); (2) Evangelista et al. (2008); (3) Schady et al. (2008); (4) Goldstein & van der Horst (2008); (5) Perri et al. (2009); (6) Krimm et al. (2009); (7) Ukwatta et al. (2009); (8) B. A. Rowlinson et al. (2009); (9) A. Rowlinson et al. (2010); (10) Mereghetti et al. (2010); (11) Marshall et al. (2010); (12) Saxton et al. (2011); (13) M. J. Page et al. (2012); (14) Yershov et al. (2012); (15) Ukwatta et al. (2013); (16) M. J. Page et al. (2013); (17) Racusin et al. (2014); (18) Kocevski et al. (2014); (19) D'Avanzo et al. (2014); (20) K. L. Page et al. (2014); (21) Ukwatta et al. (2015); (22) Malesani, Barthelmy et al. (2015) .

Table 3.5: Light curve models and parameters used to flux normalize XRT X-ray and GROND NIR/optical data to a common reference time.

	Model	α_1	α_2	α_3	t_{break} (ks)	host (y/n)	additional data [a] (reference)
				GRB 071025			
NIR/opt.	PL	1.32 ± 0.11	...	...	...	no	PAIRTEL JHK_s (1)
X-ray	PL	1.60 ± 0.01	...	...	...		
				GRB 080825B [b]			
NIR/opt.	BRPL	1.1 ± 0.1	2.2 ± 0.6	...	59 ± 24	no	DFOSC I (2)
X-ray	PL	1.8 ± 0.6	...	...	...		
				GRB 080913			
NIR/opt.	PL	1.13 ± 0.08	...	...	...	no	
X-ray	PL	1.22 ± 0.06	...	...	...		
				GRB 080916C			
NIR/opt.	PL	1.73 ± 0.39	...	...	...	no	
X-ray	PL	1.30 ± 0.09	...	...	...		
				GRB 090205			
NIR/opt.	PL	1.35 ± 0.04	...	...	...	yes	FORS1 RI (3)
X-ray	BRPL	0.91 ± 0.03	2.12 ± 0.07	...	23 ± 1		
				GRB 090423			
NIR/opt.	BRPL	0.05 ± 0.01	1.00 ± 0.03	...	24 ± 8	no	HAWKI KJ / WFCAM K
X-ray	PL + BRPL	1.38 ± 0.04	-3.75 ± 4.20	1.34 ± 0.15	3.0 ± 4.6		NIRI HJ / ISAAK J (4)(5)
				GRB 090429B [c]			
NIR/opt.	PL	0.61 ± 0.08	...	...	...	no	NIRI JHK (6)
X-ray	BRPL	-1.14 ± 0.59	1.37 ± 0.10	...	0.65 ± 0.18		
				GRB 090516A			
NIR/opt.	PL	1.72 ± 0.05	...	...	...	yes	FORS2 R (7) / NOT R (8)
X-ray	BRPL	0.78 ± 0.06	1.75 ± 0.05	...	16 ± 1		
				GRB 100219A			
NIR/opt.	PL	1.68 ± 0.46	...	...	...	yes	HAWKI KHJ / GMG r'
X-ray	BRPL	1.72 ± 0.25	> 3.0	...	...		GTC i' (9)
				GRB 100513A			
NIR/opt.	PL	0.48 ± 0.17	...	...	...	no	PAIRITEL JHK_s (10)
X-ray	PL	0.96 ± 0.06	...	...	...		
				GRB 100905A			
NIR/opt.	PL	0.60 ± 0.06	...	...	...	no	
X-ray	PL	0.88 ± 0.03	...	...	...		
				GRB 111008A			
NIR/opt.	PL	1.02 ± 0.06	...	...	...	no	

Table 3.5: continued.

	Model	α_1	α_2	α_3	t_b (ks)	host (y/n)	add. data[a] (reference)
X-ray	BRPL	0.97 ± 0.09	1.42 ± 0.05	...	41 ± 11		
				GRB 120712A			
NIR/opt.	BRPL	0.04 ± 0.08	1.66 ± 0.16	...	102 ± 13	no	
X-ray	BRPL	0.95 ± 0.03	1.80 ± 0.11	...	6 ± 1		
				GRB 130606A			
NIR/opt.	PL	1.71 ± 0.03	...	...	...	no	NOT $r'i'z'$ / TNG $i'z'$ (11)
X-ray	PL	1.71 ± 0.03	...	...	...		GTC $i'z'$ (12)
				GRB 131117A			
NIR/opt.	PL	0.86 ± 0.01	...	...	...	no	
X-ray	PL + G	0.95 ± 0.02	...	...	...		
				GRB 140304A			
NIR/opt.	PL + BRPL	2.25 ± 0.24	-7.42 ± 5.94	1.86 ± 0.20	25 ± 2	no	RATIR $grizJH$ (13)
X-ray	PL + BRPL	1.93 ± 0.14	-9.71 ± 6.89	1.50 ± 0.09	16 ± 2		Nanshan R (14) / NOT gr (15)
							MONDY R(16) / ORI-40 R (17)
				GRB 140311A			
NIR/opt.	PL	0.95 ± 0.04	...	...	...	no	NOT $r'i'$ (18)
X-ray	BRPL	1.20 ± 0.07	1.97 ± 0.58	...	121 ± 65		
				GRB 140428A			
NIR/opt.	PL	1.81 ± 0.08	...	...	...	no	OSN I (19)
X-ray	BRPL	0.96 ± 0.07	> 2.0	...	19 ± 9		LRIS i (20)
				GRB 140515A			
NIR/opt.	BRPL	0.77 ± 0.25	> 2.5	...	...	no	GMOS z' (21)
X-ray	PL + BRPL	3.10 ± 0.19	-3.77 ± 0.69	1.03 ± 0.05	2.3 ± 0.2		Chandra (22)
				GRB 140614A			
NIR/opt.	PL	1.20 ± 0.04	...	...	...	no	
X-ray	PL + BRPL	1.92 ± 0.07	-0.27 ± 0.32	1.49 ± 0.08	7 ± 1		
				GRB 151027B			
NIR/opt.	BRPL	0.44 ± 0.19	1.44 ± 0.14	...	34 ± 28	no	NOT R (23)
X-ray	BRPL	0.44 ± 0.19	1.44 ± 0.14	...	34 ± 28		RATIR $r'i'$ (24)
				GRB 151112A			
NIR/opt.	BRPL	0.84 ± 0.06	2.10 ± 0.29	...	128 ± 14	no	
X-ray	BRPL	0.84 ± 0.06	> 1.2	...	128 ± 14		

Notes. [(a)] GROND optical and near-infrared data were extended with data collected from GCNs and refereed publications. The magnitudes were, if necessary, converted to the AB system. [(b)] The XRT light curve is also consistent with the model for the NIR/optical afterglow (see Fig. 3.13). [(c)] We used the temporal decay slope as derived from the NIRI K band data to re-scale the NIRI J, H, and K-band observation to a common reference time (see Fig. 3.16).

References. (1) Perley et al. (2010); (2) Thoene et al. (2008); (3) D'Avanzo et al. (2010); (4) Tanvir et al. (2009); (5) Salvaterra et al. (2009); (6) Cucchiara et al. (2011); (7) Gorosabel et al. (2009); (8) de Ugarte Postigo et al. (2009); (9) Thöne et al. (2013); (10) A. N. Morgan et al. (2010); (11)Hartoog et al. (2015); (12) Castro-Tirado et al. (2013); (13) Butler et al. (2014); (14) Xu, Niu et al. (2014); (15) de Ugarte Postigo et al. (2014); (16) Volnova, Pozanenko et al. (2014); (17) Volnova, Tungalag et al. (2014); (18) Xu, Bai et al. (2014); (19) Aceituno et al. (2014); (20) Perley (2014a); (21) Melandri et al. (2015); (22) Margutti et al. (2014); (23) Malesani, Tanvir et al. (2015); (24) A. M. Watson et al. (2015) .

Chapter 4

Evidence for diffuse molecular gas and dust in the hearts of gamma-ray burst host galaxies: *Unveiling the nature of high-redshift damped Lyman-α systems*

As published in Astronomy & Astrophysics, Volume 623, A43, March 2019
DOI: https://doi.org/10.1051/0004-6361/201834422
Evidence for diffuse molecular gas and dust in the hearts of gamma-ray burst host galaxies: Unveiling the nature of high-redshift damped Lyman-α systems

As outlined in Chapter 1, the absorption lines imprinted onto the spectra of GRB afterglows can be used to study the different phases of the gas in the ISM of their host galaxies line-of-sight. Molecular hydrogen is of particular interest because its presence is tightly correlated with the formation of stars (Bigiel et al., 2008, 2011; Leroy et al., 2013; Krumholz et al., 2012). However, due to the lacking dipole moment and the low mass of the molecule, it is hard to study H_2 in emission at high redshift ($z \gtrsim 2$), because the rotational transitions require high temperatures to be excited (Kennicutt & Evans, 2012). Therefore carbon monoxide is commonly used as a tracer of molecular gas, but with the drawback that the conversion factor to H_2 is still uncertain and likely also varies on different scales and for different gas properties (Tacconi et al., 2008; Bolatto et al., 2013; Gong et al., 2018). Fortunately, for DLAs at redshifts larger than $z > 2$ the Lyman and Werner bands of molecular hydrogen are shifted into the observed UV band and H_2 absorption lines can thus be detected in spectra of GRBs and QSOs obtained with ground-based instruments like VLT/X-shooter (Vernet et al., 2011).

The H_2 content of a star-forming region is the result of the balance between its formation on dust grains and its dissociation by UV photons from the interstellar radiation field. For GRB-DLAs also the UV flux from the GRB itself could potentially photodissociate the molecular gas or pump it to its vibrationally-excited states (Draine, 2000; Draine & Hao, 2002). Additionally, large dust masses or the molecular hydrogen itself can provide (self-)shielding against the destructive UV radiation (Krumholz et al., 2009). Dust, however, also efficiently attenuates the background UV flux from the GRB, which makes it difficult to obtain high-resolution spectra of very dusty sight-lines ($A_V \gtrsim 1$ mag, Greiner et al., 2011), and adds to the difficulty of identifying the H_2 absorption lines and

distinguish them from the Lyman-α forest. So, while it remains difficult to study dark molecular clouds ($A_V > 0.5$ mag), GRBs offer an ideal probe of the diffuse or translucent gas in high-redshift galaxies.

Absorption from H_2 is generally detected in 10% or less of QSO-DLA systems (Ledoux et al., 2003; Noterdaeme et al., 2008; Balashev et al., 2014; Jorgenson et al., 2014), but with a strong dependence on the neutral hydrogen column density, with the fraction increasing when selecting QSO-DLAs with large neutral hydrogen column densities (Noterdaeme, Petitjean & Srianand, 2015). Recently Balashev et al. (2017) and Ranjan et al. (2018) also reported the detection of very large H_2 column densities in two other extremely strong DLAs (ESDLAs, defined as having $\log N(\mathrm{H\,I}) \gtrsim 21.5$). Since GRBs are linked to star formation and originate from the inner regions of their host galaxies (Fruchter et al., 2006; Lyman et al., 2017), where they are usually behind very high column densities of gas (Jakobsson et al., 2006; Pontzen et al., 2008), one would expect to find a higher fraction of H_2-bearing systems in GRB-DLAs compared to QSO-DLAs (Zwaan & Prochaska, 2006); also because the absorbing gas is located at distances from the explosion site where the influence of the ionizing UV radiation of the GRB itself should be negligible (50 to more than several hundred parsec; Prochaska et al., 2006; Vreeswijk et al., 2007, 2011; Ledoux et al., 2009; D'Elia et al., 2009; Hartoog et al., 2013). Yet, first searches for absorption from molecular hydrogen in small samples of GRB-DLAs were surprisingly unsuccessful. For example, from the lack of molecular hydrogen in a sample of 5 GRB afterglows, Tumlinson et al. (2007) argues that a deficiency of molecular gas in GRB-DLAs compared to QSO-DLAs, could be the result of a combination of lower metallicity and a stronger UV radiation field in GRB host galaxies. Later, from the analysis of the physical conditions in a sample of 7 GRB-DLAs, Ledoux et al. (2009) concludes that the lack of H_2 can be explained by the low metallicities and depletion factors, but also by the moderate particle densities in the systems: large ($\gtrsim 100$ pc), metal-poor atomic clouds with high temperatures ($T > 1000$ K). Since then, absorption from molecular hydrogen has only been identified in a handful of GRB-DLAs: GRB080607 (Prochaska et al., 2009), 120327A (D'Elia et al., 2014), 120815A (Krühler et al., 2013), and 121024A (Friis et al., 2015) (possibly also in GRB060206; Fynbo, Starling et al., 2006). [1]

Recently, Selsing et al. (2018) published the X-shooter GRB optical afterglow legacy sample, which is the result of an extensive follow-up of 103 GRB afterglows with VLT/X-shooter between 2009 and 2017. Based on their work, we here aim to use a subsample of 22 GRBs at redshifts $z > 2$ to perform a systematic search for absorption lines from molecular hydrogen, in order to answer the question whether, and if so why, there is a lack of H_2 in GRB-DLAs. A full exploration of the column densities of the entire X-shooter sample will be presented in Thöne (2019, in prep.). For the purpose of the present paper, we only use such measurements to analyze the metal and dust depletion characteristics of the GRB-DLAs where H_2 can be searched for.

The Chapter is organized as follows. In Sect. 4.1, we describe the H_2 GRB afterglow

[1] Recently, the CH^+ molecule was also detected in the optical spectrum of GRB140506A at $z = 0.889$ (Fynbo et al., 2014).

X-shooter subsample, and in Sect. 4.2 the absorption line analysis methods we have developed. Our main results are summarized in Sect. 4.3 and discussed in Sect. 4.4. We conclude in Sect. 4.5. Throughout the Chapter, when referring to GRBs, we refer to the class of long-duration GRBs, and column densities are given in cm^{-2}.

4.1 Sample selection

The GRB sample presented in this Chapter was selected based on the complete sample of GRB afterglows observed with X-shooter as presented in Selsing et al. (2018). This sample is selected to be unbiased with respect to the parent *Swift* GRB sample, while at the same time optimising observability. This was done on the basis of a set of selection criteria, as described in Selsing et al. (2018). Out of the full statistical sample, afterglow observations were possible for 93 bursts. From this complete sample of 93 GRBs, 41 are at redshift $z > 1.7$, which allows measuring the neutral hydrogen column density (see their table 4). From these 41 bursts, we further select the 33 bursts at redshift $z > 2.0$, where enough Lyman and Werner lines of molecular hydrogen are shifted into the X-shooter UVB arm, which is required to properly constrain the H_2 column density. This sample of 33 GRBs is presented in Table 4.1, where we list the individual redshifts as well as the instrumental resolution in each X-shooter arm, as taken from Selsing et al. (2018), and also the S/N measured in the range of the expected H_2 absorption lines.

From these 33 bursts, however, only 22 have X-shooter spectra with a S/N ratio that is high enough to perform a rigorous analysis of the H_2 absorption lines (S/N $\geq$ 2). Therefore, 11 bursts were excluded from the final sample and are consequently listed at the bottom of the table, including a small note indicating the potential reason for the S/N being so low. This selection does not come without possible biases, which are important to address, and which we discuss below.

First of all, it is usually found that about 20% to 40% of the GRB population, the so-called *dark* bursts, are behind significant amounts of dust ($A_V > 0.5$ mag) along the GRB host galaxies' line-of-sight (Perley et al., 2011; Greiner et al., 2011; Covino et al., 2013), although we note that the fraction might get lower at redshift $z > 4$ (Bolmer et al., 2018; Zafar, Møller et al., 2018). This is important, because the attenuation of the GRB afterglow by dust usually increases from red to blue wavelengths, which has a stronger effect on the observed spectrum with increasing redshift of the GRB, meaning that dusty and/or high-redshift bursts are likely missed in spectral follow-up campaigns. For example, GRB 110128A, 130612A, and 161014A, that were excluded from the sample, were already very faint only several hours after the GRB trigger and might, therefore, be behind substantial dust columns. And, since all 22 GRBs in our sample are only behind small to moderate amounts of dust ($A_V < 0.5$ mag, see Table 4.5), our sample might very well be biased toward sight-lines with small foreground host galaxy dust columns. All the other burst that were excluded from the sample could only be observed later than $T_0 + 12$ hrs or were observed under poor seeing conditions, and their exclusion should therefore not add any biases to the sample selection.

Another bias, however, might be introduced by including GRBs at redshift $z > 4$,

Table 4.1: Our sample of 22 GRB afterglows at $z > 2$ observed with X-shooter. Out of the 33 initially-selected bursts, 11 were excluded because of poor S/N, which are additionally listed at the bottom of the table.

GRB	Redshift	Instrumental Resolution (FWHM)			S/N
yymmdd#	(z)	UVB [km/s]	VIS [km/s]	NIR [km/s]	
090809A	2.7373	50.8	29.4	44.8	3
090926A	2.1069	49.1	28.4	42.2	14
100219A	4.6676	48.7	28.7	46.9	3
111008A	4.9910	-	22.7	38.5	5
111107A	2.8930	49.3	20.6	40.5	4
120327A	2.8143	47.9	29.0	41.0	15
120712A	4.1719	53.2	34.5	55.6	2
120716A	2.4874	56.1	33.0	48.9	4
120815A	2.3582	48.6	26.8	48.4	6
120909A	3.9290	60.1	32.0	55.6	11
121024A	2.3005	50.2	24.6	38.0	5
130408A	3.7579	50.6	22.9	38.5	12
130606A	5.9127	-	24.2	46.2	15
140311A	4.9550	-	28.5	40.4	3
141028A	2.3333	51.2	30.6	44.7	4
141109A	2.9940	51.7	29.9	44.9	9
150403A	2.0571	51.9	29.9	44.9	6
151021A	2.3297	52.7	28.3	46.9	3
151027B	4.0650	54.3	31.2	47.3	8
160203A	3.5187	51.5	23.1	38.5	14
161023A	2.7100	50.7	29.3	44.0	16
170202A	3.6456	46.9	27.3	40.0	9
Excluded		Comment			
100728B	2.106	obs. $T_0 + 22.0$ hrs			< 2
110128A	2.339	*dark* burst? high A_V?			< 2
120404A	2.876	obs. $T_0 + 15.7$ hrs, $A_V \sim 0.07$ mag			< 2
121201A	3.385	obs. $T_0 + 12.0$ hrs, $A_V \sim 0.17$ mag			< 2
121229A	2.707	poor seeing			< 2
130427B	2.780	obs. $T_0 + 20.6$ hrs, twilight			< 2
130612A	2.007	*dark* burst? high A_V?			< 2
131117A	4.042	$A_V < 0.20$ mag, $z > 4$			< 2
140515A	6.327	obs. $T_0 + 15.5$ hrs, $z > 6$			< 2
140614A	4.233	$A_V < 0.50$ mag, $z > 4$			< 2
161014A	2.823	*dark* burst? anomalous extinction?			< 2

Notes. Columns from left to right: name of the GRB; redshift; FWHM of the instrumental resolution in km/s inferred in the UVB, VIS, and NIR arms of X-shooter (taken from Selsing et al., 2018); S/N in the range of the expected H_2 absorption lines. For the 11 bursts at the end of the table that were excluded from the sample, we write a small comment indicating the potential reason for the S/N being so low.

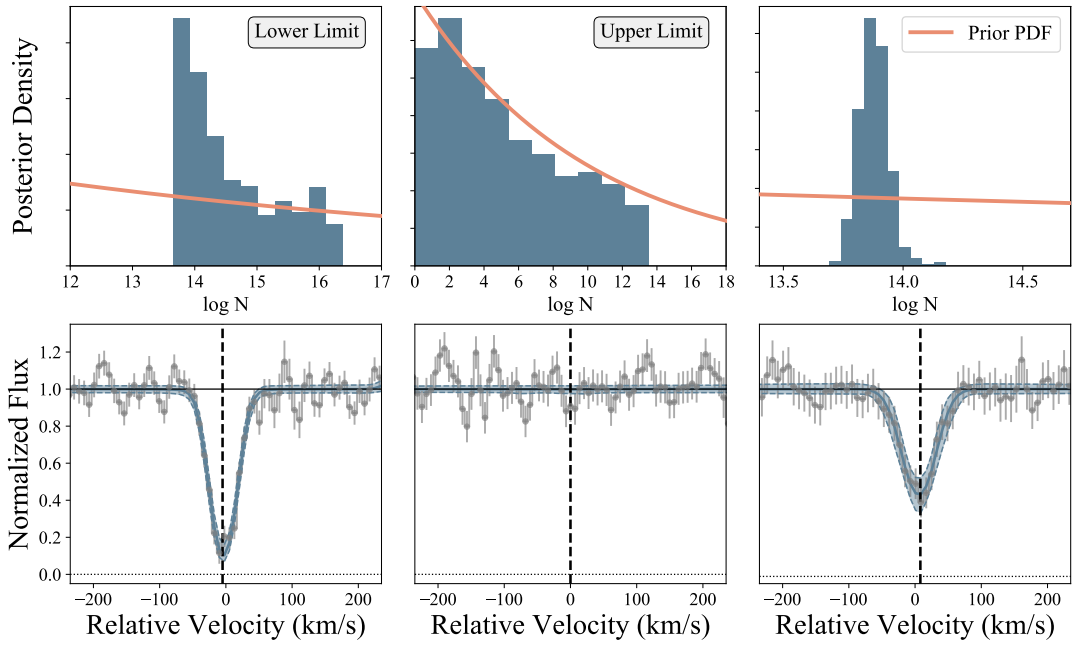

Figure 4.1: Typical posterior distributions for a saturated line, a non-detection, and a line which can be used to derive a column density accurately. In the case of a non-detection, the posterior distribution is completely determined by the prior PDF, which is expected in case there is in the data no information about the assumed model, in this case a Voigt-profile-like absorption.

where the Lyman$-\alpha$ forest becomes an increasing hindrance in detecting the absorption lines from molecular hydrogen, which all fall blue-wards of 1215 Å. Also, at redshift $z > 4$ the Lyman blanketing significantly reduces the observed flux bluewards of Lyα. This is the case for 6 of the 22 GRBs (27%), which will thus be discussed and labeled separately throughout the Chapter. Also, three of the excluded bursts are at redshift $z > 4$.

4.2 Methods

Kinematic or velocity profiles of absorption lines are a powerful tool to analyze the different gas phases in DLA absorbers. The predominant absorption features imprinted on the afterglow spectrum of the GRB are from singly-ionized metal species, residing in the cold, neutral gas of the GRB host galaxy. In most cases, also absorption lines from higher ionization species are seen in the spectra, which trace the warm, ionized gas and therefore usually have a different kinematic profile, offset to the singly-ionized lines (A. J. Fox et al., 2008; Wiseman, Perley et al., 2017; Heintz et al., 2018). Since we are only interested in the neutral gas phase, these high ionization species will not be considered in this Chapter.

To analyze and fit the absorption lines in the afterglow spectra in our sample of 22 GRBs, we developed our own, state-of-the-art routines, which are entirely written in

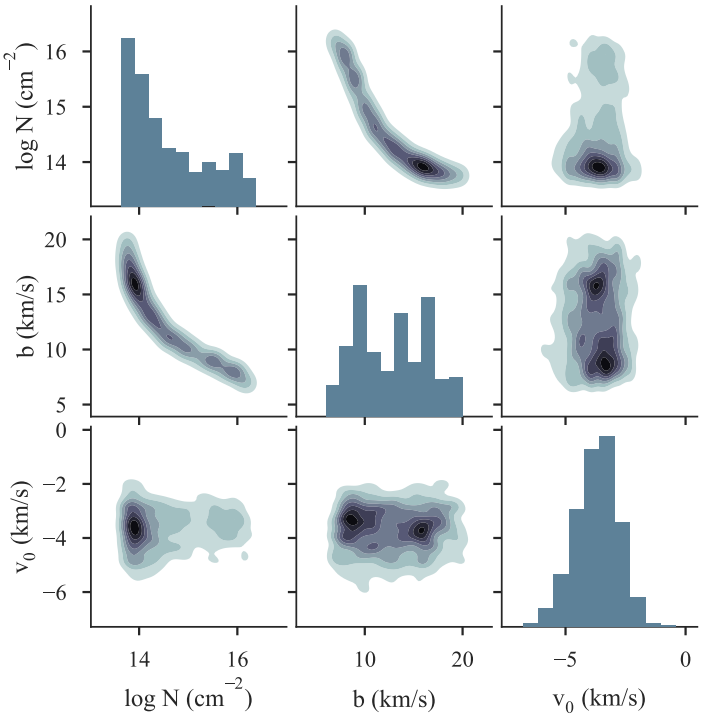

Figure 4.2: Pairwise contour plots and posterior distributions for the column density, the broadening parameter, and the position of the saturated absorption line shown in Fig. 4.1.

PYTHON and are based on the Markov chain Monte Carlo (MCMC) Bayesian inference library PyMC 2.3.7 [2].

Absorption lines are usually modeled with Voigt line profiles, which are fitted to the spectra simultaneously with the continuum flux of the GRB. The model for such an absorption profile in velocity space with a number of n absorption components is described by

$$F_{\rm model} = F_{\rm c} \cdot \prod_{j=1}^{n} e^{-\tau_j}; \quad F_{\rm c} = A + Bv + Cv^2 \tag{4.1}$$

where the optical depth τ is given by

$$\tau = \frac{\pi e^2}{m_{\rm e} c} f_{ik} \lambda_{ik} N \cdot \phi_V \left(v - v_0, \frac{b}{\sqrt{2}}, \Gamma \right) \tag{4.2}$$

where ϕ_V is the Voigt profile in velocity space, and with f_{ik}, λ_{ik} and Γ, being the oscillator strength, wavelength and damping constant for transition $i \rightarrow k$. The relative velocity of the absorption component v_0, the broadening parameter b, the column density N, and possibly also the number of components n, are the parameters of interest for our

[2] https://pymc-devs.github.io/pymc

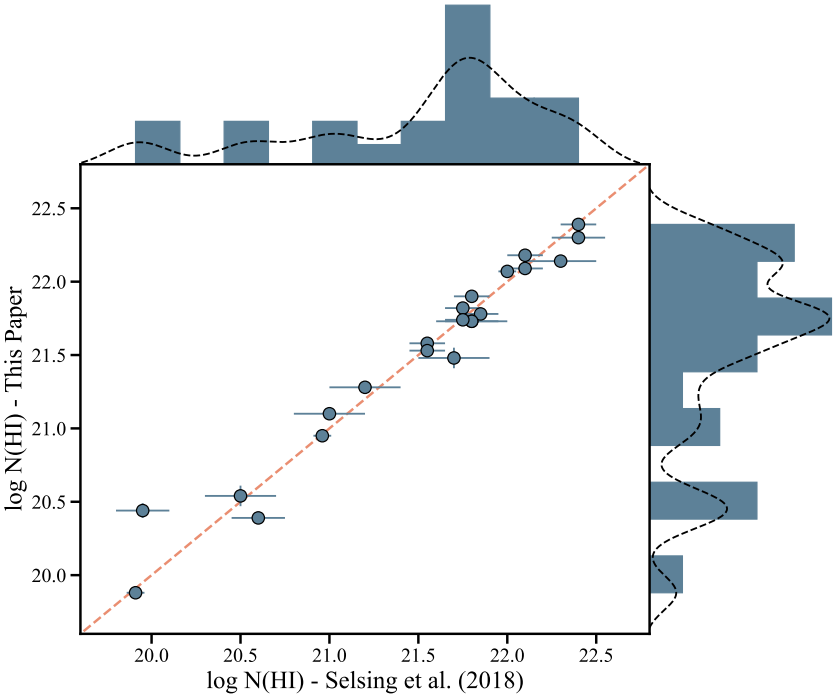

Figure 4.3: The neutral hydrogen column densities determined in this Chapter versus those from Selsing et al. (2018). The dashed line is the line of equality. Additionally we show histograms and corresponding kernel density estimates.

analysis. For the continuum flux of the GRB F_c, which is usually best described by a simple power law, we assume a second order polynomial, which introduces another three free parameters (A, B, and C). The Voigt profile ϕ_V is a convolution of a Gaussian (thermal and turbulent motion) and a Lorentzian (uncertainty of transition frequencies) profile, and is related to the real part of the Faddeeva function $w(z)$ that we imported from the Python package SciPy [3]. Finally, the absorption line profile is convolved with a Gaussian with a FWHM of the instrumental resolution in the given arm, as determined by Selsing et al. (2018) (see Table 4.1).

$$\phi_V = \frac{\mathrm{Re}\,(w(z))}{b\sqrt{\pi}}; \quad z = \frac{v - v_0 + i\Gamma}{b} \tag{4.3}$$

Given this model, our parameters of interest are constrained in the following way. First, we select transitions that display a distinct absorption profile, that is unblended lines that fall in a segment of the spectrum with a good S/N, usually Si II 1808.0129, Fe II 1608.4509, or Mg II 2803.5311, and compare them in order to identify the number of required absorption components. This is done by fitting these lines with multiple MCMC runs for a realistic range of the number n of possible absorption components

[3] https://docs.scipy.org/doc/scipy/reference/generated/scipy.special.wofz.html

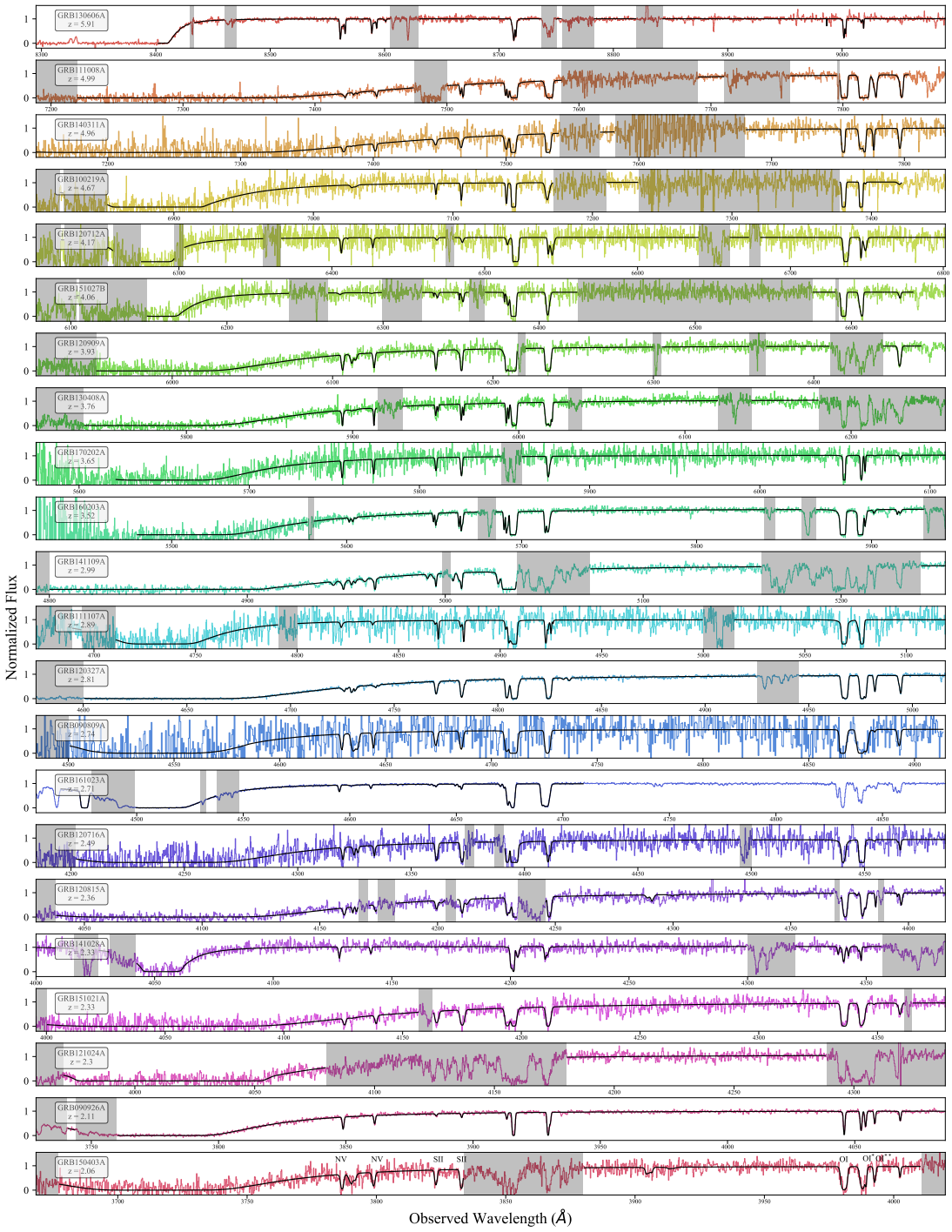

Figure 4.4: Normalized X-shooter spectra around the Lyman-α line for the 22 GRBs analyzed in this Chapter with increasing redshift from the bottom to the top. The best fit model is indicated by the solid black line. The gray shaded areas show the regions that were ignored for the fit, mostly due to telluric lines or too complex absorption structures.

with each of a total of 100 000 iterations and with a warm-up phase of 95 000 iterations. For DLAs with three or more distinct absorption components we doubled or tripled the number of iterations, and for the relative velocity of each component we start by putting a uniform prior on the whole input velocity range, which was usually $v_0 \pm 1000$ km/s. After each run, we analyzed the resulting fit and posterior distributions and compared the models for a different number of components by calculating χ^2 until a convincing solution was found. Once the required number n and the relative velocity v_0 of each absorption component were identified by also comparing the results from different lines, we fixed n and continued to fit the other lines by using smaller uniform priors on v_0, usually allowing for a small variation of $v_0 \pm 20$ km/s. For the broadening parameter, we generally also used uniform priors between the minimum resolvable value, usually 5 to 15 km/s, and a maximum value of 80 km/s. Finally, for the column density, we chose an exponential prior, which ensures that lower column densities are preferred when there is no information about absorption in the data, that it the flux around the position of the expected absorption line is consistent with the noise. As an example, in Fig. 4.1, we show the posterior distributions for the column density of a single absorption line in three different cases: a saturated line, a non-detection, and a line which can be used to measure a column density.

As expected for the resolution of X-shooter (R $\approx$ 4000 to 17 000 or equivalently 75 to 18 km/s), even mildly saturated lines show a strong degeneracy between the column density and the broadening parameter (hidden saturation; Prochaska, 2006; Wiseman, Schady et al., 2017), which to identify requires sufficient sampling of the parameter space, which is growing exponentially with increasing number of absorption components. The effect of hidden saturation is demonstrated in Fig. 4.2, where we show pairwise contour plots and posteriors distributions of the three parameters from the saturated line shown in Fig. 4.1. Since the column density and the broadening parameter are highly correlated we use the adaptive Metropolis algorithm implemented in PyMC for these parameters[4]. For all other parameters, also the three parameters from the second order polynomial for the background flux (normal priors around $A = 1$, $B = 0$ and $C = 0$ with variance $\sigma = 0.5$), we use the Metropolis–Hastings step method. For the likelihood, we chose a Gaussian whose standard deviation is equal to the flux error. Finally, we want to note, that for the resolution of X-shooter, individual absorption components are often blended with each other, and therefore the decomposition of the profile is not necessarily unambiguous, such that the resultant b-values might not be physical.

4.3 Results

4.3.1 Neutral hydrogen and metal abundances

The most prominent absorption feature in GRB afterglow spectra is the Lyman-α line, which is used to measure the neutral hydrogen column density $N(\mathrm{H\,I})$. For each of the 22

[4]For a general introduction on MCMC methods and algorithms for Bayesian data analysis, we refer the reader to Betancourt (2017) or Sharma (2017) and the references therein.

bursts in the selected sample, N(H I) was previously inferred by Selsing et al. (2018), by simply plotting synthetic absorption lines over the normalized spectra until a satisfying match was reached (which is a standard procedure, e.g., Fynbo et al., 2009). We are able to derive slightly more accurate values by fitting the Lyman-α line by also including all absorption lines in the red and blue damping wing. The results are listed in Table 4.3 and shown in Fig. 4.4. Those parts of the spectrum that were ignored for the fit, mostly due to telluric and Lyα forest lines or too complex absorption structures, are marked by the gray shaded areas. To compare the results from both methods, in Fig. 4.3, we additionally plot the values derived in this Chapter versus those from Selsing et al. (2018). Besides one outlier, GRB120712A, which has the lowest S/N, all values are consistent within in the errors, confirming the robustness of both methods.

Furthermore, to measure the metallicity and study the dust depletion in each system, for all 22 GRB spectra we also fit lines and measure column densities of ten different metal species, O I, Zn II, S II, Si II, Mg II, Mn II, Cr II, Ni II, Fe II, and Ti II, at least in those cases where it is possible and the spectrum is not affected by, for example, strong telluric lines. Besides Ti II, all of these absorption lines are commonly detected in GRB afterglow spectra (Christensen et al., 2011). In case of non-detections or saturated lines we determine 3-σ upper or lower limits, respectively. All measured column densities, as well as upper or lower limits, are listed in Table 4.3 and the corresponding plots showing the most constraining fits for each burst are shown at the end of this Chapter in Fig. 4.18 to 4.39.

The values for the oscillator strength f and damping constant Γ are taken from the atomic data file (`atom.dat`) which is distributed in VPFIT version 10.2 and originally based on Morton (2003). For Zn II and S II, however, we use the updated oscillator strength values from Kisielius et al. (2014, 2015) instead. While the difference in case of S II is almost negligible, the column densities of Zn II are about 0.1 dex lower when using the new values. We also note that in most cases, the three sulfur lines (λ = 1250.58, 1253.81, and 1259.52 Å) were fitted simultaneously with Lyα, because they fall into the red part of the damping wing for column densities larger than $\log N(\mathrm{H\,I}) \gtrsim 21.0$, which is true for the majority of the bursts in the sample (see Fig. 4.4). Finally, since the two Zn II lines at $\lambda = 2026.14$, 2062.66 Å are blended with lines from Cr II and Mg I, we fit all of these lines simultaneously.

To compare the column densities measured in this Chapter with those previously published in the literature, in Fig. 4.5, we plot our values compared to those collected from Wiseman, Schady et al. (2017). The latter are partially determined by Wiseman, Schady et al. (2017) and otherwise taken from different papers, i.e.: GRB090809 from Skuladottir (2010), 090926A from D'Elia et al. (2010), 100219A from Thöne et al. (2013), 111008A from Sparre et al. (2014), 120327A from D'Elia et al. (2014), 120815A from Krühler et al. (2013), and 121024A from Friis et al. (2015). Additionally we also plot the values for GRB161023A from de Ugarte Postigo et al. (2018). Since we are able to better identify any strong degeneracies in the N versus b parameters space, we are generally more conservative and put more upper or lower limits on the column densities compared to previous published values, which are not plotted in Fig. 4.5. Otherwise, our measurements are in

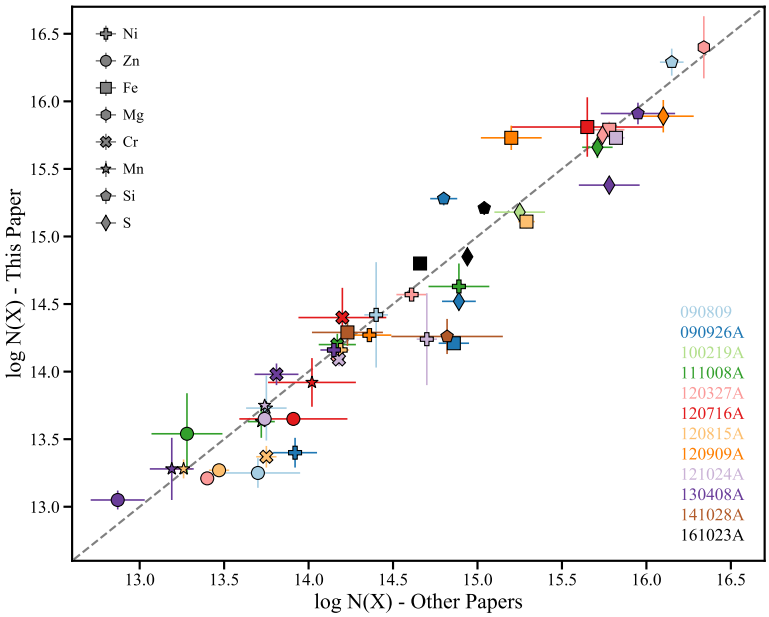

Figure 4.5: Column densities as derived in this Chapter versus those published in Wiseman, Schady et al. (2017), which are partially collected from various papers. Also plotted are the values for GRB 161023A from de Ugarte Postigo et al. (2018). The dashed line is the line of equality. The individual metal species X are indicated by different symbols (as labeled).

reasonable agreement with the previous published values. The major differences can be explained by the updated oscillator strength values in case of Zn II, a better exploration of the parameter space in case of blended lines (Zn II and Cr II), or the in general advanced analysis method, which allows a better and more efficient exploration of the parameter space compared to the least squared approach of VPFIT.

4.3.2 Dust depletion

Due to their apparent faintness, most of our knowledge on the elemental abundances in high-redshift galaxies ($z > 2$), originates from absorption line studies of DLA systems in the spectra of QSOs and GRBs (Schady, 2017) [5]. However, refractory elements, like Fe, Ni or Cr, can be heavily depleted by condensation onto interstellar dust grains, with different strength of the depletion depending on the element and the sight-line (Savage & Sembach, 1996; Jenkins, 2009; De Cia et al., 2016). Thus, if some elements are partially locked onto dust grains, they are not completely accounted for when measuring the gas-phase abundances using absorption line analysis, and we, therefore, have to analyze the depletion in each sight-line independently. The analysis of the dust depletion can thus be

[5] First attempts have been made to also use superluminous supernova as background sources to study high-redshift galaxies in absorption (Vreeswijk et al., 2014; Yan et al., 2018).

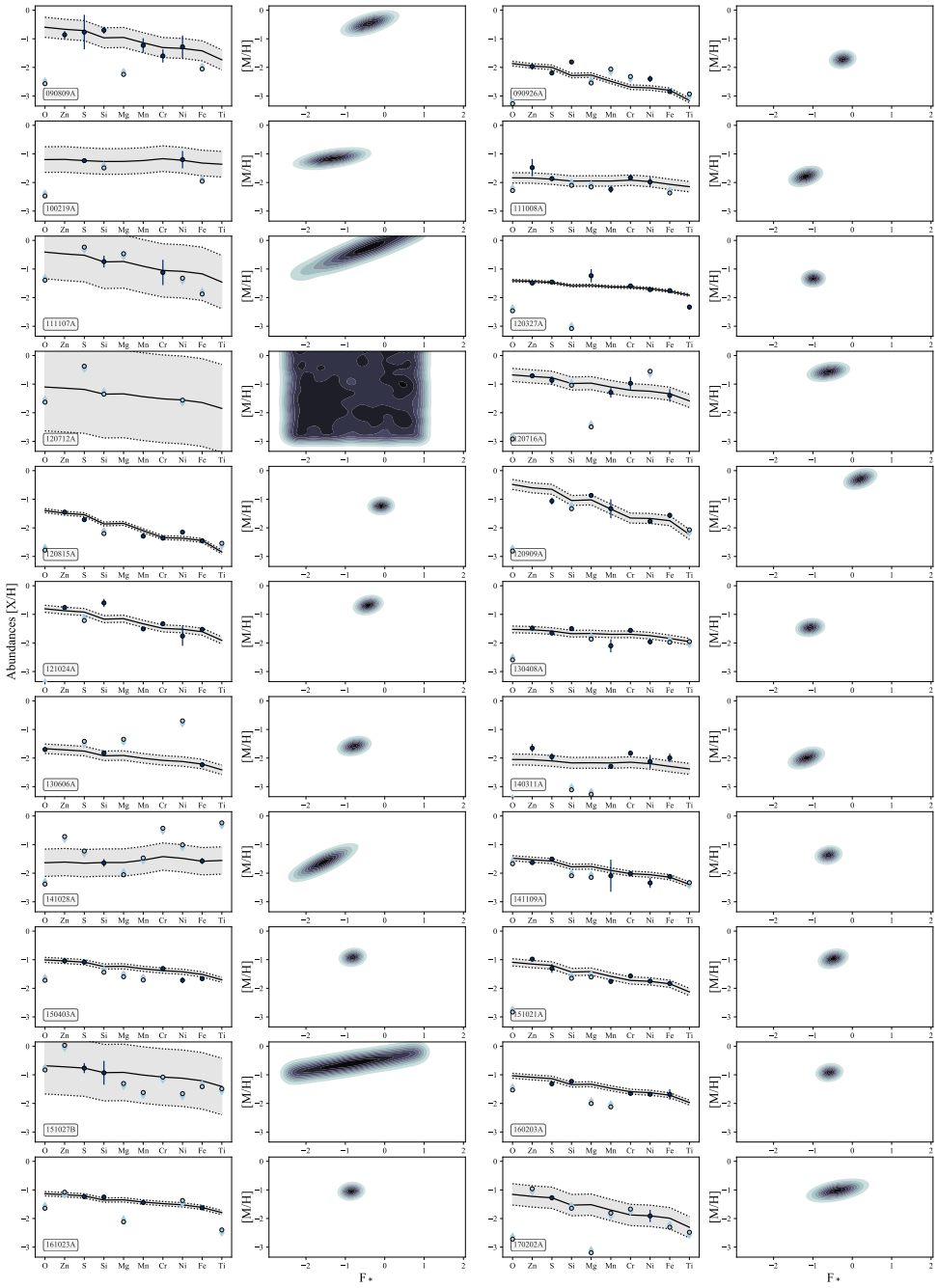

Figure 4.6: Results from fitting the dust depletion sequences for the 22 GRBs in our H_2 sample. The relatives abundances of the elements used for the fit are plotted with dark blue dots. Upper and lower limits for the other elements are plotted in light blue. The black line indicates the best fit; and the dashed lines and gray shaded areas the corresponding 3-σ confidence intervals. A contour plot of dust-corrected metallicity [M/H] versus F_* is shown right next to every depletion sequence.

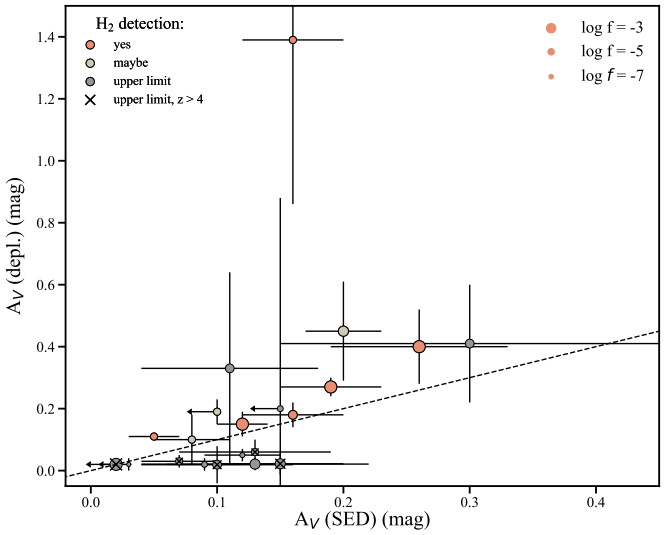

Figure 4.7: Host intrinsic visual extinction as measured from the depletion analysis A_V (depl.) versus the measurement from a fit to a spectral energy distribution from photometric data A_V (SED). The dashed line is the line of equality.

used to measure the dust content in the GRB host galaxies line-of-sight and to determine the dust-corrected metallicity [M/H] of the DLA.

As a first indicator of the strength of depletion, one can calculate the depletion factor $[\mathrm{Y/Fe}] \equiv \log(N(\mathrm{Y})/N(\mathrm{Fe})) - \log(N(\mathrm{Y})/N(\mathrm{Fe}))_\odot$, where Y is a non-refractory element that is only marginally depleted onto dust grains, like Zn or S, and is compared to iron, that is usually heavily depleted.

A more sophisticated way to study the dust depletion in each of the GRB-DLAs, is to compare the relative abundances of multiple refractory and non-refractory elements and use relations found in the Milky Way and QSO-DLAs to interpret the depletion pattern (Jenkins, 2009; De Cia et al., 2013, 2016; Wiseman, Schady et al., 2017). This method can be justified by the homogeneous properties regarding the metal and dust content found for different environments and redshift, that indicate that most of the dust content is built up from grain growth in the ISM, independent of the specific star formation history (De Cia, 2018). To calculate the relative abundances $[\mathrm{X/H}] \equiv \log(N(\mathrm{X})/N(\mathrm{H})) - \log(\mathrm{X/H})_\odot$ we adopt the solar abundances from Asplund et al. (2009), following the recommendations of Lodders et al. (2009), as listed in table 1 of De Cia et al. (2016). We also assume that our measurement of the column density of an element that is singly ionized is representative of the total gas-phase abundance of that element. This is justified by the large pool of neutral gas $\log N(\mathrm{H\,I}) \gtrsim 20.3$, found for all GRBs in our sample besides 130606A, indicating that only a small, negligible fraction of higher ionized elements should exist (Wolfe et al., 2005; Kanekar et al., 2011).

After calculating the relative abundances, our analysis of the dust depletion sequences was done following the work of Wiseman, Schady et al. (2017), which is based on the results from De Cia et al. (2016). However, instead of using their minimum least squares

approach, we again use a Bayesian framework and sample the posterior distributions using PyMC. For the depletion strength factor we use a uniform prior between $F_* = -2.5$ and 1.0 and for the dust-corrected metallicity of the system a uniform prior between [M/H] $= -3$ and 1.0. [6] We then run an MCMC with 100 000 iterations and sample the posterior distributions with the last 10 000 iterations after a warm-up phase of 90,000 iterations. The model for the expected relative abundance in element X is given by

$$[\mathrm{X/H}]_{\mathrm{exp}} = A + B\frac{(F_* - 1.50)}{1.48} + [\mathrm{M/H}] \tag{4.4}$$

where A and B are the updated linear depletion parameters taken from De Cia et al. (2016). The best-fit F_* and [M/H] can then be used to determine the dust-to-metals ratio $\mathcal{DTM}$ (normalized to the Milky Way), and further the expected visual extinction A_V (depl.) in the host galaxy line-of-sight. The dust-to-metals ratio is the ratio between the total dust column density in terms of atoms in the dust phase and the total metal column density, which is further normalized to the Milky Way value. It is derived using Eq. (C.3) of De Cia et al. (2013) and assuming an average $[\mathrm{Fe/Zn}]_{\mathrm{Gal}} = 1.22$ found in Galactic sight-lines (Jenkins, 2009). A_V (depl.) is calculated using the average extinction for a given hydrogen column density in the Milky Way, and using the $N(\mathrm{H})/A_V$ derived by D. Watson (2011) (for more details, see Sect. 4.2 and 6.2 in Wiseman, Schady et al. (2017), and also Savaglio & Fall (2004) and De Cia et al. 2016). For all 22 GRBs, the results of the best-fit depletion pattern, as well as the corresponding contour plots for the dust-corrected metallicity [M/H] versus the depletion strength factor F_*, are shown in Fig. 4.6 and the best-fit results are listed in Table 4.5. Finally, we note that elements that are intrinsically under- or over-abundant, can badly influence the results of the depletion analysis in those cases where only a few elements are available. Also, the negative values of F* we find in DLAs are based on the assumption of a linear relation between [Zn/Fe] and F_* which is extrapolated at negative F_*.

A detailed analysis of nucleosynthesis effects is beyond the scope of this Chapter and may be studied in a forthcoming paper.

4.3.3 Visual extinction

Measurements of the host intrinsic visual extinction from fitting extinction curves to the afterglow SED, A_V (SED), are available in the literature for all bursts from our H_2 sample. The individual values and corresponding references are listed in Table 4.5. Most of them were taken from Bolmer et al. (2018), in case of the GRBs at $z > 4$, or from the measurements for the GROND 4h sample (Greiner et al., 2011; Greiner, 2019, in prep.).

Following Wiseman, Schady et al. (2017), in Fig. 4.7, we plot the host intrinsic visual extinction as derived from the depletion analysis A_V (depl.) versus the measurement from the SED fit A_V (SED). Similar to Wiseman, Schady et al. (2017) and Savaglio & Fall (2004), we find that for some of the sight-lines the values are not consistent with

[6] F_* represents the strength of dust depletion and is defined by Jenkins (2009) to range between 0 and 1 for the Galactic ISM.

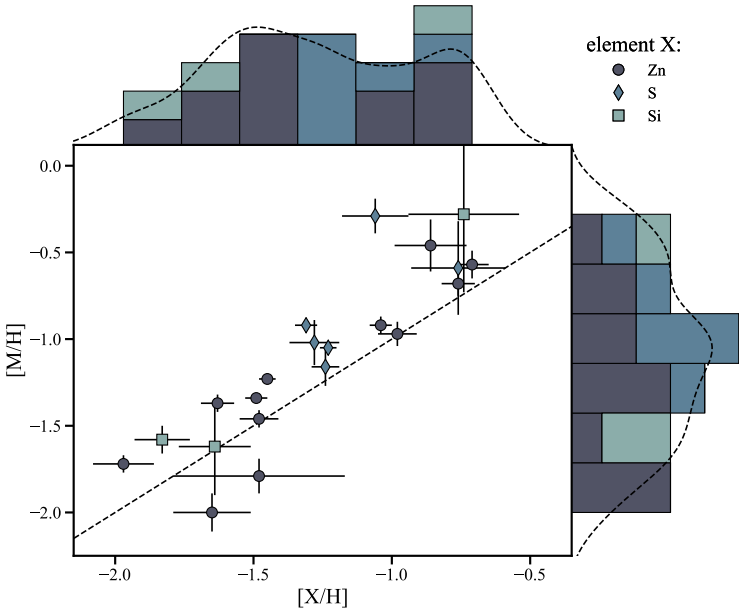

Figure 4.8: Dust-corrected metallicity [M/H] as derived from the depletion analysis versus the metallicity derived using a single line of an element X with low depletion [X/H]. For each burst the used element is colored as labeled. The dashed line is the line of equality.

being identical, and that data points can fall both below and above the line of equality. In contrast to Wiseman, Schady et al. (2017), however, we find a better agreement between both methods, at least within the errors. Interestingly, most of the GRBs for which the extinction measured from the SED fit is higher, are from $z > 4$. This can thus be explained by the higher probability of intervening systems in the lines of sight, which can contain dust that only contributes to the extinction derived from the SED fit (Ellison et al., 2006; Ménard & Fukugita, 2012). In addition, we note that the depletion-derived A_V only probes non-carbonaceous dust, for example, silicates or iron-rich grains, because it is based on the measurements of several metals, but not C. One possibility is therefore also that the $z > 4$ systems contain more C-rich dust, such as amorphous carbons or Polycyclic Aromatic Hydrocarbons (PAH). At $z > 4$, cosmic effects may importantly affect the dust composition, because of the less amount of heavy metals in the diffuse ISM which would increase the significance of C-rich molecular clouds as dust sources (Heintz et al., 2019, in prep.). Also, there is less cosmic time for the build up of dust grains, potentially making SNe more important dust producers at high redshift (Todini & Ferrara, 2001; Vladilo et al., 2018).

Data points that fall above the line of equality, that is sight-lines for which the depletion derived value is higher, could be the result of additional uncertainties coming from SED fitting; that is from the choice of extinction laws and whether the SED is fitted with a simple or broken power law (see also the discussion in Wiseman, Schady et al., 2017). Due to these reasons, and also because the A_V (SED) values are collected from different

works and are thus not derived as consistently as the A_V (depl.) values in this work, we believe that the latter is a better estimate for the GRB host galaxies' line of sight, and we will therefore in the following only discuss our results in respect to A_V (depl.) where necessary.

4.3.4 Dust-corrected metallicities

In Fig. 4.8, we plot the dust-corrected metallicity [M/H] as derived from the depletion analysis versus the metallicity derived using a single line of an element X with low depletion [X/H]. As previously found by, for example, De Cia et al. (2018), we find that even Zn is slightly depleted onto dust grains, which explains that almost all of the data points fall above the line of equality. The two exception are GRB111008A and 140311, which are both at redshift $z > 4$. Looking at the depletion pattern of these two bursts, it appears that Zn is intrinsically over-abundant compared to Fe, or more likely that Mn, which is an odd-Z element known to be intrinsically under-abundant in QSO-DLAs, is pulling the fit down.

On average, the dust-corrected metallicities are with $\overline{[\mathrm{M/H}]} = -1.09 \pm 0.50$ on about 0.2 dex higher than those derived from Zn or S ($\overline{[\mathrm{X/H}]} = -1.27 \pm 0.37$), but also have larger errors. Nevertheless, since dust corrections were not applied to the QSO-DLA samples we want to compare our GRB-DLAs against, we will for the further analysis only use [X/H], but keep in mind that the actual metallicities might be slightly higher.

4.3.5 Molecular hydrogen

The Lyman and Werner absorption lines of molecular hydrogen, although numerous, are relatively hard to detect in the spectra of GRBs and QSOs, because they fall at rest frame wavelengths $\lambda < 1150$ Å, in the Lyman-α forest, where the spectrum is speckled with random absorption lines with column densities of $\log N(\mathrm{H\,I}) \lesssim 17$ (e.g., Kim et al., 2002). The number of these forest lines usually increases with redshift, and in case of additional absorption from dust in the GRB host galaxy or the Milky Way, the flux is additionally suppressed, especially at these blue wavelengths.

We therefore searched for absorption from molecular hydrogen by creating synthetic spectra with H_2 absorption lines for different column densities $N(H_2)$ and around different redshifts known from the low-ionisation lines and compared them with the normalized GRB spectra in both wavelength and velocity space. In the case of the comparison in velocity space, we plotted the strongest absorption lines on top of each other in order to look for coincidences. Following this method, we confirm the presence of molecular hydrogen lines in the previously known spectra, GRB120327A, 120815A, and 121024A (Krühler et al., 2013; D'Elia et al., 2014; Friis et al., 2015). Additionally, we find conclusive evidence for absorption from H_2 in three more systems, which are GRB120909A, 141109A, and 150403A. For these six systems, we identified the most constraining lines in the rotational levels $J = 0$, 1, and 2, where most of the H_2 is expected, and fit them simultaneously. In cases where the observed velocity width of the H_2 absorption lines is close to the instrumental resolution, we decided to measure the column density for both,

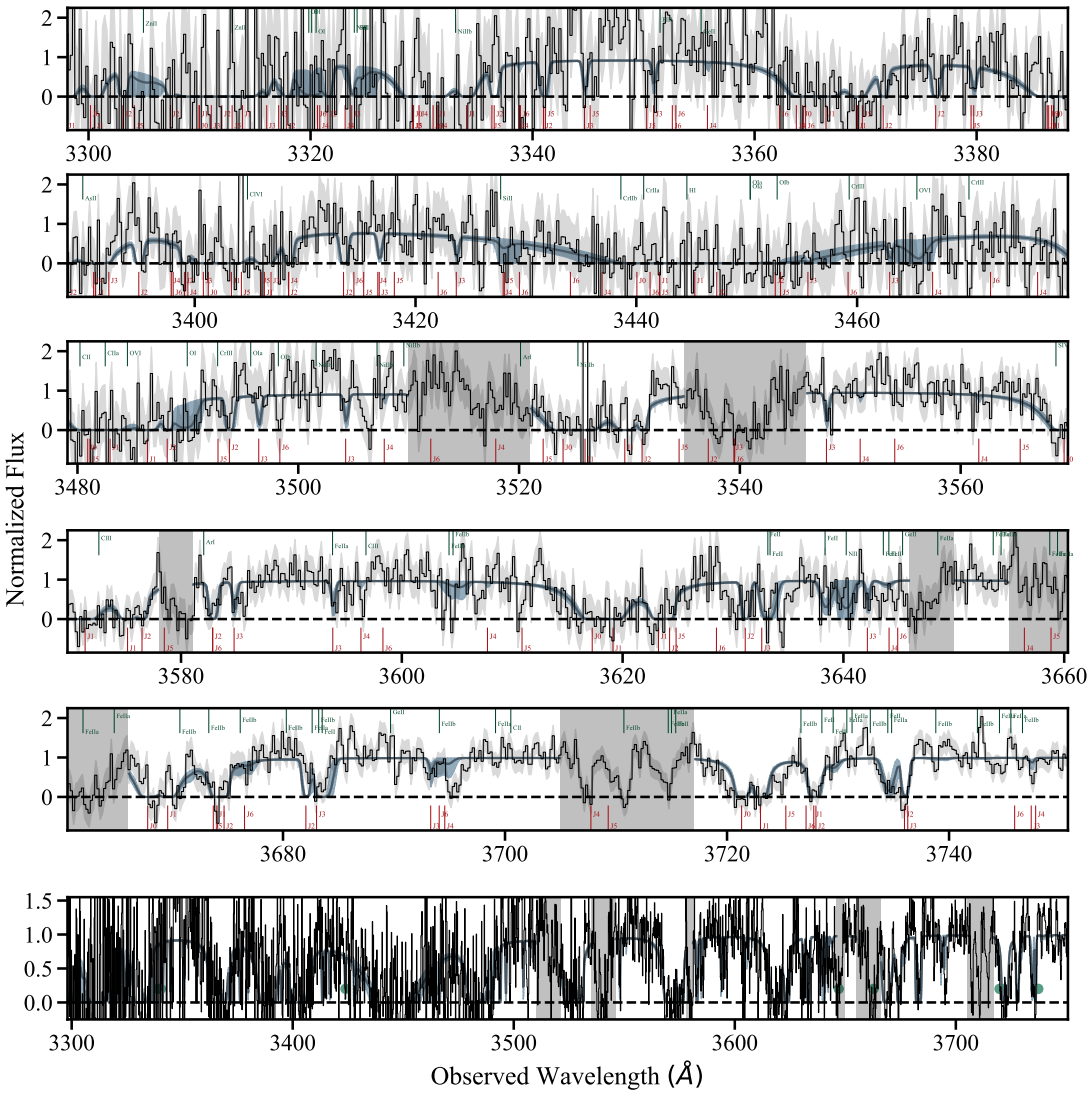

Figure 4.9: X-shooter spectrum of GRB120815A covering the Lyman and Werner absorption lines of molecular hydrogen. The best fit model is indicated by the solid blue lines and the corresponding 3-σ confidence intervals by the blue shaded regions. Gray shaded regions were ignored for the fit. The green circles in the bottom panel indicate the position of telluric lines.

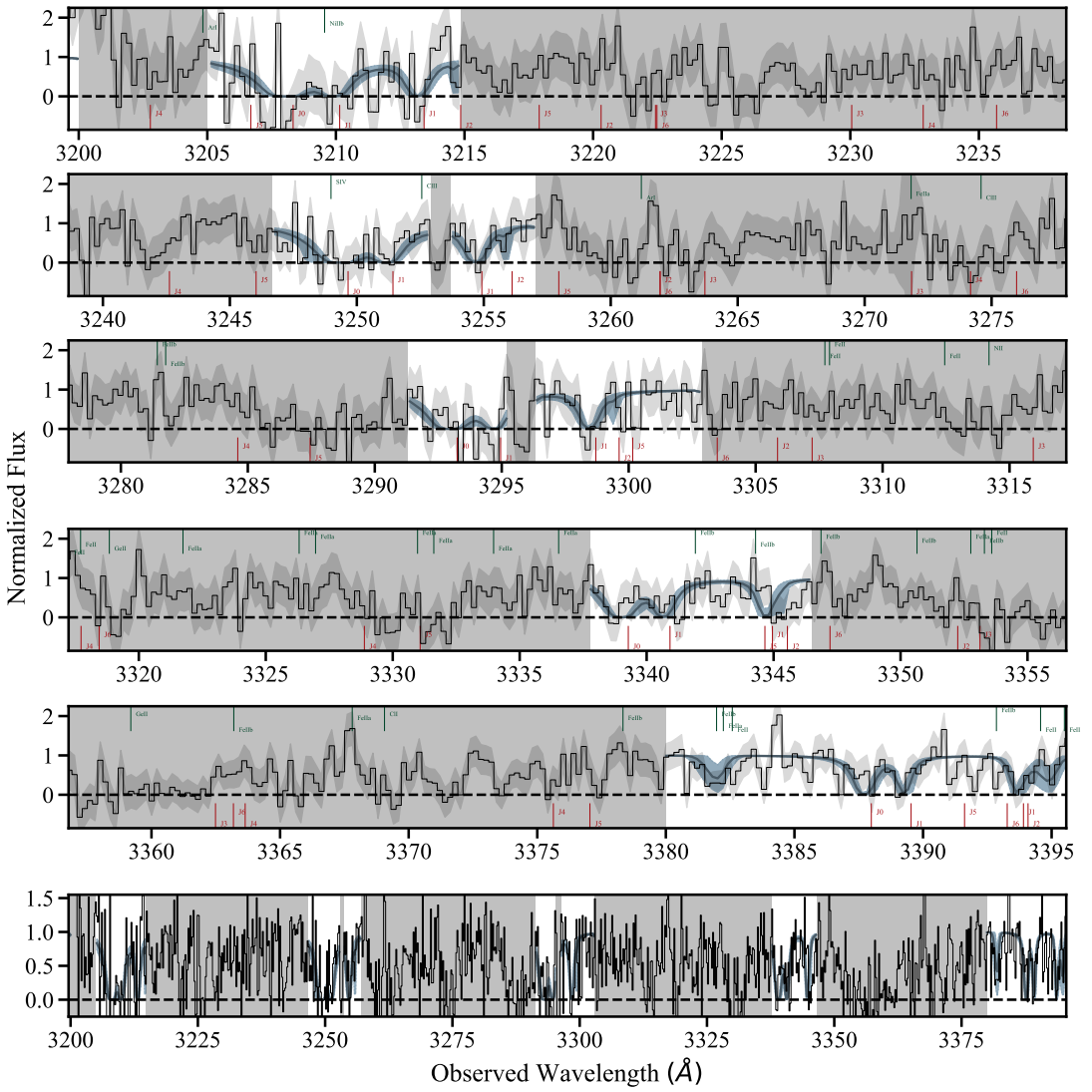

Figure 4.10: X-shooter spectrum of GRB150403A covering the Lyman and Werner absorption lines of molecular hydrogen. The best fit model is indicated by the solid blue line and the corresponding 3-σ confidence intervals by the blue shaded regions. Gray shaded regions were ignored for the fit.

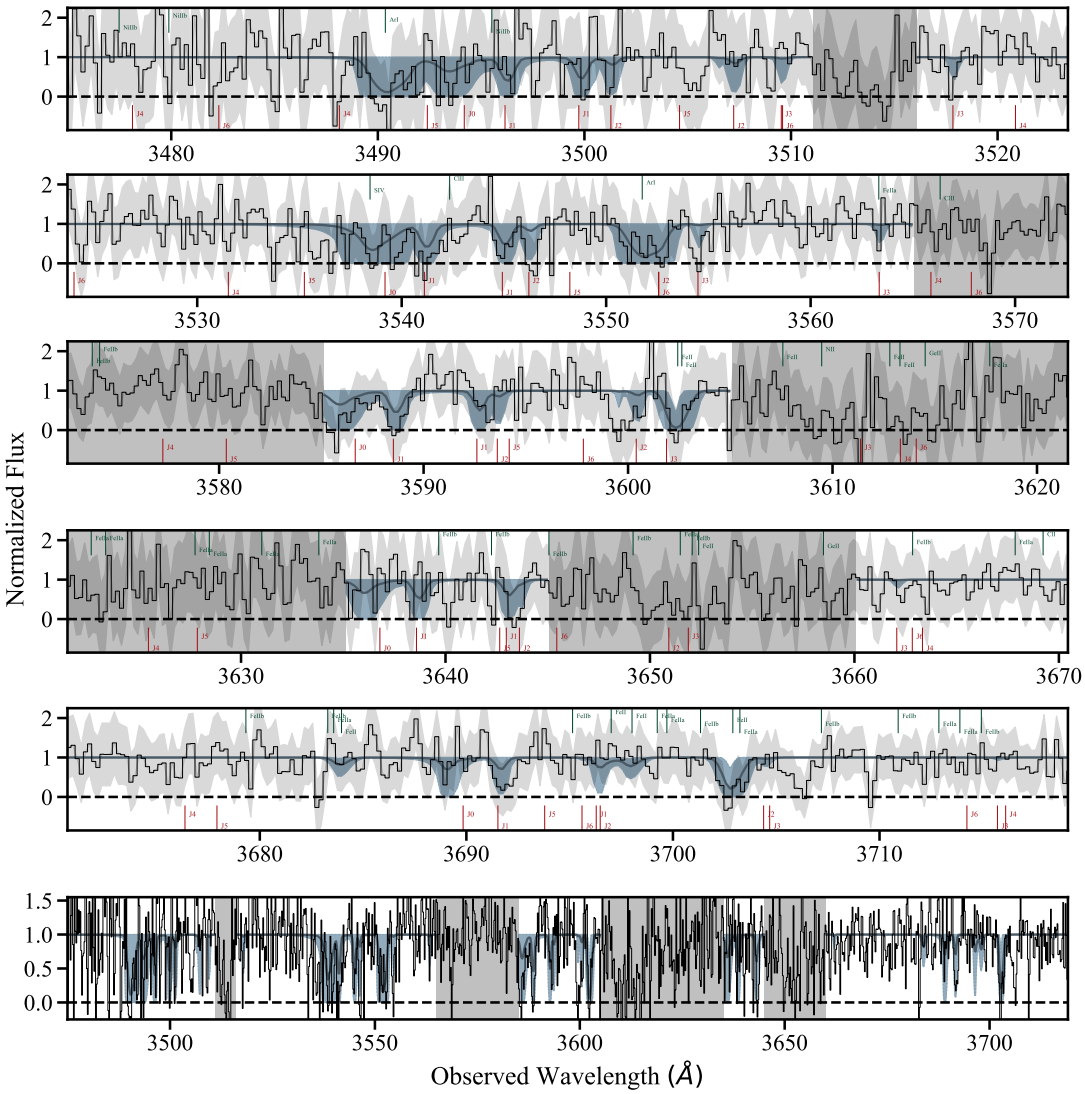

Figure 4.11: X-shooter spectrum of GRB151021A covering the Lyman and Werner absorption lines of molecular hydrogen. The best fit model is indicated by the solid blue lines and the corresponding 3-σ confidence intervals by the blue shaded regions. Gray shaded regions were ignored for the fit.

a fixed broadening parameter of $b = 2$ km/s and $b = 10$ km/s, in order to determine a realistic range for the total H_2 column density. This is the case for four GRBs, namely GRB120327A, 120909A, 121024A, and 141109A. For GRB121024A the total molecular hydrogen column density remains unchanged regardless of the broadening parameter assumed, but for the other three burst the total molecular hydrogen column density is about $\Delta \log N(H_2) \sim 2$ higher for $b = 2$ km/s. However, for the following analysis, we will adopt the column densities measured for $b = 2$ km/s, which is a more realistic value, given the temperatures of molecular gas. For the other two GRBs, 120815A and 150403A, because the lines are saturated, we are able to fit a large part of the spectrum with all rotational levels simultaneously and by including other blending lines from, for example, Fe II as well (see Fig. 4.9 and 4.10).

Most of the other spectra do not show convincing evidence for absorption from molecular hydrogen. Some, however, are still consistent with relatively high column densities, but can only be labeled as possible detections, mostly because of poor S/N or a strong Lyman-α forest. This is the case for three GRBs, namely GRB151021A, 160203A, and 170202A. In Fig. 4.11, we show part of the spectrum of GRB151021A, demonstrating the difficulty in claiming a detection of H_2.

In these three cases and for the rest of the bursts for which we do not find any convincing evidence for absorption from molecular hydrogen in the spectra, we determine upper limits for the total molecular hydrogen column density with the following steps. First, we identify the three most constraining lines for the rotational levels $J = 0$, 1, and 2, fit them simultaneously, and determine the upper limits as we did for metals lines and as described in Sect. 4.2. We then use these upper limits to create a synthetic spectrum, which we plot over the whole range of covered H_2 lines in order to check if the determined upper limits are consistent with the rest of the spectrum. For some of the bursts we were not able to find regions of the spectrum where a proper fit is possible, mostly because the S/N is relatively poor, or the spectrum is covered with too many forest lines. In this case we create synthetic spectra with H_2 absorption lines at the position of the strongest component of the metal lines, and increase the column density until the synthetic spectrum is not consistent with the data anymore (e.g., the right panels in Fig. 4.30). We here also assume a broadening parameter of $b = 2$ km/s as a conservative value, and find upper limits that are, depending on S/N, spectral coverage, and instrumental resolution, more or less constraining.

We note that we do not detect H_2 in the 6 GRB-DLAs at $z > 4$. However, the upper limits for most of them are not very constraining due to the strong Lyman-α forest. Especially for GRB130606A, the forest is so strong that it is impossible to rule out that there is no absorption from molecular hydrogen. For this reason, the bursts at $z > 4$ are labeled separately in some plots. Additionally, Lyman blanketing strongly affects the reliability of the measurements for the GRBs at reshift $z > 4$. So far, H_2 has only been detected in one QSO-DLA at redshift $z > 4$ (Ledoux et al., 2006). GRB120909A is the H_2-bearing GRB-DLA with the highest redshift ($z = 3.929$) found to date.

The results of our search for H_2 are listed in Table 4.4, which is divided into three

parts: the six detections, the three tentative detections, and the rest of the bursts for which we do not find any convincing evidence for absorption from molecular hydrogen.

During our analysis, we found that some of the oscillator strength values for molecular hydrogen that we took from the compilation of Malec et al. (2010) are wrong, most likely due to a missing factor coming from the statistical weights. [7] We thus calculated the correct values following Morton (2003) and created a new data file which is available under the following link: `https://doi.org/10.5281/zenodo.1442558`. While the values for the oscillator strength f and the damping constant Γ, are still better than anything that can be currently measured, the wavelength or frequency positions are taken from the most recent lab experiments (Bailly et al., 2010, see their tables 11 & 12).

4.3.6 Vibrationally-excited molecular hydrogen

The UV radiation from the GRB afterglow can theoretically pump any foreground H_2 into its vibrationally-excited levels that absorb at rest frame wavelengths $\lambda < 1650$ Å. For the six H_2-bearing DLAs, as well as for the three tentative detections of H_2 and the bursts at $z > 4$, we thus additionally searched for vibrationally-excited molecular hydrogen H_2^* by cross-correlating the observed spectra with the theoretical model from Draine (2000) and Draine & Hao (2002), as was done before for GRB120815A in Krühler et al. (2013) and for GRB121024A in Friis et al. (2015).[8] We confirm the detection in GRB120815A and also find tentative evidence for vibrationally excited molecular hydrogen in the spectrum of GRB150403A (see Fig. 4.12). For GRB121024A, we confirm the non-detection and we also find no evidence for H_2^* in 120327A, 120909A, 141109A, GRB151021A, 160203A, and 170202A. In the case of the six GRB at $z > 4$, we also find no convincing evidence for absorption from H_2^*.

4.3.7 Carbon monoxide

We do not find evidence for carbon monoxide absorption lines in any of the 22 GRB spectra. CO, which is primarily formed in the presence of H_2, was previously detected in the H_2-bearing DLA of GRB080607 (Prochaska et al., 2009) and various H_2-bearing QSO-DLAs (e.g., Srianand et al., 2008; Noterdaeme et al., 2010, 2018). However, the presence of molecular hydrogen seems not to be a sufficient condition for the presence of CO (Noterdaeme, Srianand et al., 2015). To determine upper limits for the CO column density for the six H_2-bearing GRB-DLAs in our sample, we fitted the six strongest CO AX bandheads (CO AX(0-0) to CO AX(5-0)) simultaneously, under the conservative assumption that $b = 2.0$ km/s. The resulting upper limits and also the corresponding upper limits for the $N(\mathrm{CO})$ to $N(H_2)$ ratio are listed in Table 4.2. The upper limits on the $N(\mathrm{CO})/N(H_2)$ ratio range from $< 10^{-2.1}$ to $< 10^{-5.5}$ and are consistent with values found for diffuse molecular clouds, or translucent clouds, which are in the transition region between diffuse and dark (Burgh et al., 2010). This is further supported by the

[7] See also the recently published paper by Ubachs et al. (2019).
[8] H_2^* was first detected by Sheffer et al. (2009) in GRB080607.

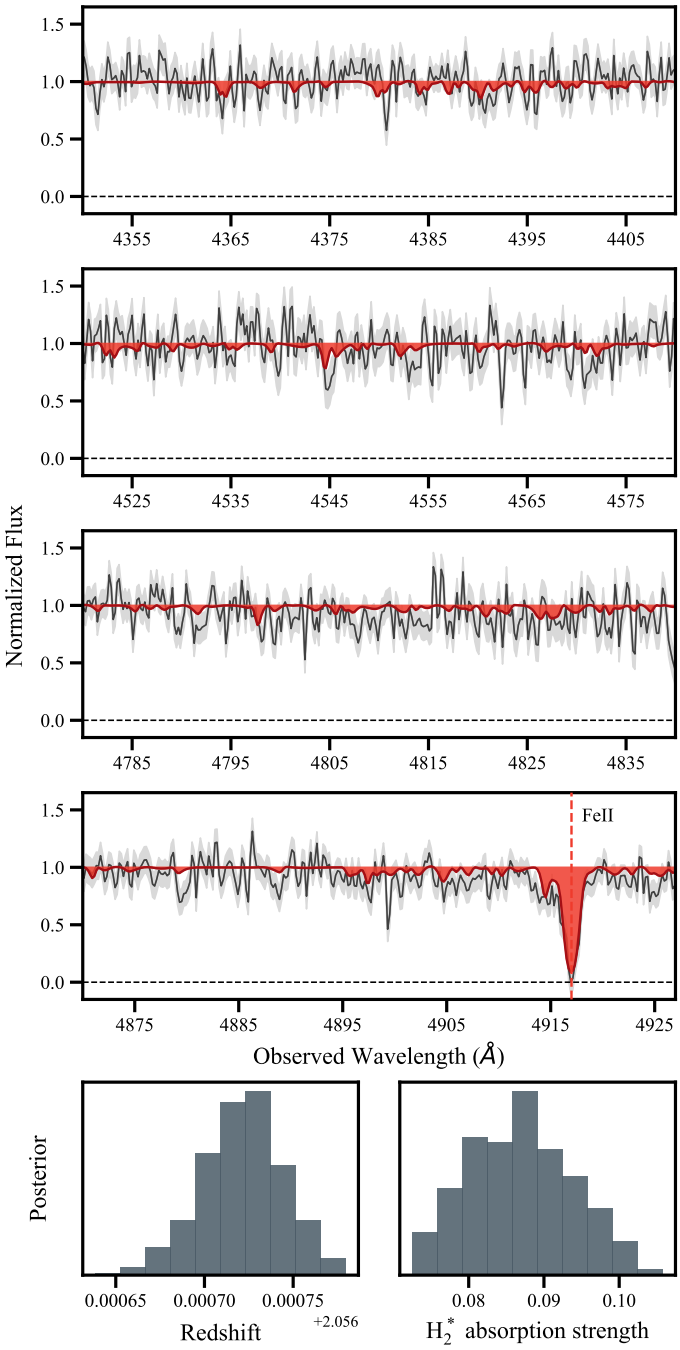

Figure 4.12: Normalized spectrum of GRB150403A showing tentative evidence for absorption from vibrationally-excited molecular hydrogen H_2^*. The model is indicated by the solid red line. In the insets at the bottom we show the posterior distribution of the redshift z and the H_2^* absorption strength from the Draine & Hao (2002) model that we fitted to the data. An intervening absorption line from Fe II is indicated by the dashed orange line.

Table 4.2: Upper limits on the CO column density in the six H_2 bearing GRB DLAs as well as the $N(CO)/N(H_2)$ ratios. Also listed are the values for GRB 080607 as taken from Prochaska et al. (2009).

GRB yymmdd#	log $N(CO)$ AX(0-0) to (5-0)	$N(CO)/N(H_2)$
120327A	< 15.3	$< 10^{-2.1}$
120815A	< 15.0	$< 10^{-5.4}$
120909A	< 14.2	$< 10^{-3.2}$
121024A	< 14.4	$< 10^{-5.5}$
141109A	< 15.9	$< 10^{-2.1}$
150403A	< 14.9	$< 10^{-5.0}$
080607	16.5 ± 0.3	$\sim 10^{-4.7}$

Notes. The CO upper limits (3-σ) were determined assuming $b = 2.0$ km/s as a conservative value. In case of GRB120327A, 120909A and 141109A, the $N(CO)/N(H_2)$ ratio was determined taking the H_2 column densities measured for $b = 2.0$ km/s as given in Tab. 4.4.

relatively low extinction on the line-of-sight to the GRBs in our sample (A_V (depl.) < 1.5 mag).

4.3.8 Overall results

To summarize our results, we analysed X-shooter spectra of 22 GRB afterglows in order to derive the column densities of 10 different metal species as well as those of neutral atomic and molecular hydrogen in each GRB host galaxies line of sight (see Table 4.3 and 4.4). By using these measurements we derive the elements relative abundances [X/H] and further analyse their depletion pattern in order to infer dust-corrected metallicities [M/H], the dust-to-metals ratio $\mathcal{DTM}$, and the expected host intrinsic visual extinction A_V (depl.). Additionally, we collected the visual extinction as derived from SED fits A_V (SED), compared it with A_V (depl.), and argued that the latter provides the better estimate. We also calculate the depletion factor [Y/Fe] as another tracer of dust. Finally, given the column densities or their derived upper limits of molecular hydrogen, we calculate the molecular gas fraction $f(H_2) = 2N(H_2)/(2N(H_2)+N(H\,I))$. The complete data set is presented in Table 4.5 and in Fig. 4.13 we show pairwise scatter plots and histograms of the most important properties. By color and symbol, we differentiate between four different cases: (1) Detections and (2) possible detections of absorption from molecular hydrogen as well as non-detections for (3) GRBs at redshift $z < 4$ and the non-detections for (4) GRBs at redshift $z > 4$.

The mean neutral hydrogen column density for the GRB-DLAs in our sample is $\log \overline{N(H\,I)} = 21.50 \pm 0.67$, and the individual values range from $\log N(H\,I) = 19.88 \pm 0.01$ (GRB130606, the only sub-DLA) to $\log N(H\,I) = 22.39 \pm 0.01$ for GRB111008A, which is among the highest values observed to date (Prochaska et al., 2009; Sparre et al., 2014; Noterdaeme, Srianand et al., 2015). DLAs with such high column densities are expected

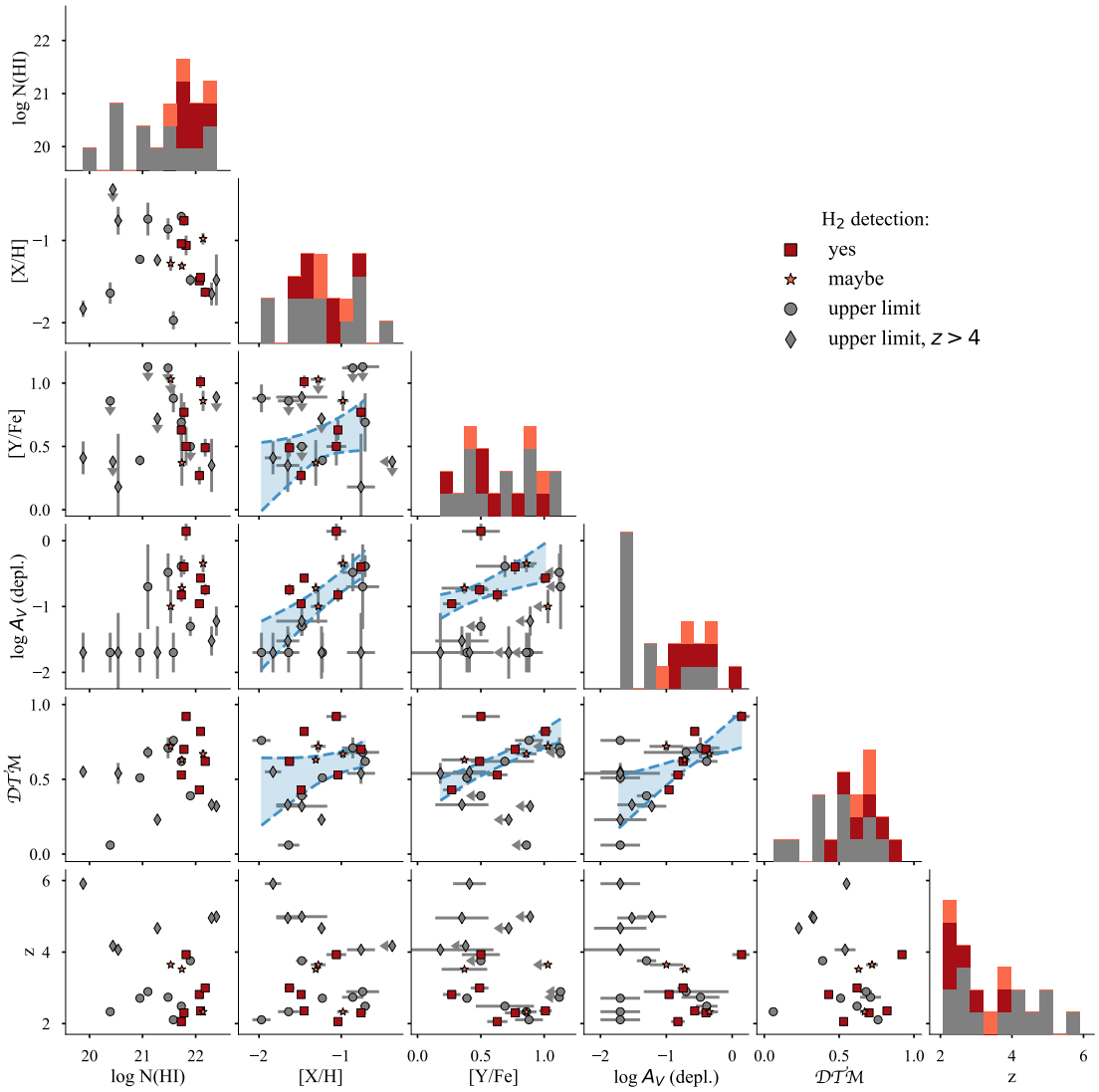

Figure 4.13: Pairwise scatter plots and histograms of the most important properties of our sample of 22 GRB-DLAs at $z > 2$. In case absorption from molecular hydrogen is detected, the data points are squares colored in red. Possible detections are indicated by orange stars, and upper limits are gray diamonds in case of DLAs at $z > 4$ and circles otherwise. In blue, we show the results of a Baysian linear-regression analysis as described in Sect. 4.4..

to be very rare, because at $\log N(\mathrm{H\,I}) > 21.5$ the conversion from H I to H_2 effectively steepens the column density distribution (Schaye, 2001; Altay et al., 2011).

On average, the 22 GRB-DLAs have a metallicity of $\overline{[\mathrm{X/H}]} = -1.27 \pm 0.37$, which is comparable to metallicities found for QSO-ESDLAs (Noterdaeme, Petitjean & Srianand, 2015). The average metallicity of the GRB-DLAs at $z > 4$ is $\overline{[\mathrm{X/H}]} = -1.39 \pm 0.42$, which is slightly lower than the mean metallicity for the bursts at redshift $2 < z < 4$ ($\overline{[\mathrm{X/H}]} = -1.23 \pm 0.37$). This is in accordance with the results from Rafelski et al. (2012) and De Cia et al. (2018), that DLA metallicities decrease by a factor of 50-100 from redshift $z = 0$ to $z = 5$.

Interestingly we find that, while H_2 is detected over almost the whole range of covered metallicities [X/H], all detections and possible detections of molecular hydrogen are for DLAs with neutral hydrogen column densities larger than $\log N(\mathrm{H\,I}) > 21.7$. However, not all GRB-DLAs with $\log N(\mathrm{H\,I}) > 21.7$ show absorption from H_2. Also, as indicated by the dashed blue lines, which are the result of a Bayesian linear regression as described in Sect. 4.4, we find positive correlations for [Y/Fe] and log A_V (depl.) versus metallicity, as well as for $\mathcal{DTM}$ versus depletion [Y/Fe] and log A_V (depl.). A weak correlation is also found for $\mathcal{DTM}$ versus metallicity, which is, however, not as tight as the one determined by Wiseman, Schady et al. (2017). Also, all H_2-bearing systems have dust-to-metals ratios larger than $\mathcal{DTM} > 0.4$ and significant line-of-sight dust columns (A_V (depl.) > 0.1 mag). See also Fig. 4.7, which shows that for all H_2-bearing GRB-DLAs as well as the tentative detections A_V (depl.) is higher than A_V (SED), indicating that the phase of the (high redshift) ISM that is amenable to H_2 formation might have a different dust composition or grain sizes. Furthermore, we do not find any evidence for absorption of CO in any of the spectra. And finally, we confirm the detection of vibrationally excited H_2^* in GRB120815A and additionally find tentative evidence for H_2^* in GRB150403A.

4.4 Discussion

The two main questions we seek to address in this Chapter are: (1) is there a lack of H_2-bearing GRB-DLAs and, if so, why, and (2) how do GRB-DLAs compare to QSO-DLAs?

4.4.1 H_2 detection fraction in GRB-DLAs

To answer the first question: there is no lack of H_2-bearing GRB-DLAs. We here find evidence for absorption from H_2 in 6/22 (27%) of our GRB spectra, or even 9/22 (41%) when including the tentative detections. When selecting GRB-DLAs at redshifts $2 < z < 4$ and with large neutral hydrogen column densities, $\log N(\mathrm{H\,I}) > 21.7$, the H_2 detection fraction increases to 6/10 (60%), or 8/10 (80%), respectively. We want to stress that, although this is the first time a systematic search for H_2 has been carried out in such a large sample of 22 GRB-DLAs, we are probably still biased against dusty sight-lines ($A_V > 0.5$ mag). Since the production of molecular hydrogen is enabled by its formation onto dust grains, and because dust and H I provide shielding against H_2

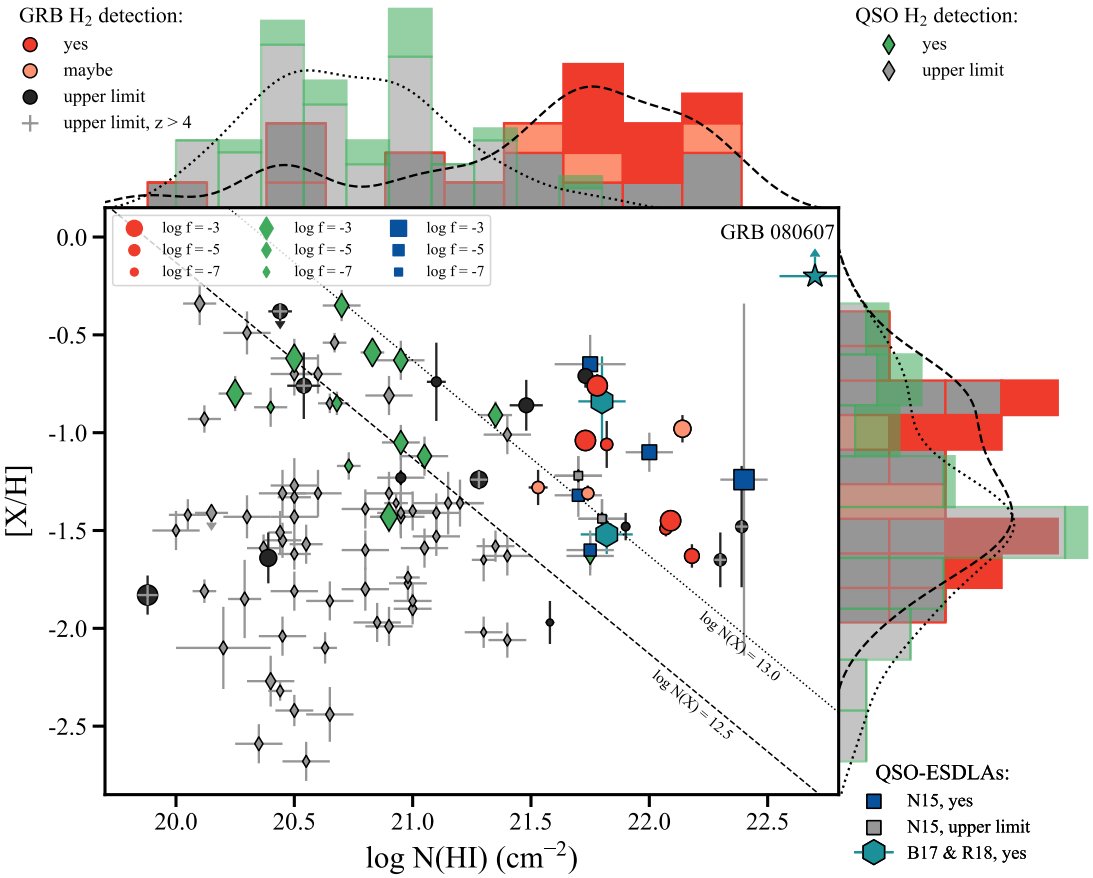

Figure 4.14: Metallicity versus neutral atomic-hydrogen column density for the GRB-DLAs in our sample and the QSO-DLAs from Noterdaeme et al. (2008) and Noterdaeme, Petitjean & Srianand (2015) (N15). Also shown are the two extremely-strong QSO-DLAs from Balashev et al. (2017) (B17) and Ranjan et al. (2018) (B18). When molecular hydrogen is detected, the data points are colored (GRB-DLAs in red, QSO-DLAs in green and blue, as labeled). The symbol size represents the overall molecular fraction $\log f$, and in case of a non-detection the corresponding upper limit. The GRB-DLAs at $z > 4$ are additionally marked with a cross. The dotted and dashed lines represent a constant metal column density of $\log N(\mathrm{X}) = 12.5$ and $\log N(\mathrm{X}) = 13.0$, respectively. Above and to the right of the scatter plot, we show the histograms and corresponding kernel density estimates for our GRB-DLAs and the N08 QSO-DLA sample. Systems with H_2 detections are colored as labeled.

dissociating radiation, the true fraction of H_2-bearing GRB-DLAs might be even higher than found here; also, because our upper limits on the H_2 column density are not in all cases stringent, meaning that the relatively low spectral resolution of X-shooter and sometimes a poor S/N and/or a strong Lyman-α forest blanketing make it difficult to detect the narrow absorption lines from molecular hydrogen.

The lack of H_2-bearing GRB-DLAs previously found by Ledoux et al. (2009) is consistent with our results. Indeed, from their sample of seven systems, five have neutral hydrogen column densities larger than $\log N(\mathrm{H\,I}) > 21.0$, and three have $\log N(\mathrm{H\,I}) > 21.7$. These three DLAs, however, have lower metallicities ($\overline{[\mathrm{X/H}]} < -1.5$) than the average of our 6 detections ($\overline{[\mathrm{X/H}]} = -1.24 \pm 0.33$), and also relatively low depletion factors, [Y/Fe] < 0.2, compared to the average of our H_2-bearing GRB-DLAs ($\overline{[\mathrm{Y/Fe}]} = 0.62 \pm 0.26$). Since these 7 bursts were observed at high resolution using UVES, this sample is limited to the brightest and therefore least extinguished GRBs, which explains the aforementioned differences.

Since molecular gas has a small covering fraction, one can also use neutral carbon lines as tracers of cold gas and dust (Srianand et al., 2005; Ledoux et al., 2015). Heintz et al. (2019) systematically searched for absorption from C I in a sample of GRB-DLAs similar to ours. They find conclusive or tentative evidence for C I in the spectra of GRB120815A, 121024A, and 150403A, which are three out of the six H_2-bearing systems we found[9]. We note that C I is not detected in the H_2-bearing system on the line-of-sight toward GRB141109A and in neither of our three possible detections (151021A, 160203A, and 170202A). GRB120909A did not enter their sample because the C I lines are blended with tellurics. Heintz et al. (2019) found a fraction of 25% of C I-detected GRB-DLAs, or 46% for DLAs with $\log N(\mathrm{H\,I}) > 21.7$. This is lower than our H_2-detection fraction for systems with $\log N(\mathrm{H\,I}) > 21.7$, which is likely a consequence of the relatively low metallicities, which make it difficult to detect C I. For example, the DLA toward GRB141109A is, with [X/H] ~ -1.6, one of the most metal-poor absorbers in the sample.

Finally, that we do not find a lack of H_2-bearing GRB-DLAs is also in agreement with the recent results from Arabsalmani, Le Floc'h et al. (2018), who report the detection of a molecular-gas-rich GRB host galaxy at $z = 2.086$ based on the observation of CO emission lines. They showed that the GRB hosts with measured molecular gas mass are quite normal in terms of gas content when compared to the general population, and suggested that there is no sign of molecular gas deficiency, at variance with results based on low-redshift GRB hosts (Hatsukade et al., 2014; Stanway et al., 2015; Michałowski et al., 2016).

4.4.2 Comparison of GRB- with QSO-DLA properties

The fraction of H_2-bearing systems in the general QSO-DLA population is only about 10% or less (Ledoux et al., 2003; Noterdaeme et al., 2008; Balashev et al., 2014; Jorgenson

[9] Heintz et al. (2019) also found C I in the spectra of GRB120119A and 180325A. GRB120119A is not part of our sample because of its lower redshift ($z \sim 1.73$). GRB180325A, at $z = 2.248$, is not included in the present study either, because it is not in the complete sample presented in Selsing et al. (2018). In addition, its high visual extinction prevents the search for H_2.

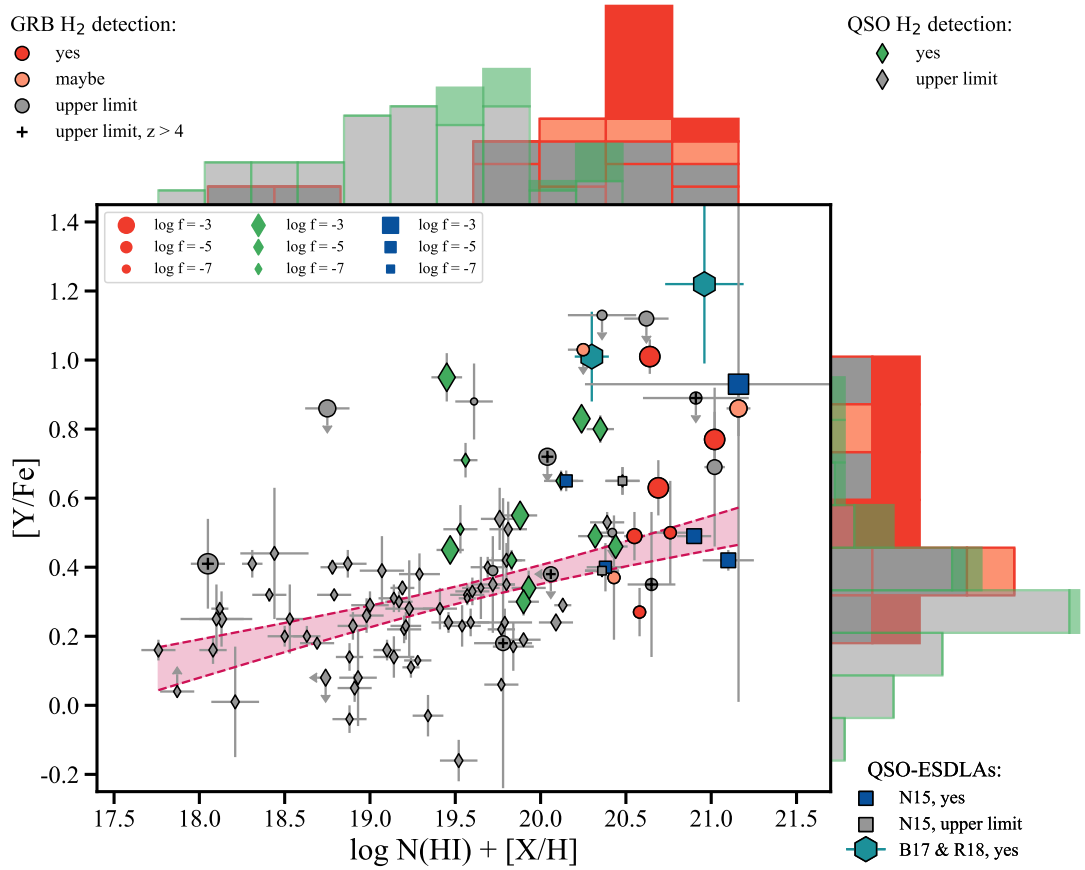

Figure 4.15: Depletion factor, [Y/Fe], versus metal column density, $\log N(\mathrm{H\,I}) + [\mathrm{X/H}]$, for the GRB-DLAs in our sample and the QSO-DLAs from Noterdaeme et al. (2008) and Noterdaeme, Petitjean & Srianand (2015) (N15). Also shown are the two QSO-ESDLAs from Balashev et al. (2017) (B17) and Ranjan et al. (2018) (B18). When molecular hydrogen is detected, the data points are colored (GRB-DLAs in red, QSO-DLAs in green and blue, as labeled). The symbol size represents the overall molecular fraction $\log f$, and in case of a non-detection the corresponding upper limit. The GRB-DLAs at $z > 4$ are additionally marked with a cross. The solid and dashed lines indicate the best-fit linear model and corresponding 3σ errors. Above and to the right of the scatter plot, we also show the histograms for our GRB-DLAs and the N08 QSO-DLA sample. Again, systems with H_2 detections are colored as labeled. Upper limits are not included in the histograms.

et al., 2014; Balashev & Noterdaeme, 2018). This is about three to four times lower than what we found for GRB-DLAs. However, one should be cautious when comparing GRB- and QSO-DLA properties. In Fig. 4.14, we plot the metallicity, [X/H], versus neutral hydrogen column density for the GRB-DLAs in our sample as well as for the QSO-DLAs from Noterdaeme et al. (2008) (N08) and Noterdaeme, Petitjean & Srianand (2015) (N15). Additionally, we plot two QSO-ESDLAs from Balashev et al. (2017) (B17) and Ranjan et al. (2018) (R18). The histograms over metallicity for our GRB sample and for the QSO sample from N08 show that both GRB- and QSO-DLAs cover more or less the same range of metallicities, the only difference residing in the tail at lower metallicities which is covered by QSO-DLAs. However, looking at the histograms over $\log N(\mathrm{H\,I})$ reveals that we are likely dealing with different populations: GRBs generally tend to probe DLAs with higher neutral hydrogen column densities, $\log N(\mathrm{H\,I}) > 21.5$, with an average of $\log \overline{N(\mathrm{H\,I})} = 21.50 \pm 0.67$, while most QSO-DLAs have $\log N(\mathrm{H\,I}) < 21.5$ and $\log \overline{N(\mathrm{H\,I})} = 20.75 \pm 0.41$.

Concerning both the GRB- and QSO-DLAs bearing H_2, all of them are found at metallicities $[\mathrm{X/H}] \gtrsim -1.7$. However, only H_2-bearing QSO-DLAs are found below $\log N(\mathrm{H\,I}) < 21.7$. When considering DLAs at redshifts $2 < z < 4$ and with large neutral hydrogen column densities, $\log N(\mathrm{H\,I}) > 21.7$, the H_2-detection fraction among QSO-DLAs is essentially the same as that of GRB-DLAs, that is 7/9 (78%) of the QSO-DLAs bear H_2 (Noterdaeme, Srianand et al., 2015; Noterdaeme, Petitjean & Srianand, 2015). The majority of H_2-bearing GRB- and QSO-DLAs is found at metal columns $\log N(\mathrm{X}) > 12.5$, and $\log N(\mathrm{X}) > 13.0$ for $\log N(\mathrm{H\,I}) > 21.5$, as indicated in Fig. 4.14 by the dashed and dotted lines, respectively. This means that at higher H I column densities a lower metallicity is required to have the same metal column, and thus amount of dust, which needs a cold and dense environment but also a high cross-section of metals to form. Also, as previously shown by De Cia et al. (2016) and Wiseman, Schady et al. (2017), we find that the $\mathcal{DTM}$ increases with metallicity and that all H_2 bearing GRB-DLAs have $\mathcal{DTM}$ ratios higher than 0.4, supporting the importance of grain growth for the production of dust and molecules.

A natural explanation for the higher fraction of H_2-bearing systems in our 22 GRB-DLAs compared to the general population of QSO-DLAs, and the similar detection fractions at high $N(\mathrm{H\,I})$ column densities, is the impact parameter (Arabsalmani et al., 2015). While higher H I and metal column densities are on average related to absorbing cold neutral gas within a galaxy, low column densities likely trace cool, circumgalactic environments (Pontzen et al., 2008; Prochaska et al., 2011; Noterdaeme, Srianand et al., 2015). As randomly-distributed background sources, QSOs probe a wide range of impact parameters and therefore H I and metal column densities. GRBs, on the other hand, are usually found to originate from the central and/or brighter regions of their host galaxies (Fruchter et al., 2006; Lyman et al., 2017), where they are in most cases located behind relatively large column densities (Fynbo et al., 2009; Selsing et al., 2018).

Theoretical models predict that the $N(\mathrm{H\,I})$ threshold for the conversion from atomic to molecular hydrogen increases with decreasing metallicity (Savage et al., 1977; McKee & Krumholz, 2010; Sternberg et al., 2014). This is because systems with higher metallicities

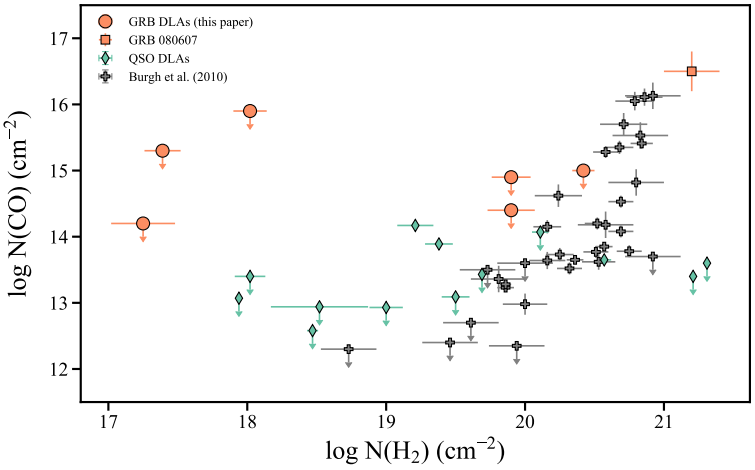

Figure 4.16: CO versus H_2 column densities for the H_2-bearing GRB-DLAs presented in this Chapter compared to the H_2-bearing QSO-DLAs from Balashev et al. (2017); Noterdaeme et al. (2018); Ranjan et al. (2018). Additionally, we plot the results from Burgh et al. (2010) for sight-lines through diffuse and translucent clouds in the Galaxy and the result from Prochaska et al. (2009) for the DLA toward GRB080607.

usually contain more dust (see Fig. 4.15), which provides shielding against UV radiation and enables the production of molecular hydrogen. This explains why the H_2-bearing QSO-DLAs from the sample of N08 at $\log N(\mathrm{H\,I}) \lesssim 21.0$ have relatively high metallicities ($[\mathrm{X/H}] \gtrsim -1.2$; with only one exception) and fall in a region that is barely probed by our GRB-DLAs. Only two GRBs fall in that regime, 120712A and 151027B, which are both at redshift $z > 4$ where H_2 is hard to detect. Therefore, and also due to low number statistics in this regime, it is not surprising that we do not detect any H_2-bearing GRB-DLAs with $\log N(\mathrm{H\,I}) < 21.0$. We note that for the intermediate regime with $21.0 < \log N(\mathrm{H\,I}) < 21.5$ and $[\mathrm{X/H}] > -1.5$ the number statistics is very low for both the GRB- and QSO-DLAs and that it will be interesting to select a sample of DLAs in that region for future studies.

The impact parameter also has an effect on the metallicity distribution of DLAs, that is predicted to cluster between $[\mathrm{X/H}] = -1.5$ and -1 (Cen, 2012), which is true for our sample of 22 GRB-DLAs and also for the QSO-DLA sample from N08. The overall metallicity should floor at $[\mathrm{X/H}] \sim -3$ at $z = 1.6 - 4$, which is what we see as a tail of low metallicities covered by QSO-DLAs. These systems with $[\mathrm{X/H}] < -1.7$ are likely associated with the cold gas outside the galactic disk or halo, where the metallicity is low and little star formation takes place. GRBs, again, generally tend to probe the inner, star-forming regions of their host galaxies, where the metallicity is expected to be higher ($[\mathrm{X/H}] > -1.7$) (e.g., Belfiore et al., 2017; Sánchez-Menguiano et al., 2018).

As mentioned earlier, DLAs with higher metal columns usually contain more dust. This is evident from Fig. 4.15, which is similar to Fig. 4.14, but this time we plot the dust depletion factor, [Y/Fe], versus metal column density $\log N(\mathrm{H\,I}) + [\mathrm{X/H}]$. One can see that H_2-bearing DLAs are exclusively found at $[\mathrm{Y/Fe}] \gtrsim 0.2$ and $\log N(\mathrm{H\,I}) + [\mathrm{X/H}]$

$\gtrsim 19.5$. Also, the molecular fraction f and the fraction of H_2-bearing DLAs increase with the dust depletion factor and metal column density. At metal column densities larger than $\log N(\mathrm{H\,I}) + [\mathrm{X/H}] > 20.0$ and redshifts $2 < z < 4$, we detect H_2 in six of 13 (46%) systems, or nine of 13 (69%) systems when including the tentative detections. For the QSO-DLAs from N08, this fraction is 4/9 (44%) and for the QSO-ESDLAs from N15 it is 5/7 (71%). So, also when selecting GRB- and QSO-DLAs based on metal column densities, the fraction of H_2-bearing systems are similar.

Additionally, looking at the data points from both QSO- and GRB-DLAs, one can see that the dust depletion increases with increasing metal column density. The red line indicates the best linear fit and the dashed lines the corresponding 3-σ confidence intervals. The fit was performed with a Bayesian linear regression and the posteriors on slope and intercept were computed using PyMC. To account for outliers, we use a Cauchy distribution as likelihood function. For the slope and intercept, we use normal priors centered on the best estimates from a simple first fit using `scipy.stats.linregress`. Upper limits were not included in the fit. It is interesting to note that almost all the DLAs that fall as outliers above this trend are strong H_2-bearing systems. This is likely a result of the dust production that is enabled and the shielding provided by dust in those systems, which protects H_2 from being photo-dissociated by Lyman-Werner photons. Therefore, most DLAs that follow the trend supposedly trace diffuse gas in the intercloud medium, whereas the outliers above more likely indicate diffuse molecular-rich gas.

4.4.3 Nucleosynthesis signatures in the ISM

The gas-phase metal abundances [X/H] that we observe in GRB-DLAs do not directly represent the metallicity of the absorbing systems, because of dust depletion. Indeed dust depletion can dramatically lower the observed abundances, such as that it must be properly taken into account to be able to recover the real (dust-corrected) metallicity, [M/H], and any nucleosynthetic signatures in the ISM. In Sect. 4.3.2 we fit the observed abundances of several metals with the depletion patterns found in the Galaxy and QSO-DLAs by De Cia et al. (2016), and following Wiseman, Schady et al. (2017). Any deviations from this fit could in principle indicate peculiar abundances, for example, those produced by specific nucleosynthetic processes, such as α-element enhancement. As notable in Fig. 4.6, the fit to the depletion pattern is overall very good for most GRBs, with little deviations from QSO-DLAs. This is remarkable, given the different star-formation histories of galaxy counterparts of GRB- and QSO-DLAs. In particular, because of the higher star-formation rates of GRB host galaxies (e.g., Krühler et al., 2015), α-element enhancement could be expected. We only observe a tentative case of α-element enhancement for GRB121024A, with a Si overabundance of ~ 0.5 dex, but no confirmation from other α-elements such as O, Mg, Ti, nor S. On the other hand, there is a tentative ~ 0.2 overabundance of the Fe-group elements Fe and Cr, and the somewhat related Zn, but with no apparent overabundance of Ni, albeit the large error bar. Titanium is unfortunately constrained in only a few cases, because of the weakness of the Ti II absorption lines. Nevertheless, for two cases, namely GRB120327A and GRB161023A the observed Ti columns seem significantly lower than what can be

expected from the depletion patterns. In both cases, no deviations of the other α-elements are observed. One possibility is that this is indeed a peculiar underabundance of Ti. Alternatively, and perhaps more likely, this may signal that the values for Ti in the depletion patterns may be imprecise. Indeed, the depletion sequences were not characterized for DLAs for Ti and Ni, but instead their slope was extrapolated to low-metallicity systems by De Cia et al. (2016) from the Galactic values of Jenkins (2009). This might have caused a somewhat shallower slope of the depletion sequence of Ti, and thus a significant effect in the Ti depletion pattern, because Ti depletes very heavily. Quantifying this possible effect requires analyzing a large sample of QSO-DLAs and is beyond the scope of this Chapter.

4.4.4 The lack of carbon monoxide

The lack of carbon monoxide could be related to the low metallicity and/or the relatively low dust content (A_V(depl.) < 1.5 mag) of the systems, meaning that not enough oxygen and carbon are present to form CO, or not enough shielding against the photodissociating radiation is provided (Bolatto et al., 2013; Glover & Clark, 2016; Balashev et al., 2017). Alternatively, the lack of CO absorption could be the result of a geometrical effect, because CO should only reside in the inner core of the molecular cloud, where more shielding is provided. In this scenario, the GRB line-of-sight would cross through the outer edge of the cloud where only H_2 is present. In Fig. 4.16, we plot the CO versus the H_2 column densities for GRB and QSO-DLAs as well as for Galactic sight-lines. All our upper limits on the CO column density are consistent with the relation found by Burgh et al. (2010) for diffuse and translucent clouds in the Milky Way.

4.4.5 Comparison with Galactic sight-lines

In general, a comparison with Galactic sight-lines is complicated, due to the fact that QSO and GRB-DLAs do not have metallicities close to solar, but rather relatively low metallicities on the order of one tenth of solar. Also the dust-to-metal ratios are usally lower than in the Galaxy (De Cia et al., 2013, 2016; Wiseman, Schady et al., 2017), so that even for the same amount of metals, one would expect less dust and thus less molecules. Nevertheless, in Fig. 4.17, we plot the molecular fraction f versus the molecular hydrogen column density for GRB and QSO-DLAs in comparison to Galactic sight-lines. One can see that only about half of the H_2-bearing DLAs with log N(HI) > 21.7 have molecular fractions consistent with the galactic diffuse and translucent clouds from (Burgh et al., 2010). For the rest of the DLAs, the molecular fraction is much lower, which is also the case for the upper limits we could put on the non-detections. This could be a result of the generally low metallicities and low dust columns.

4.4.6 Distances and nature of the absorbing clouds

To determine the distance of the absorbing cloud to the GRB explosion site, it is necessary to observe absorption-line variability to trace the electronic populations in different

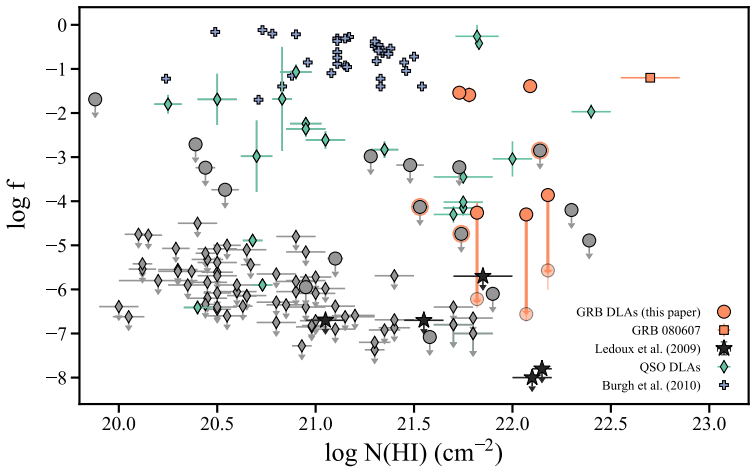

Figure 4.17: Molecular fraction versus neutral atomic-hydrogen column density for the GRB-DLAs from this Chapter and Ledoux et al. (2009); Prochaska et al. (2009) compared to QSO-DLAs (Noterdaeme et al., 2008; Noterdaeme, Petitjean & Srianand, 2015; Balashev et al., 2017; Ranjan et al., 2018) and Galactic sight-lines probing diffuse and translucent clouds (Burgh et al., 2010). H_2-bearing DLAs are plotted with colored symbols and the non-detections in gray. For GRB120327A, 120909A, and 141109A, we plot the molecular fraction for both $b = 2$ and $b = 10$ km/s.

energy levels. Such an analysis has only been possible for a handful of cases and the distances were all found to be 50 to more than several hundred parsecs (Vreeswijk et al., 2007; Ledoux et al., 2009; D'Elia et al., 2009; Vreeswijk et al., 2011; Hartoog et al., 2013). Alternatively, we could use the H_2^* detections and non-detections of our six H_2-bearing GRB-DLAs, to determine the required UV flux to populate the vibrationally-excited levels. This flux could be compared with the actual UV flux measured for the afterglow light curve in order to put a constraint or a lower limit to the distance of the absorbing cloud. Nevertheless, this exercise is beyond the scope of this Chapter, and we just note that the detection of molecular hydrogen alone, should imply a distance of at least $\gtrsim 0.5$ to 1 kpc between the GRB and the absorbing gas to avoid photo-ionization. For example, Ledoux et al. (2009) find for GRB050730 that H_2 photo-dissociation can only be effective in clouds with distances smaller than $d < 500$ pc (see their Fig. 7).

Additionally, we detect the fine-structure levels of O I, O I* and O I**, in almost all of the GRB spectra (see Fig. 4.4). These lines are commonly detected in GRB-DLAs and indicative of high densities and temperatures, and therefore add to the picture of the absorbing gas having mixed phases and being under the influence of a local radiation field, i.e., diffuse molecular clouds.

Our results are thus pointing to a picture where GRB and QSO-DLAs with very high neutral column densities ($\log N(\mathrm{H\,I}) > 21.7$) or metal column densities ($\log N(\mathrm{H\,I}) + [\mathrm{X/H}] > 20$) are associated with sight-lines passing close to the galactic center, where the gas pressure is higher (Blitz & Rosolowsky, 2006; Balashev et al., 2017), the conversion of H I to H_2 steepens the column density distribution (Altay et al., 2011; Noterdaeme et

al., 2014), and thus a higher fraction of H_2-bearing systems is expected. And, since the absorbing gas is likely located at distances of several hundred parsec from the GRB, the H_2-bearing GRB-DLAs are not associated with the star-forming regions where the GRB progenitors are born, but with diffuse molecular clouds within the host galaxy.

4.5 Summary

For the first time, we were able to use a large, less-biased sample of 22 GRBs, to perform a systematic search for molecular hydrogen in DLAs associated with GRB host galaxies, and to study the effects of metallicity and dust depletion in the diffuse interstellar medium of these galaxies at high redshift. The main results derived from our analysis can be summarized as follows:

1. There is no lack of H_2 in GRB-DLAs. We find evidence for absorption from molecular hydrogen in 6 out of 22 such systems and claim three additional tentative detections. This constitutes a fraction of 27% (41%), which is three to four times larger than in the general population of QSO-DLAs ($\leq$ 10%), but comparable to the fraction of H_2-bearing QSO-DLAs that cover the same range of neutral hydrogen column densities and redshifts, the so-called extremely-strong QSO-DLAs (ES-DLAs). Also, all H_2-bearing GRB-DLAs are found to be associated with significant dust extinction, $A_V > 0.1$ mag, and have dust-to-metals ratios $\mathcal{DTM} > 0.4$, confirming the importance of dust grains for the production of molecules.

2. Both, QSO- and GRB-DLAs, with column densities $\log N(\mathrm{H\,I}) > 21.7$ at redshifts $2 < z < 4$ appear to probe similar systems, that is sight-lines with small impact parameters that are passing close to the galactic central regions, where the gas pressure is higher and the transition of H I to H_2 is facilitated. In this range, the fraction of H_2-bearing systems is much higher and comparable in both QSO- and GRB-DLAs (60 to 80%). These systems are likely diffuse molecular clouds, which in the case of GRBs, are unrelated to the star-forming region where the explosion occurred.

3. At lower column densities ($\log N(\mathrm{H\,I}) < 21.7$), QSO-DLAs need on average a higher metallicity to contain significant amounts of molecular hydrogen. This can be explained naturally by the fact that systems with a higher metallicity contain on average more dust, which provides shielding and enables the production of H_2. Our sample of GRB-DLAs does not significantly probe low hydrogen column densities (i.e., only 22% of the sample has $\log N(\mathrm{H\,I}) < 21.0$) because GRBs are found to originate from or closer to the central regions of their host galaxies. On the other hand, as randomly distributed background sources, QSOs sample a wide range of impact parameters.

4. The actual fraction of H_2-bearing GRB-DLAs might be higher than the one we found here because our sample is probably still biased against dusty sight-lines (no

sight-line with A_V(SED) > 0.5 mag). More dust provides more shielding, adds more catalyst to aid H_2 production, and indicates an advanced grain chemistry and thus a higher chance to detect molecules. Our upper limits on the H_2 column density are also not in all cases stringent, meaning that the relatively low spectral resolution of X-shooter and sometimes a poor S/N and/or a crowded Lyman-α forest make it difficult to detect the narrow absorption lines of molecular hydrogen.

5. In the future, it will be important to expand the surveys of GRBs with prompt optical spectroscopy in order to increase sample sizes. With a new class of 30 m telescopes like the ELT, we should also be able to detect GRB afterglows behind translucent ($1 < A_V < 5$ mag) and possibly also Giant Molecular Clouds ($A_V > 5$ mag). This will allow to study the physical conditions in dense molecular gas at high redshift.

4.6 Additional tables and figures

Table 4.3: Hydrogen and metal abundances for all 22 GRBs in the sample. Upper and lower limits are given at the 3-σ confidence level.

GRB	z	$\log N(\mathrm{H\,I})$	$\log N(\mathrm{O})$	$\log N(\mathrm{Zn})$	$\log N(\mathrm{S})$	$\log N(\mathrm{Si})$	$\log N(\mathrm{Mg})$	$\log N(\mathrm{Mn})$	$\log N(\mathrm{Cr})$	$\log N(\mathrm{Ni})$	$\log N(\mathrm{Fe})$	$\log N(\mathrm{Ti})$
090809A	2.737	21.48 ± 0.07	> 15.6	13.25 ± 0.11	15.85 ± 0.60	16.29 ± 0.10	> 14.8	13.73 ± 0.24	13.52 ± 0.22	14.42 ± 0.39	> 14.9	-
090926A	2.106	21.58 ± 0.01	> 15.0	12.24 ± 0.11	14.52 ± 0.04	15.28 ± 0.05	> 14.6	< 13.0	< 12.9	13.40 ± 0.11	14.21 ± 0.02	< 11.6
100219A	4.667	21.28 ± 0.02	> 15.5	-	15.18 ± 0.05	> 15.3	-	-	-	14.30 ± 0.30	> 14.8	-
111008A	4.991	22.39 ± 0.01	> 16.8	13.54 ± 0.30	15.66 ± 0.08	> 15.8	> 15.8	13.63 ± 0.12	14.20 ± 0.08	14.63 ± 0.17	> 15.5	-
111107A	2.893	21.10 ± 0.04	> 16.4	-	< 16.0	15.87 ± 0.20	< 16.2	-	13.62 ± 0.44	< 14.0	> 14.7	-
120327A	2.814	22.07 ± 0.01	> 16.3	13.21 ± 0.04	15.75 ± 0.02	> 14.5	16.40 ± 0.23	-	14.12 ± 0.02	14.57 ± 0.04	15.79 ± 0.06	12.69 ± 0.08
120712A	4.171	20.44 ± 0.05	> 15.5	-	< 15.2	> 14.6	-	-	-	< 13.1	-	-
120716A	2.487	21.73 ± 0.03	> 15.5	13.65 ± 0.05	16.00 ± 0.14	> 16.2	> 14.8	13.92 ± 0.18	14.40 ± 0.22	< 15.4	15.81 ± 0.22	-
120815A	2.358	22.09 ± 0.01	> 16.0	13.27 ± 0.02	15.51 ± 0.05	> 15.4	-	13.28 ± 0.07	13.37 ± 0.08	14.16 ± 0.08	15.11 ± 0.05	< 12.5
120909A	3.929	21.82 ± 0.02	> 15.7	-	15.89 ± 0.12	> 16.0	16.52 ± 0.06	13.97 ± 0.33	-	14.27 ± 0.05	15.73 ± 0.09	< 12.7
121024A	2.300	21.78 ± 0.02	> 15.0	13.65 ± 0.06	> 15.7	16.69 ± 0.14	> 17.8	13.75 ± 0.03	14.09 ± 0.05	14.24 ± 0.34	15.73 ± 0.05	-
130408A	3.757	21.90 ± 0.01	> 16.0	13.05 ± 0.07	15.38 ± 0.05	15.91 ± 0.08	> 15.6	13.28 ± 0.23	13.98 ± 0.08	14.16 ± 0.09	> 15.4	< 12.9
130606A	5.912	19.88 ± 0.01	14.87 ± 0.07	-	< 13.6	13.56 ± 0.10	< 14.1	< 14.4	-	< 13.4	13.12 ± 0.08	-
140311A	4.955	22.30 ± 0.02	> 15.5	13.28 ± 0.14	15.48 ± 0.12	> 14.7	> 14.6	13.49 ± 0.03	14.11 ± 0.08	14.40 ± 0.23	15.78 ± 0.15	-
141028A	2.333	20.39 ± 0.03	> 14.7	< 12.3	< 14.3	14.26 ± 0.13	> 13.9	< 12.4	< 13.6	< 13.6	14.29 ± 0.10	< 13.1
141109A	2.994	22.18 ± 0.02	> 17.2	13.18 ± 0.06	15.81 ± 0.05	> 15.6	> 15.6	13.57 ± 0.56	13.80 ± 0.03	14.06 ± 0.17	15.54 ± 0.04	< 12.8
150403A	2.057	21.73 ± 0.02	> 16.7	13.32 ± 0.04	15.78 ± 0.08	> 15.8	> 15.7	> 13.5	14.06 ± 0.03	14.23 ± 0.10	15.54 ± 0.07	-
151021A	2.329	22.14 ± 0.03	> 16.0	13.79 ± 0.06	15.97 ± 0.15	> 16.0	> 16.1	13.86 ± 0.03	14.21 ± 0.04	14.61 ± 0.07	15.78 ± 0.06	-
151027B	4.065	20.54 ± 0.07	> 16.4	< 13.2	14.91 ± 0.16	15.12 ± 0.41	< 14.8	< 12.4	< 13.1	< 13.1	15.07 ± 0.39	< 12.0
160203A	3.518	21.74 ± 0.02	> 16.9	-	15.56 ± 0.04	16.02 ± 0.02	> 15.3	> 13.1	13.73 ± 0.04	14.28 ± 0.05	15.53 ± 0.18	-
161023A	2.710	20.95 ± 0.01	> 16.0	< 12.5	14.85 ± 0.03	15.21 ± 0.05	> 14.4	12.99 ± 0.06	-	< 13.8	14.80 ± 0.03	< 11.5
170202A	3.645	21.53 ± 0.04	> 15.5	< 13.2	15.39 ± 0.08	> 15.4	> 13.9	< 13.2	< 13.5	13.84 ± 0.21	> 14.7	< 12.0

Table 4.4: Molecular hydrogen column densities and upper limits. Upper limits are given at 3σ confidence and are determined assuming a broadening parameter of $b = 2$ km/s. In case of 120327A, 120909A, 121024A and 141109A the observed velocity width is close to the instrumental resolution, and we therefore measured the column density for $b = 2$ km/s and $b = 10$ km/s in order to determine a realistic range for the total H_2 column density.

GRB	$\log N(H_2)$				b	fitted and/or most constraining transitions		
	total	J0	J1	J2	(km/s)	J0	J1	J2
120327A	17.39 ± 0.13	< 13.8	17.29 ± 0.08	< 17	2	L4R(0); L10R(0); L2R(0)	W0Q(1); L4R(1); L4P(1)	W2Q(2); L3R(2); L5P(5)
	15.21 ± 0.17	< 12.9	15.07 ± 0.20	14.63 ± 0.05	10	L4R(0); L10R(0); L2R(0)	W0Q(1); L4R(1); L4P(1)	W2Q(2); L3R(2); L5P(5)
120815A	20.42 ± 0.08	20.09 ± 0.08	20.14 ± 0.07	17.82 ± 0.49	14 ± 3	all lines between 982Å to 1117Å		
120909A	17.25 ± 0.23	< 14.4	17.23 ± 0.23	< 16.1	2	L8R(0); L4R(0); L0R(0)	W2Q(1); W1R(1); W0Q(1)	W2R(2); W0R(2); L10R(2)
	15.23 ± 0.25	< 14.0	15.14 ± 0.24	< 14.7	10	L8R(0); L4R(0); L0R(0)	W2Q(1); W1R(1); W0Q(1)	W2R(2); W0R(2); L10R(2)
121024A	19.90 ± 0.17	19.78 ± 0.15	19.29 ± 0.22	< 18.3	2	L1R(0)	L2P(1)	
	19.87 ± 0.19	19.77 ± 0.16	19.19 ± 0.29	< 18.3	10	L1R(0)	L2P(1)	
141109A	18.02 ± 0.12	17.21 ± 0.28	17.94 ± 0.09	< 16.4	2	W1R(0); L4R(0); L10R(0)	W1R(1); W0Q(1); L10R(1)	W1R(2); L10R(2); L5P(2)
	16.31 ± 0.42	15.37 ± 0.35	16.25 ± 0.43	< 14.4	10	W1R(0); L4R(0); L10R(0)	W1R(1); W0Q(1); L10R(1)	W1R(2); L10R(2); L5P(2)
150403A	19.90 ± 0.14	19.69 ± 0.13	19.47 ± 0.15	< 17.8	5 ± 3	all lines between 1046Å to 1110Å		
151021A	$< 18.99 \pm 1.28$	< 19.1	18.35 ± 1.89	< 18.4	2	all lines between 1043Å to 1117Å		
160203A	< 16.7	< 14.0	< 16.7	< 14.0	2	L7R(0)	W1Q(1); W3Q(1); L9R(1)	W3R(2); L8P(2)
170202A	< 17.1	< 16.4	< 17.0	< 14.9	2	W1R(0); L4R(0); L2R(0)	W1R(1); L7R(1); L2P(1)	W0Q(2); L9R(2)
090809A	< 18.0	< 18.0	< 16.4	< 16.9	2	W1R(0); L8R(0); L0R(0)	W1Q(1); W1R(1); L0R(1)	W2R(2); W1R(2); L7R(2)
090926A	< 14.2	< 13.6	< 14.0	< 13.4	2	L0R(0); L2R(0)	L4R(1); L3R(1); L2R(1)	L4R(2); L3R(2)
100219A	< 18.0	< 17.6	< 17.6	< 17.4	2	W0R(0); L8R(0); L4R(0)	W0R(1); L4R(1); L5P(1)	L7R(2); L8P(2); L4P(2)
111008A	< 17.2	< 16.5	< 17.0	< 16.5	2	L9R(0); L4R(0); L12R(0)	W0Q(1); L9R(1); L8P(1)	L4R(2); L4P(2); W1P(2)
111107A	< 15.5	< 14.8	< 15.0	< 15.2	2	W0R(0); L9R(0); L4R(0)	W1Q(1); W0Q(1); L7R(1)	W0Q(2); L7R(2); L9R(2)
120712A	< 16.9	< 16.2	< 16.6	< 16.2	2	W1R(0); W3R(0); L7R(0)	W0Q(1); L7R(1); L10R(1)	W1R(2); W0Q(2); L8R(2)
120716A	< 18.2	< 17.6	< 18.0	< 17.4	2	L2R(0); L1R(0); L0R(0)	L3P(1); L2P(1); L0P(1)	L2R(2); L2P(2); L1R(2)
130408A	< 15.5	< 14.1	< 15.2	< 15.1	2	W1R(0); L2R(0); L12R(0)	L9R(1); L0R(1); L0P(1)	W1R(2); L7R(2); L4P(2)
130606A	< 17.9	< 17.5	< 17.5	< 17.4	2	L5R(0); L10R(0); L0R(0)	L5R(1); L5P(1); L12R(1)	L5R(2); L6P(2); L7P(2)
140311A	< 17.8	< 17.2	< 17.5	< 17.0	2	W1R(0); L2R(0); L1R(0)	W1Q(1); L5R(1); L5P(1)	W1R(2); L7R(2); L4R(2)
141028A	< 17.4	< 16.4	< 17.1	< 17.0	2	L7R(0), L4R(0)	L2R(1)	L4R(2)
151027B	< 16.5	< 16.0	< 16.2	< 15.8	2	W1R(0); W3R(0); L7R(0)	W1R(1); L5R(1); L10R(1)	L7R(2); L10R(2); L5P(2)
161023A	< 14.7	< 14.6	< 14.0	< 13.5	2	W1R(0); W2R(0); L8R(0)	W0R(1); L7R(1); L3P(1)	L4R(2); L3P(2)

Table 4.5: Overall properties of the H_2 GRB sample. The last four columns are the results from fitting the depletion sequences following Wiseman, Schady et al. (2017). The Molecular fraction is $f(H_2) = 2N(H_2)/(2N(H_2)+N(H))$
References: (1) Bolmer et al. (2018); (2) Greiner (2019, in prep.); (3) D'Elia et al. (2010); (4) Zafar, Watson et al. (2018); (5) de Ugarte Postigo et al. (2018); (6) Heintz et al. (2019)

GRB	Redshift	A_V (SED)	$\log N(\mathrm{H\,I})$	$\log N(H_2)$	$\log f(H_2)$	[X/H]	Ion	[Y/Fe]	Ion	F_*	[M/H]	$\mathcal{DTM}$	A_V (depl.)
yymmdd#	(z)	(mag)	(cm^{-2})	(cm^{-2})			X		Y				(mag)
090809A	2.7373	$0.11^{+0.04}_{-0.04}$ (2)	21.48 ± 0.07	< 18.0	< -3.18	-0.86 ± 0.13	Zn	< 1.12	Zn	-0.39 ± 0.31	-0.46 ± 0.15	0.71 ± 0.11	0.33 ± 0.31
090926A	2.1069	< 0.03 (3)	21.58 ± 0.01	< 14.2	< -7.08	-1.97 ± 0.11	Zn	0.88 ± 0.11	Zn	-0.25 ± 0.07	-1.72 ± 0.05	0.76 ± 0.02	0.02 ± 0.02
100219A	4.6676	$0.15^{+0.04}_{-0.05}$ (1)	21.28 ± 0.02	< 18.0	< -2.98	-1.24 ± 0.05	S	< 0.72	S	-1.32 ± 0.44	-1.16 ± 0.11	0.23 ± 0.26	0.01 ± 0.03
111008A	4.9910	$0.13^{+0.03}_{-0.07}$ (1)	22.39 ± 0.01	< 17.2	< -4.89	-1.48 ± 0.31	Zn	< 0.89	Zn	-1.18 ± 0.15	-1.79 ± 0.10	0.32 ± 0.09	0.06 ± 0.04
111107A	2.8930	< 0.15 (2)	21.10 ± 0.04	< 15.5	< -5.30	-0.74 ± 0.20	Si	< 1.13	Si	-0.47 ± 0.81	-0.28 ± 0.45	0.68 ± 0.28	0.20 ± 0.68
120327A	2.8143	$0.05^{+0.02}_{-0.02}$ (2)	22.07 ± 0.01	17.39 ± 0.13	-4.38 ± 0.14	-1.49 ± 0.04	Zn	0.27 ± 0.07	Zn	-0.99 ± 0.04	-1.34 ± 0.02	0.43 ± 0.02	0.11 ± 0.01
120712A	4.1719	$0.08^{+0.03}_{-0.08}$ (1)	20.44 ± 0.05	< 16.9	< -3.24	< -0.38	S	< 0.38	S	-	-	-	-
120716A	2.4874	$0.30^{+0.15}_{-0.15}$ (2)	21.73 ± 0.03	< 18.2	< -3.23	-0.71 ± 0.06	Zn	0.69 ± 0.23	Zn	-0.61 ± 0.22	-0.57 ± 0.08	0.62 ± 0.09	0.41 ± 0.19
120815A	2.3582	$0.19^{+0.04}_{-0.04}$ (4)	22.09 ± 0.01	20.42 ± 0.08	-1.39 ± 0.09	-1.45 ± 0.03	Zn	1.01 ± 0.05	Zn	-0.09 ± 0.06	-1.23 ± 0.03	0.82 ± 0.02	0.27 ± 0.03
120909A	3.9290	$0.16^{+0.04}_{-0.04}$ (2)	21.82 ± 0.02	17.25 ± 0.23	-4.27 ± 0.25	-1.06 ± 0.12	S	0.50 ± 0.15	S	$+0.20 \pm 0.14$	-0.29 ± 0.10	0.92 ± 0.04	1.39 ± 0.53
121024A	2.3005	$0.26^{+0.07}_{-0.07}$ (2)	21.78 ± 0.02	19.90 ± 0.17	-1.59 ± 0.18	-0.76 ± 0.06	Zn	0.77 ± 0.08	Zn	-0.42 ± 0.10	-0.68 ± 0.07	0.70 ± 0.04	0.40 ± 0.12
130408A	3.7579	$0.12^{+0.03}_{-0.03}$ (2)	21.90 ± 0.01	< 15.5	< -6.10	-1.48 ± 0.07	Zn	< 0.50	Zn	-1.07 ± 0.10	-1.46 ± 0.05	0.39 ± 0.06	0.05 ± 0.02
130606A	5.9127	< 0.02 (1)	19.88 ± 0.01	< 17.9	< -1.69	-1.83 ± 0.10	Si	0.41 ± 0.13	Si	-0.77 ± 0.15	-1.58 ± 0.08	0.55 ± 0.07	0.02 ± 0.02
140311A	4.9550	$0.07^{+0.03}_{-0.03}$ (1)	22.30 ± 0.02	< 17.8	< -4.20	-1.65 ± 0.14	Zn	0.34 ± 0.2	Zn	-1.16 ± 0.16	-2.00 ± 0.11	0.33 ± 0.09	0.03 ± 0.02
141028A	2.3333	$0.13^{+0.09}_{-0.09}$ (2)	20.39 ± 0.03	< 17.4	< -2.71	-1.64 ± 0.13	Si	< 0.86	Zn	-1.56 ± 0.39	-1.62 ± 0.28	0.06 ± 0.27	0.02 ± 0.02
141109A	2.9940	$0.16^{+0.04}_{-0.04}$ (2)	22.18 ± 0.02	18.02 ± 0.12	-3.86 ± 0.14	-1.63 ± 0.06	Zn	0.49 ± 0.07	Zn	-0.60 ± 0.07	-1.37 ± 0.05	0.62 ± 0.03	0.18 ± 0.04
150403A	2.0571	$0.12^{+0.02}_{-0.02}$ (6)	21.73 ± 0.02	19.90 ± 0.14	-1.54 ± 0.15	-1.04 ± 0.04	Zn	0.63 ± 0.08	Zn	-0.81 ± 0.07	-0.92 ± 0.05	0.53 ± 0.03	0.15 ± 0.04
151021A	2.3297	$0.20^{+0.03}_{-0.03}$ (6)	22.14 ± 0.03	18.99 ± 1.28	< -2.85	-0.98 ± 0.07	Zn	0.86 ± 0.08	Zn	-0.48 ± 0.10	-0.97 ± 0.07	0.67 ± 0.04	0.45 ± 0.16
151027B	4.0650	$0.10^{+0.05}_{-0.06}$ (1)	20.54 ± 0.07	< 16.5	< -3.74	-0.76 ± 0.17	S	0.18 ± 0.42	S	-0.78 ± 0.95	-0.59 ± 0.27	0.54 ± 0.36	0.02 ± 0.06
160203A	3.5187	< 0.10 (2)	21.74 ± 0.02	< 16.7	< -4.74	-1.31 ± 0.04	S	0.37 ± 0.18	S	-0.58 ± 0.07	-0.92 ± 0.04	0.63 ± 0.03	0.19 ± 0.04
161023A	2.7100	$0.09^{+0.03}_{-0.03}$ (5)	20.95 ± 0.01	< 14.7	< -5.95	-1.23 ± 0.03	S	0.39 ± 0.04	S	-0.85 ± 0.06	-1.05 ± 0.04	0.51 ± 0.03	0.02 ± 0.02
170202A	3.6456	$0.08^{+0.03}_{-0.03}$ (6)	21.53 ± 0.04	< 17.1	< -4.13	-1.28 ± 0.09	S	< 1.03	S	-0.37 ± 0.34	-1.02 ± 0.13	0.72 ± 0.12	0.10 ± 0.08

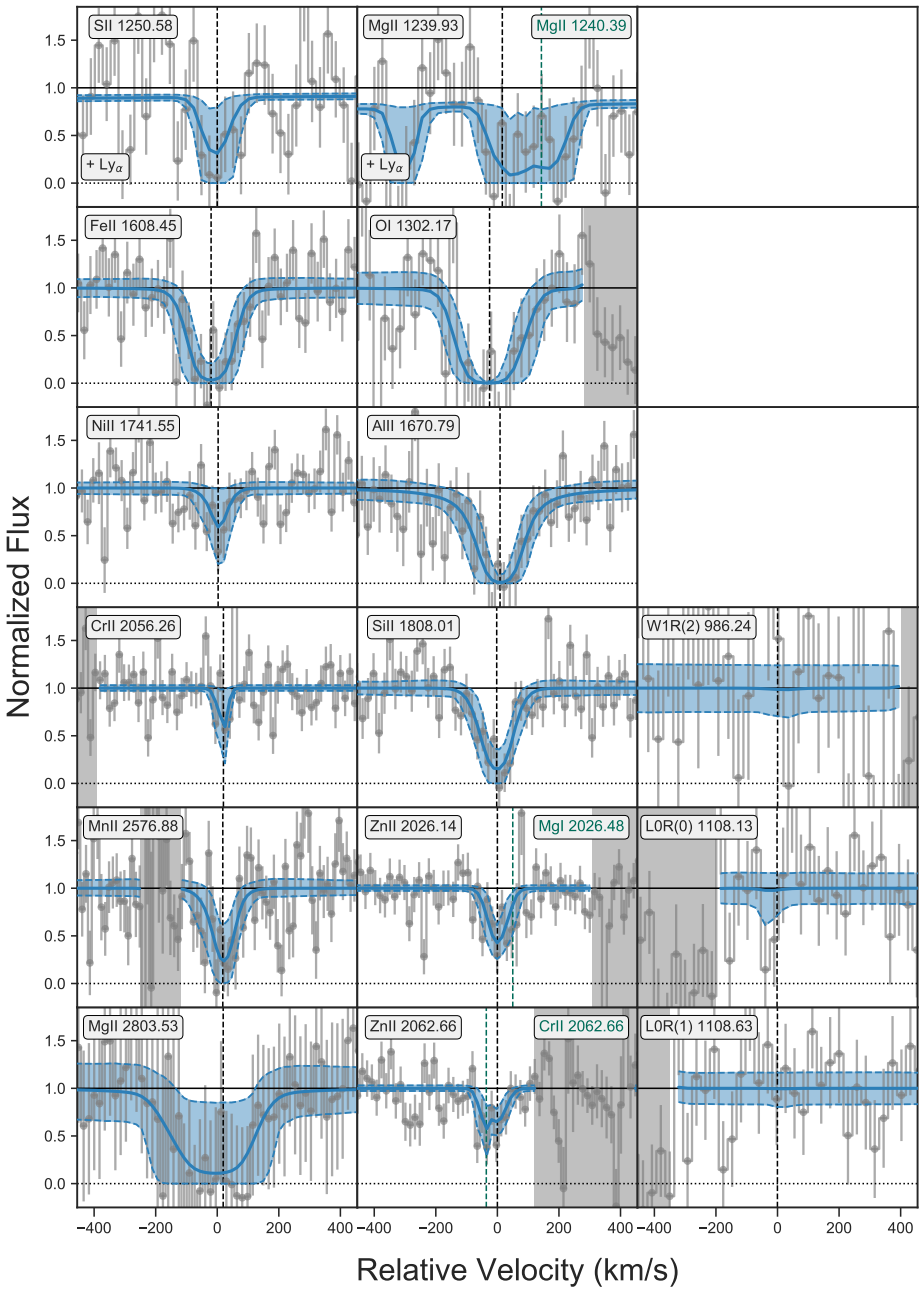

Figure 4.18: Results from fitting the absorption lines in the X-shooter spectrum of GRB090809A. As shown to the right, we do not find any evidence for absorption from molecular hydrogen. This X-shooter spectrum was previously also analysed by Skuladottir (2010).

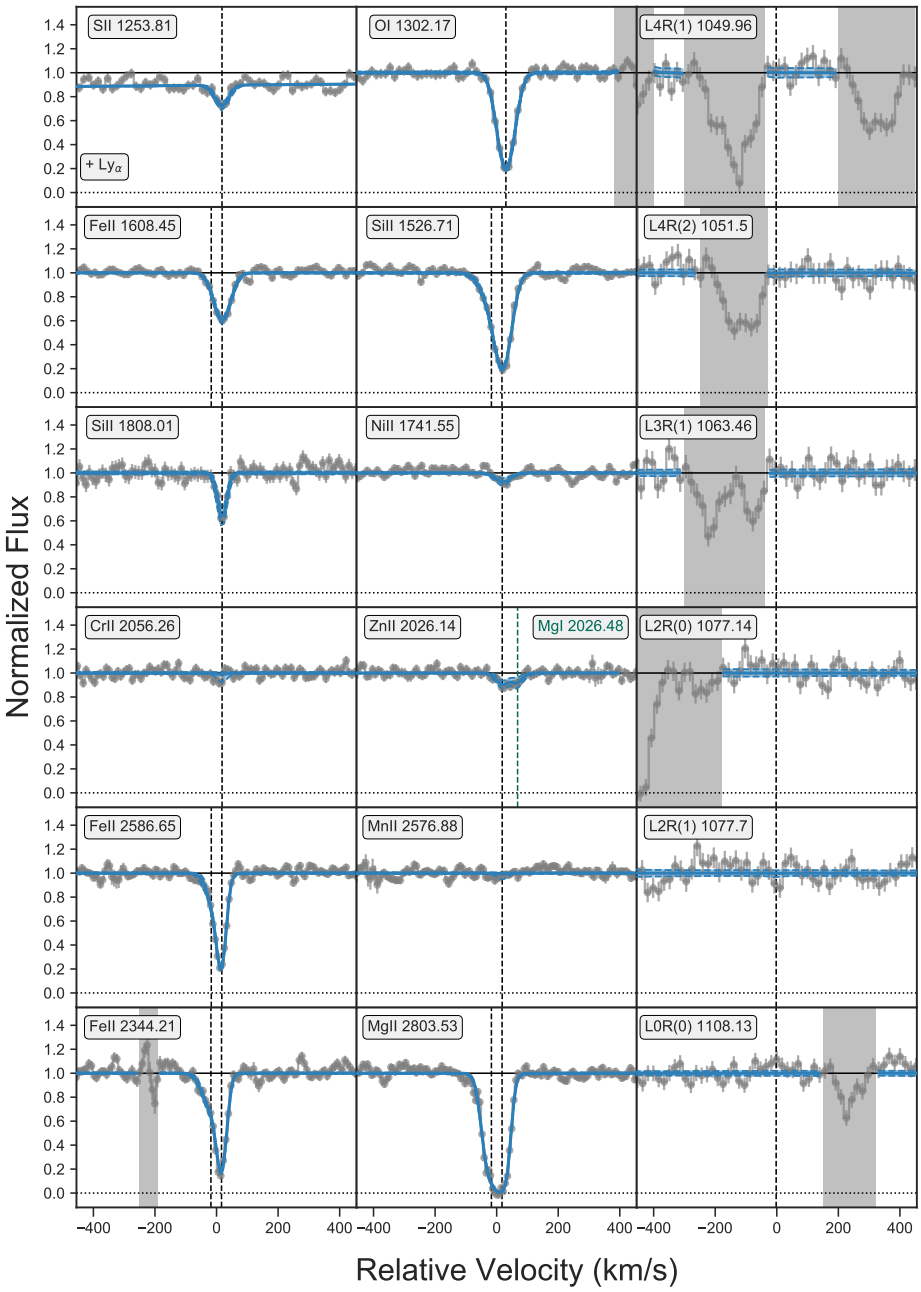

Figure 4.19: Results from fitting the absorption lines in the X-shooter spectrum of GRB090926A. As shown to the right, we do not find any evidence for absorption from molecular hydrogen. This X-shooter spectrum was previously also analysed by D'Elia et al. (2010).

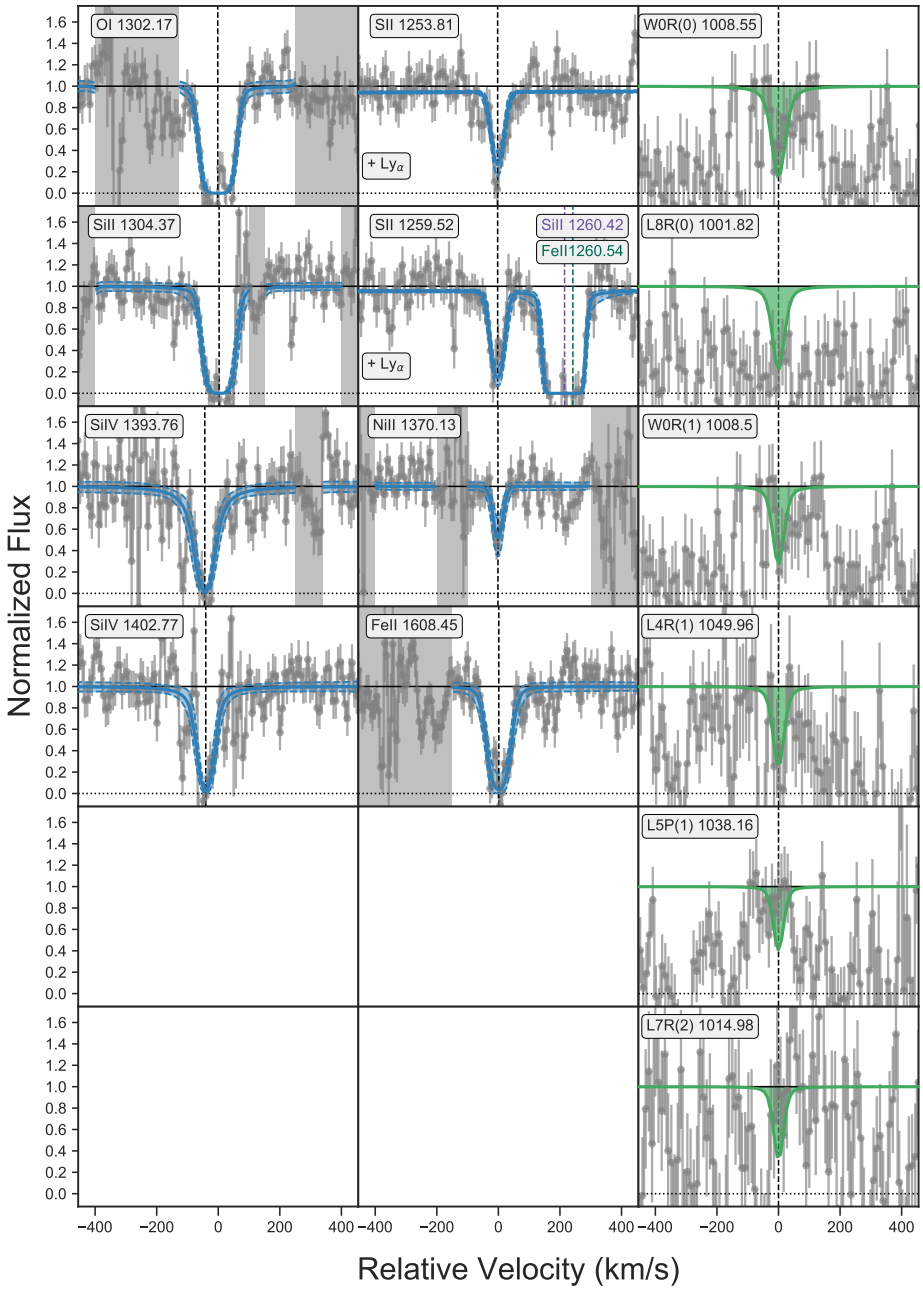

Figure 4.20: Results from fitting the absorption lines in the X-shooter spectrum of GRB100219A. As shown to the right, we do not find compelling evidence for absorption from molecular hydrogen, however, due to the strong Lyman-α forest only down to relatively loose upper limits (see Table 4.4). These upper limits are over-plotted in green for the 6 most constraining lines. This X-shooter spectrum was previously also analysed by Thöne et al. (2013).

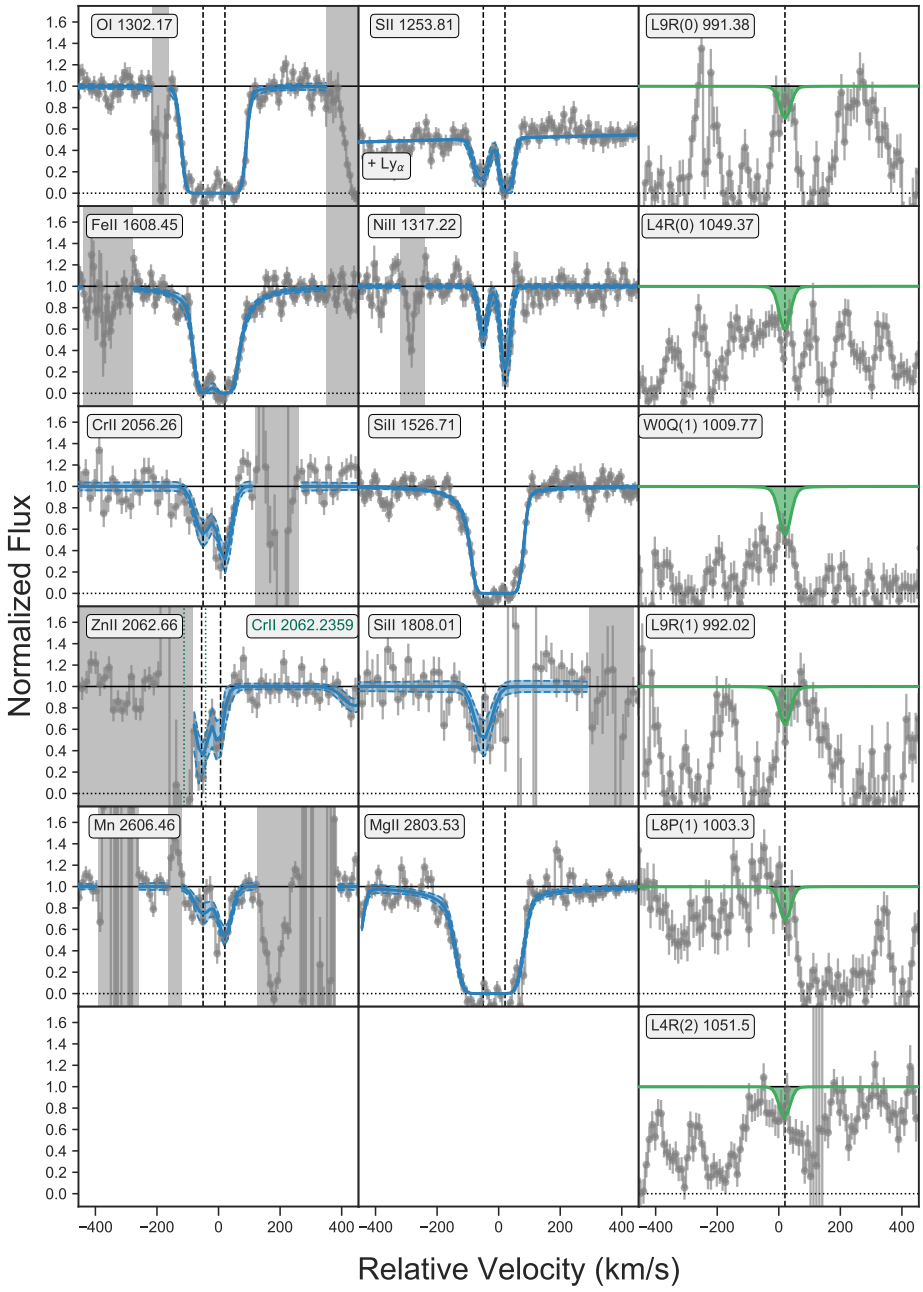

Figure 4.21: Results from fitting the absorption lines in the X-shooter spectrum of GRB111008A. As shown to the right, we do not find compelling evidence for absorption from molecular hydrogen, however, due to the strong Lyman-α forest only down to relatively loose upper limits (see Table 4.4). These upper limits are over-plotted in green for the 6 most constraining lines. This X-shooter spectrum was previously also analysed by Sparre et al. (2014).

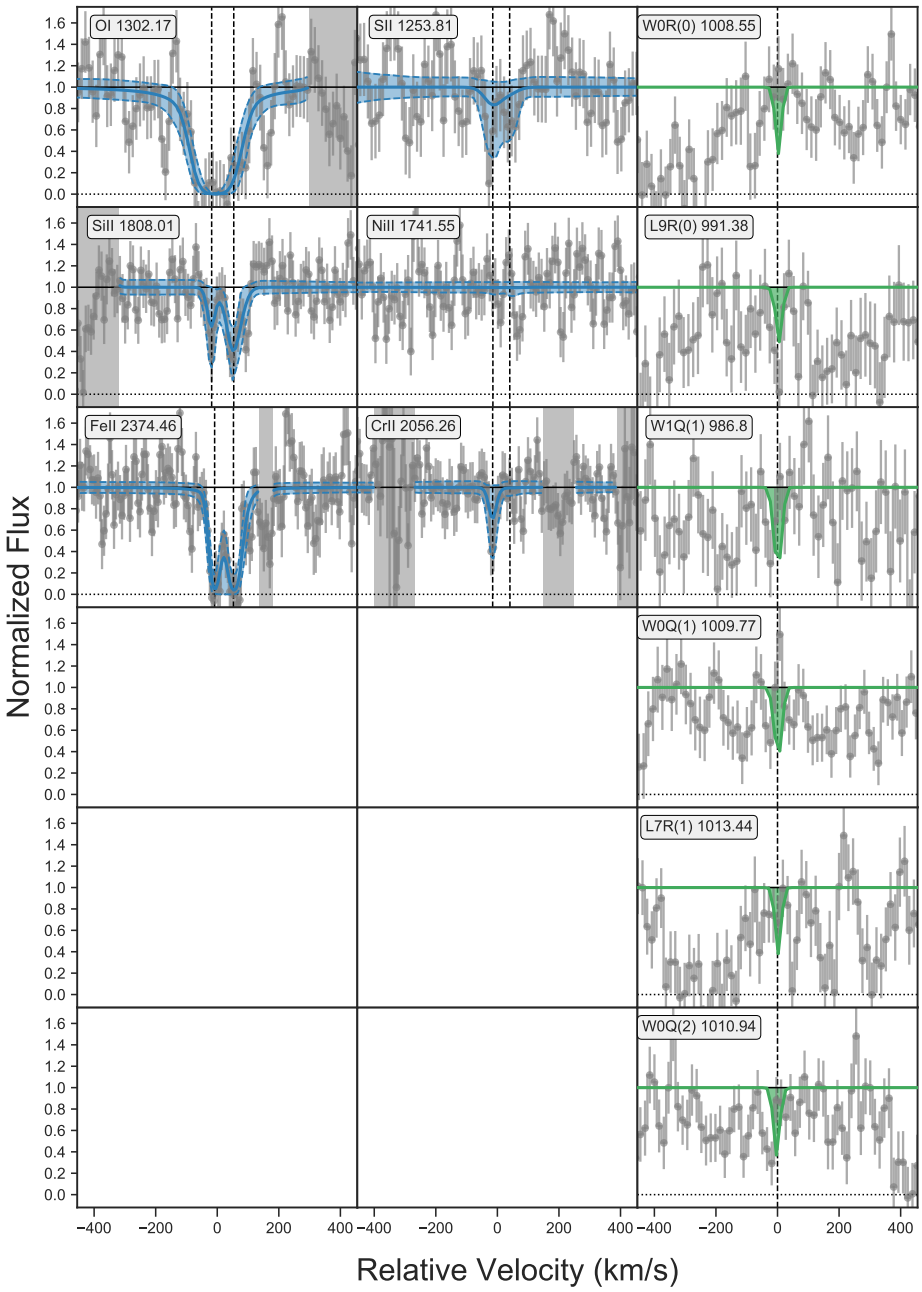

Figure 4.22: Results from fitting the absorption lines in the X-shooter spectrum of GRB111107A. As shown to the right, we do not find evidence for absorption from molecular hydrogen down to the upper limits given in Table 4.4. These upper limits are over-plotted in green for the 6 most constraining lines.

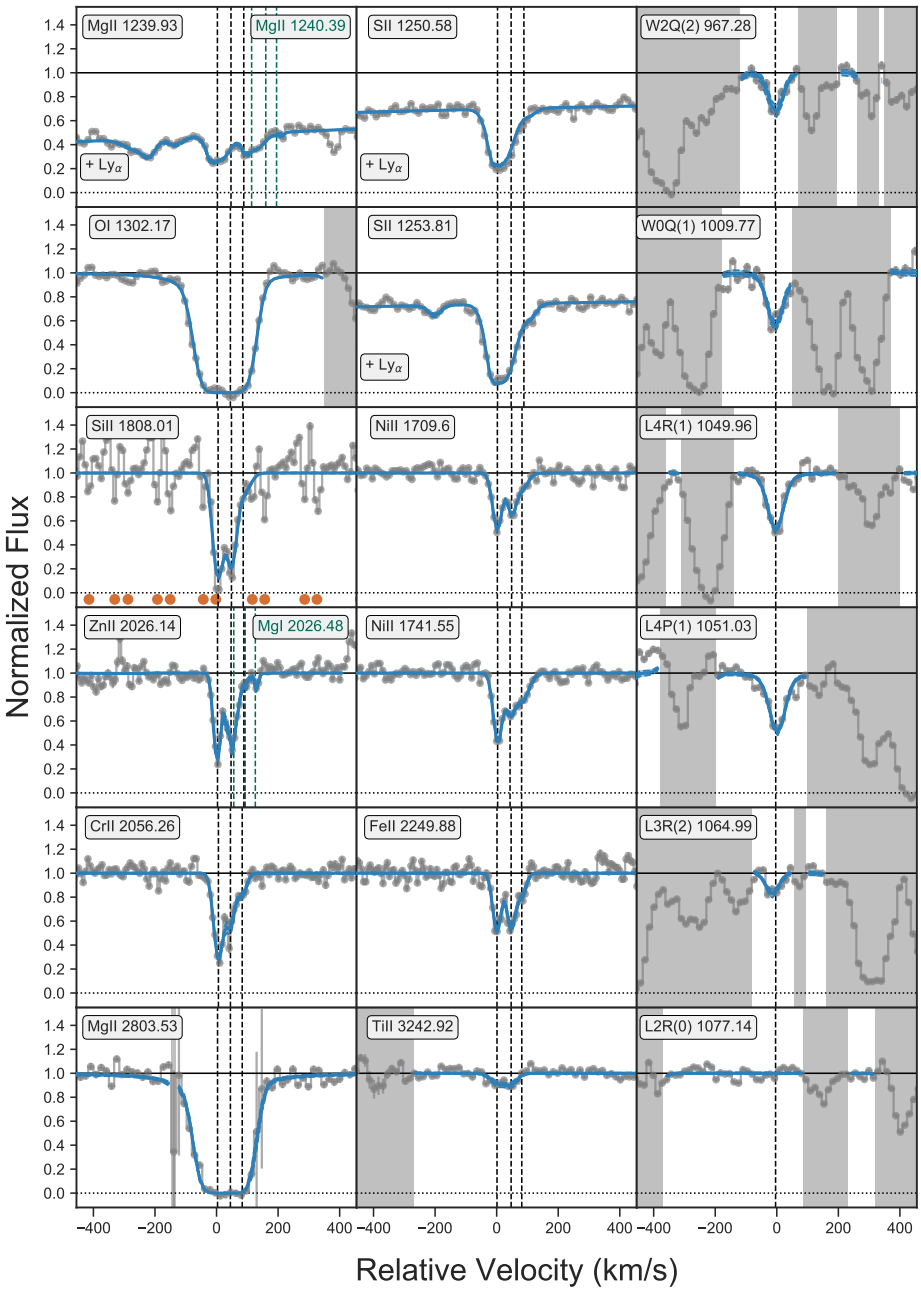

Figure 4.23: Results from fitting the absorption lines in the X-shooter spectrum of GRB120327A. The position of telluric lines, which were corrected, are marked by red dots. As shown to the right, we find absorption lines from molecular hydrogen consistent with strongest component. This X-shooter spectrum was previously also analysed by D'Elia et al. (2014).

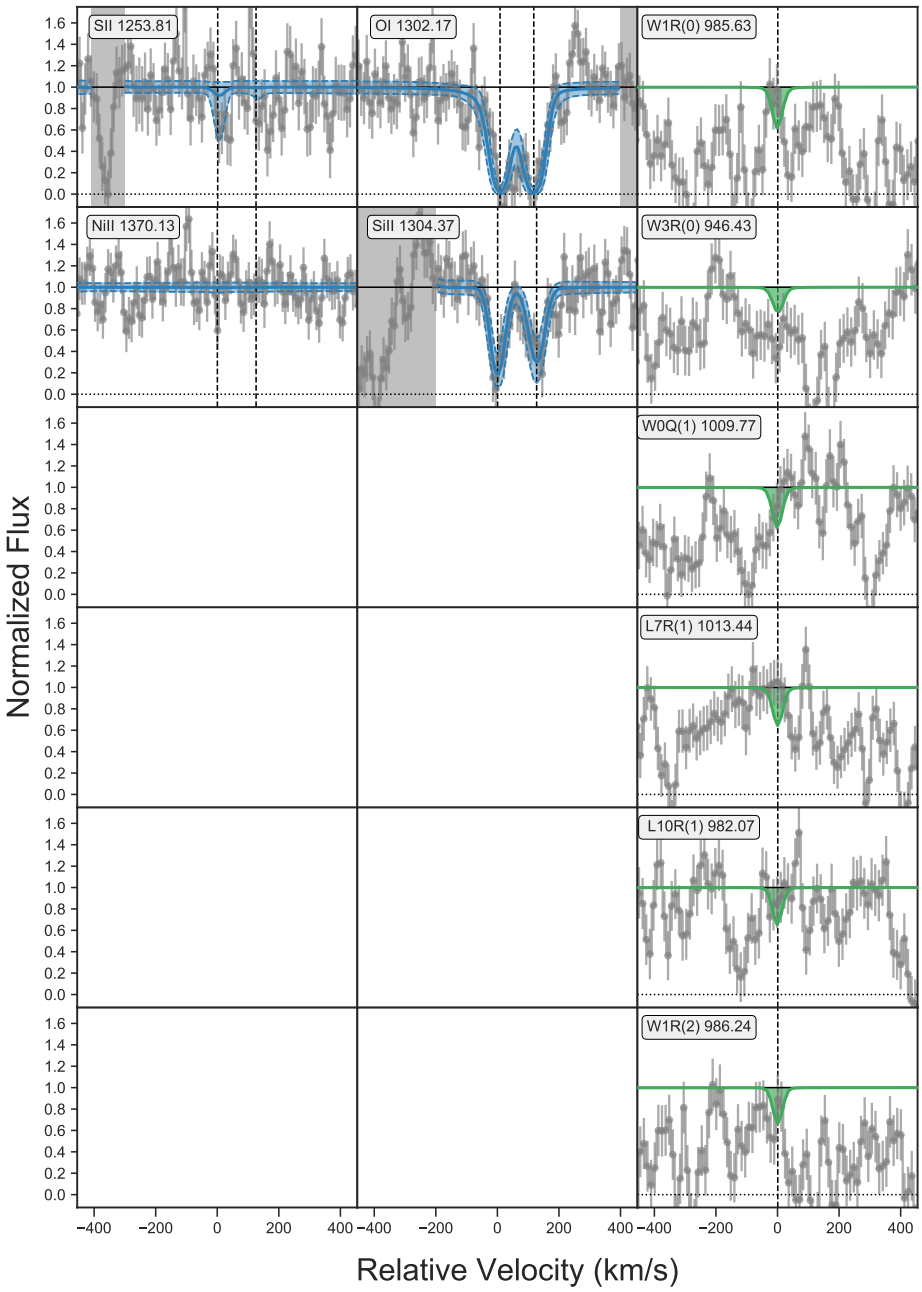

Figure 4.24: Results from fitting the absorption lines in the X-shooter spectrum of GRB120712A. As shown to the right, we do not find convincing evidence for absorption from molecular hydrogen down to the upper limits given in Table 4.4. These upper limits are over-plotted in green for the 6 most constraining lines.

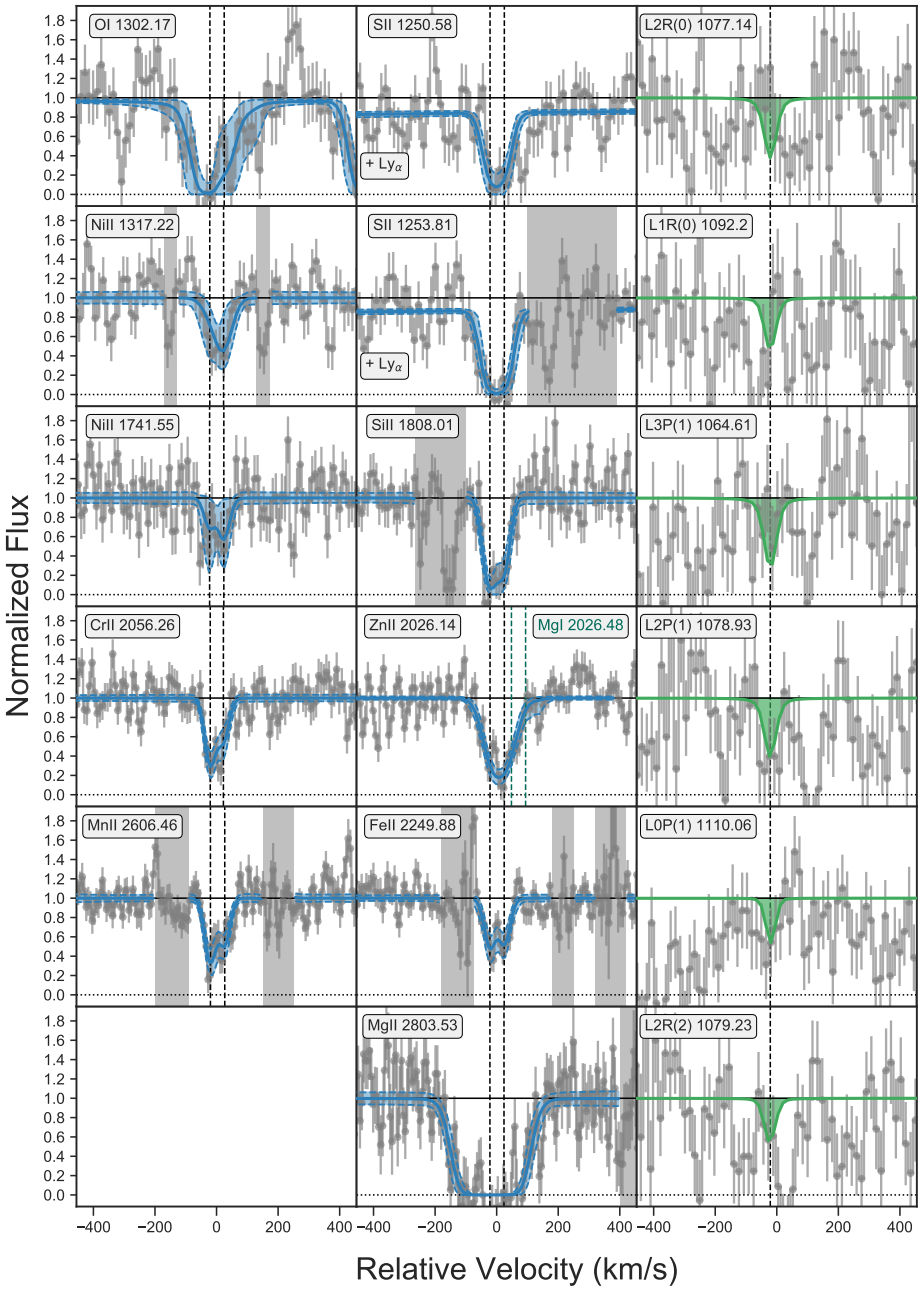

Figure 4.25: Results from fitting the absorption lines in the X-shooter spectrum of GRB120716A. As shown to the right, we do not find compelling evidence for absorption from molecular hydrogen, however, due to the poor S/N only down to relatively loose upper limits (see Table 4.4). These upper limits are over-plotted in green for the 6 most constraining lines. This X-shooter spectrum was previously also analysed by Wiseman, Schady et al. (2017).

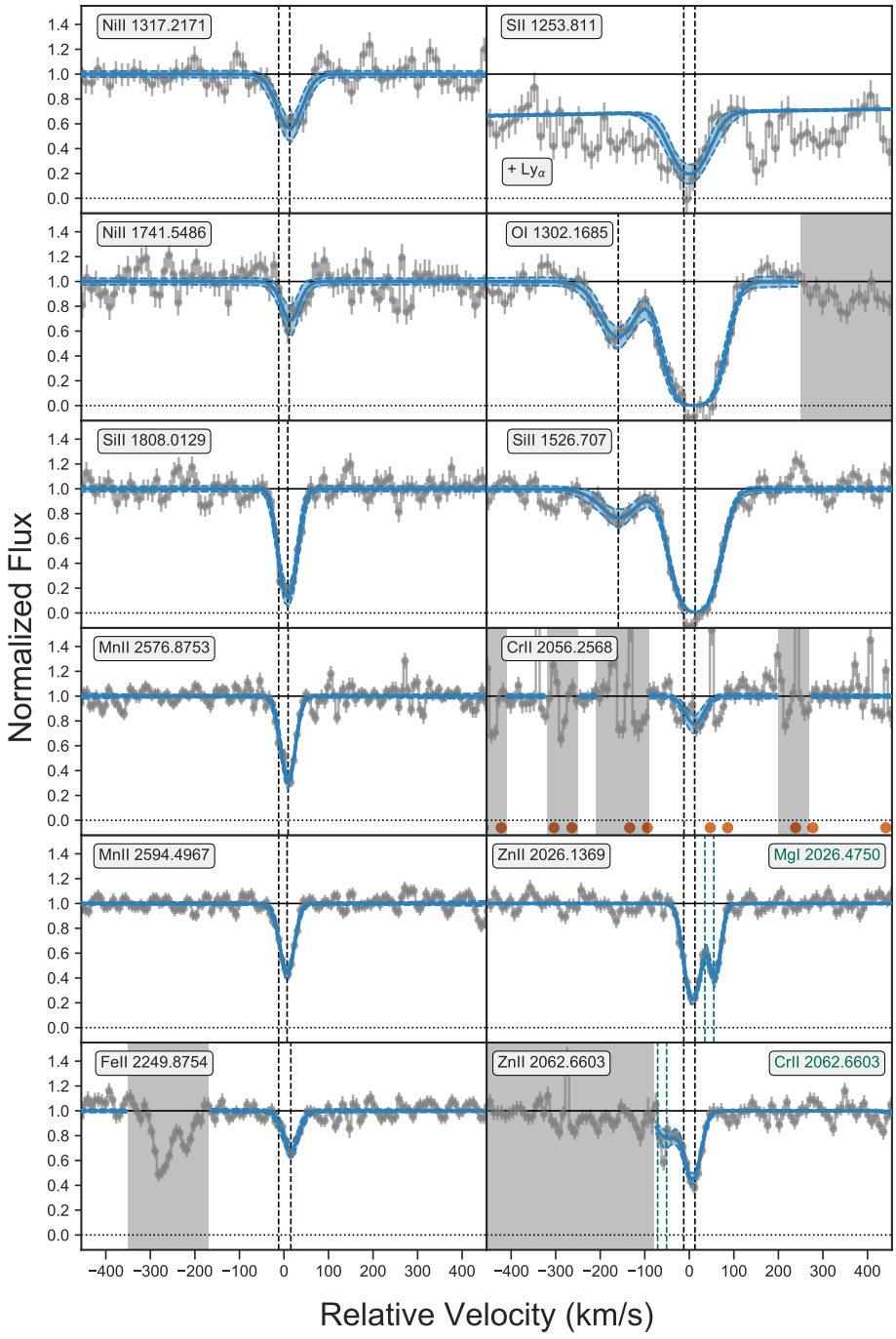

Figure 4.26: Results from fitting the absorption lines in the X-shooter spectrum of GRB120815A. The result of fitting the H_2 lines is shown in Fig. 4.9. This X-shooter spectrum was previously also analysed by Krühler et al. (2013).

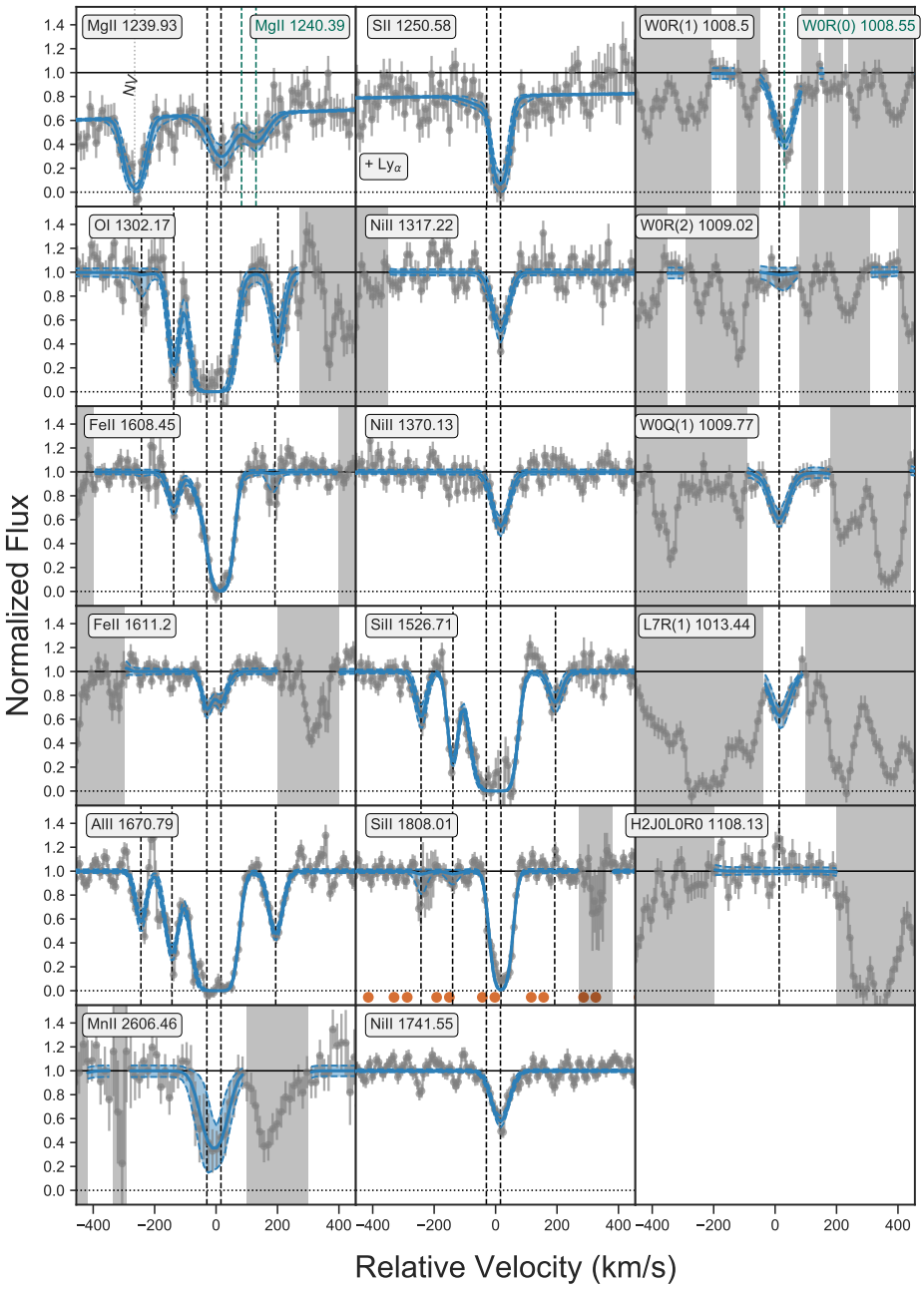

Figure 4.27: Results from fitting the absorption lines in the X-shooter spectrum of GRB120909A. As shown to the right, we find evidence for absorption from molecular hydrogen consistent with the strongest component. This X-shooter spectrum was previously also analysed by Wiseman, Schady et al. (2017).

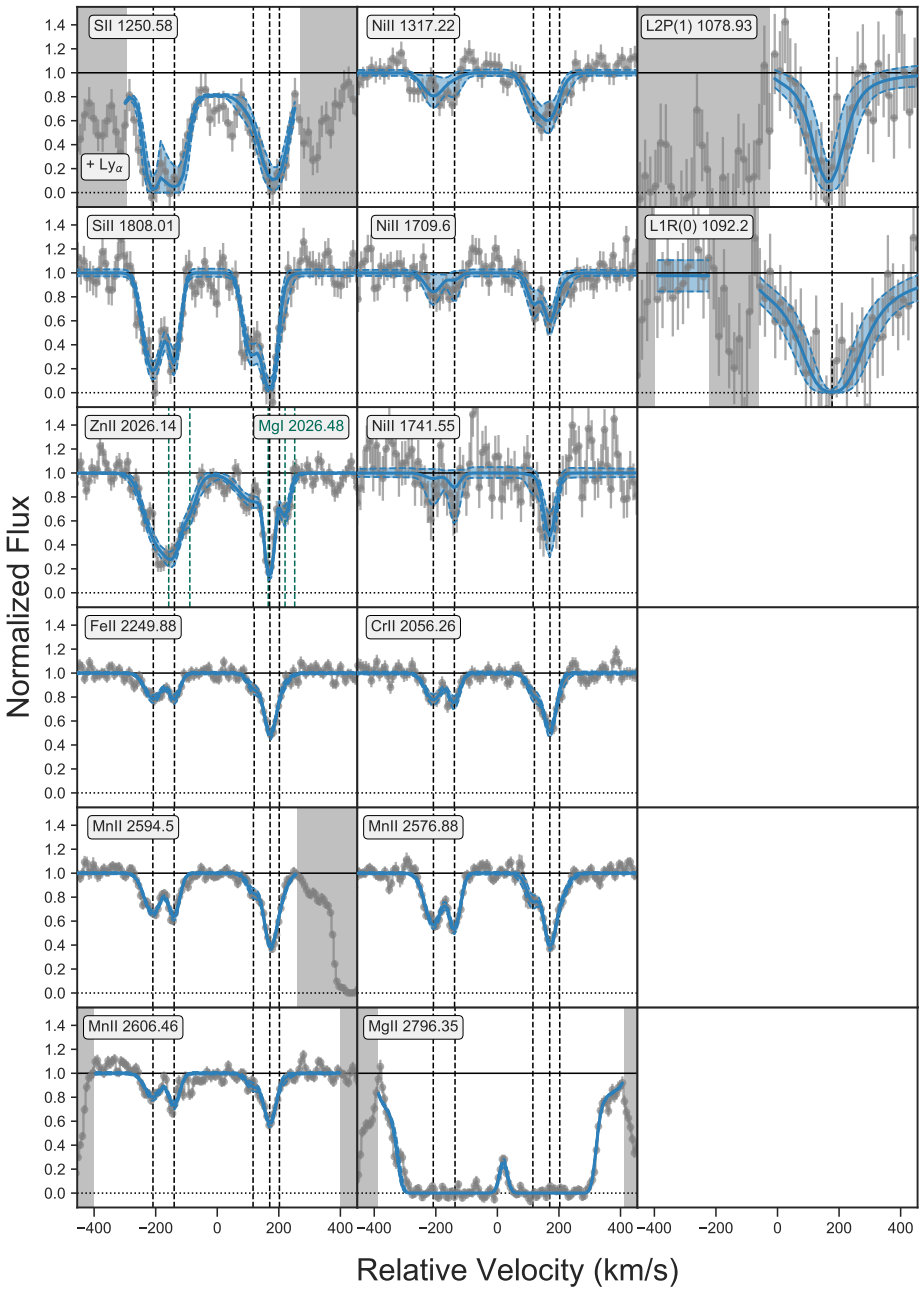

Figure 4.28: Results from fitting the absorption lines in the X-shooter spectrum of GRB121024A. As shown to the right, we find evidence for absorption from molecular hydrogen consistent with the three red components. This X-shooter spectrum was previously also analysed by Friis et al. (2015).

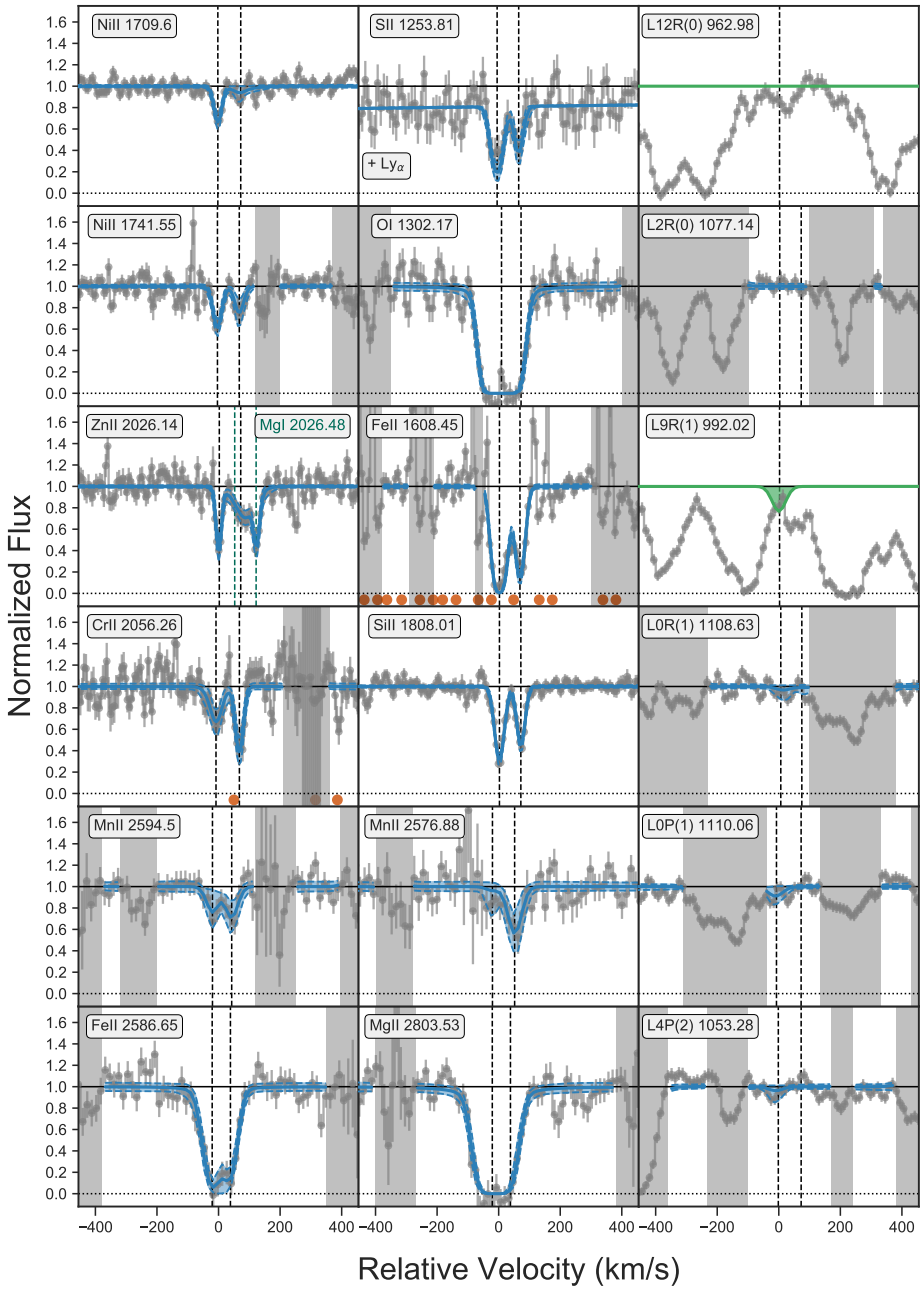

Figure 4.29: Results from fitting the absorption lines in the X-shooter spectrum of GRB130408A. As shown to the right, we do not find evidence for absorption from molecular hydrogen down to the upper limits given in Table 4.4. These upper limits were derived from the fits shown in blue and are additionally over-plotted for two additional lines in green. This X-shooter spectrum was previously also analysed by Wiseman, Schady et al. (2017).

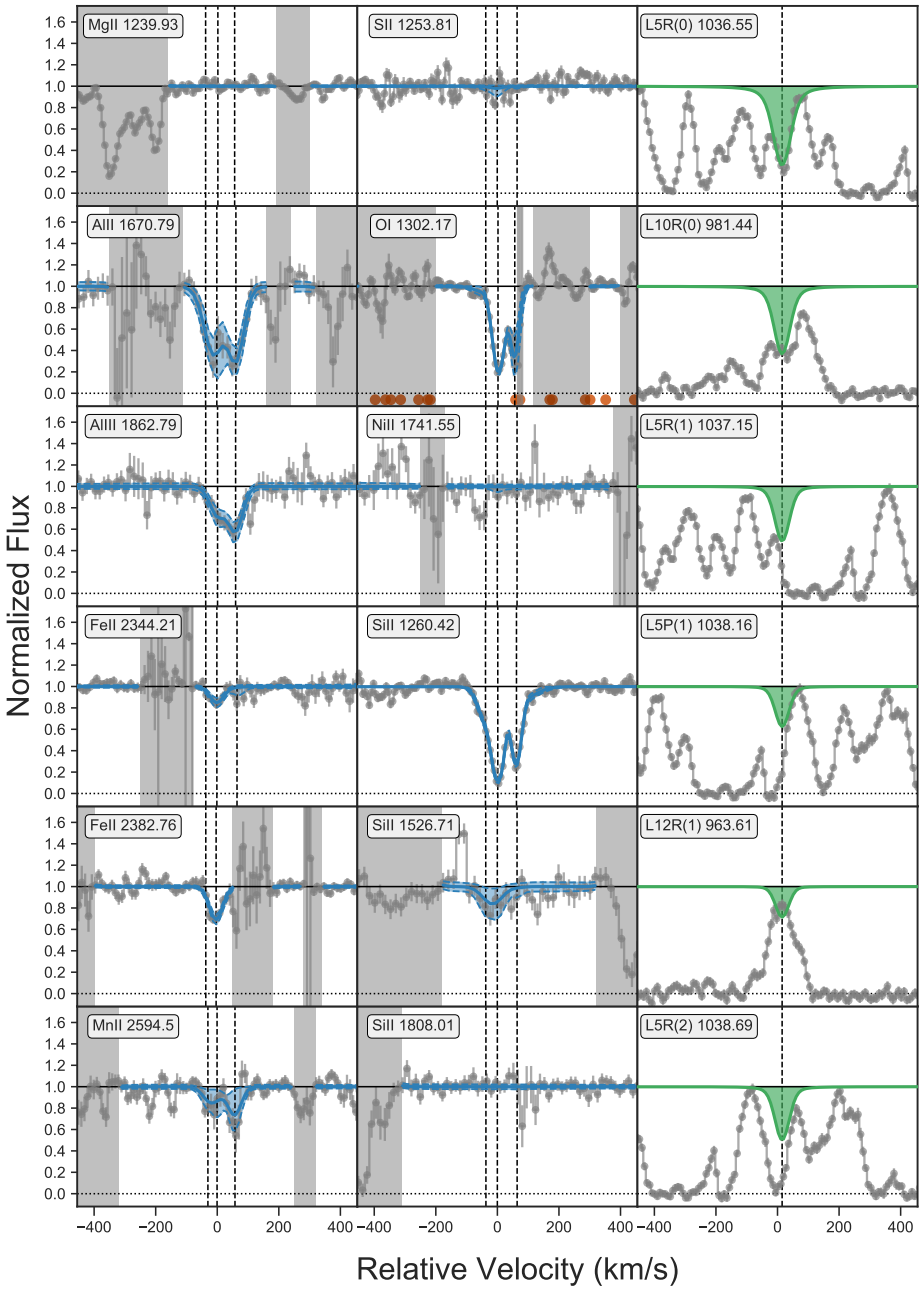

Figure 4.30: Results from fitting the absorption lines in the X-shooter spectrum of GRB130606A. As shown to the right, we do not find compelling evidence for absorption from molecular hydrogen, however, due to the strong Lyman-α forest only down to relatively loose upper limits (see Table 4.4). These upper limits are over-plotted in green for the 6 most constraining lines. This X-shooter spectrum was previously also analysed by Hartoog et al. (2015).

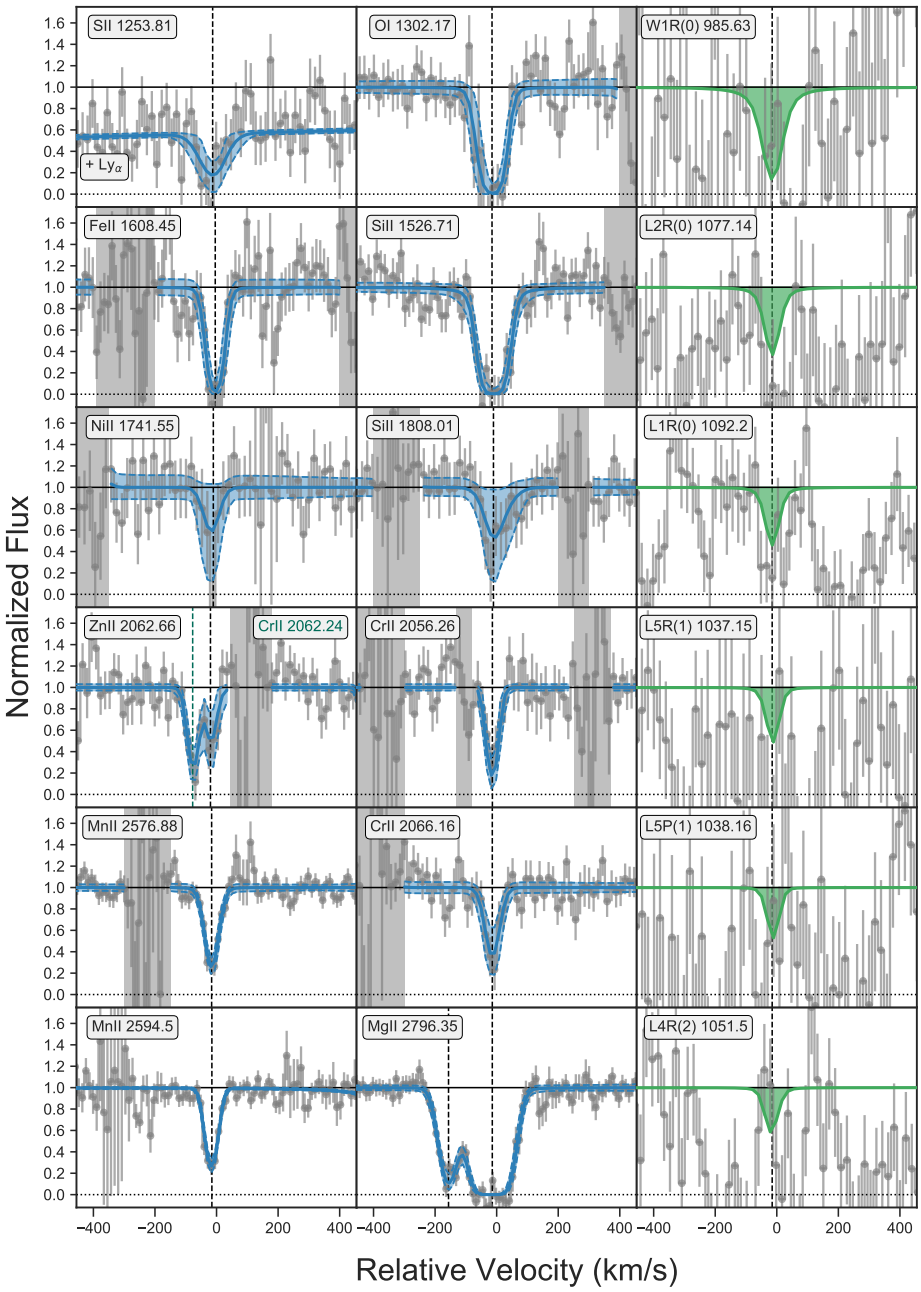

Figure 4.31: Results from fitting the absorption lines in the X-shooter spectrum of GRB140311A. As shown to the right, we do not find compelling evidence for absorption from molecular hydrogen, however, due to the poor S/N only down to relatively loose upper limits (see Table 4.4). These upper limits are over-plotted in green for the 6 most constraining lines.

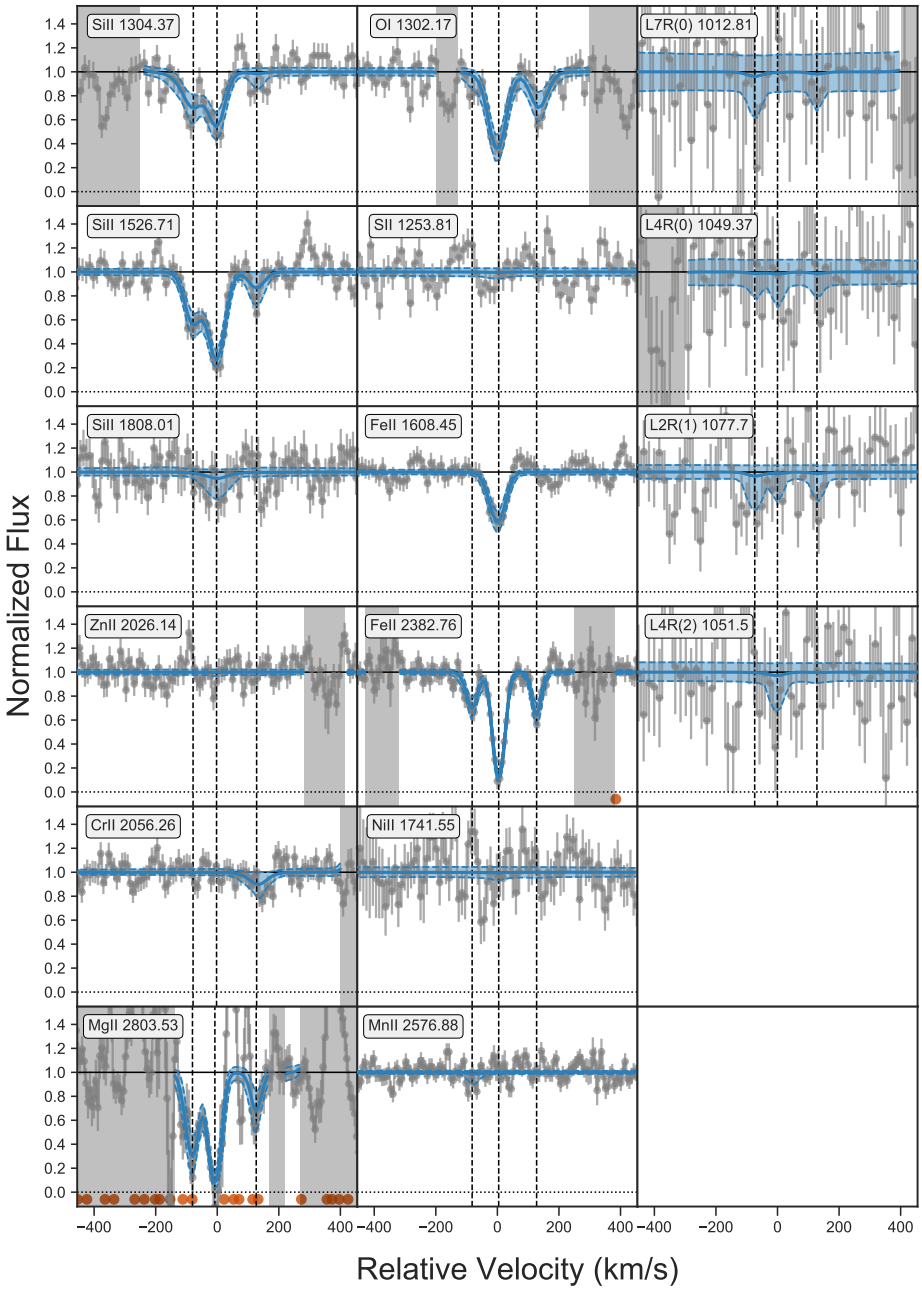

Figure 4.32: Results from fitting the absorption lines in the X-shooter spectrum of GRB141028A. The position of telluric lines, which were corrected, are marked by red dots. As shown to the right, we do not find evidence for absorption from molecular hydrogen, however, due to the poor S/N only down to relatively loose upper limits (see Table 4.4). This X-shooter spectrum was previously also analysed by Wiseman, Schady et al. (2017).

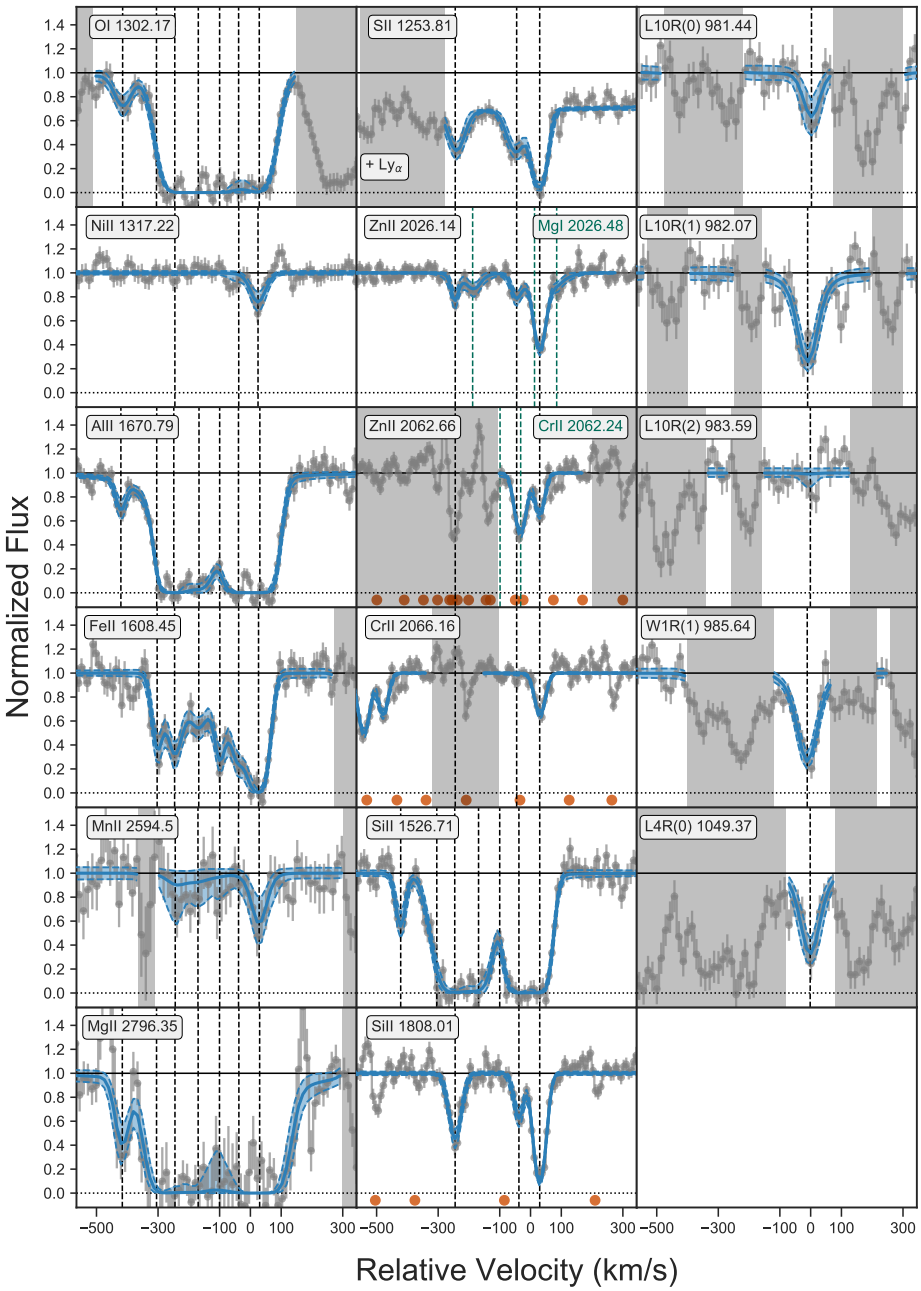

Figure 4.33: Results from fitting the absorption lines in the X-shooter spectrum of GRB141109A. The position of telluric lines, which were corrected, are marked by red dots. As shown to the right, we find absorption lines from molecular hydrogen consistent with the two red components.

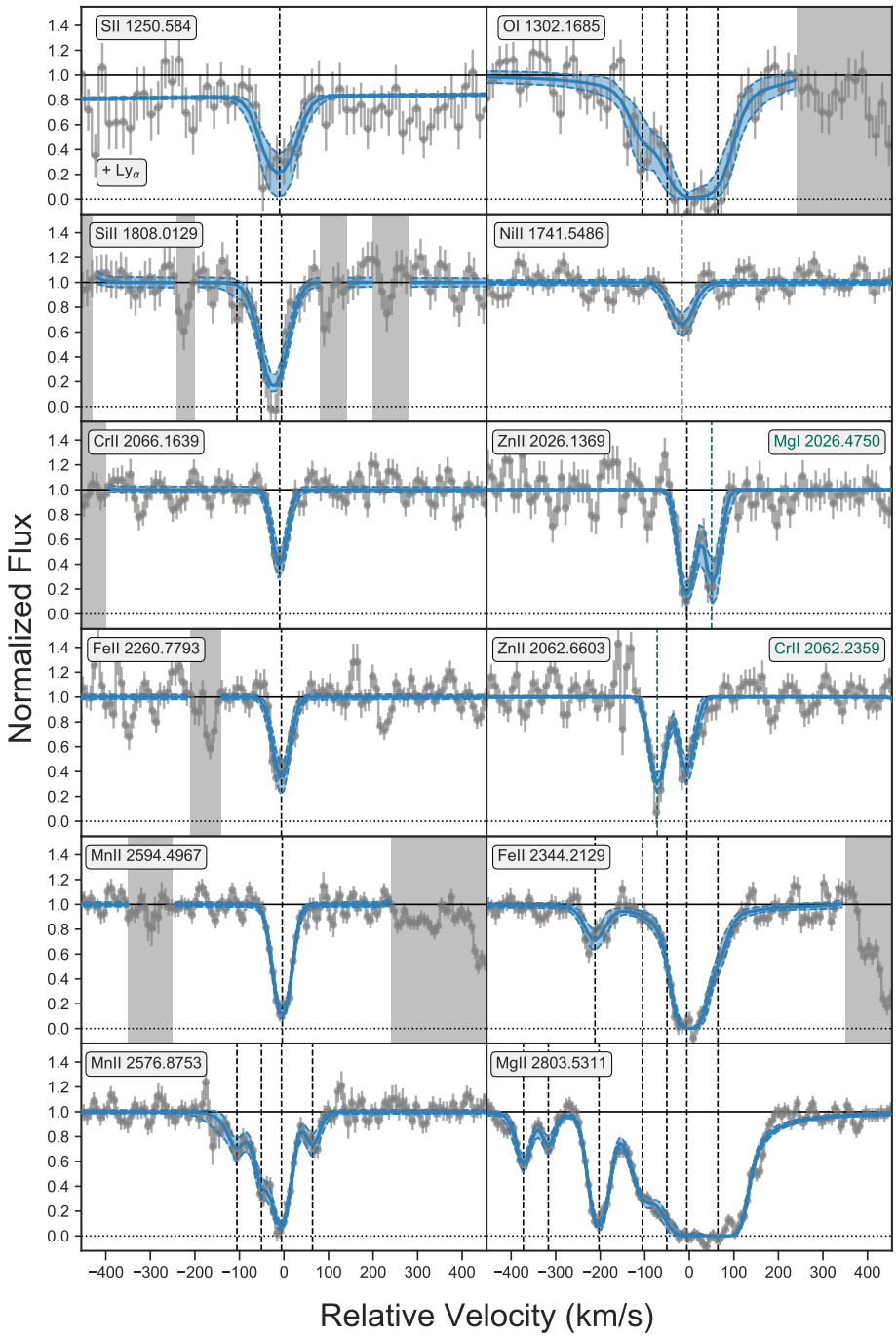

Figure 4.34: Results from fitting the absorption lines in the X-shooter spectrum of GRB150403A. The result of fitting the H_2 lines is shown in Fig. 4.10.

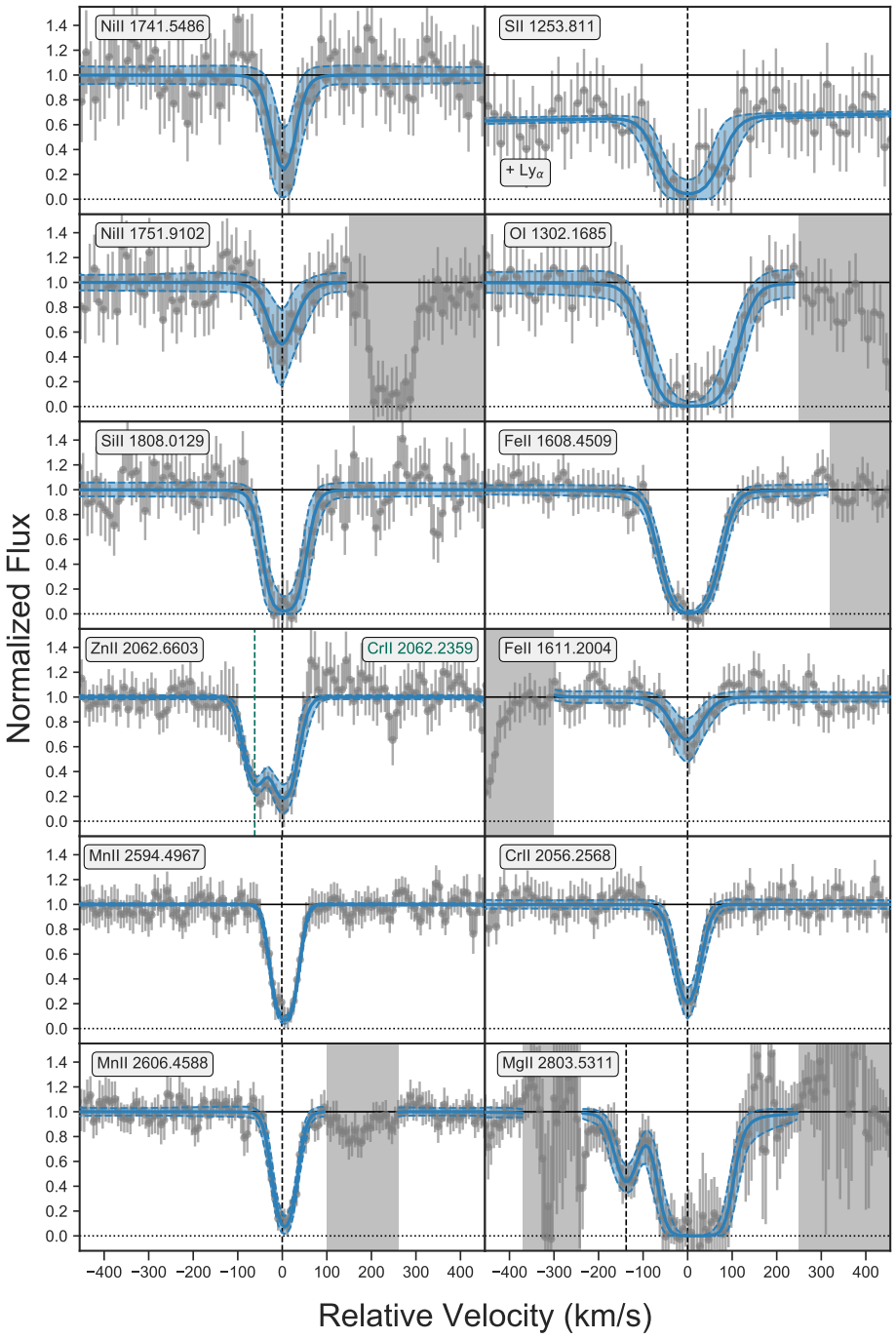

Figure 4.35: Results from fitting the absorption lines in the X-shooter spectrum of GRB151021A. The result of fitting the H_2 lines is shown in Fig. 4.11.

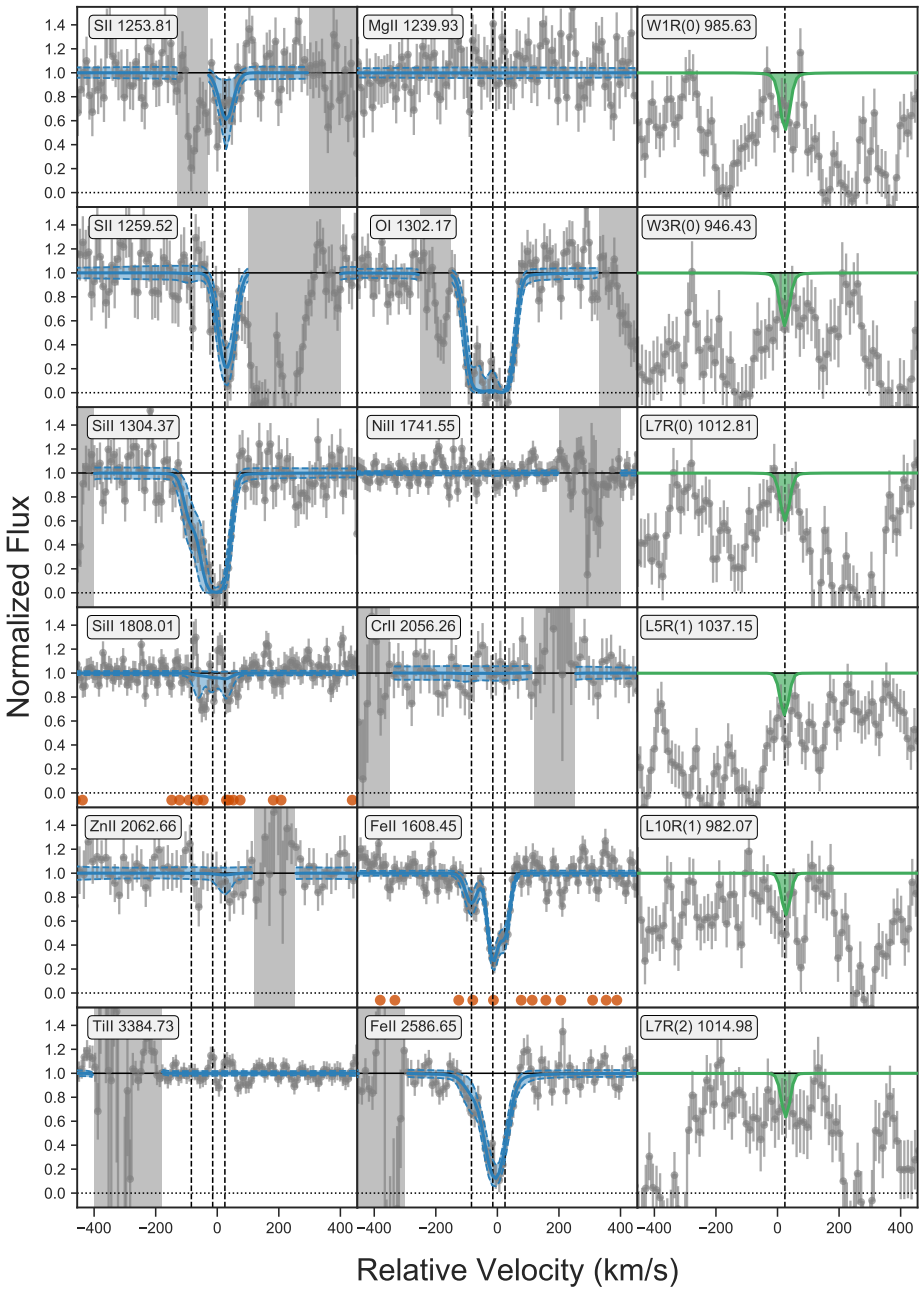

Figure 4.36: Results from fitting the absorption lines in the X-shooter spectrum of GRB151027B. The position of telluric lines, which were corrected, are marked by red dots. We do not find compelling evidence for absorption from molecular hydrogen down to the limits given in Table 4.4. To the right, in green, we plot synthetic spectra for these limits

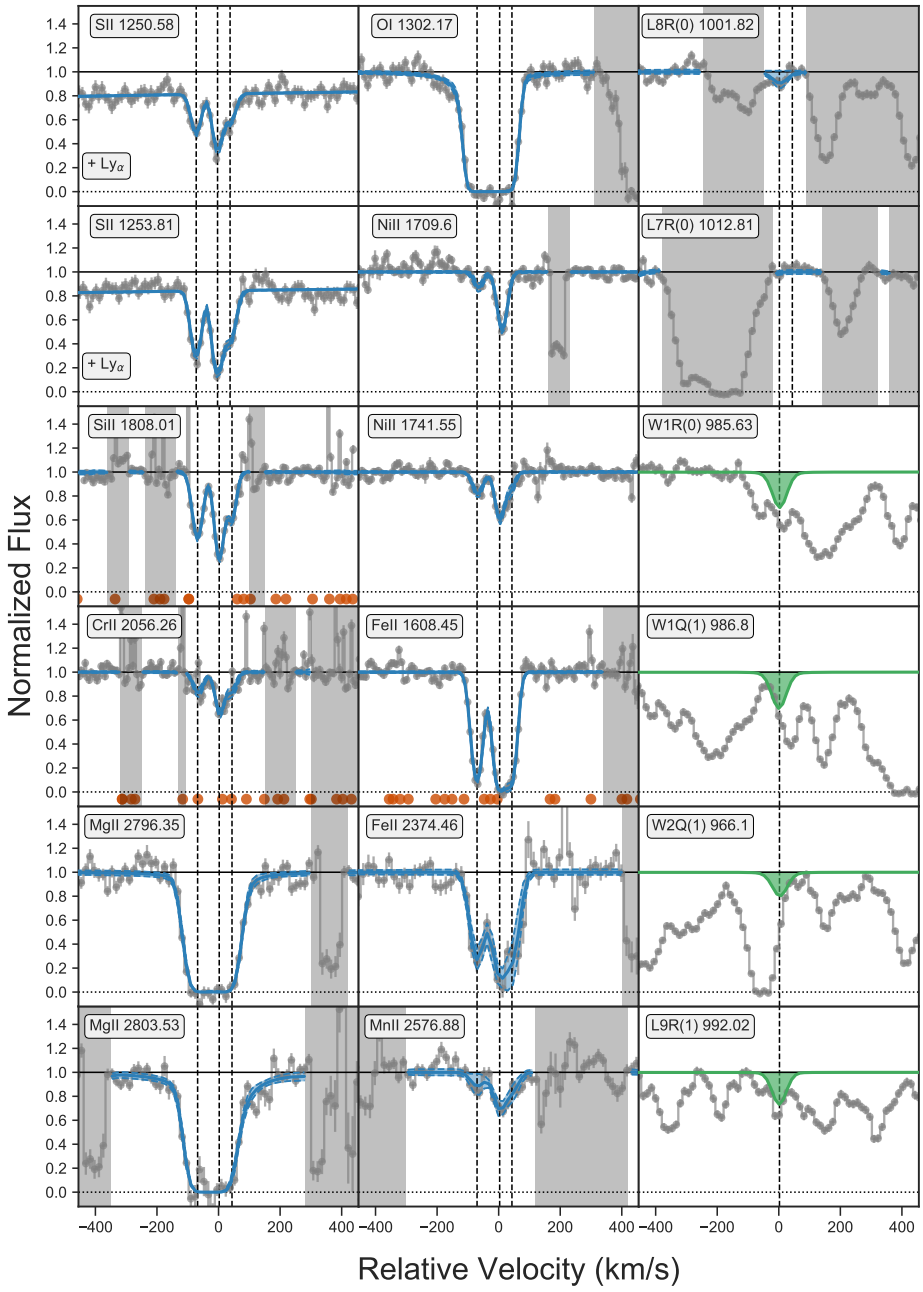

Figure 4.37: Results from fitting the absorption lines in the X-shooter spectrum of GRB160203A. The position of telluric lines, which were corrected, are marked by red dots. As shown in the 6 subplots to the right, the spectrum is consistent with absorption from molecular hydrogen, but only to the agree of claiming a *possible* detection. In green we plot synthetic spectra for the upper limits given in Table 4.4.

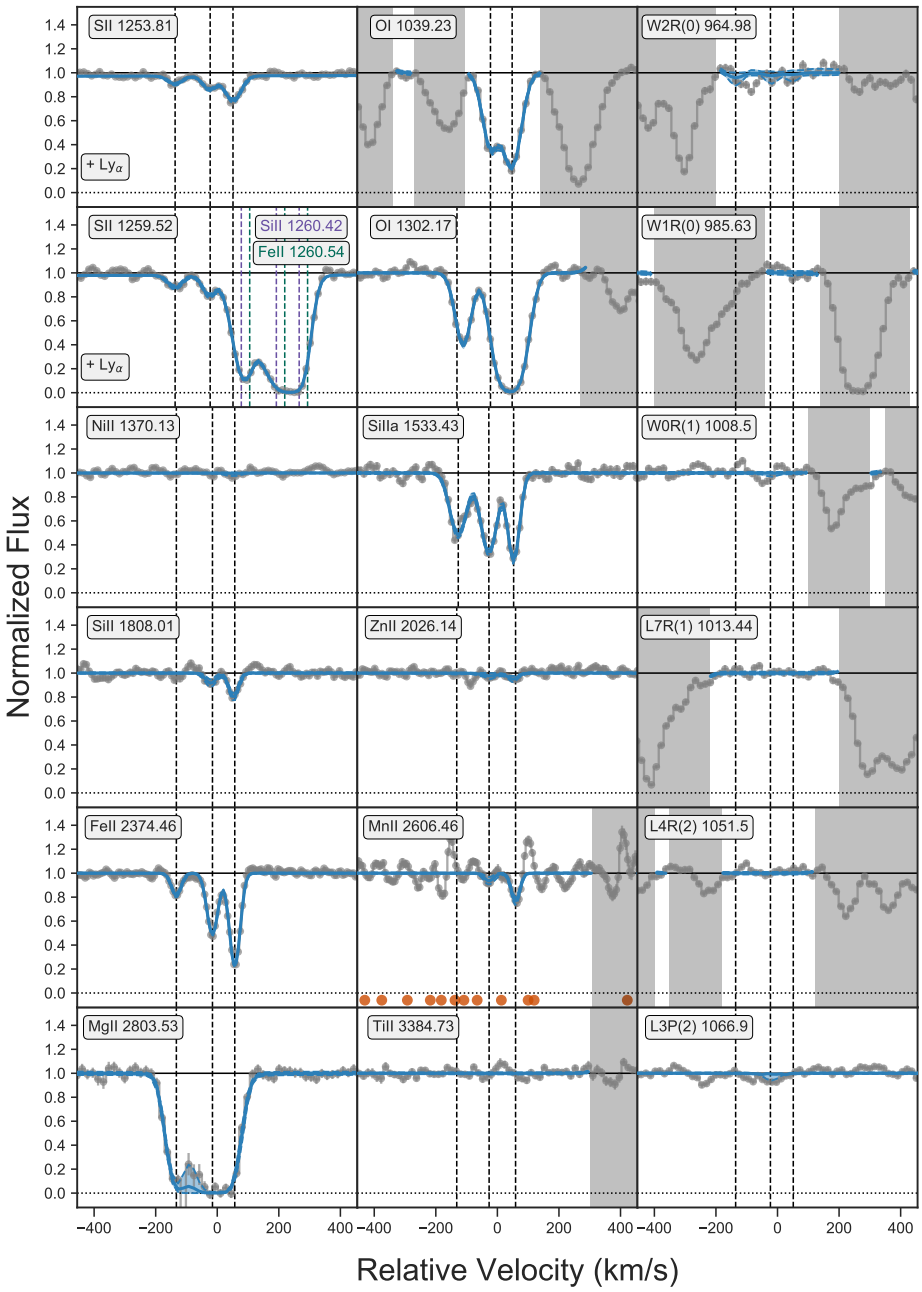

Figure 4.38: Results from fitting the absorption lines in the X-shooter spectrum of GRB161023A. The position of telluric lines, which were corrected, are marked by red dots. As shown to the right, we do not find any evidence for absorption from molecular hydrogen. This X-shooter spectrum was previously also analysed by de Ugarte Postigo et al. (2018).

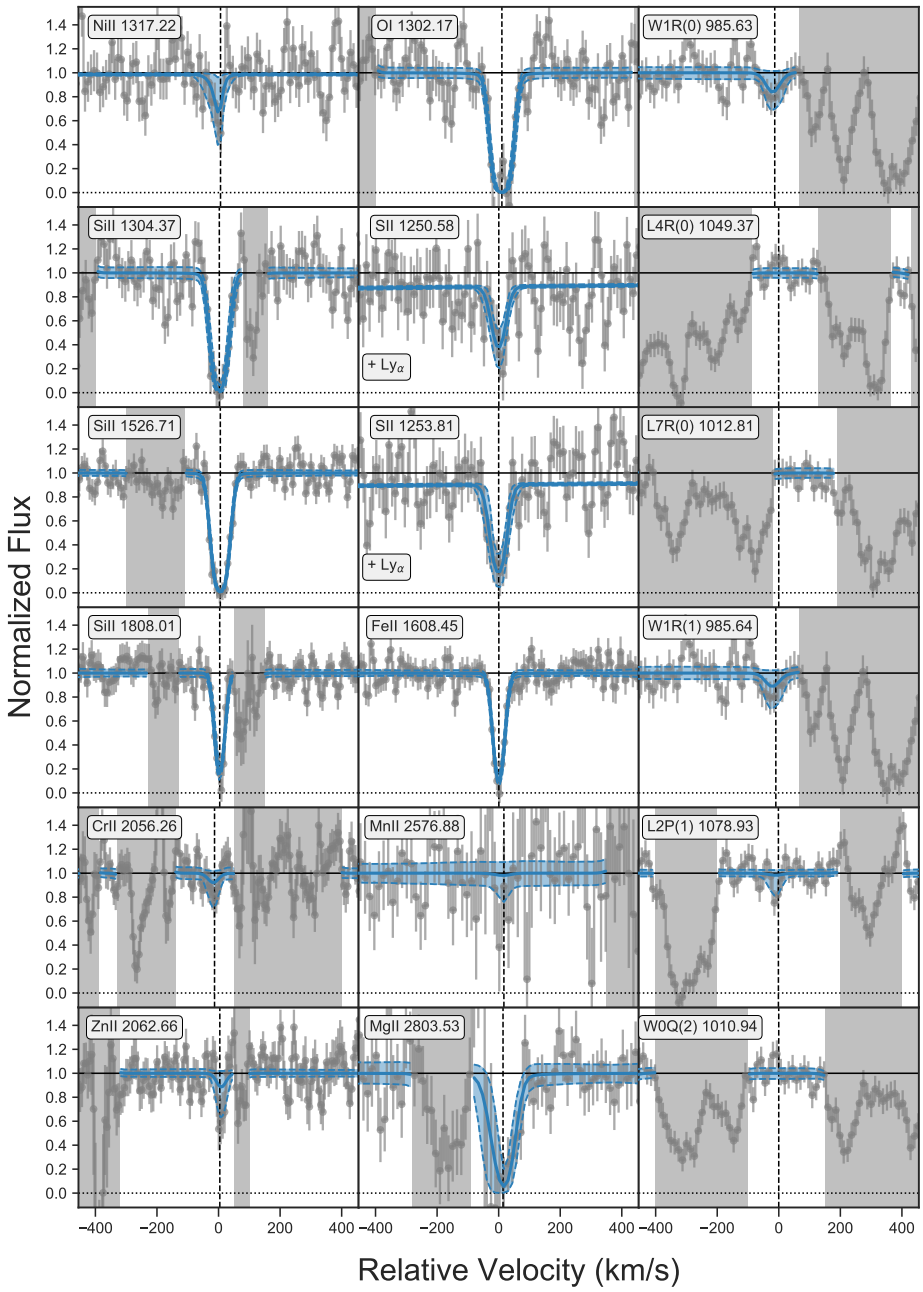

Figure 4.39: Results from fitting the absorption lines in the X-shooter spectrum of GRB170202A. As shown in the 6 subplots to the right, the spectrum is consistent with absorption from molecular hydrogen in the strongest J = 0 and J = 1 at $\lambda \sim 985.6$ Å, which led us to claim a *possible* detection.

Chapter 5

Prospects and outlook

As shown in the previous section, based on a direct search of absorption signatures of molecular hydrogen, GRBs offer an ideal probe of diffuse molecular gas in the ISM of high redshift galaxies. This is because, in contrast to previous beliefs, H_2 is indeed commonly detected in GRB-DLAs, especially in those with high neutral hydrogen column densities $\log N(\mathrm{H\,I}) > 21.5$. Similar evidence recently also came from a survey for neutral atomic-carbon along GRB sight-lines, which is known to be a tracer of cold, molecular gas as well (Heintz et al., 2019). Since both of the studied samples are based on the X-shooter GRB afterglow legacy sample (Selsing et al., 2018), the next step toward understanding the physical condition in these H_2-bearing DLAs at redshift $z > 2$, is to combine the results of both approaches. For example, the excitation temperature, T_{ij}, of the cold gas can be inferred from the column densities of the two lowest rotational levels of H_2, and it was found that T_{01} is a good representation of the overall kinetic temperature of the cold neutral medium (Roy et al., 2006). On the other hand, the density of the molecular gas can be inferred from the relative abundances of the three fine-structure transitions of neutral carbon's ground state. Based on these measurements and additional photo-ionization modeling with, e.g., CLOUDY (Ferland et al., 2017), it will be possible to constrain the cloud sizes and their internal thermal pressure as well as the role of dust and the influence of the GRB on these DLA (a paper is already in preparation Heintz et al., 2019, in prep.). The current sample of 10 H_2 and C I-bearing GRB absorbers at $z > 1.8$ is listed in Tab. 5.1.

The influence of the GRB on its surroundings can also be studied in case vibrationally excited molecular hydrogen is detected. Since the tentative detection in the spectrum of GRB 150403A (see Sect. 4), H_2^* has additionally been identified in another two, or maybe even three, GRB afterglows: after the publication of Bolmer, J. et al. (2019), two new GRBs with H_2-bearing DLAs have been observed, which are both showing clear evidence for H_2^* as well. Additionally, H_2^* is tentatively detected in the spectrum of GRB 131030A at $z = 1.296$. The latter was identified after searching for H_2^* absorption signatures in the spectra of the GRBs at $1.1 < z < 2.0$ from the sample presented in (Selsing et al., 2018). While cold H_2 only absorbs at wavelength blue-wards of Lyman-α ($\lambda < 1130$ Å), where the detection in GRB spectra is hampered by intervening absorption from dust and Ly-α forest lines, the H_2^* lines at $1300 \lesssim \lambda < 1650$ Å are easily distinguished from the continuum flux of the afterglow, and it is also possible to detect them in the X-shooter UVB arm for bursts at $1.1 < z < 2.0$.

The column densities of H_2^* in these spectra were modeled by fitting the afterglow

Table 5.1: Sample of ten H_2- and C I-bearing GRB absorbers at $z > 1.8$

GRB yymmdd#	Redshift (z)	log N(H I)	log N(H_2)	$N(H_2^*)$ $(6.73 \cdot 10^{16})$	[X/H]	A_V (mag)
080607	3.0363	22.70 ± 0.15	21.20 ± 0.20	7 ± 6	> -0.2	2.58 ± 0.45
120327A	2.8143	22.07 ± 0.01	17.39 ± 0.13	< 0.04	-1.49 ± 0.04	< 0.03
120815A	2.3582	22.09 ± 0.01	20.42 ± 0.08	0.19 ± 0.02	-1.45 ± 0.03	0.19 ± 0.04
120909A	3.9290	21.82 ± 0.02	17.25 ± 0.23	< 0.05	-1.06 ± 0.12	0.16 ± 0.04
121024A	2.3005	21.78 ± 0.02	19.90 ± 0.17	< 0.07	-0.76 ± 0.06	0.26 ± 0.07
141109A	2.9940	22.18 ± 0.02	18.02 ± 0.12	< 0.07	-1.63 ± 0.06	0.11 ± 0.03
150403A	2.0571	21.73 ± 0.02	19.90 ± 0.14	$\leq 0.09 \pm 0.02$	-1.04 ± 0.04	< 0.03
180325A[a]	2.2486	22.30 ± 0.14	< 20.60[a]	< 0.11	> -0.96	1.58 ± 0.12
181020A	2.9380	22.20 ± 0.05	20.40 ± 0.04	0.28 ± 0.03	-1.57 ± 0.06	0.29 ± 0.02
190114A	3.3764	22.15 ± 0.05	19.44 ± 0.04	0.20 ± 0.05[b]	-1.23 ± 0.07	0.36 ± 0.02

Notes. [a]Due to the high A_V no search for H_2 could be performed in case of GRB 180325A, but its presence is likely given the detection of C I (Zafar, Heintz et al., 2018). The upper limit was derived using the relation found by Balashev et al. (2015) between N(H_2) and the column density of neutral chlorine, which is $\log N(\mathrm{Cl\,I}) < 14.2$ for GRB180325A. [b]Average value.

spectra with the synthetic spectrum from Draine & Hao (2002) for $R = 10\,000$, which is downgraded to the resolution of the given arm (usually the UVB arm with $R \sim 6000$). Any intervening lines are either blended out or included in the fit. The resulting column densities are listed in Tab. 5.1 and the spectra are shown in Fig. 5.2 and 5.3. Here, the H_2^* *absorption strength* is defined as the multiplier of the model from Draine & Hao (2002) which was created for a column density of $N(H_2^*) = 6.73 \cdot 10^{16}\mathrm{cm}^{-2}$. From Fig. 5.1, one can see that on average $\log N(H_2^*)$ seems to increase with $\log N(H_2)$ and also with the total metal column $\log N(\mathrm{H\,I})$ + [X/H]. The sample, however, is far from being large enough to draw any significant statistical conclusion. Nonetheless, the most important aspect to address is the question whether the molecular hydrogen in the DLA is excited through UV radiation from the interstellar radiation field, or by UV pumping from the GRB itself (as suggested by Draine, 2000; Draine & Hao, 2002).

In the Milky Way, H_2^* can be detected toward stars behind or within diffuse and translucent clouds (Federman et al., 1995; Meyer et al., 2001; Boissé et al., 2005; Rachford et al., 2014), indicating that there is a close interaction between the molecular gas in these clouds and the UV radiation field of the observed, nearby stars. Similarly, the H_2^* detected in GRB-DLAs could be the natural consequence of the UV radiation field in their host galaxies, supported by the fact that GRB-DLAs are consistently shown to be located at least a few hundreds of parsecs from the GRB itself (e.g., Hartoog et al., 2013, and references therein). Direct evidence for UV pumping of H_2 from the radiation of the GRB itself could thus only come from a temporal change in the column density of H_2^*. As a matter of fact, the recent GRB 190114A could be observed with a sequence of X-shooter spectra, shortly after the detection of the prompt emission. Individual modeling of each of the spectra revealed that an increasing H_2^* column density, consistent with

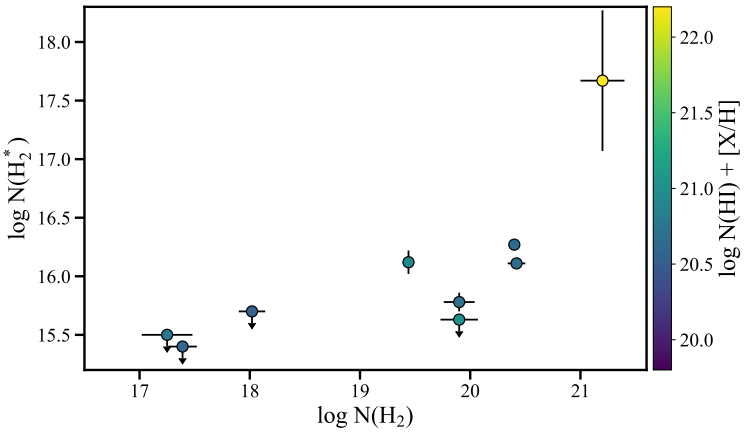

Figure 5.1: Column density of H_2^* versus column density of H_2. The color denotes the total metal column as indicated by the colorbar to the right.

similar behavior in Fe II*, and O I* (see Fig. 5.3). The increasing column densities of these excited states can only be explained by UV pumping from the GRB itself, and with a detailed modeling with CLOUDY it will be possible to constrain the distance and possibly also the size of the absorbing cloud (e.g., Vreeswijk et al., 2007).

To build a proper model in CLOUDY, it is essential to know the spectral index and the temporal evolution of the optical afterglow. Traditionally, NIR/optical afterglow light-curves of individual bursts are modeled with smoothly connected power-laws (e.g., Filgas et al., 2011; Zaninoni et al., 2013; Nardini et al., 2014). These broadband modeling studies for different GRB afterglows have resulted in widely varying values for the physical parameters of the shock accelerated region (also for the same bursts but from different authors) showing the complexity of this type of analysis (e.g., Beniamini & van der Horst, 2017, and references therein). Uncertainties can arise from unknown quantities like the circumburst environment, wind or ISM, and its density, the viewing angle, contributions from a reverse shock, or suppression of the synchrotron flux due to Inverse Compton cooling. These problems arise, because instruments like GROND can only operate during the night and observations are then additionally restricted to right weather conditions, such that individual light curves are typically incomplete. Also, while X-ray afterglow light-curves are relatively similar and show characteristic features (Zhang et al., 2006), NIR/optical afterglows vary more greatly between individual events (e.g., Zaninoni et al., 2013; Li et al., 2018; Bolmer et al., 2018). As the next step toward an understanding of the underlying physics of GRB afterglows, one approach would be to model the light-curves on a population based level. Sanders et al. (2015), for example, constructed a hierarchical and multi-level Bayesian model in STAN in order to fit a large sample of Type IIP SNe by partial pooling among the different objects, resulting in a tighter distribution for the parameters of interest. A similar model could be created for the now around 50 well covered GROND NIR/optical GRB afterglows. Such a model could

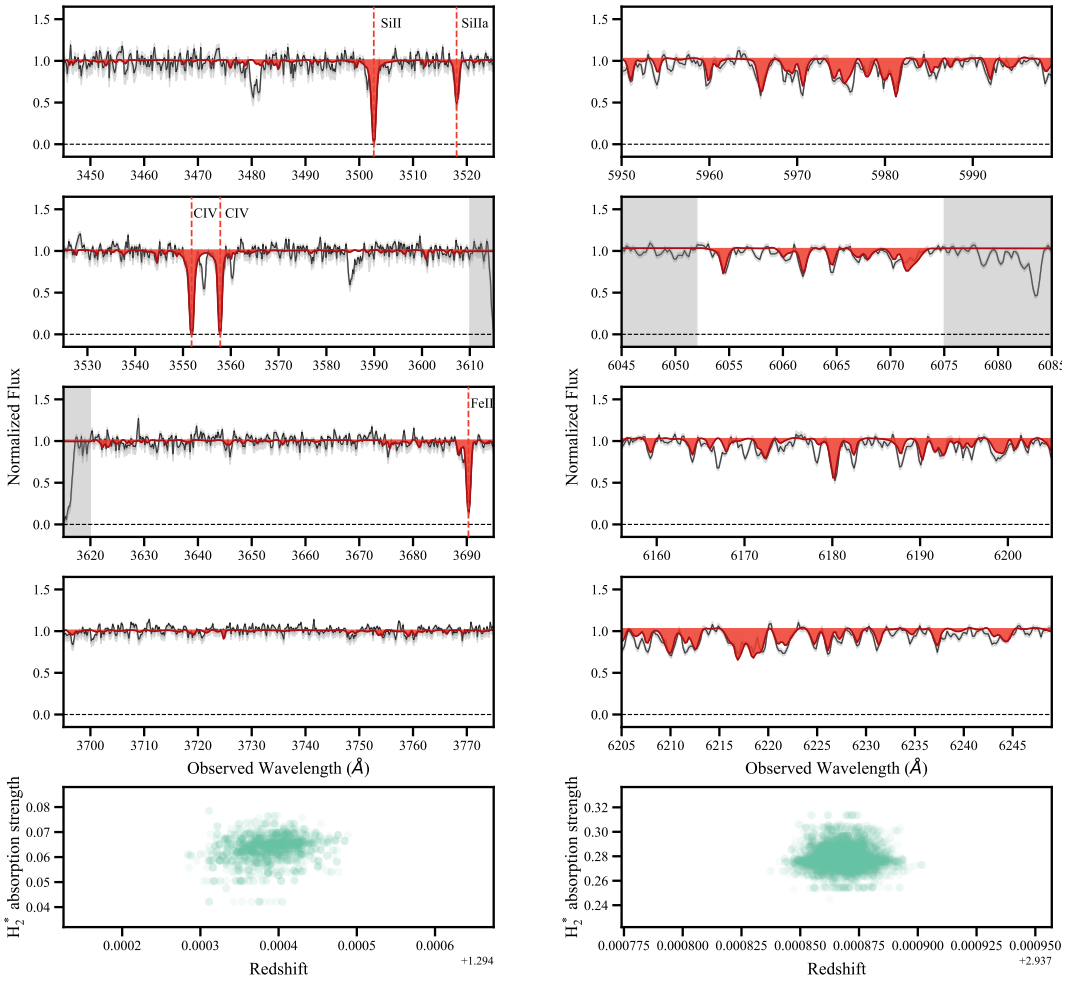

(a) GRB 131030A **(b)** GRB 181020A

Figure 5.2: Normalized spectrum of 131030A (a) and GRB 181020A (b) showing evidence for absorption from vibrationally-excited molecular hydrogen H_2^*. The model is indicated by the solid red line. In the insets at the bottom we show the posterior distribution of the redshift z and the H_2^* absorption strength from the Draine & Hao (2002) model that we fitted to the data.

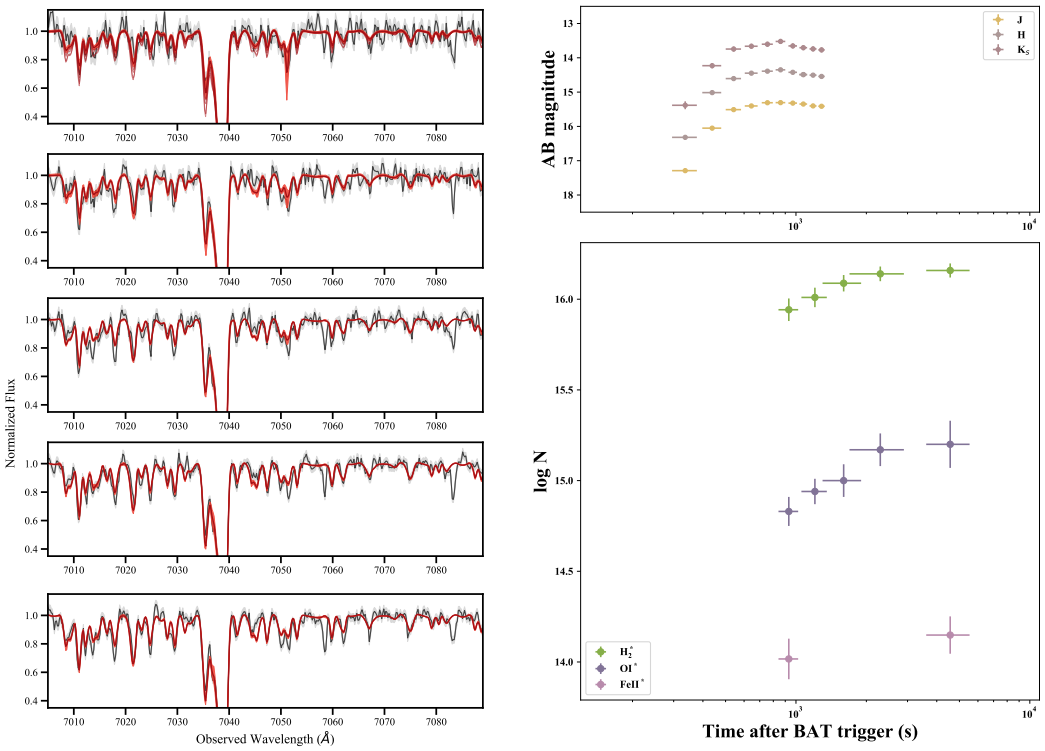

(a) Epoch 1 to 5 from top to bottom, corresponding to the data points in the lower right inset.

(b) *Upper panel*: GROND JHK_s light curves. *Bottom panel*: column densities of H_2^*, Fe II*, and O I* as a function of time.

Figure 5.3: Vibrationally excited H_2 in the sequence of five X-shooter spectra of GRB 19011A, taken between 12 and 108 min after the BAT trigger.

in principle include the full three-dimensional information such as the evolution of the spectral shape, including K-corrections and dust extinction.

Finally, future observations with current instruments like X-shooter or GROND are furthermore of great importance to detect more exceptional events as well as to increase sample sizes and thus statistics. Additionally, deep NIR/optical imaging and spectroscopy from upcoming missions like the *James Webb Space Telescope* or the instruments that are going to be mounted at the 39 meter *European Extremely Large Telescope* will allow to detect GRB afterglows and host galaxies at higher redshift. With these observatories it will also be possible to detect GRBs behind translucent or dark molecular clouds as well as to study the time variability of excited transitions for a longer period and with higher temporal resolution.

Appendix A

Contributions to other works

Some of the methods and analysis techniques required or developed for the goals of this thesis were also used to contribute to a number of other projects. For example, reduction and calibration of numerous GROND observations are now published in a variety of papers studying GRBs (Fynbo et al., 2014; Greiner et al., 2014; Varela et al., 2016; Schady et al., 2015; Melandri et al., 2017; Greiner et al., 2018; Izzo et al., 2019), their host galaxies (Greiner, Fox et al., 2015; Wiseman, Schady et al., 2017), or blazars (Ajello et al., 2014; Kaur et al., 2017). Also the code developed for Bolmer, J. et al. (2019), was already used for other projects (de Ugarte Postigo et al., 2018; Zafar, Heintz et al., 2018; Heintz et al., 2018, 2019, 2019, in prep.). The complete list of publications between 2014 and the end of 2018 can be found under the following link: https://ui.adsabs.harvard.edu/#search/q=author%3A%22Bolmer%2C%20Jan%22%20year%3A2014-2018&sort=date%20desc%2C%20bibcode%20desc&p_=0

Bibliography

Aceituno, F. J., Castro-Tirado, A. J., Sanchez-Ramirez, R. & Gorosabel, J. (2014, Apr). GRB 140428A: 1.5m OSN I-band detection. *GRB Coordinates Network*, *16182*.

Afonso, P., Greiner, J., Pian, E. et al. (2011, Feb). GRB 050502B optical afterglow: a jet-break at high redshift. *A&A*, *526*, A154. doi: 10.1051/0004-6361/200913965

Ajello, M., Romani, R. W., Gasparrini, D., Shaw, M. S. et al. (2014, Jan). The Cosmic Evolution of Fermi BL Lacertae Objects. *ApJ*, *780*, 73. doi: 10.1088/0004-637X/780/1/73

Altay, G., Theuns, T., Schaye, J. et al. (2011, Aug). Through Thick and Thin: H I Absorption in Cosmological Simulations. *ApJ*, *737*, L37. doi: 10.1088/2041-8205/737/2/L37

Amanullah, R., Goobar, A., Johansson, J. et al. (2014, Jun). The Peculiar Extinction Law of SN 2014J Measured with the Hubble Space Telescope. *ApJ*, *788*, L21. doi: 10.1088/2041-8205/788/2/L21

Andersen, M. I., Hjorth, J., Pedersen, H. et al. (2000, Dec). VLT identification of the optical afterglow of the gamma-ray burst GRB 000131 at $z = 4.50$. *A&A*, *364*, L54-L61.

Arabsalmani, M., Le Floc'h, E., Dannerbauer, H. et al. (2018, May). A molecular gas-rich GRB host galaxy at the peak of cosmic star formation. *MNRAS*, *476*, 2332-2338. doi: 10.1093/mnras/sty194

Arabsalmani, M., Møller, P., Fynbo, J. P. U. et al. (2015, Jan). On the mass-metallicity relation, velocity dispersion, and gravitational well depth of GRB host galaxies. *MNRAS*, *446*, 990-999. doi: 10.1093/mnras/stu2138

Arabsalmani, M., Møller, P., Perley, D. A. et al. (2018, Jan). Mass and metallicity scaling relations of high-redshift star-forming galaxies selected by GRBs. *MNRAS*, *473*, 3312-3324. doi: 10.1093/mnras/stx2451

Asplund, M., Grevesse, N., Sauval, A. J. & Scott, P. (2009, Sep). The Chemical Composition of the Sun. *Annual Review of Astronomy and Astrophysics*, *47*, 481-522. doi: 10.1146/annurev.astro.46.060407.145222

Bailly, D., Salumbides, E., Vervloet, M. & Ubachs, W. (2010). Accurate level energies in the $EF\,^1\Sigma_g^+$, $GK\,^1\Sigma_g^+$, $H\,^1\Sigma_g^+$, $B\,^1\Sigma_u^+$, $C\,^1\Pi_u$, $B'\,^1\Sigma_u^+$, $D\,^1\Pi_u$, $I\,^1\Pi_g$, $J\,^1\Delta_g$ states of H_2. *Molecular Physics*, *108*(7-9), 827-846. doi: 10.1080/00268970903413350

Balashev, S. A., Klimenko, V. V., Ivanchik, A. V. et al. (2014, May). Molecular hydrogen absorption systems in Sloan Digital Sky Survey. *MNRAS*, *440*, 225-239. doi: 10.1093/mnras/stu275

Balashev, S. A. & Noterdaeme, P. (2018, Jul). Constraining the H_2 column density distribution at $z \sim 3$ from composite DLA spectra. *MNRAS*, *478*, L7-L11. doi: 10.1093/mnrasl/sly067

Balashev, S. A., Noterdaeme, P., Klimenko, V. V. et al. (2015, Mar). Neutral chlorine and molecular hydrogen at high redshift. *A&A*, *575*, L8. doi: 10.1051/0004-6361/201425553

Balashev, S. A., Noterdaeme, P., Rahmani, H. et al. (2017, Sep). CO-dark molecular gas at high redshift: very large H_2 content and high pressure in a low-metallicity damped Lyman alpha system. *MNRAS*, *470*, 2890-2910. doi: 10.1093/mnras/stx1339

Barnes, J., Duffell, P. C., Liu, Y. et al. (2018, Jun). A GRB and Broad-lined Type Ic Supernova from a Single Central Engine. *ApJ*, *860*, 38. doi: 10.3847/1538-4357/aabf84

Barthelmy, S. D., Baumgartner, W. H., Cummings, J. R. et al. (2010, Sep). GRB 100905A: Swift-BAT refined analysis. *GRB Coordinates Network*, *11218*.

Barthelmy, S. D., Chincarini, G., Burrows, D. N. et al. (2005, Dec). An origin for short γ-ray bursts unassociated with current star formation. *Nature*, *438*, 994-996. doi: 10.1038/nature04392

Baumgartner, W. H., Tueller, J., Markwardt, C. B. et al. (2013, Jul). The 70 month *Swift*-bat all-sky hard x-ray survey. *The Astrophysical Journal Supplement Series*, *207*(2), 19. doi: 10.1088/0067-0049/207/2/19

Belfiore, F., Maiolino, R., Tremonti, C. et al. (2017, Jul). SDSS IV MaNGA - metallicity and nitrogen abundance gradients in local galaxies. *MNRAS*, *469*, 151-170. doi: 10.1093/mnras/stx789

Beniamini, P. & van der Horst, A. J. (2017, Dec). Electrons' energy in GRB afterglows implied by radio peaks. *MNRAS*, *472*, 3161-3168. doi: 10.1093/mnras/stx2203

Berger, E. (2014). Short-duration gamma-ray bursts. *Annual Review of Astronomy and Astrophysics*, *52*(1), 43-105. doi: 10.1146/annurev-astro-081913-035926

Berger, E., Penprase, B. E., Cenko, S. B. et al. (2006, May). Spectroscopy of GRB 050505 at $z = 4.275$: A $\log N(\mathrm{H\,I}) = 22.1$ DLA Host Galaxy and the Nature of the Progenitor. *ApJ*, *642*, 979-988. doi: 10.1086/501162

Betancourt, M. (2017, Jun). The Convergence of Markov chain Monte Carlo Methods: From the Metropolis method to Hamiltonian Monte Carlo. *ArXiv e-prints*, arXiv:1706.01520.

Bianchi, S. & Schneider, R. (2007, Jul). Dust formation and survival in supernova ejecta. *MNRAS*, *378*, 973-982. doi: 10.1111/j.1365-2966.2007.11829.x

Bigiel, F., Leroy, A., Walter, F. et al. (2008, Dec). The Star Formation Law in Nearby Galaxies on Sub-Kpc Scales. *AJ*, *136*, 2846-2871. doi: 10.1088/0004-6256/136/6/2846

Bigiel, F., Leroy, A. K., Walter, F. et al. (2011, Apr). A Constant Molecular Gas Depletion Time in Nearby Disk Galaxies. *ApJ*, *730*, L13. doi: 10.1088/2041-8205/730/2/L13

Bignone, L. A., Tissera, P. B. & Pellizza, L. J. (2017, Aug). The metallicity and star formation activity of long gamma-ray burst hosts for $z \sim 3$: insights from the Illustris simulation. *MNRAS*, *469*, 4921-4932. doi: 10.1093/mnras/stx1132

Blitz, L. & Rosolowsky, E. (2006, Oct). The Role of Pressure in GMC Formation II: The H_2-Pressure Relation. *ApJ*, *650*, 933-944. doi: 10.1086/505417

Boissé, P., Le Petit, F., Rollinde, E. et al. (2005, Jan). A far UV study of interstellar gas towards HD 34078: High excitation H_2 and small scale structure. *A&A*, *429*, 509-523. doi: 10.1051/0004-6361:20047135

Bolatto, A. D., Wolfire, M. & Leroy, A. K. (2013, Aug). The CO-to-H_2 Conversion Factor. *Annual Review of Astronomy and Astrophysics*, *51*, 207-268. doi: 10.1146/annurev-astro-082812-140944

Bolmer, J., Greiner, J., Krühler, T. et al. (2018, Jan). Dust reddening and extinction curves toward gamma-ray bursts at $z > 4$. *A&A*, *609*, A62. doi: 10.1051/0004-6361/201731255

Bolmer, J., Knust, F. & Greiner, J. (2015, Nov). GRB 151112A: GROND photometric redshift and i'-band prediction. *GRB Coordinates Network*, *18603*.

Bolmer, J., Ledoux, C., Wiseman, P. et al. (2019, Mar). Evidence for diffuse molecular gas and dust in the hearts of gamma-ray burst host galaxies: Unveiling the nature of high-redshift damped Lyman-α systems. *A&A*, *623*, A43. doi: 10.1051/0004-6361/201834422

Bolton, J. S., Puchwein, E., Sijacki, D. et al. (2017, Jan). The Sherwood simulation suite: overview and data comparisons with the Lyman-α forest at redshifts $2 \leq z \leq 5$. *MNRAS*, *464*, 897-914. doi: 10.1093/mnras/stw2397

Bouwens, R. J., Illingworth, G. D., Oesch, P. A. et al. (2012, Aug). UV-continuum Slopes at $z \sim$ 4-7 from the HUDF09+ERS+CANDELS Observations: Discovery of a Well-defined UV Color-Magnitude Relationship for $z = 4$ Star-forming Galaxies. *ApJ*, *754*, 83. doi: 10.1088/0004-637X/754/2/83

Bouwens, R. J., Illingworth, G. D., Oesch, P. A. et al. (2015, Apr). UV Luminosity Functions at Redshifts $z \sim 4$ to $z \sim 10$: 10,000 Galaxies from HST Legacy Fields. *ApJ*, *803*, 34. doi: 10.1088/0004-637X/803/1/34

Bucciantini, N., Quataert, E., Arons, J. et al. (2007, Oct). Magnetar-driven bubbles and the origin of collimated outflows in gamma-ray bursts. *MNRAS*, *380*, 1541-1553. doi: 10.1111/j.1365-2966.2007.12164.x

Buchner, J., Schulze, S. & Bauer, F. E. (2017, Feb). Galaxy gas as obscurer - I. GRBs x-ray galaxies and find an $N_H^3 \propto M_*$ relation. *MNRAS*, *464*, 4545-4566. doi: 10.1093/mnras/stw2423

Burgess, J. M., Bégué, D., Bacelj, A. et al. (2018, Oct). Gamma-ray bursts as cool synchrotron sources. *arXiv e-prints*, arXiv:1810.06965.

Burgh, E. B., France, K. & Jenkins, E. B. (2010, Jan). Atomic and Molecular Carbon as a Tracer of Translucent Clouds. *ApJ*, *708*, 334-341. doi: 10.1088/0004-637X/708/1/334

Burrows, A., Dessart, L., Livne, E. et al. (2007, Jul). Simulations of Magnetically Driven Supernova and Hypernova Explosions in the Context of Rapid Rotation. *ApJ*, *664*, 416-434. doi: 10.1086/519161

Burrows, D. N., Hill, J. E., Nousek, J. A. et al. (2005, Oct). The swift x-ray telescope. *Space Science Reviews*, *120*(3), 165–195. doi: 10.1007/s11214-005-5097-2

Butler, N., Watson, A. M., Kutyrev, A. et al. (2014, Mar). GRB 140304A: RATIR g-band dropout. *GRB Coordinates Network*, *15928*.

Callingham, J. R., Tuthill, P. G., Pope, B. J. S. et al. (2019, Jan). Anisotropic winds in a Wolf-Rayet binary identify a potential gamma-ray burst progenitor. *Nature Astronomy*, *3*, 82-87. doi: 10.1038/s41550-018-0617-7

Campana, S., Salvaterra, R., Ferrara, A. & Pallottini, A. (2015, Mar). Missing cosmic metals revealed by X-ray absorption towards distant sources. *A&A*, *575*, A43. doi: 10.1051/0004-6361/201425083

Cano, Z., Wang, S.-Q., Dai, Z.-G. & Wu, X.-F. (2017, Jan). The Observer's Guide to the Gamma-Ray Burst Supernova Connection. *Advances in Astronomy*, *2017*, 8929054. doi: 10.1155/2017/8929054

Cardelli, J. A., Clayton, G. C. & Mathis, J. S. (1989, Oct). The relationship between infrared, optical, and ultraviolet extinction. *ApJ*, *345*, 245-256. doi: 10.1086/167900

Castro-Tirado, A. J., Møller, P., García-Segura, G. et al. (2010, Jul). GRB 021004: Tomography of a gamma-ray burst progenitor and its host galaxy. *A&A*, *517*, A61. doi: 10.1051/0004-6361/200913966

Castro-Tirado, A. J., Sánchez-Ramírez, R., Ellison, S. L. et al. (2013, Dec). GRB 130606A within a sub-DLA at redshift 5.91. *ArXiv e-prints*.

Cazaux, S. & Spaans, M. (2004, Aug). Molecular Hydrogen Formation on Dust Grains in the High-Redshift Universe. *ApJ*, *611*, 40-51. doi: 10.1086/422087

Cen, R. (2012, Apr). The Nature of Damped Lyα Systems and Their Hosts in the Standard Cold Dark Matter Universe. *ApJ*, *748*, 121. doi: 10.1088/0004-637X/748/2/121

Cenko, S. B., Berger, E., Djorgovski, S. G. et al. (2006, May). GRB060522: $z = 5.11$ Keck-LRIS redshift. *GRB Coordinates Network*, *5155*.

Cenko, S. B., Butler, N. R., Ofek, E. O. et al. (2010, Jul). Unveiling the Origin of GRB 090709A: Lack of Periodicity in a Reddened Cosmological Long-Duration Gamma-Ray Burst. *AJ*, *140*, 224-234. doi: 10.1088/0004-6256/140/1/224

Cenko, S. B. & Fox, D. B. (2006). GRB 061222A: confirmation of Gemini afterglow candidate. *GRB Coordinates Network*, *5978*.

Cenko, S. B., Kelemen, J., Harrison, F. A. et al. (2009, Mar). Dark Bursts in the Swift Era: The Palomar 60 Inch-Swift Early Optical Afterglow Catalog. *ApJ*, *693*, 1484-1493. doi: 10.1088/0004-637X/693/2/1484

Cenko, S. B., Perley, D. A., Morgan, A. N. et al. (2010, May). GRB 100513A: Gemini/GMOS spectroscopic redshift. *GRB Coordinates Network*, *10752*.

Chary, R., Berger, E. & Cowie, L. (2007, Dec). Spitzer Observations of Gamma-Ray Burst Host Galaxies: A Unique Window into High-Redshift Chemical Evolution and Star Formation. *ApJ*, *671*, 272-277. doi: 10.1086/522692

Chen, H.-W., Prochaska, J. X. & Gnedin, N. Y. (2007, Oct). A New Constraint on the Escape Fraction in Distant Galaxies Using γ-Ray Burst Afterglow Spectroscopy. *ApJ*, *667*, L125-L128. doi: 10.1086/522306

Chornock, R., Berger, E., Fox, D. B., Lunnan, R. et al. (2013, Sep). GRB 130606A as a Probe of the Intergalactic Medium and the Interstellar Medium in a Star-forming Galaxy in the First Gyr after the Big Bang. *ApJ*, *774*, 26. doi: 10.1088/0004-637X/774/1/26

Chornock, R., Berger, E., Fox, D. B. et al. (2014, May). GRB 140515A at $z = 6.33$: Constraints on the End of Reionization From a Gamma-ray Burst in a Low Hydrogen Column Density Environment. *ArXiv e-prints*.

Chornock, R., Cucchiara, A., Fox, D. & Berger, E. (2010, Mar). GRB 100302A: gemini-north redshift. *GRB Coordinates Network*, *10466*.

Christensen, L., Fynbo, J. P. U., Prochaska, J. X. et al. (2011, Feb). A High Signal-to-noise Ratio Composite Spectrum of Gamma-ray Burst Afterglows. *ApJ*, *727*, 73. doi: 10.1088/0004-637X/727/2/73

Cooke, R. J., Pettini, M., Nollett, K. M. & Jorgenson, R. (2016, Oct). The Primordial Deuterium Abundance of the Most Metal-poor Damped Lyman-α System. *ApJ*, *830*, 148. doi: 10.3847/0004-637X/830/2/148

Cooke, R. J., Pettini, M. & Steidel, C. C. (2017, May). Discovery of the most metal-poor damped Lyman-α system. *MNRAS*, *467*, 802-811. doi: 10.1093/mnras/stx037

Costa, E., Frontera, F., Heise, J. et al. (1997, Jun). Discovery of an X-ray afterglow associated with the γ-ray burst of 28 February 1997. *Nature*, *387*, 783-785. doi: 10.1038/42885

Covino, S., Melandri, A., Salvaterra, R. et al. (2013, Jun). Dust extinctions for an unbiased sample of gamma-ray burst afterglows. *MNRAS*, *432*, 1231-1244. doi: 10.1093/mnras/stt540

Cucchiara, A. & Cenko, S. B. (2013, Dec). GRB 131227A: gemini-north redshift. *GRB Coordinates Network*, *15624*.

Cucchiara, A., Levan, A. J., Fox, D. B. et al. (2011, Jul). A Photometric Redshift of $z \sim 9.4$ for GRB 090429B. *ApJ*, *736*, 7. doi: 10.1088/0004-637X/736/1/7

Curran, P. A., Wijers, R. A. M. J., Heemskerk, M. H. M. et al. (2008, Nov). Robust photometric redshift determinations of gamma-ray burst afterglows at z $\gtrsim$ 2. *A&A*, *490*, 1047-1053. doi: 10.1051/0004-6361:200810545

D'Avanzo, P., Bernardini, M. G., D'Elia, V. et al. (2014, May). GRB 140515A: Swift detection of a burst. *GRB Coordinates Network*, *16267*.

D'Avanzo, P., Perri, M., Fugazza, D. et al. (2010, Nov). The afterglow and host galaxy of GRB 090205: evidence of a Ly-α emitter at $z = 4.65$. *A&A*, *522*, A20. doi: 10.1051/0004-6361/201014801

De Cia, A. (2018, May). Metals and dust in the neutral ISM: the Galaxy, Magellanic Clouds, and damped Lyman-α absorbers. *A&A*, *613*, L2. doi: 10.1051/0004-6361/201833034

De Cia, A., Ledoux, C., Mattsson, L. et al. (2016, Dec). Dust-depletion sequences in damped Lyman-α absorbers. A unified picture from low-metallicity systems to the Galaxy. *A&A*, *596*, A97. doi: 10.1051/0004-6361/201527895

De Cia, A., Ledoux, C., Petitjean, P. & Savaglio, S. (2018, Apr). The cosmic evolution of dust-corrected metallicity in the neutral gas. *A&A*, *611*, A76. doi: 10.1051/0004-6361/201731970

De Cia, A., Ledoux, C., Savaglio, S. et al. (2013, Dec). Dust-to-metal ratios in damped Lyman-α absorbers. Fresh clues to the origins of dust and optical extinction towards γ-ray bursts. *A&A*, *560*, A88. doi: 10.1051/0004-6361/201321834

De Looze, I., Barlow, M. J., Swinyard, B. M. et al. (2017, Mar). The dust mass in Cassiopeia A from a spatially resolved Herschel analysis. *MNRAS*, *465*, 3309-3342. doi: 10.1093/mnras/stw2837

de Ugarte Postigo, A., Gorosabel, J., Malesani, D. et al. (2009, May). GRB 090516: VLT redshift. *GRB Coordinates Network*, *9381*.

de Ugarte Postigo, A., Gorosabel, J., Xu, D. et al. (2014, Mar). GRB 140304A: NOT observations and redshift estimate. *GRB Coordinates Network*, *15921*.

de Ugarte Postigo, A., Thöne, C. C., Bolmer, J. et al. (2018, Dec). X-shooter and ALMA spectroscopy of GRB 161023A. A study of metals and molecules in the line of sight towards a luminous GRB. *A&A*, *620*, A119. doi: 10.1051/0004-6361/201833094

D'Elia, V., Fiore, F., Perna, R. et al. (2009, Mar). The Prompt, High-Resolution Spectroscopic View of the "Naked-Eye" GRB080319B. *ApJ*, *694*, 332-338. doi: 10.1088/0004-637X/694/1/332

D'Elia, V., Fynbo, J. P. U., Covino, S. et al. (2010, Nov). VLT/X-shooter spectroscopy of the GRB 090926A afterglow. *A&A*, *523*, A36. doi: 10.1051/0004-6361/201015216

D'Elia, V., Fynbo, J. P. U., Goldoni, P. et al. (2014, Apr). VLT/X-shooter spectroscopy of the GRB 120327A afterglow. *A&A*, *564*, A38. doi: 10.1051/0004-6361/201323057

D'Elia, V., Pian, E., Melandri, A. et al. (2015, May). SN 2013dx associated with GRB 130702A: a detailed photometric and spectroscopic monitoring and a study of the environment. *A&A*, *577*, A116. doi: 10.1051/0004-6361/201425381

Dessart, L., John Hillier, D., Yoon, S.-C. et al. (2017, Jul). Radiative-transfer models for explosions from rotating and non-rotating single WC stars. Implications for SN 1998bw and LGRB/SNe. *A&A*, *603*, A51. doi: 10.1051/0004-6361/201730873

Draine, B. T. (2000, Mar). Gamma-Ray Bursts in Molecular Clouds: H_2 Absorption and Fluorescence. *ApJ*, *532*, 273-280. doi: 10.1086/308581

Draine, B. T. (2011). *Physics of the Interstellar and Intergalactic Medium*. Princeton University Press.

Draine, B. T. & Hao, L. (2002, Apr). Gamma-Ray Burst in a Molecular Cloud: Destruction of Dust and H_2 and the Emergent Spectrum. *ApJ*, *569*, 780-791. doi: 10.1086/339394

Elliott, J., Krühler, T., Greiner, J. et al. (2013, Aug). The low-extinction afterglow in the solar-metallicity host galaxy of γ-ray burst 110918A. *A&A*, *556*, A23. doi: 10.1051/0004-6361/201220968

Ellison, S. L., Vreeswijk, P., Ledoux, C. et al. (2006, Oct). Three intervening galaxy absorbers towards GRB 060418: faint and dusty? *MNRAS*, *372*, L38-L42. doi: 10.1111/j.1745-3933.2006.00221.x

Evangelista, Y., Soffitta, P., Del Monte, E. et al. (2008, Aug). GRB 080825B: GRB localization by SuperAGILE. *GRB Coordinates Network*, *8133*.

Evans, N. J., Heiderman, A. & Vutisalchavakul, N. (2014, Feb). Star Formation Relations in Nearby Molecular Clouds. *ApJ*, *782*(2), 114. doi: 10.1088/0004-637x/782/2/114

Evans, P. A., Beardmore, A. P., Page, K. L. et al. (2009, Aug). Methods and results of an automatic analysis of a complete sample of Swift-XRT observations of GRBs. *MNRAS*, *397*, 1177-1201. doi: 10.1111/j.1365-2966.2009.14913.x

Evans, P. A., Willingale, R., Osborne, J. P. et al. (2014, Oct). GRB 130925A: an ultralong gamma ray burst with a dust-echo afterglow, and implications for the origin of the ultralong GRBs. *MNRAS*, *444*, 250-267. doi: 10.1093/mnras/stu1459

Fan, X., Strauss, M. A., Becker, R. H. et al. (2006, Jul). Constraining the Evolution of the Ionizing Background and the Epoch of Reionization with $z \sim 6$ Quasars. II. A Sample of 19 Quasars. *AJ*, *132*, 117-136. doi: 10.1086/504836

Federman, S. R., Cardell, J. A., van Dishoeck, E. F. et al. (1995, May). Vibrationally Excited H_2, HCl, and NO^+ in the Diffuse Clouds toward zeta Ophiuchi. *ApJ*, *445*, 325. doi: 10.1086/175696

Ferland, G. J., Chatzikos, M., Guzmán, F. et al. (2017, Oct). The 2017 Release Cloudy. *Rev. Mexicana Astron. Astrofis.*, *53*, 385-438.

Filgas, R., Krühler, T., Greiner, J. et al. (2011, Feb). The two-component jet of GRB 080413B. *A&A*, *526*, A113. doi: 10.1051/0004-6361/201015320

Fitzpatrick, E. L. & Massa, D. (1986, Aug). An analysis on the shapes of ultraviolet extinction curves. I - The 2175 Å bump. *ApJ*, *307*, 286-294. doi: 10.1086/164415

Fontana, A. & Ballester, P. (1995, Jun). FITLYMAN: a Midas tool for the analysis of absorption spectra. *The Messenger*, *80*, 37-41.

Fox, A. J., Ledoux, C., Vreeswijk, P. M. et al. (2008, Nov). High-ion absorption in seven GRB host galaxies at $z = 2$-4. Evidence for both circumburst plasma and outflowing interstellar gas. *A&A*, *491*, 189-207. doi: 10.1051/0004-6361:200810286

Fox, D. B., Frail, D. A., Price, P. A. et al. (2005, Oct). The afterglow of GRB 050709 and the nature of the short-hard γ-ray bursts. *Nature*, *437*, 845-850. doi: 10.1038/nature04189

Frail, D. A., Kulkarni, S. R., Nicastro, L. et al. (1997, Sep). The radio afterglow from the γ-ray burst of 8 May 1997. *Nature*, *389*, 261-263. doi: 10.1038/38451

Friis, M., De Cia, A., Krühler, T. et al. (2015, Jul). The warm, the excited, and the molecular gas: GRB 121024A shining through its star-forming galaxy. *MNRAS*, *451*, 167-183. doi: 10.1093/mnras/stv960

Fruchter, A. S., Levan, A. J., Strolger, L. et al. (2006, May). Long γ-ray bursts and core-collapse supernovae have different environments. *Nature*, *441*, 463-468. doi: 10.1038/nature04787

Fugazza, D., Thoene, C. C., D'Elia, V. et al. (2009, Feb). GRB 090205: VLT refined redshift. *GRB Coordinates Network*, *8892*.

Fynbo, J. P. U., Jakobsson, P., Prochaska, J. X. et al. (2009, Dec). Low-resolution Spectroscopy of Gamma-ray Burst Optical Afterglows: Biases in the Swift Sample and Characterization of the Absorbers. *The Astrophysical Journal Supplement Series*, *185*, 526-573. doi: 10.1088/0067-0049/185/2/526

Fynbo, J. P. U., Krühler, T., Leighly, K. et al. (2014, Dec). The mysterious optical afterglow spectrum of GRB 140506A at $z = 0.889$. *A&A*, *572*, A12. doi: 10.1051/0004-6361/201424726

Fynbo, J. P. U., Starling, R. L. C., Ledoux, C. et al. (2006, Jun). Probing cosmic chemical evolution with gamma-ray bursts: GRB 060206 at $z = 4.048$. *A&A*, *451*, L47-L50. doi: 10.1051/0004-6361:20065056

Fynbo, J. P. U., Watson, D., Thöne, C. C. et al. (2006, Dec). No supernovae associated with two long-duration γ-ray bursts. *Nature*, *444*, 1047-1049. doi: 10.1038/nature05375

Gal-Yam, A. (2018, Nov). The Most Luminous Supernovae. *arXiv e-prints*, arXiv:1812.01428.

Galama, T. J., Vreeswijk, P. M., van Paradijs, J. et al. (1998, Oct). An unusual supernova in the error box of the γ-ray burst of 25 April 1998. *Nature*, *395*, 670-672. doi: 10.1038/27150

Gehrels, N., Chincarini, G., Giommi, P. et al. (2004, Aug). The Swift Gamma-Ray Burst Mission. *ApJ*, *611*, 1005-1020. doi: 10.1086/422091

Gehrels, N., Sarazin, C. L., O'Brien, P. T. et al. (2005, Oct). A short γ-ray burst apparently associated with an elliptical galaxy at redshift z = 0.225. *Nature*, *437*, 851-854. doi: 10.1038/nature04142

Georgy, C., Ekström, S., Meynet, G. et al. (2012, Jun). Grids of stellar models with rotation. II. WR populations and supernovae/GRB progenitors at Z = 0.014. *A&A*, *542*, A29. doi: 10.1051/0004-6361/201118340

Glover, S. C. O. & Clark, P. C. (2016, Mar). Is atomic carbon a good tracer of molecular gas in metal-poor galaxies? *MNRAS*, *456*, 3596-3609. doi: 10.1093/mnras/stv2863

Goldstein, A. & van der Horst, A. (2008, Sep). GRB 080916C: Fermi GBM detection. *GRB Coordinates Network*, *8245*.

Gomez, H. L., Krause, O., Barlow, M. J. et al. (2012, Nov). A Cool Dust Factory in the Crab Nebula: A Herschel Study of the Filaments. *ApJ*, *760*, 96. doi: 10.1088/0004-637X/760/1/96

Gong, M., Ostriker, E. C. & Kim, C.-G. (2018, May). The X_{CO} Conversion Factor from Galactic Multiphase ISM Simulations. *ApJ*, *858*, 16. doi: 10.3847/1538-4357/aab9af

Goobar, A. (2008, Oct). Low R_V from Circumstellar Dust around Supernovae. *ApJ*, *686*, L103. doi: 10.1086/593060

Gorosabel, J., de Ugarte Postigo, A., Montes, D., Klutsch, A. & Castro-Tirado, A. J. (2009, May). GRB 090516: NOT optical observations. *GRB Coordinates Network*, *9379*.

Graham, J. F. & Fruchter, A. S. (2013, Sep). The Metal Aversion of Long-duration Gamma-Ray Bursts. *ApJ*, *774*, 119. doi: 10.1088/0004-637X/774/2/119

Graham, J. F. & Fruchter, A. S. (2017, Jan). The Relative Rate of LGRB Formation as a Function of Metallicity. *ApJ*, *834*, 170. doi: 10.3847/1538-4357/834/2/170

Granot, J. & Sari, R. (2002, Apr). The Shape of Spectral Breaks in Gamma-Ray Burst Afterglows. *ApJ*, *568*, 820-829. doi: 10.1086/338966

Greig, B., Mesinger, A., Haiman, Z. & Simcoe, R. A. (2017, Apr). Are we witnessing the epoch of reionisation at $z = 7.1$ from the spectrum of J1120+0641? *MNRAS*, *466*, 4239-4249. doi: 10.1093/mnras/stw3351

Greiner, J. (2019, Jan). The Benefit of Simultaneous Seven-filter Imaging: 10 Years of GROND Observations. *PASP*, *131*, 015002. doi: 10.1088/1538-3873/aaec5d

Greiner, J. (2019, in prep.).
A&A.

Greiner, J., Bolmer, J., Wieringa, M. et al. (2018, Jun). Large-amplitude late-time radio variability in GRB 151027B. *A&A*, *614*, A29. doi: 10.1051/0004-6361/201731755

Greiner, J., Bornemann, W., Clemens, C. et al. (2008, Apr). GROND: a 7-Channel Imager. *PASP*, *120*, 405. doi: 10.1086/587032

Greiner, J., Clemens, C., Krühler, T. et al. (2009, Apr). The redshift and afterglow of the extremely energetic gamma-ray burst GRB 080916C. *A&A*, *498*, 89-94. doi: 10.1051/0004-6361/200811571

Greiner, J., Fox, D. B., Schady, P. et al. (2015, Aug). Gamma-Ray Bursts Trace UV Metrics of Star Formation over $3 < z < 5$. *ApJ*, *809*, 76. doi: 10.1088/0004-637X/809/1/76

Greiner, J., Krühler, T., Fynbo, J. P. U. et al. (2009, Mar). GRB 080913 at Redshift 6.7. *ApJ*, *693*, 1610-1620. doi: 10.1088/0004-637X/693/2/1610

Greiner, J., Krühler, T., Klose, S. et al. (2011, Feb). The nature of "dark" gamma-ray bursts. *A&A*, *526*, A30. doi: 10.1051/0004-6361/201015458

Greiner, J., Krühler, T., McBreen, S. et al. (2009, Mar). A Strong Optical Flare Before the Rising Afterglow of GRB 080129. *ApJ*, *693*, 1912-1919. doi: 10.1088/0004-637X/693/2/1912

Greiner, J., Mazzali, P. A., Kann, D. A. et al. (2015, Jul). A very luminous magnetar-powered supernova associated with an ultra-long γ-ray burst. *Nature*, *523*, 189-192. doi: 10.1038/nature14579

Greiner, J., Yu, H. F., Krühler, T. et al. (2014, Aug). GROND coverage of the main peak of gamma-ray burst 130925A. *A&A*, *568*, A75. doi: 10.1051/0004-6361/201424250

Haario, H., Saksman, E. & Tamminen, J. (2001, Apr). An adaptive metropolis algorithm. *Bernoulli*, *7*(2), 223–242.

Hansen, S. H. & Haiman, Z. (2004, Jan). Do We Need Stars to Reionize the Universe at High Redshifts? Early Reionization by Decaying Heavy Sterile Neutrinos. *ApJ*, *600*, 26-31. doi: 10.1086/379636

Hartoog, O. E., Malesani, D., Fynbo, J. P. U. et al. (2015, Aug). VLT/X-Shooter spectroscopy of the afterglow of the Swift GRB 130606A. Chemical abundances and reionisation at z ˜6. *A&A*, *580*, A139. doi: 10.1051/0004-6361/201425001

Hartoog, O. E., Wiersema, K., Vreeswijk, P. M. et al. (2013, Apr). The host-galaxy response to the afterglow of GRB 100901A. *MNRAS*, *430*, 2739-2754. doi: 10.1093/mnras/stt078

Hatsukade, B., Ohta, K., Endo, A. et al. (2014, Jun). Two γ-ray bursts from dusty regions with little molecular gas. *Nature*, *510*, 247-249. doi: 10.1038/nature13325

Heintz, K. E., Bolmer, J., Ledoux, C. et al. (2019, in prep.). Physical conditions in the diffuse molecular gas-phase of high-redshift GRB host galaxies. *As going to be submitted to A&A*.

Heintz, K. E., Ledoux, C., Fynbo, J. P. U. et al. (2019, Jan). Cold gas in the early Universe. Survey for neutral atomic-carbon in GRB host galaxies at $1 < z < 6$ from optical afterglow spectroscopy. *A&A*, *621*, A20. doi: 10.1051/0004-6361/201834246

Heintz, K. E., Watson, D., Jakobsson, P. et al. (2018, Jun). Highly-ionized metals as probes of the circumburst gas in the natal regions of gamma-ray bursts. *MNRAS*, 1393. doi: 10.1093/mnras/sty1447

Hirashita, H., Ferrara, A., Dayal, P. & Ouchi, M. (2014, Sep). Constraining dust formation in high-redshift young galaxies. *MNRAS*, *443*, 1704-1712. doi: 10.1093/mnras/stu1290

Hirashita, H., Nozawa, T., Takeuchi, T. T. & Kozasa, T. (2008, Mar). Extinction curves flattened by reverse shocks in supernovae. *MNRAS*, *384*, 1725-1732. doi: 10.1111/j.1365-2966.2007.12834.x

Hirashita, H., Nozawa, T., Yan, H. & Kozasa, T. (2010, May). Effects of grain shattering by turbulence on extinction curves in starburst galaxies. *MNRAS*, *404*, 1437-1448. doi: 10.1111/j.1365-2966.2010.16354.x

Hirschi, R., Meynet, G. & Maeder, A. (2005, Nov). Stellar evolution with rotation. XIII. Predicted GRB rates at various Z. *A&A*, *443*, 581-591. doi: 10.1051/0004-6361:20053329

Hjorth, J., Malesani, D., Jakobsson, P. et al. (2012, Sep). The Optically Unbiased Gamma-Ray Burst Host (TOUGH) Survey. I. Survey Design and Catalogs. *ApJ*, *756*, 187. doi: 10.1088/0004-637X/756/2/187

Hjorth, J., Sollerman, J., Møller, P. et al. (2003, Jun). A very energetic supernova associated with the γ-ray burst of 29 March 2003. *Nature*, *423*, 847-850. doi: 10.1038/nature01750

Hjorth, J., Vreeswijk, P. M., Gall, C. & Watson, D. (2013, May). On Inferring Extinction Laws in $z \sim 6$ Quasars as Signatures of Supernova Dust. *ApJ*, *768*, 173. doi: 10.1088/0004-637X/768/2/173

Hollenbach, D. J., Werner, M. W. & Salpeter, E. E. (1971, Jan). Molecular Hydrogen in H I Regions. *ApJ*, *163*, 165. doi: 10.1086/150755

Hou, S.-J., Gao, H., Liu, T. et al. (2014, Jul). Variability of the giant X-ray bump in GRB 121027A and its possible origin. *MNRAS*, *441*, 2375-2379. doi: 10.1093/mnras/stu682

Hunt, L. K., Palazzi, E., Michałowski, M. J. et al. (2014, May). New light on gamma-ray burst host galaxies with Herschel. *A&A*, *565*, A112. doi: 10.1051/0004-6361/201323340

Hurkett, C. P., Osborne, J. P., Page, K. L. et al. (2006, May). GRB 050505: a high-redshift burst discovered by Swift. *MNRAS*, *368*, 1101-1109. doi: 10.1111/j.1365-2966.2006.10188.x

Im, M., Choi, C., Jun, H., Kang, E. et al. (2010, Sep). GRB 100905A: UKIRT zJHK observation. *GRB Coordinates Network*, *11222*.

Indebetouw, R., Matsuura, M., Dwek, E. et al. (2014, Feb). Dust Production and Particle Acceleration in Supernova 1987A Revealed with ALMA. *ApJ*, *782*, L2. doi: 10.1088/2041-8205/782/1/L2

Izzard, R. G., Ramirez-Ruiz, E. & Tout, C. A. (2004, Mar). Formation rates of core-collapse supernovae and gamma-ray bursts. *MNRAS*, *348*, 1215-1228. doi: 10.1111/j.1365-2966.2004.07436.x

Izzo, L., de Ugarte Postigo, A., Maeda, K. et al. (2019, Jan). Signatures of a jet cocoon in early spectra of a supernova associated with a γ-ray burst. *Nature*, *565*(7739), 324–327.

Izzo, L., Thöne, C. C., Schulze, S. et al. (2017, Dec). The MUSE view of the host galaxy of GRB 100316D. *MNRAS*, *472*, 4480-4496. doi: 10.1093/mnras/stx2244

Jakobsson, P., Fynbo, J. P. U., Ledoux, C. et al. (2006, Dec). H I column densities of $z > 2$ Swift gamma-ray bursts. *A&A*, *460*, L13-L17. doi: 10.1051/0004-6361:20066405

Jang, M., Im, M., Lee, I. et al. (2011, Nov). Dust Properties in the Afterglow of GRB 071025 at $z \sim 5$. *ApJ*, *741*, L20. doi: 10.1088/2041-8205/741/1/L20

Japelj, J., Vergani, S. D., Salvaterra, R. et al. (2016, Oct). Taking stock of superluminous supernovae and long gamma-ray burst host galaxy comparison using a complete sample of LGRBs. *A&A*, *593*, A115. doi: 10.1051/0004-6361/201628603

Jaunsen, A. O., Rol, E., Watson, D. J. et al. (2008, Jul). GRB 070306: A Highly Extinguished Afterglow. *ApJ*, *681*, 453-461. doi: 10.1086/588602

Jenkins, E. B. (1987, Jan). Element Abundances in the Interstellar Atomic Material. In D. J. Hollenbach & J. Thronson Harley A. (Eds.), *Interstellar processes* (Vol. 134, p. 533). doi: 10.1007/978-94-009-3861-8_20

Jenkins, E. B. (2009, Aug). A Unified Representation of Gas-Phase Element Depletions in the Interstellar Medium. *ApJ*, *700*, 1299-1348. doi: 10.1088/0004-637X/700/2/1299

Jenkins, E. B. & Wallerstein, G. (2017, Apr). Interstellar Gas-phase Element Depletions in the Small Magellanic Cloud: A Guide to Correcting for Dust in QSO Absorption Line Systems. *ApJ*, *838*, 85. doi: 10.3847/1538-4357/aa64d4

Jeong, S., Sanchez-Ramirez, R., Gorosabel, J. & Castro-Tirado, A. J. (2014, Mar). GRB 140304A: 10.4m GTC refined redshift z = 5.283. *GRB Coordinates Network*, *15936*.

Jorgenson, R. A., Murphy, M. T., Thompson, R. & Carswell, R. F. (2014, Sep). The Magellan uniform survey of damped Lyman α systems - II. Paucity of strong molecular hydrogen absorption. *MNRAS*, *443*, 2783-2800. doi: 10.1093/mnras/stu1314

Kalberla, P. M. W., Burton, W. B., Hartmann, D. et al. (2005, Sep). The Leiden/Argentine/Bonn (LAB) Survey of Galactic HI. Final data release of the combined LDS and IAR surveys with improved stray-radiation corrections. *A&A*, *440*, 775-782. doi: 10.1051/0004-6361:20041864

Kanekar, N., Braun, R. & Roy, N. (2011, Aug). An H I Column Density Threshold for Cold Gas Formation in the Galaxy. *ApJ*, *737*, L33. doi: 10.1088/2041-8205/737/2/L33

Kann, D. A., Nicuesa Guelbenzu, A. & Greiner, J. (2013, Dec). GRB 131227A: GROND upper limits. *GRB Coordinates Network*, *15632*.

Kaur, A., Rau, A., Ajello, M. et al. (2017, Jan). New High-z Fermi BL Lacs with the Photometric Dropout Technique. *ApJ*, *834*, 41. doi: 10.3847/1538-4357/834/1/41

Kawai, N., Kosugi, G., Aoki, K. et al. (2006, Mar). An optical spectrum of the afterglow of a γ-ray burst at a redshift of $z = 6.295$. *Nature*, *440*, 184-186. doi: 10.1038/nature04498

Kennicutt, R. C. & Evans, N. J. (2012, Sep). Star Formation in the Milky Way and Nearby Galaxies. *Annual Review of Astronomy and Astrophysics*, *50*, 531-608. doi: 10.1146/annurev-astro-081811-125610

Kewley, L. J. & Ellison, S. L. (2008, Jul). Metallicity Calibrations and the Mass-Metallicity Relation for Star-forming Galaxies. *ApJ*, *681*, 1183-1204. doi: 10.1086/587500

Khaire, V., Srianand, R., Choudhury, T. R. & Gaikwad, P. (2016, Apr). The redshift evolution of escape fraction of hydrogen ionizing photons from galaxies. *MNRAS*, *457*, 4051-4062. doi: 10.1093/mnras/stw192

Kim, T. S., Carswell, R. F., Cristiani, S., D'Odorico, S. & Giallongo, E. (2002, Sep). The physical properties of the Lyα forest at z > 1.5. *MNRAS*, *335*, 555-573. doi: 10.1046/j.1365-8711.2002.05599.x

Kisielius, R., Kulkarni, V. P., Ferland, G. J. et al. (2014, Jan). Atomic Data for S II—Toward Better Diagnostics of Chemical Evolution in High-redshift Galaxies. *ApJ*, *780*, 76. doi: 10.1088/0004-637X/780/1/76

Kisielius, R., Kulkarni, V. P., Ferland, G. J. et al. (2015, May). Atomic Data for Zn II: Improving Spectral Diagnostics of Chemical Evolution in High-redshift Galaxies. *ApJ*, *804*, 76. doi: 10.1088/0004-637X/804/1/76

Klebesadel, R. W., Strong, I. B. & Olson, R. A. (1973, Jun). Observations of Gamma-Ray Bursts of Cosmic Origin. *ApJ*, *182*, L85. doi: 10.1086/181225

Kocevski, D., Barthelmy, S. D., Lien, A. Y. et al. (2014, Apr). GRB 140428A: Swift Detection of a Possible Burst. *GRB Coordinates Network*, *16177*.

Krimm, H. A., Beardmore, A. P., Evans, P. A. et al. (2009, Apr). GRB 090423: Swift detection of a burst. *GRB Coordinates Network*, *9198*.

Krühler, T., Fynbo, J. P. U., Geier, S. et al. (2012, Oct). The metal-enriched host of an energetic γ-ray burst at $z \sim 1.6$. *A&A*, *546*, A8. doi: 10.1051/0004-6361/201118670

Krühler, T., Greiner, J., Schady, P. et al. (2011, Oct). The SEDs and host galaxies of the dustiest GRB afterglows. *A&A*, *534*, A108. doi: 10.1051/0004-6361/201117428

Krühler, T., Kuncarayakti, H., Schady, P. et al. (2017, Jun). Hot gas around SN 1998bw: Inferring the progenitor from its environment. *A&A*, *602*, A85. doi: 10.1051/0004-6361/201630268

Krühler, T., Küpcü Yoldaş, A., Greiner, J. et al. (2008, Sep). The 2175 Å Dust Feature in a Gamma-Ray Burst Afterglow at Redshift 2.45. *ApJ*, *685*, 376-383. doi: 10.1086/590240

Krühler, T., Ledoux, C., Fynbo, J. P. U. et al. (2013, Sep). Molecular hydrogen in the damped Lyman-α system towards GRB 120815A at $z = 2.36$. *A&A*, *557*, A18. doi: 10.1051/0004-6361/201321772

Krühler, T., Malesani, D., Fynbo, J. P. U. et al. (2015, Sep). GRB hosts through cosmic time. VLT/X-Shooter emission-line spectroscopy of 96 γ-ray-burst-selected galaxies at $0.1 < z < 3.6$. *A&A*, *581*, A125. doi: 10.1051/0004-6361/201425561

Krühler, T., Schady, P., Greiner, J. et al. (2011, Feb). Photometric redshifts for gamma-ray burst afterglows from GROND and Swift/UVOT. *A&A*, *526*, A153. doi: 10.1051/0004-6361/201015327

Krühler, T., Vreeswijk, P. M. & Fynbo, J. P. U. (2014, Jun). GRB 140614A: X-shooter redshift. *GRB Coordinates Network*, *16401*.

Krumholz, M. R. (2014, Jun). The big problems in star formation: The star formation rate, stellar clustering, and the initial mass function. *Phys. Rep.*, *539*, 49-134. doi: 10.1016/j.physrep.2014.02.001

Krumholz, M. R., Dekel, A. & McKee, C. F. (2012, Jan). A Universal, Local Star Formation Law in Galactic Clouds, nearby Galaxies, High-redshift Disks, and Starbursts. *ApJ*, *745*, 69. doi: 10.1088/0004-637X/745/1/69

Krumholz, M. R., McKee, C. F. & Tumlinson, J. (2009, Mar). The Atomic-to-Molecular Transition in Galaxies. II: H I and H_2 Column Densities. *ApJ*, *693*, 216-235. doi: 10.1088/0004-637X/693/1/216

Lamb, D. Q. & Reichart, D. E. (2000, Jun). Gamma-Ray Bursts as a Probe of the Very High Redshift Universe. *ApJ*, *536*, 1-18. doi: 10.1086/308918

Laporte, N., Ellis, R. S., Boone, F. et al. (2017, Mar). Dust in the reionization era: Alma observations of a $z = 8.38$ gravitationally lensed galaxy. *ApJ*, *837*(2), L21.

Laskar, T., Berger, E., Tanvir, N. et al. (2014, Jan). GRB 120521C at $z \sim 6$ and the Properties of High-redshift γ-Ray Bursts. *ApJ*, *781*, 1. doi: 10.1088/0004-637X/781/1/1

Ledoux, C., Noterdaeme, P., Petitjean, P. & Srianand, R. (2015, Aug). Neutral atomic-carbon quasar absorption-line systems at $z > 1.5$. Sample selection, H I content, reddening, and 2175 Å extinction feature. *A&A*, *580*, A8. doi: 10.1051/0004-6361/201424122

Ledoux, C., Petitjean, P. & Srianand, R. (2003, Nov). The Very Large Telescope Ultraviolet and Visible Echelle Spectrograph survey for molecular hydrogen in high-redshift damped Lyman α systems. *MNRAS*, *346*, 209-228. doi: 10.1046/j.1365-2966.2003.07082.x

Ledoux, C., Petitjean, P. & Srianand, R. (2006, Mar). Molecular Hydrogen in a Damped Lyα System at $z_{\rm abs} = 4.224$. *ApJ*, *640*, L25-L28. doi: 10.1086/503278

Ledoux, C., Vreeswijk, P. M., Smette, A. et al. (2009, Nov). Physical conditions in high-redshift GRB-DLA absorbers observed with VLT/UVES: implications for molecular hydrogen searches. *A&A*, *506*, 661-675. doi: 10.1051/0004-6361/200811572

Lee, E. J., Miville-Deschênes, M.-A. & Murray, N. W. (2016, Dec). Observational Evidence of Dynamic Star Formation Rate in Milky Way Giant Molecular Clouds. *ApJ*, *833*(2), 229. doi: 10.3847/1538-4357/833/2/229

Lehner, N., O'Meara, J. M., Howk, J. C. et al. (2016, Dec). The Cosmic Evolution of the Metallicity Distribution of Ionized Gas Traced by Lyman Limit Systems. *ApJ*, *833*, 283. doi: 10.3847/1538-4357/833/2/283

Leighly, K. M., Terndrup, D. M., Baron, E. et al. (2014, Jun). Evidence for Active Galactic Nucleus Feedback in the Broad Absorption Lines and Reddening of Mrk 231. *ApJ*, *788*, 123. doi: 10.1088/0004-637X/788/2/123

Leroy, A. K., Walter, F., Sandstrom, K. et al. (2013, Aug). Molecular Gas and Star Formation in nearby Disk Galaxies. *AJ*, *146*, 19. doi: 10.1088/0004-6256/146/2/19

Levan, A. J., Tanvir, N. R., Starling, R. L. C. et al. (2014, Jan). A New Population of Ultra-long Duration Gamma-Ray Bursts. *ApJ*, *781*, 13. doi: 10.1088/0004-637X/781/1/13

Levshakov, S. A. & Varshalovich, D. A. (1985, Feb). Molecular hydrogen in the z=2.811 absorbing material toward the quasar PKS 0528-250. *MNRAS*, *212*, 517-521. doi: 10.1093/mnras/212.3.517

Li, L., Wang, Y., Shao, L., Wu, X.-F., Huang, Y.-F., Zhang, B., ... Yu, H.-F. (2018, Feb). A Large Catalog of Multiwavelength GRB Afterglows. I. Color Evolution and Its Physical Implication. *The Astrophysical Journal Supplement Series*, *234*, 26. doi: 10.3847/1538-4365/aaa02a

LIGO Scientific Collaboration & Virgo Collaboration. (2017, Oct). GW170817: Observation of Gravitational Waves from a Binary Neutron Star Inspiral. *Phys. Rev. Lett.*, *119*, 161101. doi: 10.1103/PhysRevLett.119.161101

Littlejohns, O. M., Butler, N. R., Cucchiara, A. et al. (2015, May). A detailed study of the optical attenuation of gamma-ray bursts in the Swift era. *MNRAS*, *449*, 2919-2936. doi: 10.1093/mnras/stv479

Littlejohns, O. M., Tanvir, N. R., Willingale, R. et al. (2013, Dec). Are gamma-ray bursts the same at high redshift and low redshift? *MNRAS*, *436*, 3640-3655. doi: 10.1093/mnras/stt1841

Livermore, R. C., Finkelstein, S. L. & Lotz, J. M. (2017, Feb). Directly Observing the Galaxies Likely Responsible for Reionization. *ApJ*, *835*, 113. doi: 10.3847/1538-4357/835/2/113

Lodders, K., Palme, H. & Gail, H. P. (2009, Jan). Abundances of the Elements in the Solar System. *Landolt Börnstein*, *4B*, 44. doi: 10.1007/978-3-540-88055-4_34

Lyman, J. D., Levan, A. J., Tanvir, N. R. et al. (2017, May). The host galaxies and explosion sites of long-duration gamma ray bursts: Hubble Space Telescope near-infrared imaging. *MNRAS*, *467*, 1795-1817. doi: 10.1093/mnras/stx220

Ma, J., Ge, J., Prochaska, J. X. et al. (2018, Mar). Quasar 2175 Å dust absorbers - II. Correlation analysis and relationship with other absorption line systems. *MNRAS*, *474*, 4870-4880. doi: 10.1093/mnras/stx3123

MacFadyen, A. I. & Woosley, S. E. (1999, Oct). Collapsars: Gamma-Ray Bursts and Explosions in "Failed Supernovae". *ApJ*, *524*, 262-289. doi: 10.1086/307790

Madau, P. & Fragos, T. (2017, May). Radiation Backgrounds at Cosmic Dawn: X-Rays from Compact Binaries. *ApJ*, *840*, 39. doi: 10.3847/1538-4357/aa6af9

Maiolino, R. & Mannucci, F. (2019, Feb). De re metallica: the cosmic chemical evolution of galaxies. *Astronomy and Astrophysics Review*, *27*, 3. doi: 10.1007/s00159-018-0112-2

Maiolino, R., Nagao, T., Grazian, A. et al. (2008, Sep). AMAZE. I. The evolution of the mass-metallicity relation at $z \sim 3$. *A&A*, *488*, 463-479. doi: 10.1051/0004-6361:200809678

Maiolino, R., Schneider, R., Oliva, E. et al. (2004, Sep). A supernova origin for dust in a high-redshift quasar. *Nature*, *431*, 533-535. doi: 10.1038/nature02930

Malec, A. L., Buning, R., Murphy, M. T. et al. (2010, Apr). Keck telescope constraint on cosmological variation of the proton-to- electron mass ratio. *MNRAS*, *403*, 1541-1555. doi: 10.1111/j.1365-2966.2009.16227.x

Malesani, D., Barthelmy, S. D., Evans, P. A. et al. (2015, Nov). GRB 151112A: Swift detection of a burst. *GRB Coordinates Network*, *18588*.

Malesani, D., Tanvir, N. R., Xu, D. et al. (2015, Oct). GRB 151027B: NOT optical afterglow candidate. *GRB Coordinates Network*, *18501*.

Mancini, M., Schneider, R., Graziani, L. et al. (2015, Jul). The dust mass in $z > 6$ normal star-forming galaxies. *MNRAS*, *451*, L70-L74. doi: 10.1093/mnrasl/slv070

Mao, J., Malesani, D., D'Avanzo, P. et al. (2012, Feb). Diversity of multiwavelength emission bumps in the GRB 100219A afterglow. *A&A*, *538*, A1. doi: 10.1051/0004-6361/201117770

Margutti, R., Berger, E., Chornock, R. et al. (2014, May). Chandra late-time observations of GRB140515A. *GRB Coordinates Network*, *16338*.

Marshall, F. E., Barthelmy, S. D., Beardmore, A. P. et al. (2010, Sep). GRB 100905A: Swift detection of a burst. *GRB Coordinates Network*, *11214*.

Mathis, J. S. (1994, Feb). The Origin of Variations in the 2175 Angstrom Extinction Bump. *ApJ*, *422*, 176. doi: 10.1086/173715

Matsuura, M., Dwek, E., Barlow, M. J. et al. (2015, Feb). A Stubbornly Large Mass of Cold Dust in the Ejecta of Supernova 1987A. *ApJ*, *800*, 50. doi: 10.1088/0004-637X/800/1/50

McGreer, I. D., Mesinger, A. & D'Odorico, V. (2015, Feb). Model-independent evidence in favour of an end to reionization by $z \approx 6$. *MNRAS*, *447*(1), 499-505. doi: 10.1093/mnras/stu2449

McGuire, J. T. W., Tanvir, N. R., Levan, A. J. et al. (2016, Jul). Detection of Three Gamma-ray Burst Host Galaxies at $z \sim 6$. *ApJ*, *825*, 135. doi: 10.3847/0004-637X/825/2/135

McKee, C. F. & Krumholz, M. R. (2010, Jan). The Atomic-to-Molecular Transition in Galaxies. III. A New Method for Determining the Molecular Content of Primordial and Dusty Clouds. *ApJ*, *709*, 308-320. doi: 10.1088/0004-637X/709/1/308

McKee, C. F. & Ostriker, E. C. (2007, Sep). Theory of Star Formation. *Annual Review of Astronomy and Astrophysics*, *45*, 565-687. doi: 10.1146/annurev.astro.45.051806.110602

Meidt, S. E., Leroy, A. K., Rosolowsky, E. et al. (2018, Feb). A Model for the Onset of Self-gravitation and Star Formation in Molecular Gas Governed by Galactic Forces. I. Cloud-scale Gas Motions. *ApJ*, *854*, 100. doi: 10.3847/1538-4357/aaa290

Melandri, A., Bernardini, M. G., D'Avanzo, P. et al. (2015, Sep). The high-redshift gamma-ray burst GRB 140515A. A comprehensive X-ray and optical study. *A&A*, *581*, A86. doi: 10.1051/0004-6361/201526660

Melandri, A., Covino, S., Zaninoni, E. et al. (2017, Oct). Colour variations in the GRB 120327A afterglow. *A&A*, *607*, A29. doi: 10.1051/0004-6361/201731759

Melia, F. (2009). *High-Energy Astrophysics*. Princeton University Press.

Ménard, B. & Fukugita, M. (2012, Aug). Cosmic Dust in Mg II Absorbers. *ApJ*, *754*, 116. doi: 10.1088/0004-637X/754/2/116

Mereghetti, S., Paizis, A., Gotz, D. et al. (2010, May). GRB 100518A: a long GRB detected with INTEGRAL. *GRB Coordinates Network*, *10772*.

Metzger, M. R., Djorgovski, S. G., Kulkarni, S. R. et al. (1997, Jun). Spectral constraints on the redshift of the optical counterpart to the γ-ray burst of 8 May 1997. *Nature*, *387*, 878-880. doi: 10.1038/43132

Meyer, D. M., Lauroesch, J. T., Sofia, U. J. et al. (2001, May). The Rich Ultraviolet Spectrum of Vibrationally Excited Interstellar H_2 toward HD 37903. *ApJ*, *553*, L59-L62. doi: 10.1086/320504

Michałowski, M. J. (2015, May). Dust production 680-850 million years after the Big Bang. *A&A*, *577*, A80. doi: 10.1051/0004-6361/201525644

Michałowski, M. J., Castro Cerón, J. M., Wardlow, J. L. et al. (2016, Nov). GRB 980425 host: [CII], [OI], and CO lines reveal recent enhancement of star formation due to atomic gas inflow. *A&A*, *595*, A72. doi: 10.1051/0004-6361/201629441

MichałowskI, M. J., Xu, D., Stevens, J. et al. (2018, Sep). The second-closest gamma-ray burst: sub-luminous GRB 111005A with no supernova in a super-solar metallicity environment. *A&A*, *616*, A169. doi: 10.1051/0004-6361/201629942

Mirzoyan, R. (2019, Jan). First time detection of a GRB at sub-TeV energies; MAGIC detects the GRB 190114C. *The Astronomer's Telegram*, *12390*, 1.

Mishra, A. & Li, A. (2017, Dec). Interstellar Silicon Depletion and the Ultraviolet Extinction. *ApJ*, *850*, 138. doi: 10.3847/1538-4357/aa937a

Modjaz, M., Liu, Y. Q., Bianco, F. B. & Graur, O. (2016, Dec). The Spectral SN-GRB Connection: Systematic Spectral Comparisons between Type Ic Supernovae and Broad-lined Type Ic Supernovae with and without Gamma-Ray Bursts. *ApJ*, *832*, 108. doi: 10.3847/0004-637X/832/2/108

Morgan, A. N., Perley, D. A., Klein, C. R. & Bloom, J. S. (2010, May). GRB 100513A: PAIRITEL NIR afterglow candidate. *GRB Coordinates Network*, *10747*.

Morgan, H. L. & Edmunds, M. G. (2003, Aug). Dust formation in early galaxies. *MNRAS*, *343*, 427-442. doi: 10.1046/j.1365-8711.2003.06681.x

Morton, D. C. (2003, Nov). Atomic Data for Resonance Absorption Lines. III. Wavelengths Longward of the Lyman Limit for the Elements Hydrogen to Gallium. *The Astrophysical Journal Supplement Series*, *149*, 205-238. doi: 10.1086/377639

Murray, N. (2011, Feb). Star Formation Efficiencies and Lifetimes of Giant Molecular Clouds in the Milky Way. *ApJ*, *729*(2), 133. doi: 10.1088/0004-637x/729/2/133

Nardini, M., Elliott, J., Filgas, R. et al. (2014, Feb). Afterglow rebrightenings as a signature of a long-lasting central engine activity?. The emblematic case of GRB 100814A. *A&A*, *562*, A29. doi: 10.1051/0004-6361/201321525

Noterdaeme, P., Ledoux, C., Petitjean, P. & Srianand, R. (2008, Apr). Molecular hydrogen in high-redshift damped Lyman-α systems: the VLT/UVES database. *A&A*, *481*, 327-336. doi: 10.1051/0004-6361:20078780

Noterdaeme, P., Ledoux, C., Zou, S. et al. (2018, Apr). Spotting high-z molecular absorbers using neutral carbon. Results from a complete spectroscopic survey with the VLT. *A&A*, *612*, A58. doi: 10.1051/0004-6361/201732266

Noterdaeme, P., Petitjean, P., Ledoux, C. et al. (2010, Nov). A translucent interstellar cloud at $z = 2.69$. CO, H_2, and HD in the line-of-sight to SDSS J123714.60+064759.5. *A&A*, *523*, A80. doi: 10.1051/0004-6361/201015147

Noterdaeme, P., Petitjean, P., Pâris, I. et al. (2014, Jun). A connection between extremely strong damped Lyman-α systems and Lyman-α emitting galaxies at small impact parameters. *A&A*, *566*, A24. doi: 10.1051/0004-6361/201322809

Noterdaeme, P., Petitjean, P. & Srianand, R. (2015, Jun). The elusive H I to H_2 transition in high-z damped Lyman-α systems. *A&A*, *578*, L5. doi: 10.1051/0004-6361/201526018

Noterdaeme, P., Petitjean, P., Srianand, R. et al. (2011, Feb). The evolution of the cosmic microwave background temperature. Measurements of T_{CMB} at high redshift from carbon monoxide excitation. *A&A*, *526*, L7. doi: 10.1051/0004-6361/201016140

Noterdaeme, P., Srianand, R., Rahmani, H. et al. (2015, May). VLT/UVES observations of extremely strong intervening damped Lyman-α systems. Molecular hydrogen and excited carbon, oxygen, and silicon at $\log N(\mathrm{H\,I}) = 22.4$. *A&A*, *577*, A24. doi: 10.1051/0004-6361/201425376

Nozawa, T., Asano, R. S., Hirashita, H. & Takeuchi, T. T. (2015, Feb). Evolution of grain size distribution in high-redshift dusty quasars: integrating large amounts of dust and unusual extinction curves. *MNRAS*, *447*, L16-L20. doi: 10.1093/mnrasl/slu175

Nozawa, T., Kozasa, T., Habe, A. et al. (2007, Sep). Evolution of Dust in Primordial Supernova Remnants: Can Dust Grains Formed in the Ejecta Survive and Be Injected into the Early Interstellar Medium? *ApJ*, *666*, 955-966. doi: 10.1086/520621

Nozawa, T., Kozasa, T. & Nomoto, K. (2012, Sep). Can the Growth of Dust Grains in Low-metallicity Star-forming Clouds Affect the Formation of Metal-poor Low-mass Stars? *ApJ*, *756*, L35. doi: 10.1088/2041-8205/756/2/L35

Padoan, P., Haugbølle, T. & Nordlund, Å. (2012, Oct). A simple law of star formation. *ApJ*, *759*(2), L27. doi: 10.1088/2041-8205/759/2/l27

Pagani, C., Baumgartner, W. H., Burrows, D. N. et al. (2007, Oct). GRB 071025: Swift detection of a burst. *GRB Coordinates Network*, *6986*.

Page, K. L., Barthelmy, S. D., Burrows, D. N. et al. (2014, Jun). GRB 140614A: Swift detection of a burst. *GRB Coordinates Network*, *16391*.

Page, M. J., Barthelmy, S. D., Burrows, D. N. et al. (2013, Nov). GRB 131117A: Swift detection of a burst. *GRB Coordinates Network*, *15490*.

Page, M. J., Breeveld, A. A., Burrows, D. N. et al. (2012, Jul). GRB 120712A: Swift detection of a burst with optical afterglow. *GRB Coordinates Network*, *13454*.

Patel, M., Warren, S. J., Mortlock, D. J. & Fynbo, J. P. U. (2010, Mar). The reanalysis of spectra of GRB 080913 to estimate the neutral fraction of the IGM at a redshift of 6.7. *A&A*, *512*, L3. doi: 10.1051/0004-6361/200913876

Pei, Y. C. (1992, Aug). Interstellar Dust from the Milky Way to the Magellanic Clouds. *ApJ*, *395*, 130. doi: 10.1086/171637

Perley, D. A. (2014a, Apr). GRB 140428A: Keck detection of a red optical afterglow candidate. *GRB Coordinates Network*, *16180*.

Perley, D. A. (2014b, Apr). GRB 140428A: Keck redshift estimate. *GRB Coordinates Network*, *16181*.

Perley, D. A., Bloom, J. S., Butler, N. R. et al. (2008, Jan). The Troublesome Broadband Evolution of GRB 061126: Does a Gray Burst Imply Gray Dust? *ApJ*, *672*, 449-464. doi: 10.1086/523929

Perley, D. A., Bloom, J. S., Klein, C. R. et al. (2010, Aug). Evidence for supernova-synthesized dust from the rising afterglow of GRB071025 at $z \sim 5$. *MNRAS*, *406*, 2473-2487. doi: 10.1111/j.1365-2966.2010.16772.x

Perley, D. A., Cenko, S. B., Corsi, A. et al. (2014, Jan). The Afterglow of GRB 130427A from 1 to 10^{16} GHz. *ApJ*, *781*, 37. doi: 10.1088/0004-637X/781/1/37

Perley, D. A., Krühler, T., Schady, P. et al. (2017, Feb). A revised host galaxy association for GRB 020819B: a high-redshift dusty starburst, not a low-redshift gas-poor spiral. *MNRAS*, *465*, L89-L93. doi: 10.1093/mnrasl/slw221

Perley, D. A., Krühler, T., Schulze, S. et al. (2016, Jan). The Swift Gamma-Ray Burst Host Galaxy Legacy Survey. I. Sample Selection and Redshift Distribution. *ApJ*, *817*, 7. doi: 10.3847/0004-637X/817/1/7

Perley, D. A., Levan, A. J., Tanvir, N. R. et al. (2013, Dec). A Population of Massive, Luminous Galaxies Hosting Heavily Dust-obscured Gamma-Ray Bursts: Implications for the Use of GRBs as Tracers of Cosmic Star Formation. *ApJ*, *778*, 128. doi: 10.1088/0004-637X/778/2/128

Perley, D. A., Morgan, A. N., Updike, A. et al. (2011, Feb). Monster in the dark: the ultraluminous GRB 080607 and its dusty environment. *AJ*, *141*, 36. doi: 10.1088/0004-6256/141/2/36

Perley, D. A., Tanvir, N. R., Hjorth, J. et al. (2016, Jan). The Swift GRB Host Galaxy Legacy Survey. II. Rest-frame Near-IR Luminosity Distribution and Evidence for a Near-solar Metallicity Threshold. *ApJ*, *817*, 8. doi: 10.3847/0004-637X/817/1/8

Perri, M., Barthelmy, S. D., Baumgartner, W. H. et al. (2009, Feb). GRB 090205: Swift detection of a burst. *GRB Coordinates Network*, *8884*.

Petrovic, J., Langer, N., Yoon, S. C. & Heger, A. (2005, May). Which massive stars are gamma-ray burst progenitors? *A&A*, *435*, 247-259. doi: 10.1051/0004-6361:20042545

Pian, E., D'Avanzo, P., Benetti, S. et al. (2017, Nov). Spectroscopic identification of r-process nucleosynthesis in a double neutron-star merger. *Nature*, *551*, 67-70. doi: 10.1038/nature24298

Planck Collaboration. (2016, Sep). Planck 2015 results. XIII. Cosmological parameters. *A&A*, *594*, A13. doi: 10.1051/0004-6361/201525830

Pontzen, A., Governato, F., Pettini, M. et al. (2008, Nov). Damped Lyman-α systems in galaxy formation simulations. *MNRAS*, *390*, 1349-1371. doi: 10.1111/j.1365-2966.2008.13782.x

Price, P. A., Songaila, A., Cowie, L. L. et al. (2007, Jul). Properties of a Gamma-Ray Burst Host Galaxy at $z \sim 5$. *ApJ*, *663*, L57-L60. doi: 10.1086/520047

Prochaska, J. X. (2006, Oct). On the Perils of Curve-of-Growth Analysis: Systematic Abundance Underestimates for the Gas in Gamma-Ray Burst Host Galaxies. *ApJ*, *650*, 272-280. doi: 10.1086/507126

Prochaska, J. X., Chen, H.-W. & Bloom, J. S. (2006, Sep). Dissecting the Circumstellar Environment of γ-Ray Burst Progenitors. *ApJ*, *648*, 95-110. doi: 10.1086/505737

Prochaska, J. X., Sheffer, Y., Perley, D. A. et al. (2009, Jan). The First Positive Detection of Molecular Gas in a GRB Host Galaxy. *ApJ*, *691*, L27-L32. doi: 10.1088/0004-637X/691/1/L27

Prochaska, J. X., Weiner, B., Chen, H. W. et al. (2011, Oct). Probing the Intergalactic Medium/Galaxy Connection. V. On the Origin of Ly-α and OVI Absorption at $z < 0.2$. *ApJ*, *740*, 91. doi: 10.1088/0004-637X/740/2/91

Quimby, R. M., Kulkarni, S. R., Kasliwal, M. M. et al. (2011, Jun). Hydrogen-poor superluminous stellar explosions. *Nature*, *474*, 487-489. doi: 10.1038/nature10095

Rachford, B. L., Snow, T. P. & Ross, T. L. (2014, May). Vibrationally Excited Molecular Hydrogen near Herschel 36. *ApJ*, *786*, 159. doi: 10.1088/0004-637X/786/2/159

Racusin, J. L., Baumgartner, W. H., Gehrels, N. et al. (2014, Mar). GRB 140311A: Swift detection of a probable burst. *GRB Coordinates Network*, *15944*.

Rafelski, M., Neeleman, M., Fumagalli, M. et al. (2014, Feb). The Rapid Decline in Metallicity of Damped Ly-α Systems at $z \sim 5$. *ApJ*, *782*, L29. doi: 10.1088/2041-8205/782/2/L29

Rafelski, M., Wolfe, A. M., Prochaska, J. X. et al. (2012, Aug). Metallicity Evolution of Damped Lyα Systems Out to $z \sim 5$. *ApJ*, *755*, 89. doi: 10.1088/0004-637X/755/2/89

Rahmani, H., Péroux, C., Schroetter, I. et al. (2018, Nov). A Lyman limit system associated with galactic winds. *MNRAS*, *480*, 5046-5059. doi: 10.1093/mnras/sty2216

Ranjan, A., Noterdaeme, P., Krogager, J. K. et al. (2018, Nov). Molecular gas and star formation in an absorption-selected galaxy: Hitting the bull's eye at $z \approx 2.46$. *A&A*, *618*, A184. doi: 10.1051/0004-6361/201833446

Raskutti, S., Ostriker, E. C. & Skinner, M. A. (2016, Sep). Numerical Simulations of Turbulent Molecular Clouds Regulated by Radiation Feedback Forces. I. Star Formation Rate and Efficiency. *ApJ*, *829*(2), 130. doi: 10.3847/0004-637x/829/2/130

Rau, A., Schady, P., Greiner, J. et al. (2012, Feb). BL Lacertae objects beyond redshift 1.3 – UV-to-NIR photometry and photometric redshift for Fermi/LAT blazars. *A&A*, *538*, A26. doi: 10.1051/0004-6361/201118159

Robert, P. F., Murphy, M. T., O'Meara, J. M. et al. (2019, Feb). Exploring the origins of a new, apparently metal-free gas cloud at $z = 4.4$. *MNRAS*, *483*, 2736-2747. doi: 10.1093/mnras/sty3287

Robertson, B. E., Ellis, R. S., Furlanetto, S. R. & Dunlop, J. S. (2015, Apr). Cosmic Reionization and Early Star-forming Galaxies: A Joint Analysis of New Constraints from Planck and the Hubble Space Telescope. *ApJ*, *802*, L19. doi: 10.1088/2041-8205/802/2/L19

Roming, P. W. A., Kennedy, T. E. et al. (2005, Oct). The Swift Ultra-Violet/Optical Telescope. *Space Sci. Rev.*, *120*, 95-142. doi: 10.1007/s11214-005-5095-4

Rossi, A., Klose, S., Ferrero, P. et al. (2012, Sep). A deep search for the host galaxies of gamma-ray bursts with no detected optical afterglow. *A&A*, *545*, A77. doi: 10.1051/0004-6361/201117201

Rowlinson, A., Barthelmy, S. D., Baumgartner, W. H. et al. (2010, Feb). GRB 100219A: Swift detection of a burst. *GRB Coordinates Network*, *10430*.

Rowlinson, B. A., Beardmore, A. P., Evans, P. A. et al. (2009, May). GRB 090516: Swift detection of a burst. *GRB Coordinates Network*, *9374*.

Roy, N., Chengalur, J. N. & Srianand, R. (2006, Jan). A multiwavelength investigation of the temperature of the cold neutral medium. *MNRAS*, *365*, L1-L5. doi: 10.1111/j.1745-3933.2005.00114.x

Ruffini, R., Wang, Y., Aimuratov, Y. et al. (2018, Jan). Early X-Ray Flares in GRBs. *ApJ*, *852*, 53. doi: 10.3847/1538-4357/aa9e8b

Ruiz-Velasco, A. E., Swan, H., Troja, E. et al. (2007, Nov). Detection of GRB 060927 at $z = 5.47$: Implications for the Use of Gamma-Ray Bursts as Probes of the End of the Dark Ages. *ApJ*, *669*, 1-9. doi: 10.1086/521546

Salvaterra, R., Campana, S., Vergani, S. D. et al. (2012, Apr). A Complete Sample of Bright Swift Long Gamma-Ray Bursts. I. Sample Presentation, Luminosity Function and Evolution. *ApJ*, *749*, 68. doi: 10.1088/0004-637X/749/1/68

Salvaterra, R., Della Valle, M., Campana, S. et al. (2009, Oct). GRB090423 at a redshift of $z \sim 8.1$. *Nature*, *461*, 1258-1260. doi: 10.1038/nature08445

Sánchez-Menguiano, L., Sánchez, S. F., Pérez, I. et al. (2018, Feb). The shape of oxygen abundance profiles explored with MUSE: evidence for widespread deviations from single gradients. *A&A*, *609*, A119. doi: 10.1051/0004-6361/201731486

Sánchez-Ramírez, R., Ellison, S. L., Prochaska, J. X. et al. (2016, Mar). The evolution of neutral gas in damped Lyman-α systems from the XQ-100 survey. *MNRAS*, *456*, 4488-4505. doi: 10.1093/mnras/stv2732

Sanders, N. E., Betancourt, M. & Soderberg, A. M. (2015, Feb). Unsupervised Transient Light Curve Analysis via Hierarchical Bayesian Inference. *ApJ*, *800*, 36. doi: 10.1088/0004-637X/800/1/36

Sarangi, A. & Cherchneff, I. (2013, Oct). The Chemically Controlled Synthesis of Dust in Type II-P Supernovae. *ApJ*, *776*, 107. doi: 10.1088/0004-637X/776/2/107

Sari, R., Piran, T. & Narayan, R. (1998, Apr). Spectra and Light Curves of Gamma-Ray Burst Afterglows. *ApJ*, *497*, L17-L20. doi: 10.1086/311269

Savage, B. D., Bohlin, R. C., Drake, J. F. & Budich, W. (1977, Aug). A survey of interstellar molecular hydrogen. I. *ApJ*, *216*, 291-307. doi: 10.1086/155471

Savage, B. D. & Sembach, K. R. (1996, Oct). Interstellar Gas-Phase Abundances and Physical Conditions toward Two Distant High-Latitude Halo Stars. *ApJ*, *470*, 893. doi: 10.1086/177919

Savaglio, S. & Fall, S. M. (2004, Oct). Dust Depletion and Extinction in a Gamma-Ray Burst Afterglow. *ApJ*, *614*, 293-300. doi: 10.1086/423447

Savaglio, S., Glazebrook, K. & Le Borgne, D. (2009, Jan). The Galaxy Population Hosting Gamma-Ray Bursts. *ApJ*, *691*, 182-211. doi: 10.1088/0004-637X/691/1/182

Savaglio, S., Rau, A., Greiner, J. et al. (2012, Feb). Supersolar metal abundances in two galaxies at $z \sim 3.57$ revealed by the GRB 090323 afterglow spectrum. *MNRAS*, *420*, 627-636. doi: 10.1111/j.1365-2966.2011.20074.x

Saxton, C. J., Barthelmy, S. D., Beardmore, A. P. et al. (2011, Nov). GRB 111008A: Swift detection of a burst. *GRB Coordinates Network*, *12423*.

Schady, P. (2017, Jul). Gamma-ray bursts and their use as cosmic probes. *Royal Society Open Science*, *4*, 170304. doi: 10.1098/rsos.170304

Schady, P., Beardmore, A. P., Cummings, J. R. et al. (2008, Sep). GRB 080913: Swift detection of a burst. *GRB Coordinates Network*, *8217*.

Schady, P., Dwelly, T., Page, M. J. et al. (2012, Jan). The dust extinction curves of gamma-ray burst host galaxies. *A&A*, *537*, A15. doi: 10.1051/0004-6361/201117414

Schady, P., Krühler, T., Greiner, J. et al. (2015, Jul). Super-solar metallicity at the position of the ultra-long GRB 130925A. *A&A*, *579*, A126. doi: 10.1051/0004-6361/201526060

Schady, P., Savaglio, S., Krühler, T. et al. (2011, Jan). The missing gas problem in GRB host galaxies: evidence for a highly ionised component. *A&A*, *525*, A113. doi: 10.1051/0004-6361/201015608

Schaye, J. (2001, Nov). A Physical Upper Limit on the H I Column Density of Gas Clouds. *ApJ*, *562*, L95-L98. doi: 10.1086/338106

Schlafly, E. F. & Finkbeiner, D. P. (2011, Aug). Measuring Reddening with Sloan Digital Sky Survey Stellar Spectra and Recalibrating SFD. *ApJ*, *737*, 103. doi: 10.1088/0004-637X/737/2/103

Schneider, R., Omukai, K., Bianchi, S. & Valiante, R. (2012, Jan). The first low-mass stars: critical metallicity or dust-to-gas ratio? *MNRAS*, *419*, 1566-1575. doi: 10.1111/j.1365-2966.2011.19818.x

Schneider, R., Omukai, K., Limongi, M. et al. (2012, Jun). The formation of the extremely primitive star SDSS J102915+172927 relies on dust. *MNRAS*, *423*, L60-L64. doi: 10.1111/j.1745-3933.2012.01257.x

Schulze, S., Chapman, R., Hjorth, J. et al. (2015, Jul). The Optically Unbiased GRB Host (TOUGH) Survey. VII. The Host Galaxy Luminosity Function: Probing the Relationship between GRBs and Star Formation to Redshift ~ 6. *ApJ*, *808*, 73. doi: 10.1088/0004-637X/808/1/73

Selsing, J., Malesani, D., Goldoni, P. et al. (2018, Feb). The X-shooter GRB afterglow legacy sample (XS-GRB). *ArXiv e-prints*, arXiv:1802.07727.

Sharma, S. (2017, Aug). Markov Chain Monte Carlo Methods for Bayesian Data Analysis in Astronomy. *Annual Review of Astronomy and Astrophysics*, *55*, 213-259. doi: 10.1146/annurev-astro-082214-122339

Sheffer, Y., Prochaska, J. X., Draine, B. T. et al. (2009, Aug). The Discovery of Vibrationally Excited H_2 in the Molecular Cloud Near GRB 080607. *ApJ*, *701*, L63-L67. doi: 10.1088/0004-637X/701/2/L63

Siegel, M. H. & Marshall, F. E. (2010, Sep). GRB 100905A: Swift/UVOT upper limits. *GRB Coordinates Network*, *11237*.

Silvia, D. W., Smith, B. D. & Shull, J. M. (2012, Mar). Numerical Simulations of Supernova Dust Destruction. II. Metal-enriched Ejecta Knots. *ApJ*, *748*, 12. doi: 10.1088/0004-637X/748/1/12

Skrutskie, M. F., Cutri, R. M., Stiening, R. et al. (2006, Feb). The Two Micron All Sky Survey (2MASS). *AJ*, *131*, 1163-1183. doi: 10.1086/498708

Skuladottir, A. (2010). Master Thesis, Univ. Copenhagen.

Smartt, S. J. (2015, Apr). Observational Constraints on the Progenitors of Core-Collapse Supernovae: The Case for Missing High-Mass Stars. *Publications of the Astronomical Society of Australia*, *32*, e016. doi: 10.1017/pasa.2015.17

Smartt, S. J., Chen, T. W., Jerkstrand, A. et al. (2017, Nov). A kilonova as the electromagnetic counterpart to a gravitational-wave source. *Nature*, *551*, 75-79. doi: 10.1038/nature24303

Sparre, M., Hartoog, O. E., Krühler, T. et al. (2014, Apr). The Metallicity and Dust Content of a Redshift 5 Gamma-Ray Burst Host Galaxy. *ApJ*, *785*, 150. doi: 10.1088/0004-637X/785/2/150

Spitzer, J., L. & Jenkins, E. B. (1975, Jan). Ultraviolet studies of the interstellar gas. *Annual Review of Astronomy and Astrophysics*, *13*, 133-164. doi: 10.1146/annurev.aa.13.090175.001025

Srianand, R., Noterdaeme, P., Ledoux, C. & Petitjean, P. (2008, May). First detection of CO in a high-redshift damped Lyman-α system. *A&A*, *482*, L39-L42. doi: 10.1051/0004-6361:200809727

Srianand, R., Petitjean, P., Ledoux, C. et al. (2005, Sep). The VLT-UVES survey for molecular hydrogen in high-redshift damped Lyman-α systems: physical conditions in the neutral gas. *MNRAS*, *362*, 549-568. doi: 10.1111/j.1365-2966.2005.09324.x

Stanway, E. R., Levan, A. J., Tanvir, N. R. et al. (2015, Jan). A Detection of Molecular Gas Emission in the Host Galaxy of GRB 080517. *ApJ*, *798*, L7. doi: 10.1088/2041-8205/798/1/L7

Starling, R. L. C., Willingale, R., Tanvir, N. R. et al. (2013, Jun). X-ray absorption evolution in gamma-ray bursts: intergalactic medium or evolutionary signature of their host galaxies. *MNRAS*, *431*, 3159-3176. doi: 10.1093/mnras/stt400

Steglich, M., Jäger, C., Rouillé, G. et al. (2010, Mar). Electronic Spectroscopy of Medium-sized Polycyclic Aromatic Hydrocarbons: Implications for the Carriers of the 2175 Å UV Bump. *ApJ*, *712*, L16-L20. doi: 10.1088/2041-8205/712/1/L16

Steidel, C. C., Rudie, G. C., Strom, A. L. et al. (2014, Nov). Strong Nebular Line Ratios in the Spectra of $z \sim$ 2-3 Star Forming Galaxies: First Results from KBSS-MOSFIRE. *ApJ*, *795*, 165. doi: 10.1088/0004-637X/795/2/165

Sternberg, A., Le Petit, F., Roueff, E. & Le Bourlot, J. (2014, Jul). H I to H_2 Transitions and ∋ Column Densities in Galaxy Star-forming Regions. *ApJ*, *790*, 10. doi: 10.1088/0004-637X/790/1/10

Stratta, G., Gallerani, S. & Maiolino, R. (2011, Aug). Is GRB 050904 at $z = 6.3$ absorbed by dust? *A&A*, *532*, A45. doi: 10.1051/0004-6361/201016414

Stratta, G., Maiolino, R., Fiore, F. & D'Elia, V. (2007, May). Dust Properties at $z = 6.3$ in the Host Galaxy of GRB 050904. *ApJ*, *661*, L9-L12. doi: 10.1086/518502

Tacconi, L. J., Genzel, R., Smail, I. et al. (2008, Jun). Submillimeter Galaxies at $z \sim 2$: Evidence for Major Mergers and Constraints on Lifetimes, IMF, and CO-H_2 Conversion Factor. *ApJ*, *680*, 246-262. doi: 10.1086/587168

Tanga, M., Krühler, T., Schady, P. et al. (2018, Jul). The environment of the SN-less GRB 111005A at z = 0.0133. *A&A*, *615*, A136. doi: 10.1051/0004-6361/201731799

Tanvir, N. R., Fox, D. B., Levan, A. J. et al. (2009, Oct). A γ-ray burst at a redshift of $z \sim 8.2$. *Nature*, *461*, 1254-1257. doi: 10.1038/nature08459

Tanvir, N. R., Fynbo, J. P. U., de Ugarte Postigo, A. et al. (2019, Mar). The fraction of ionizing radiation from massive stars that escapes to the intergalactic medium. *MNRAS*, *483*, 5380-5408. doi: 10.1093/mnras/sty3460

Tanvir, N. R., Laskar, T., Levan, A. J. et al. (2018, Oct). The Properties of GRB 120923A at a Spectroscopic Redshift of $z \approx 7.8$. *ApJ*, *865*, 107. doi: 10.3847/1538-4357/aadba9

Tanvir, N. R., Levan, A. J., Fruchter, A. S. et al. (2012, Jul). Star Formation in the Early Universe: Beyond the Tip of the Iceberg. *ApJ*, *754*, 46. doi: 10.1088/0004-637X/754/1/46

Tanvir, N. R., Levan, A. J., Wiersema, K. & Cucchiara, A. (2014, Mar). GRB 140311A: gemini-south redshift. *GRB Coordinates Network*, *15961*.

Tchernyshyov, K., Meixner, M., Seale, J. et al. (2015, Oct). Elemental Depletions in the Magellanic Clouds and the Evolution of Depletions with Metallicity. *ApJ*, *811*, 78. doi: 10.1088/0004-637X/811/2/78

Thoene, C. C., de Ugarte Postigo, A. & Ricci, D. (2008, Aug). GRB 080825B - optical counterpart candidate. *GRB Coordinates Network*, *8135*.

Thöne, C. C. (2019, in prep.).
A&A.

Thöne, C. C., de Ugarte Postigo, A., Fryer, C. L. et al. (2011, Dec). The unusual γ-ray burst GRB 101225A from a helium star/neutron star merger at redshift 0.33. *Nature*, *480*, 72-74. doi: 10.1038/nature10611

Thöne, C. C., Fynbo, J. P. U., Goldoni, P. et al. (2013, Feb). GRB 100219A with X-shooter - abundances in a galaxy at $z = 4.7$. *MNRAS*, *428*, 3590-3606. doi: 10.1093/mnras/sts303

Todini, P. & Ferrara, A. (2001, Aug). Dust formation in primordial Type II supernovae. *MNRAS*, *325*, 726-736. doi: 10.1046/j.1365-8711.2001.04486.x

Tody, D. (1993, Jan). IRAF in the Nineties. In *Astronomical Data Analysis Software and Systems II* (Vol. 52, p. 173).

Totani, T., Aoki, K., Hattori, T. et al. (2014). Probing intergalactic neutral hydrogen by the lyman alpha red damping wing of gamma-ray burst 130606a afterglow spectrum at $z = 5.913$. *PASJ*, *66*(3), 63. doi: 10.1093/pasj/psu032

Totani, T., Kawai, N., Kosugi, G. et al. (2006, Jun). Implications for Cosmic Reionization from the Optical Afterglow Spectrum of the Gamma-Ray Burst 050904 at $z = 6.3$. *PASJ*, *58*, 485-498. doi: 10.1093/pasj/58.3.485

Tumlinson, J., Prochaska, J. X., Chen, H.-W. et al. (2007, Oct). Missing Molecular Hydrogen and the Physical Conditions of GRB Host Galaxies. *ApJ*, *668*, 667-673. doi: 10.1086/521294

Ubachs, W., Salumbides, E. J., Murphy, M. T. et al. (2019, Feb). H_2/HD molecular data for analysis of quasar spectra in search of varying constants. *A&A*, *622*, A127. doi: 10.1051/0004-6361/201834782

Ukwatta, T. N., Barthelmy, S. D., Baumgartner, W. H. et al. (2015, Oct). GRB 151027B: Swift detection of its 1000-th burst. *GRB Coordinates Network*, *18499*.

Ukwatta, T. N., Barthelmy, S. D., Evans, P. A. et al. (2009, May). GRB 090429B: Swift detection of a burst. *GRB Coordinates Network*, *9281*.

Ukwatta, T. N., Barthelmy, S. D., Gehrels, N. et al. (2013, Jun). GRB 130606A: Swift detection of a burst. *GRB Coordinates Network*, *14781*.

Utomo, D., Sun, J., Leroy, A. K. et al. (2018, Jul). Star Formation Efficiency per Free-fall Time in nearby Galaxies. *ApJ*, *861*, L18. doi: 10.3847/2041-8213/aacf8f

Valiante, R., Schneider, R., Bianchi, S. & Andersen, A. C. (2009, Aug). Stellar sources of dust in the high-redshift Universe. *MNRAS*, *397*, 1661-1671. doi: 10.1111/j.1365-2966.2009.15076.x

van den Heuvel, E. P. J. & Portegies Zwart, S. F. (2013, Dec). Are Superluminous Supernovae and Long GRBs the Products of Dynamical Processes in Young Dense Star Clusters? *ApJ*, *779*, 114. doi: 10.1088/0004-637X/779/2/114

van Paradijs, J., Groot, P. J., Galama, T. et al. (1997, Apr). Transient optical emission from the error box of the γ-ray burst of 28 February 1997. *Nature*, *386*, 686-689. doi: 10.1038/386686a0

Varela, K., van Eerten, H., Greiner, J. et al. (2016, May). Microphysics and dynamics of the gamma-ray burst 121024A. *A&A*, *589*, A37. doi: 10.1051/0004-6361/201526260

Vergani, S. D., Palmerio, J., Salvaterra, R. et al. (2017, Mar). The chemical enrichment of long gamma-ray bursts nurseries up to $z = 2$. *A&A*, *599*, A120. doi: 10.1051/0004-6361/201629759

Vergani, S. D., Salvaterra, R., Japelj, J. et al. (2015, Sep). Are long gamma-ray bursts biased tracers of star formation? Clues from the host galaxies of the Swift/BAT6 complete sample of LGRBs. I. Stellar mass at $z < 1$. *A&A*, *581*, A102. doi: 10.1051/0004-6361/201425013

Vernet, J., Dekker, H., D'Odorico, S. et al. (2011, Dec). X-shooter, the new wide band intermediate resolution spectrograph at the ESO Very Large Telescope. *A&A*, *536*, A105. doi: 10.1051/0004-6361/201117752

Virgili, F. J., Mundell, C. G., Pal'shin, V. et al. (2013, Nov). GRB 091024A and the Nature of Ultra-long Gamma-Ray Bursts. *ApJ*, *778*, 54. doi: 10.1088/0004-637X/778/1/54

Vladilo, G., Gioannini, L., Matteucci, F. & Palla, M. (2018, Dec). Evolution of the Dust Composition in Damped Ly-α Systems. *ApJ*, *868*, 127. doi: 10.3847/1538-4357/aae8dc

Volnova, A., Pozanenko, A., Korobtsev, I. et al. (2014, Mar). GRB 140304A: mondy optical observations. *GRB Coordinates Network*, *15917*.

Volnova, A., Tungalag, N., Schmalz, S. et al. (2014, Mar). GRB 140304A: khureltogot optical observations. *GRB Coordinates Network*, *15918*.

Vreeswijk, P. M., Ledoux, C., Smette, A. et al. (2007, Jun). Rapid-response mode VLT/UVES spectroscopy of GRB 060418. Conclusive evidence for UV pumping from the time evolution of Fe II and Ni II excited- and metastable-level populations. *A&A*, *468*, 83-96. doi: 10.1051/0004-6361:20066780

Vreeswijk, P. M., Ledoux, C., Smette, A. et al. (2011, Aug). Corrigendum: Rapid-response mode VLT/UVES spectroscopy of GRB 060418. Conclusive evidence for UV pumping from the time evolution of Fe II and Ni II excited- and metastable-level populations. *A&A*, *532*, C3. doi: 10.1051/0004-6361/20066780e

Vreeswijk, P. M., Savaglio, S., Gal-Yam, A. et al. (2014, Dec). The Hydrogen-poor Superluminous Supernova iPTF 13ajg and its Host Galaxy in Absorption and Emission. *ApJ*, *797*, 24. doi: 10.1088/0004-637X/797/1/24

Watson, A. M., Butler, N., Kutyrev, A. et al. (2015, Oct). GRB 151027B: RATIR Observations. *GRB Coordinates Network*, *18512*.

Watson, D. (2011, Sep). The Galactic dust-to-metals ratio and metallicity using gamma-ray bursts. *A&A*, *533*, A16. doi: 10.1051/0004-6361/201117120

Watson, D., Christensen, L., Knudsen, K. K. et al. (2015, Mar). A dusty, normal galaxy in the epoch of reionization. *Nature*, *519*, 327-330. doi: 10.1038/nature14164

Wiersema, K., Flores, H., D'Elia, V. et al. (2011, Oct). GRB 111008A: VLT/X-shooter spectroscopy. *GRB Coordinates Network*, *12431*.

Wiseman, P., Perley, D. A., Schady, P. et al. (2017, Nov). Gas inflow and outflow in an interacting high-redshift galaxy. The remarkable host environment of GRB 080810 at $z = 3.35$. *A&A*, *607*, A107. doi: 10.1051/0004-6361/201731065

Wiseman, P., Schady, P., Bolmer, J. et al. (2017, Mar). Evolution of the dust-to-metals ratio in high-redshift galaxies probed by GRB-DLAs. *A&A*, *599*, A24. doi: 10.1051/0004-6361/201629228

Wolfe, A. M., Gawiser, E. & Prochaska, J. X. (2005, Sep). Damped Ly-α Systems. *Annual Review of Astronomy and Astrophysics*, *43*, 861-918. doi: 10.1146/annurev.astro.42.053102.133950

Woosley, S. & Bloom, J. (2006). The Supernova–Gamma-Ray Burst Connection. *Annual Review of Astronomy and Astrophysics*, *44*, 507-556. doi: 10.1146/annurev.astro.43.072103.150558

Woosley, S. E. (1993, Mar). Gamma-Ray Bursts from Stellar Mass Accretion Disks around Black Holes. *ApJ*, *405*, 273. doi: 10.1086/172359

Xu, D., Bai, C.-H., Zhang, X. et al. (2014, Mar). GRB 140311A: nanshan afterglow decay. *GRB Coordinates Network*, *15956*.

Xu, D., de Ugarte Postigo, A., Leloudas, G. et al. (2013, Oct). Discovery of the Broad-lined Type Ic SN 2013cq Associated with the Very Energetic GRB 130427A. *ApJ*, *776*, 98. doi: 10.1088/0004-637X/776/2/98

Xu, D., Fynbo, J. P. U., D'Elia, V. & Tanvir, N. R. (2012, Jul). GRB 120712A: VLT/Xshooter redshift. *GRB Coordinates Network*, *13460*.

Xu, D., Malesani, D., Schulze, S. et al. (2013, Jun). GRB 130606A: VLT/X-shooter redshift confirmation. *GRB Coordinates Network*, *14816*.

Xu, D., Niu, H.-B., Feng, G.-J. et al. (2014, Mar). GRB 140304A: afterglow decay from nanshan observations. *GRB Coordinates Network*, *15916*.

Xu, D., Tanvir, N. R., Malesani, D. & Fynbo, J. P. U. (2015, Oct). GRB 151027B: VLT/X-shooter redshift. *GRB Coordinates Network*, *18506*.

Yan, L., Perley, D. A., De Cia, A. et al. (2018, May). Far-UV HST Spectroscopy of an Unusual Hydrogen-poor Superluminous Supernova: SN2017egm. *ApJ*, *858*, 91. doi: 10.3847/1538-4357/aabad5

Yershov, V. N., Barthelmy, S. D., Krimm, H. A. et al. (2012, Sep). GRB 120923A: Swift detection of a burst. *GRB Coordinates Network*, *13796*.

Yoon, S. C. & Langer, N. (2005, Nov). Evolution of rapidly rotating metal-poor massive stars towards gamma-ray bursts. *A&A*, *443*, 643-648. doi: 10.1051/0004-6361:20054030

Zafar, T., Heintz, K. E., Fynbo, J. P. U. et al. (2018, Jun). The 2175 Å Extinction Feature in the Optical Afterglow Spectrum of GRB 180325A at $z = 2.25$. *ApJ*, *860*, L21. doi: 10.3847/2041-8213/aaca3f

Zafar, T., Møller, P., Watson, D. et al. (2018, Oct). X-shooting GRBs at high redshift: probing dust production history. *MNRAS*, *480*, 108-118. doi: 10.1093/mnras/sty1876

Zafar, T., Watson, D., Elíasdóttir, Á. et al. (2012, Jul). The Properties of the 2175 Å Extinction Feature Discovered in GRB Afterglows. *ApJ*, *753*, 82. doi: 10.1088/0004-637X/753/1/82

Zafar, T., Watson, D., Fynbo, J. P. U. et al. (2011, Aug). The extinction curves of star-forming regions from $z = 0.1$ to 6.7 using GRB afterglow spectroscopy. *A&A*, *532*, A143. doi: 10.1051/0004-6361/201116663

Zafar, T., Watson, D., Møller, P. et al. (2018, May). VLT/X-shooter GRBs: Individual extinction curves of star-forming regions. *MNRAS*, 1320. doi: 10.1093/mnras/sty1380

Zafar, T., Watson, D. J., Malesani, D. et al. (2010, Jun). No evidence for dust extinction in GRB 050904 at $z \sim 6.3$. *A&A*, *515*, A94. doi: 10.1051/0004-6361/200913795

Zafar, T., Watson, D. J., Tanvir, N. R. et al. (2011, Jul). Exploring Dust Extinction at the Edge of Reionization. *ApJ*, *735*, 2. doi: 10.1088/0004-637X/735/1/2

Zaninoni, E., Bernardini, M. G., Margutti, R. et al. (2013, Sep). Gamma-ray burst optical light-curve zoo: comparison with X-ray observations. *A&A*, *557*, A12. doi: 10.1051/0004-6361/201321221

Zhang, B., Fan, Y. Z., Dyks, J. et al. (2006, May). Physical Processes Shaping Gamma-Ray Burst X-Ray Afterglow Light Curves: Theoretical Implications from the Swift X-Ray Telescope Observations. *ApJ*, *642*, 354-370. doi: 10.1086/500723

Zuo, P., Li, D., Peek, J. E. G. et al. (2018, Nov). Catching the Birth of a Dark Molecular Cloud for the First Time. *ApJ*, *867*, 13. doi: 10.3847/1538-4357/aad571

Zwaan, M. A. & Prochaska, J. X. (2006, Jun). Where is the Molecular Hydrogen in Damped Ly-α Absorbers? *ApJ*, *643*, 675-679. doi: 10.1086/503191

Acknowledgements

I would like to thank everyone who has significantly influenced the content of this thesis and those who made this work possible. First and foremost, my supervisor Jochen Greiner, for giving me the opportunity to work in this exciting research area, as well as for his constant advice and feedback throughout the years. The same goes for Patrica Schady and Cédric Ledoux, from whom I learned a lot. I also thank all members of the GROND team and the STARGATE collaboration. In particular, Thomas Krühler, Jonathan Selsing, and Phillip Wiseman, for providing their knowledge, as well as some code and data products.